Towards Automation of Continuous Chemoenzymatic Syntheses of Plasticizers, Nitriles, and Chiral Esters from Renewable Resources

Dissertation

by Niklas Adebar

Faculty of Chemistry
Bielefeld University

"If we knew what it was we were doing, it would not be called research, would it?"

– Albert Einstein

1. Reviewer	Prof. Dr. Harald Gröger Industrial Organic Chemistry and Biotechnology Faculty of Chemistry, Bielefeld University 33615, Bielefeld, Germany.
2. Reviewer	Prof. Dr. Berthold Hoge Anorganische Chemie II Faculty of Chemistry, Bielefeld University 33615, Bielefeld, Germany.

The presented work was conducted from the 1st October 2018 until the 31st August 2021 at the Bielefeld University (Germany) under the supervision of Prof. Dr. Harald Gröger (Bielefeld University). Parts of this work were conducted at Osaka University, Japan, under the supervision of Prof. Dr. Shuji Akai (24th October 2018 to 8th December 2018) and at the University of Cambridge, UK, under the supervision of Prof. Dr. Steven V. Ley (3rd June 2019 to 19th July 2019).

Funding was received from the *Bundesministerium für Bildung und Forschung* (BMBF) through the project "Bio-Weichmacher II" (Grand No. 031B0585B) as well as the *Deutscher Akademische Austauschdienst* (DAAD) and the Japan Society for Promotion of Science (JSPS) for the research stay in Japan "DAAD PPP Japan 2017/2018" (Grand No. 57345562).

I hereby confirm that I am the sole author of this written work and this work is not submitted in any form elsewhere. I have documented all methods, data, and procedures truthfully, and I have clearly referenced all sources used in this work to the best of my knowledge. No 3rd party received any kind of monetary benefits related to the content of this work from my side. This dissertation was approved by the Faculty of Chemistry of the Bielefeld University based on the known "Promotionsordnung vom 01. Juli 2011".

Niklas Adebar

Acknowledgments

Obwohl ein einzelner Autor auf dieser Arbeit steht, wäre sie nicht ohne die Hilfe und Unterstützung zahlreicher Leute möglich gewesen. Vielen Dank an all jene, die einen Beitrag dazu geleistet haben!

Zunächst möchte ich mich herzlich bei meinem Doktorvater Prof. Dr. Harald Gröger bedanken, der mir die Gelegenheit gab, an diversen spannenden Themen forschen zu dürfen. Vielen Dank für Deine großartige Betreuung und die außerordentliche wissenschaftliche Freiheit und das damit verbundene Vertrauen in meine Arbeit.

Herrn Prof. Dr. Berthold Hoge möchte ich für die freundliche Übernahme des Zweitgutachtens herzlich danken.

Für große Teile der Finanzierung dieser Arbeit im Rahmen des „Bio-Weichmacher II“ Projekts (Födernummer: 031B0585B) möchte ich dem Bundesministerium für Bildung und Forschung (BMBF) danken. Weitere Förderung wurde dankend von dem Deutschen Akademischen Austauschdienst (DAAD) und der Japan Society for Promotion of Science (JSPS) im Rahmen des gemeinsam geförderten Projektes „DAAD PPP Japan“ (Fördernummer: 57345562) erhalten.

Dem „Bio-Weichmacher“ Team möchte ich für die hervorragende Zusammenarbeit danken. Auf Seiten der TUHH Prof. Dr. Andreas Liese, Dr. Robert Hiessl und Dr. Stefan Wahlefeld für die netten Projektbesprechungen und die nachfolgenden geselligen Abende. Auf der Seite der BASF SE möchte ich vor allem Dr. Axel Grimm für die spannenden Diskussionen über Weichmacher, Dr. Rainer Otter für seine offene Art und die netten Gespräche sowie Dr. Angelika Langsch danken.

Insbesondere danke ich Prof. Dr. Shuji Akai für die herzliche Aufnahme in seiner Arbeitsgruppe in Osaka, Japan und die spannenden wissenschaftlichen Diskussionen. Auch möchte ich der gesamten Arbeitsgruppe „Seizo“ für die überwältigende Gastfreundschaft danken. Vor allem Satoko Katsuragi und Koichi Higashio für die fantastische Zeit, abenteuerlichen Ausflüge und den Einblick in die japanische Kultur. ありがとうございます

Vielen Dank an Prof. Dr. Steven V. Ley für die herzliche Aufnahme in seiner Arbeitsgruppe in Cambridge, UK, die hilfreichen Tipps rund um die Flow Chemie, sowie die bereichernden (nicht nur) wissenschaftlichen Diskussionen. Riesigen Dank an Dr. Daniel Fitzpatrick für eine hervorragende Kooperation, auch beim Trinken von „Mexikanern“, für die Hilfe beim Aufbau einer Closed-Loop Optimierungsplattform und für das Lehren des „punting“. Vielen Dank an Oliver May und Dr. Yiding Chen für die Gastfreundschaft und den tollen Einblick in Cambridge und das College Leben. Danke an Dr. Ricardo Labes und viele weitere für die wissenschaftliche sowie organisatorische Hilfe und die großartige Zeit. Jacqui Worster möchte ich herzlich für die Organisation des Aufenthaltes danken. *Thank you so much!*

Die Zusammenarbeit mit dem „ONE-Flow“ Projektteam war ebenfalls ein Highlight. Vielen Dank für die wissenschaftliche Diskussionen, großartige Zusammenarbeit und vor allem geselligen Abende nach den Projettreffen an alle Beteiligten.

Diese Arbeit hätte ohne eine reibungslos funktionierende Infrastruktur nicht umgesetzt werden können. Insbesondere den wertvollen Werkstätten der Fakultät möchte ich einen großen Dank aussprechen. In der mechanischen Werkstatt wurden diverse komplexe Geräte in atemberaubender Zeit hergestellt. Ganz großen Dank an Andreas Helfmann für die Umsetzung der abenteuerlichsten Apparaturen und auch die netten Gespräche. Danke auch an Leo Walters und den Rest des Teams für die präzise Arbeit. Da Elektrotechnik sicherlich nicht einer meiner Schwerpunkte war, bin ich für die Hilfe der Elektronikwerkstatt der Fakultät sehr dankbar. Vor allem hat Julius Lahnt bei der Durchführung des Reaktorprojekts und seinen unermüdlichen und enthusiastischen Einsatz viel zu dessen Verwirklichung beigetragen. Auch standen Petra Albrecht und Andreas Lüdeke stets mit wertvollem Rat und Tat zur Seite.

Die diversen Sonder- und Elektronikbestellungen im Chemikalienlager wurden auch in der Lockdown Zeit mit vollem Einsatz von Heike Kosellek, Silke Hansen und Meike Adolph durchgeführt — Danke dafür!

Auch den Analytikeinheiten möchte ich für die Durchführung der Untersuchungen und das Instandhalten der Geräte danken. Marco Wißbrock im NMR Labor sowie Heinz-Werner Patruck, Sandra Heitkamp und Dr. Jens Sproß im MS Labor. Heinz-Werner und Dr. Michael Letzgus-Koppmann möchte ich für die Unterstützung bei IT-Herausforderungen danken.

Natürliche gebührt dem fantastischen IOCB Team ein enormer Dank. Ohne ein besetztes Sekretariat fehlte zwischenzeitlich ein Herzstück der Arbeitsgruppe — vielen Dank an Angelika Bendick für die großartige Organisation über die Jahre und vielen Dank an Ulrike Kraßort für das Ausfüllen dieser großen Fußstapfen! Danke an Dr. Anke Hummel nicht nur für das zwischenzeitliche provisorische Übernehmen dieser Stelle, sondern vor allem für die alltägliche Unterstützung im Labor und in der Lehre, sowie das Lehren der Grundlagen der Biochemie. Vielen Dank an die beiden unermüdlichen Techniker, ohne die das Labor nicht laufen würde: Anika Hegemann und Thomas Geisler. Danke für die spannende gemeinsame Zeit in Cambridge und Deine ständige Hilfe bei unzählbaren Dingen, Anika. Ganz großen Dank an Thomas für die Hilfe mit diversen Laborgeräten und Deine herzliche und direkte Art.

Über die Jahre hatte ich das Privileg, diverse Studierende betreuen zu dürfen und auch von ihnen im Gegenzug viel zu lernen. Danke für die tatkräftige Unterstützung an die Hiwis Manuel Diedrich und Cedric Scholz und die Masterstudierenden Nils Marquard, Manuel Warkentin und Yuri Kono. Loris Mendrina, der die Betreuung seiner Bachelorarbeit durch seine engagierte Art sehr einfach gemacht hat, möchte ich dafür danken.

Für den unbezahlbaren Beitrag zu dieser Arbeit, die ohne ihn sicherlich nicht so ausgefallen wäre, möchte ich Manuel Diedrich danken. Als Hiwi und Bachelor hast Du Dich stets mit mehr als vollem Einsatz dem Projekt gewidmet und mit brillanten Ideen die Arbeit sehr bereichert. Ich habe die Zeit mit Dir im Labor sehr genossen!

Auch wenn es in der Corona-Zeit nur spärlich besetzt war, möchte ich meinen Laborpartnern im F3-264 für die schöne Zeit danken. Vielen Dank

an Dr. Alessa Hinzmann für das herzliche Willkommen im Labor und die riesige Hilfe bei unzähligen biochemischen Fragestellungen. Danke für das Teilen Deiner Expertise und die schöne Zeit! Vielen Dank an Lukas Schober für Deine erheiternde Art und die lustige Zeit bei den ONE-Flow Projektmeetings und im Labor. Bastian Altemeier und Tim Guntelmann möchte ich ebenfalls für die schöne Zeit danken, auch wenn wir uns durch den Schichtbetrieb nur selten gesehen haben.

Vielen Dank an das IOCB Weichmacher Team Dr. Carmen Plass und Bastian Altemeier für die schöne und fruchtvolle Zeit. Danke Carmen für die schönen Dienstreisen einmal um die Welt, bei denen ich nicht nur sehr viel Spaß hatte, sondern auch viel von Dir gelernt habe. Danke für Deine wertvolle Hilfe, nicht nur bei dem Projekt!

Für die großartige Zusammenarbeit möchte ich auch dem Flow/Automatisierungsteam danken: Alina Nastke und Dr. Micol Santi. Danke für die erfolgreiche und sehr angenehme Zusammenarbeit bei der Flow Chemie und für Deine liebe Art, Alina. Es war mir immer eine große Freude mit Dir über Wissenschaft, oder oft auch nicht Wissenschaft, zu quatschen. Besonders freut mich, dass Micol den Weg nach Bielefeld gefunden hat und ich das Privileg genießen durfte wieder (vielleicht nicht das letzte Mal?) mit ihr zusammenzuarbeiten. Ich hoffe Bielefeld ist für Dich auch ein Stück zu Hause geworden – trotz der verrückten Zeiten. *Grazie mille per il tempo meraviglioso, ho imparato molto da voi.*

Vielen Dank an das Team der "alten OC1", sowie der "neuen IOCB". So wie der Name sich geändert hat, haben sich über die Zeit die Gesichter geändert. Herzlich aufgenommen wurde ich in der OC1 von Dr. Tobias Betke, Dr. Ji-Eun Choi, Drs. Michael und Alessa Hinzmann, Jannis Nonnhoff, Dr. Franziska Kühn, Dr. Jana Löwe, Dr. Keiko Oike, Dr. Carmen Plass, Dr. Matthias Pieper, Dr. Phillip Rommelmann, Lukas Schober, Dr. Florian Uthoff, Dr. Hilmi Yavuzer und Dr. Nadine Zumbrägel. Danke, dass ihr mir den Einstieg so leicht gemacht habt und ich so viel von Euch lernen durfte!

Den vielen großartigen Leuten sind ebenso großartige gefolgt, welche sich mit frischem Wind und Enthusiasmus wunderbar eingebracht haben: Adil Allahverdiyev, Bastian Altemeier, Laura Bernhard, Hannah Bork, Tim Guntelmann, Alina Guntermann, Seika Ishii, Luisa Koch, Alina Nastke,

Dr. Micol Santi, Karla Wagner und Jianing Yang. Großen Dank an Hannah und Karla für Eure Hilfe bei biochemischen Fragestellungen.

Zudem möchte ich den vielen anderen Forschenden in der Chemie danken, vor allem meinen ehemaligen Kommilitonen. Insbesondere Erik Stratmann, der immer ein offenes Ohr sowie guten Rat für mich hatte. Ebenfalls möchte ich der "zugezogenen" Hammer Gruppe für die geselligen Abende danken.

Für das Korrekturlesen dieser Arbeit möchte ich Manuel Diedrich, Alina Nastke, Dr. Micol Santi sowie Karla Wagner ganz herzlich danken. Auch Scibbr B.V. möchte ich für das Korrekturlesen eines kleinen Teils dieser Arbeit danken.

Abseits der Wissenschaft spielt das Leben – für diese stete Erinnerung möchte ich zahlreichen Menschen danken. Allem voran meiner Familie, die mich immer und jederzeit unterstützt, gestützt und motiviert hat. Danke, dass ihr mein ganzes Leben schon für mich da seid. Danke, dass ihr immer an mich glaubt.

Alte und neu geschlossene Freundschaften waren ein stabiles Fundament, ohne das diese Arbeit in sich zusammengefallen wäre. Vielen Dank an all die großartigen Freunde in der alten Heimat (auch, wenn es viele mittlerweile in die Ferne gezogen hat), an die Freunde in Bielefeld und rund um die Welt. Großartige Freundschaften sind die, die auch in diesen herausfordernden Zeiten bestehen. Danke, dass ihr mein Leben so sehr bereichert.

Publications

Parts of this work were previously published, submitted for future publication or presented in talks and posters.

Publications

[1] Plass, C., Adebar, N., Hiessl, R., Kleber, J., Grimm, A., Langsch, A., Otter, R., Liese, A. & Gröger, H. Structure-performance guided design of sustainable plasticizers from bio-renewable feedstocks. *Eur. J. Org. Chem.* accepted for publication.

[2] Adebar, N., Nastke, A., Löwe, J. & Gröger, H. Segmented Flow Processes to Overcome Hurdles of Whole-Cell Biocatalysis in the Presence of Organic Solvents. *Angew. Chem. Int. Ed.*, **60**, 15863–15869 (2021).

[3] Adebar, N., Nastke, A. & Gröger, H. Concepts for flow chemistry with whole-cell biocatalysis. *React. Chem. Eng.*, **6**, 977–988 (2021).

[4] Adebar, N. & Gröger, H. Heterogeneous Catalysts "on the Move": Flow Chemistry with Fluid Immobilised (Bio)Catalysts. *Eur. J. Org. Chem.*, 6062–6067 (2020).

[5] Higashio, K., Katsuragi, S., Kundu, D., Adebar, N., Plass, C., Kühn, F., Gröger, H. & Akai, S. Continuous-Flow Dynamic Kinetic Resolution of Racemic Alcohols by Lipase–Oxovanadium Cocatalysis. *Eur. J. Org. Chem.*, 1961–1967 (2020).

[6] Adebar, N. & Gröger, H. Flow Process for Ketone Reduction Using a Superabsorber-Immobilized Alcohol Dehydrogenase from Lactobacillus brevis in a Packed-Bed Reactor. *Bioengineering*, **6**, 99 (2019).

[7] Adebar, N., Choi, J. E., Schober, L., Miyake, R., Iura, T., Kawabata, H. & Gröger, H. Overcoming Work-Up Limitations of Biphasic Biocatalytic Reaction Mixtures Through Liquid-Liquid Segmented Flow Processes. *ChemCatChem*, **11**, 5788–5793 (2019).

[8] Hinzmann, A., Adebar, N., Betke, T., Leppin, M. & Gröger, H. Biotransformations in pure organic medium with organic solvent-labile enzymes in batch and flow exemplified for nitrile synthesis. *Eur. J. Org. Chem.*, 6911–6916 (2019).

[9] Schober, L., Ratnam, S., Yamashita, Y., Adebar, N., Pieper, M., Berkessel, A., Hessel, V. & Gröger, H. An Asymmetric Organocatalytic Aldol Reaction of a Hydrophobic Aldehyde in Aqueous Medium Running in Flow Mode. *Synthesis*, **51** (5), 1178–1184 (2019).

Talks & Posters

Oral presentation – Biocatalysis in Flow Processes. *GDCh Wissenschaftsforum Chemie*, Aachen (2019).

Poster presentation – Overcoming Work-Up Limitations of Biphasic Biocatalytic Reaction Mixtures Through Liquid-Liquid Segmented Flow Processes. *13th International CeBiTec Symposium Multi-Step Syntheses in Biology & Chemistry - An International Young Investigator Conference*, Aachen (2019).

Poster presentation – Biobased Plasticizer for Application in Polyvinyl Chloride "IBÖ-4: BioWeichmacher". *Jahrestreffen 2020 Ideenwettbewerb – Neue Produkte für die Bioökonomie*, Berlin (2019).

Abbreviations

General

ABE	acetone–butanol–ethanol fermentation
API	in chemical context: active pharmaceutical ingredient
API	in technical context: application programming interface
BMBF	*Bundesministerium für Bildung und Forschung*
BPR	back pressure regulator
CAD	computer-aided design
CPU	central processing unit
CSS	cascading style sheets
csv	comma separated value
CV	column volume
DA	Diels-Alder reaction
DC	direct current
DIN	*Deutsches Institut für Normung*
DKR	dynamic kinetic resolution
DoE	design of experiments
EDG	electron-donating group
ee	enantiomeric excess
ELS	evaporative light scattering
EN	European norm

ESI	electrospray ionization
EWG	electron-withdrawing group
FID	flame ionization detector
FID	free induction decay
FMO	frontier molecular orbital
GC	gas chromatography
GPIO	General Purpose Input/Output
GUI	graphical user interface
HOMO	highest occupied molecular orbital
HPLC	high-performance liquid chromatography
HTML	HyperText Markup Language
ID	inner diameter
IP	Internet protocol
ISO	international organization for standardization
J	coupling constant
JS	JavaScript
JSON	JavaScript object notation
LA	Lewis acid
LED	light-emitting diode
LUMO	lowest unoccupied molecular orbital
MALDI	matrix-assisted laser desorption/ionization
MS	mass spectrometry
n.d.	not determined
NM	Nelder-Mead algorithm (also: Downhill simplex)
NMR	nuclear magnetic resonance
PAT	process analysis technologies
PBR	packed bed reactor
PC	personal computer
PE	in context of electronics: protective earth

PFR	plug flow reactor
PID	proportional-integral-derivative (controller)
PR	phase ratio (here: organic/aqueous volume)
PVC	polyvinyl chloride
Q	flow rate or volumetric flow
rt	room temperature
SOHIO	Standard Oil of Ohio
SSF	simultaneous saccharification and fermentation process
SSH	secure shell
STY	space time yield
τ	residence time
TCP	transmission control protocol
TON	turnover number
TTL	transistor-transistor logic
U.S.	United States of America
UART	universal asynchronous receiver-transmitter
UI	user interface
UK	United Kingdom of Great Britain and Northern Ireland
USB	universal serial bus
VPN	virtual private network

Glossary

class	in Python: blueprint for an object
conversion	percentage of product(s) in relation to starting material
dictionary	in Python: list of key:value pairs
Flask	Python server framework
for loop	definite loop
mass transfer	here, transport of chemical species
object	in JS: list of key:value pairs, in Python: object in object-oriented programming
packed bed reactor	usually, tubular vessel packed with e.g. a catalyst
Python/JS library	(publicly) available modules/code blocks for python or JavaScript
residence time	the time substrate spends in the reactor, in batch: reaction time
segmented flow	or *snug flow*, biphasic (gas-liquid, liquid-liquid) system with alternating compartments
space time yield	short STY, produced amount of compound per time and reactor volume
while loop	indefinite loop
yield	amount of isolated product
reactor volume	effective usable volume of a reactor, in case of a packed bed reactor equal to the void volume

Chemicals

2-EH	2-ethylhexanol
ACN	acetonitrile
ADH	alcohol dehydrogenase
bmim	1-butyl-3-methylimidazolium hexafluorophosphate
CAL-B	*Candida antarctica* lipase B
DCM	dichloromethane
DEHA/-DOA	bis(2-ethylhexyl) adipate
DEHP	(bis(2-ethylhexyl) phthalate
dH_2O	deionised water
DINCH	diisononyl cyclohexane-1,2-dicarboxylate
DINP	diisononyl phthalate
DMAP	4-(dimethylamino)-pyridine
DMC	dimethyl carbonate
DOCH	bis(2-ethylhexyl) cyclohexane-1,2-dicarboxylate
HMF	5-(hydroxymethyl)furfural
MTBE	2-methoxy-2-methylpropane
OTf	trifluoromethanesulfonate
Oxd	oxime dehydratase
OxdB	oxime dehydratase from *Bacillus* sp.
PE	in context of chemicals: polyethylene
PEEK	polyether ether ketone
PFA	perfluoroalkoxy alkane
PPB	potassium phosphate buffer
PTFE	poly(tetrafluoroethylene)
TEMPO	(2,2,6,6-tetramethylpiperidin-1-yl)oxyl
THF	tetrahydrofuran

Contents

1 Abstract

The combination of sustainable chemistry, automation, and biotechnology enables the rapid development of state-of-the-art syntheses. Through the symbiotic use of cutting-edge process tools—flow chemistry, closed-loop optimization, and biocatalysis—efficient processes for fine and bulk chemicals were developed in this work. A novel bicyclic oxo-bridged diester plasticizer was synthesized from renewable starting materials like 2-methylfuran and bis(2-ethylhexyl) maleate in a Diels-Alder reaction with subsequent hydrogenation. Furthermore, it was successfully tested in an application in polyvinyl chloride and a structure-function relationship was concluded from the results and the comparison to similar structures.

Moreover, a closed-loop optimization platform for continuous synthesis was developed. This system featured a simple user interface, remote control, integration of various lab devices, and a Nelder-Mead optimization algorithm. A standard gas chromatograph was modified to allow remote access and automated analysis from the reaction stream by the control system. In addition, a modular reactor system for milliliter-scale batch and flow reactors was designed, built, and integrated into the closed-loop system.

This system was applied to one crucial step of a continuous reaction cascade towards renewable nitriles. Starting from a bio-based fatty alcohol, 1-octanol, an aldehyde was generated by nitroxyl radical-catalyzed oxidation, which was then condensed in flow with hydroxylamine to form an aldoxime. A final biocatalyzed dehydration using an aldoxime dehydratase yielded the desired nitrile. A segmented flow process for the biocatalytic step outperformed the batch process by increasing conversion up to fivefold and the yield by 18%—all with a vastly simplified downstream thanks to reduced emulsification. Meanwhile, the oxime formation provided an ideal reaction system to test the closed-loop platform.

Finally, an innovative approach to avoid the formation of undesired byproducts during the dynamic kinetic dissolution of secondary alcohols was described. The use of a dual-catalyst gradient packed bed reactor loaded with immobilized vanadium and lipase successfully suppressed the side-product formation, while simultaneously minimizing the catalyst demand.

Introduction 2

Despite all the detailed protocols, explanatory theories, and rational designs, chemistry relies mostly on intuition and experience—even today. Certainly, this is one of the reasons slowing down digitalization in chemistry. Originality and years of practical experience are difficult to replace with automated systems. Nevertheless, digitalization is an emerging research area in synthesis and has proven to enrich chemical research.

Today, chemists have more and more helpful digital tools at their disposal. Digitalization in synthesis takes many forms: Modeling, data analysis or simulation are just some of the areas. One of the most useful tools for day-to-day laboratory work is undoubtedly automation. It frees chemists from tedious, repetitive tasks and leaves them more time for other work. Often, these repetitive operations can be performed in a more reproducible manner. In the future, chemists will work hand in hand with robots to solve current and future challenges. Safer processes can be realized with the help of remote control and process analysis technologies. With data-driven decision-making, potentially more reliable results and a better understanding of the process are possible.

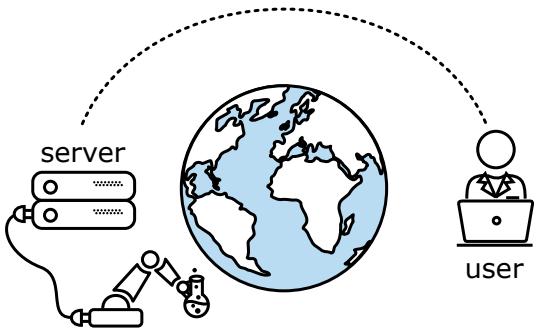

Figure 2.1: Illustration of a remote-controlled automated synthesis system. The user is remotely connected to a server that controls and conducts the experiments.

One technology that can benefit from symbiosis with automation is flow chemistry. In contrast to reactions carried out in batch reactors, flow systems offer stable and continuous production. Combined with automated in-line analysis and optimization algorithms, closed-loop reaction optimization can be realized (Figure 2.1). Compared to batch chemistry, often more efficient processes can be designed with flow tools due to the high mass and heat transfer.

A big challenge for which efficient chemical processes are crucial is climate change. In chemical process design, this problem is also addressed by switching feedstocks to renewable resources. Moreover, efficient and resource-saving synthesis routes based on biocatalysis are also part of a solution to avoid global warming and combat rapid resource depletion. Biocatalysts allow sustainable processes, as they only require ambient temperatures and operate in aqueous solvent systems. Additionally, side products can be avoided thanks to high chemo- and stereoselectivity.

Not only do the processes need to be improved to enable green synthesis, but also the feedstocks are of great importance. Fueled by availability and cheap access, petrochemical resources have been the main source of carbon building blocks in recent decades. Many industries today are shifting to renewable resources such as lignocellulose, vegetable oils or green hydrogen. Streams of municipal or industrial process waste are also progressively considered as valuable materials.

Goals and Concept 3

The aim of this work is to combine organic synthesis with digital and biotechnological tools as well as renewable feedstocks to develop sustainable processes for bulk chemicals. Projects for multiple synthetic routes for bulk and fine chemicals are presented in four chapters.

In the first chapter, the development of a novel, sustainable plasticizer candidate as an alternative to phthalate-based products is described (Scheme 3.1). The plasticizer will be synthesized starting from renewable 2-methylfuran and bis(2-ethylhexyl) maleate. A two-step synthesis starting with a Diels-Alder reaction and a final hydrogenation will be investigated. After a sample was prepared, the product will be tested and analyzed by colleagues at BASF SE for its applicability in polyvinyl chloride. From these results and the results of Plass for similar compounds, a structure-function relationship will be derived.

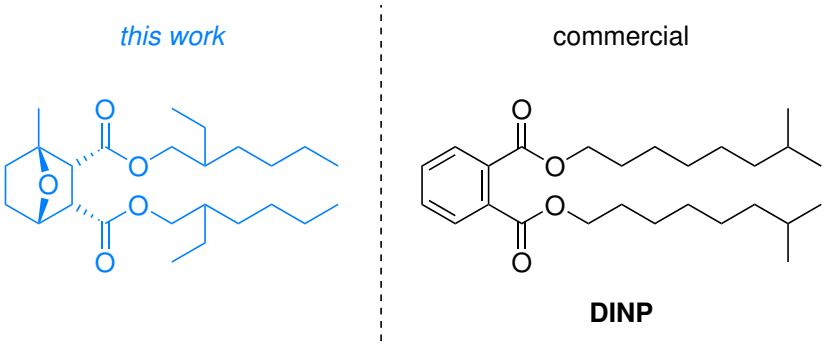

Scheme 3.1: Targeted plasticizer candidate (left) and commercial phthalate-based plasticizer (right). DINP, diisononyl phthalate.

In Chapter 5, the development of a closed-loop optimization platform is described (Figure 3.1). This platform will enable automated and remote-controlled reaction optimization of continuous reactions. A Nelder-Mead

algorithm will be implemented and a local, script-based program for initial testing will be written. Moreover, a gas chromatography system will be integrated for automated online analysis. To realize this, modules for data analysis, communication, and automation of the gas chromatography software will be programmed. The system will furthermore be modified on the hardware level to support automated analysis from a reaction stream. In addition, the design and realization of a reactor for precise temperature control of flow and milliliter-scale batch modules are presented.

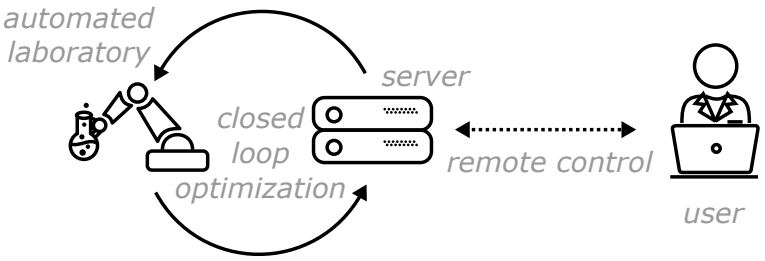

Figure 3.1: Concept of the closed-loop optimization platform.

Following this chapter, the continuous synthesis of nitriles starting from renewable fatty alcohols is introduced (Figure 3.2). In an initial TEMPO-catalyzed ((2,2,6,6-tetramethylpiperidin-1-yl)oxyl) oxidation, the alcohol will be converted to the corresponding aldehyde, which will then be condensed with hydroxylamine to form the aldoxime. Finally, this aldoxime will be dehydrated to the nitrile. Continuous syntheses will be shown for all three reaction steps. The oxime formation step will additionally serve as a test and benchmarking system for the developed closed-loop optimization platform. After a first insight into the process parameters through manual experiments, an algorithm-assisted optimization of the reaction will be performed. Ultimately, the reaction will be optimized fully automated using the developed system. Two different methods will be investigated and compared for the bio-catalytic oxime dehydration. One approach will be based on a novel concept of mobile immobilized catalysts using segmented hydrogel-organic flow, while the other will be based on biphasic segmented liquid-liquid flow.

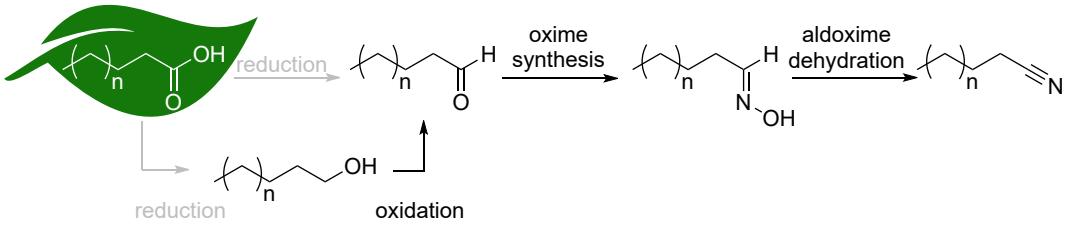

Figure 3.2: Reaction sequence for the synthesis of aliphatic nitriles starting from renewable fatty acids.

In the last chapter, the results of a collaborative project with Shuji Akai's group are presented. The aim of this project is the reduction of side product formation in a continuous dynamic kinetic resolution of secondary alcohols (Scheme 3.2). After investigating the reactions (lipase-catalyzed kinetic resolution and vanadium-catalyzed racemization) separately, a unique approach will be demonstrated using a gradient packed-bed reactor.

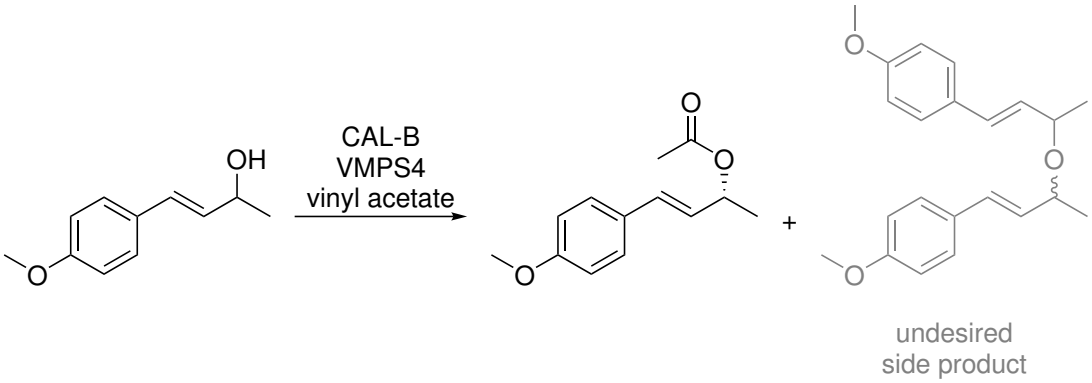

Scheme 3.2: Schematic dynamic kinetic resolution of a secondary alcohol into the acetate under the formation of an ether side product.

4 Synthesis of Novel Plasticizer Candidates

» In this project, novel, sustainable plasticizer candidates were synthesized. Application tests in polyvinyl chloride of the developed compounds were carried out by the BASF SE. Starting from renewable feedstocks, a replacement for the widely used, petrochemical-based state-of-the-art products like phthalate-based compounds was targeted. Another aspect was the potentially advantageous toxicity compared to products on the market. «

4.1 Theoretical Background

4.1.1 Sustainable Resources

In a world of steady climate change[1] and rapid resource depletion[2], alternatives to petrochemical-based resources are required. To meet the targets of the Paris agreement on climate change, swift action not only in personal mobility and the energy sector but also in the chemical industry must be taken.[3] 190 parties signed the Paris agreement until today.[4] While changing feedstocks for bulk chemicals often is challenging and expensive, efforts to make products more environmentally friendly can also be combined with the development of novel products. Sustainability generally refers to a number of concepts, such as clean energy, mindful agriculture or green technologies that allow nature and people to live in coexistence. Closely related, and often interchangeably used, is the term renewable resources. These are materials, which are considered non-depleting like solar energy or wood if exploited at an adequate rate.

Starting from nature, sustainable products can be produced in four steps (Figure 4.1). The first step is to harvest the bio-based resources (Figure 4.1; 1). Then, they are processed to platform chemicals such as 2-methylfuran (Figure 4.1; 2). High-value chemicals, such as plasticizers or lubricants, can be synthesized from these raw chemicals (Figure 4.1; 3). Finally, these chemicals can be used for the production of commercial goods like cable insulation, medical tubing or rubber toys (Figure 4.1; 4).

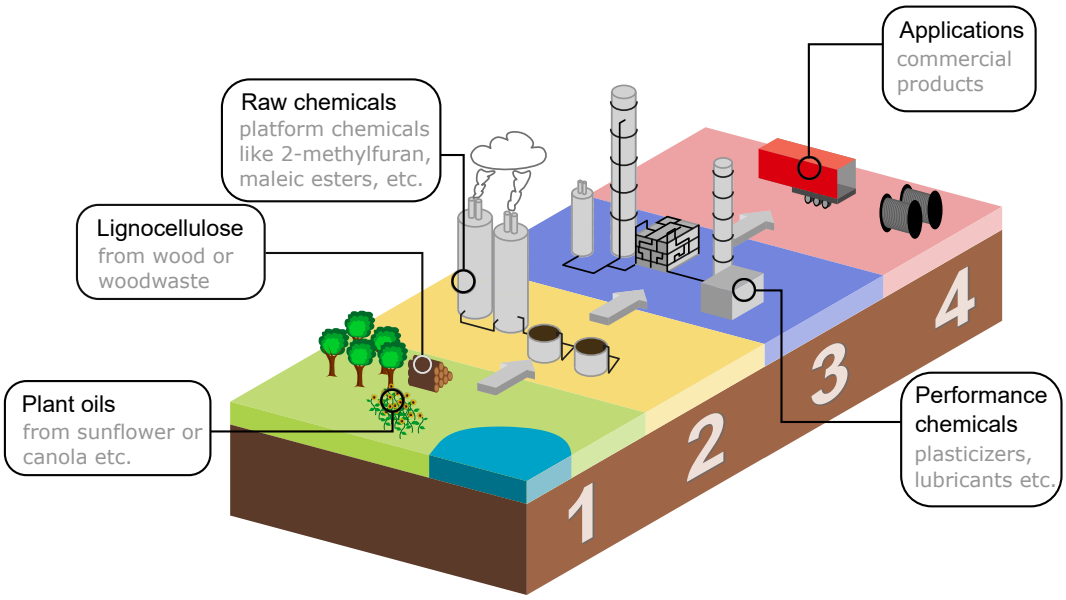

Figure 4.1: Illustration of the production steps of bio-based commercial goods starting from renewable resources.

In *step one*, raw materials from different feedstocks are acquired.[5] From lignocellulose[6–8] over algal biomass[9,10], (bio)waste[11], and cellulose[12] to carbon dioxide[13–16], many options have been investigated. Not free of conflict is however the use of edible materials, as cultivatable land is rare. Thus, the utilization of non-edible plant parts[17] and oils[18,19] or organic waste[20] is highly favored.

These raw materials are processed into various platform chemicals[21,22] in a *second step*. Many processes are related to so-called biorefineries.[23,24] In these, biomass, preferably from sustainable resources, is converted to basic chemicals analog to refineries for crude oil. Often, the utilization of furanic compounds is suggested, as they are easily accessible *via* 5-(hydroxymethyl)-furfural (HMF).[25–31] But also other platforms have been proposed.[32]

Further value is then added to the raw chemicals by converting them into performance chemicals such as plasticizers, lubricants, or drugs in a *third step*. In 2019, Liu *et al.* reported on the synthesis of renewable lubricants based on non-food biomass.[33] As plastics are tremendously important in today's world, bio-based polymer alternatives have become very popular over the past years.[34–38]

Finally, commercial goods are manufactured from these chemicals in *step four*. While the market share of sustainable products in general (including cars, food, textiles, etc.) is still very low in some sectors, awareness among the population is continuously raising.[39] However, the German Federal Environment Agency continues to emphasize that further action is needed, especially to reduce greenhouse gas emissions.

The use of sustainable raw materials offers several advantages over petrochemical-based ones. In a time of climate change, avoiding carbon dioxide is crucial. By using renewable materials, which can reduce greenhouse gas emissions and energy consumption, this can be achieved.[40–42] As some scientists and politicians argue that climate change cannot be prevented without negative carbon dioxide emissions, carbon capture and fixation has become important, but is also heavily criticized.[43,44] Renewables are per definition non-depleting; therefore, secure raw material supply is another important factor. Not only ecological considerations are important, but also the chance to rethink the chemistry behind established products and to integrate new lead structures is intriguing. This might lead to innovative products.

Despite the many potential benefits, there are also great challenges.[45] The supply chain must be adjusted, and new chemical processes need to be developed or even discovered to make efficient use of the changed feedstock. Due to the sometimes not yet efficient processes, higher costs for materials, and investments in development, the price for products based on renewables is often higher than for established products.

Two chemicals, which form the basis of the plasticizer development of this work, are reviewed in detail in the following. The starting materials 2-methylfuran and bis(2-ethylhexyl) maleate can both be obtained sustainably.

Hydrogenation of furfural to obtain 2-methylfuran is well known since the middle of the last century.[46] Still today, this reaction is investigated using cutting-edge techniques due to its outstanding importance.[47,48] As a platform chemical, furfural offers simple access to 2-methylfuran *via* reduction and dehydrogenation (Scheme 4.1).

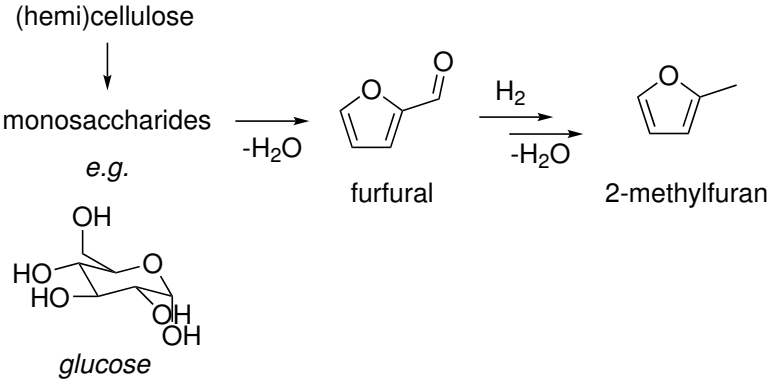

Scheme 4.1: Synthesis of 2-methylfuran starting from renewable sources such as cellulose or hemicellulose *via* reduction and dehydration to first furfural and then to the desired product.

The second starting material, bis(2-ethylhexyl) maleate, which accounts for the majority of the in this work synthesized plasticizers molecular mass, can also be obtained from renewable resources. A typical route starts from maleic anhydride, which is accessible from furanic compounds[49,50] or levulinic aicd.[51] In an esterification using the desired alcohol—often 2-ethylhexanol—the desired compound can be produced (Scheme 4.2).

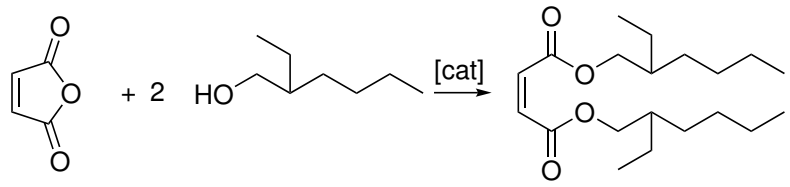

Scheme 4.2: Esterification of maleic anhydride with 2-ethylhexanol.

The alcohol component, 2-ethylhexanol (2-EH), can be obtained sustainably as well. It can, for example, be produced *via* the Guerbet reaction (Scheme 4.3).[52]

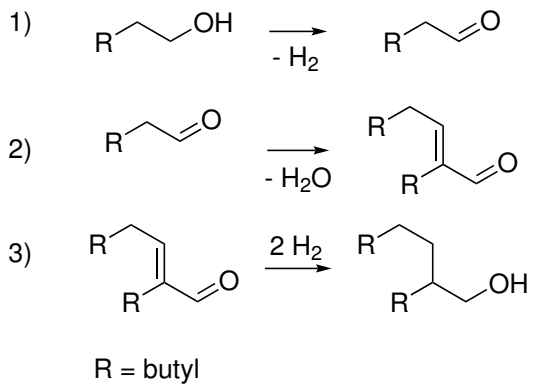

Scheme 4.3: Synthesis of 2-ethylhexanol (2-EH) *via* the Guebert reaction. 1) Dehydration, 2) Aldol condensation, 3) hydrogenation.[52]

2-EH is considered as a drop-in fuel alternative for transportation, as it can potentially bring down greenhouse gas emissions (from well-to-weel) to a fraction of that from gasoline or diesel, according to a life cycle assessment by Poulikidou *et al.*[53] The alcohol can be obtained over different routes as shown in Figure 4.2.

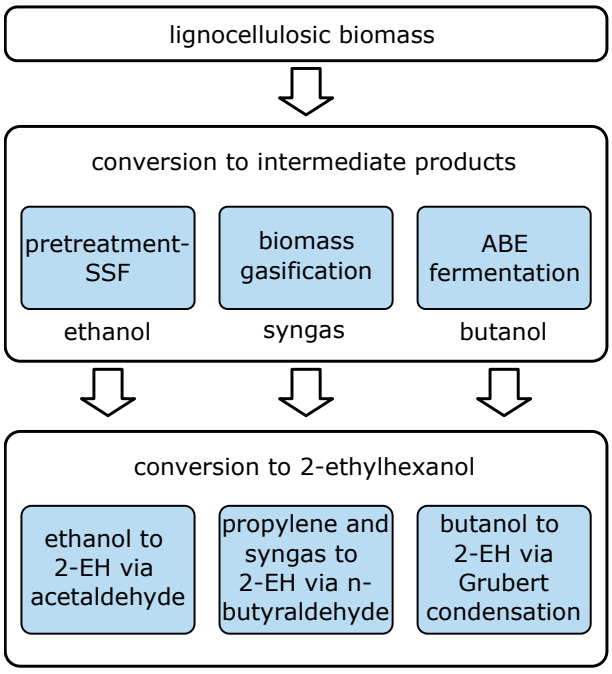

Figure 4.2: Production of 2-ethylhexanol (2-EH) from lignocellulosic biomass *via* different routes (modified from Poulikidou *et al*).[54] SSF, simultaneous saccharification and fermentation process; ABE, acetone–butanol–ethanol fermentation.

For further conversion maleates or furans, often a Diels-Alder (DA) reaction is applied. This $[4\pi + 2\pi]$ cycloaddition of an alkene and a diene was first

correctly described by the Nobel Prize-winning chemists *O. Diels* and *K. Alder* in the early 1900s.[55] Typically, electron-rich dienes react readily with electron-poor dienophiles (alkenes) to form cyclic products.[56] This case is called Diels-Alder reaction with normal electron demand. Still today, this reaction is widely applied not only in natural product synthesis[57] but also in industry.[58]

The details of the reaction mechanism are still subject to research, and lately several studies to reveal the details of the reaction based on computational approaches have been reported.[59–62] Some substrates, in particular electron-rich dienes, can be reacted with electron-poor dienophiles without catalysts. But also Lewis acid-[63–65], organo-[66] and cation-catalyzed[67] Diels-Alder reactions are well known. Recently, Beker *et al.* applied a machine learning approach to the challenge of predicting the reaction's selectivity.[68] Especially, finding a good descriptor (machine-readable representation of the molecules) was pointed out as crucial. An accuracy exceeding 90% could be achieved using a descriptor system offering the machine learning algorithm chemical 'insight' through Hammett constants and steric description of the substituents (TSEI indices). This approach outperformed even sophisticated quantum chemical methods in terms of accuracy while requiring only a fraction of the computing power.

The Diels-Alder reaction is a concerted pericyclic reaction (Figure 4.3 a). In the literature, the mechanism is often described using the *frontier molecular orbital* (FMO) concept.[69] In the case of a normal-electron demand DA reaction, the HOMO (highest occupied molecular orbital) of the diene interacts with the LUMO (lowest unoccupied molecular orbital) of the dienophile to stabilize the transition state (Figure 4.3 b).

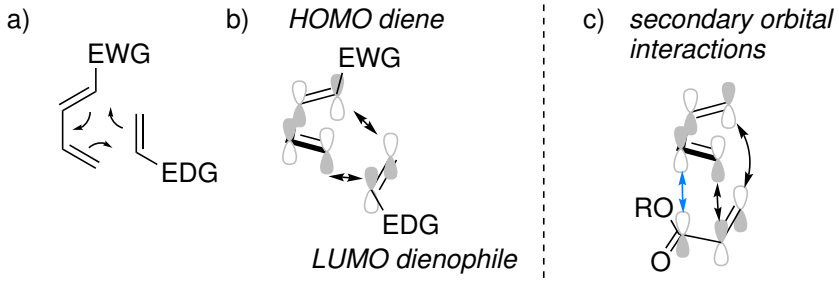

Figure 4.3: Mechanistic aspects of a normal-electron demand Diels-Alder reaction. a) Concerted pericyclic reaction, b) frontier molecular orbital (FMO) interactions in the transition state, and c) secondary orbital interactions (marked in blue) and FMOs.[69] EWG, electron-withdrawing group; EDG, electron-donating group; HOMO, highest occupied molecular orbital; LUMO, lowest unoccupied molecular orbital.

DA reactions with a cyclic diene can form two different stereoisomers—the *endo*- and the *exo*-form. In general, the more stable *exo*-product is generated under thermodynamic control, while the *endo*-product is preferred under kinetic control. Some reactions, especially those where this stereochemistry exists, could not be explained sufficiently based on previous theoretical approaches alone. A theory based on secondary orbital interactions was proposed by Woodward and Hoffmann[70], and for a long time controversially discussed.[71–73] Additionally to the interactions of HOMO(diene) and LUMO(dienophile) (Figure 4.3 b), this concept suggests interactions of the 2- and 3-position at the diene with further π-electrons from the dieneophile (Figure 4.3 c), which can, for example, be provided by carbonyl groups. While some empirical rules can often predict the selectivity correctly, other factors such as the choice of solvent are known to have a tremendous influence on the *endo* to *exo* ratio, making this prediction very challenging.[74,75]

Lewis acids are well known to catalyze DA reactions (Scheme 4.4).[76,77] A recent study by Vermeeren *et al.* suggests that not HOMO-LUMO interactions are the key to understanding the mechanism of these catalyzed reactions but reduced Pauli repulsion between diene and dienophile.[63]

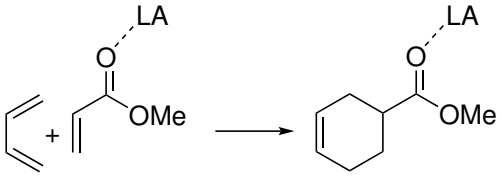

Scheme 4.4: Lewis acid-catalyzed Diels-Alder reaction of methyl acrylate and 1,3-butadiene.

4.1.2 Plasticizers

Plasticizers are additives used in polymer chemistry for the adjustment of flexibility, workability, and distensibility.[78] Many polymers rely heavily on the addition of chemicals, while others can be adjusted, for example, by using shorter polymer chains of the same material or co-monomers (e.g. polyethylene). The latter case is referred to as *internal plasticizing*, as adjustments are done on the monomer level by chemical modification.[78] In the first case, which is commonly called *external plasticizing*, an additive is used to achieve the desired flexibility.[78] For example, in many applications of polyvinyl chloride (PVC), the addition of plasticizers is crucial. This soft-PVC can be fine-tuned using up to 50% plasticizer to meet specific requirements.

Today, three vastly different plasticizing theories are used and accepted in the literature (Figure 4.4).[54] The first theory—*lubricity theory*—explains the effect of plasticizers on polymers based on the friction of polymer chains during movement. By diffusing into the polymer and reducing the internal friction, the parallel motion requires less energy; therefore, the polymer becomes more flexible. In contrast, the *gel theory* is based on the assumption that the polymer is a three-dimensional network, and the plasticizers reduce weak secondary forces between the chains. Finally, the *free volume theory* aims to explain the effect by the increased motion of the polymer chains by the introduction of extra volume between the polymer chains through the plasticizer molecules. Applying the free volume theory, Chandola *et al.* could successfully predict the behavior of 25 different PVC-plasticizer combinations.[79]

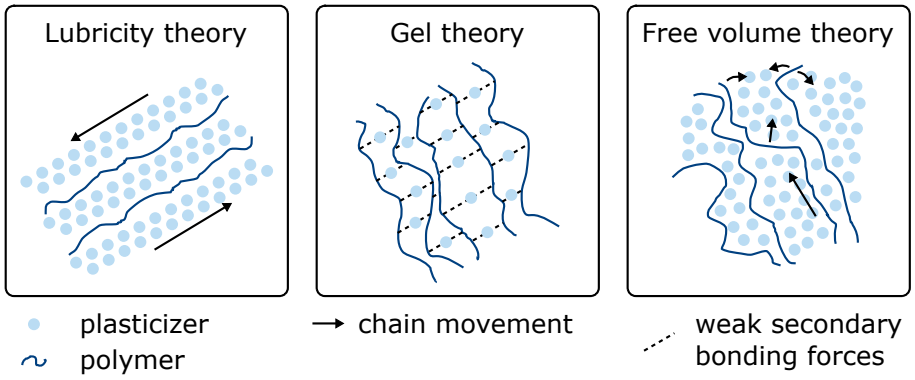

Figure 4.4: Visualization of the three major plasticizing theories (modified from Broqué *et al*).[54]

Soft-PVC is used in numerous applications, from cable insulation to flexible tubing and flooring. For a long time, plasticizers are contributing to a highly technologized world. After some time, the initial excitement over the many advantages they brought in various fields waned, and major problems—health issues and sustainability concerns—emerged. Especially the popular phthalate-based plasticizers such as DEHP (bis(2-ethylhexyl) phthalate) or DINP (diisononyl phthalate; Scheme 4.5) were partly banned for the application in certain products because of their potential long-term toxicity. In medical uses, DEHP is still recommended, for example, by the German *Bundesinstitut für Arzneimittel und Medizinprodukte* due to lack of alternatives.[80]

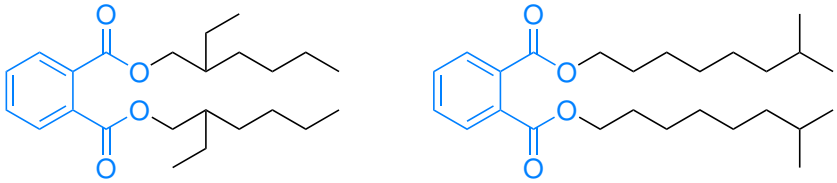

Scheme 4.5: Lewis structures of DEHP (bis(2-ethylhexyl) phthalate) and DINP (diisononyl phthalate) with highlighted phthalate moiety.

Therefore, alternatives are required to further improve the lives of many people. Over the past years, several products have been developed and brought to the market. In particular, Hexamoll® DINCH has become one of the products with a high marked share. Advancing from DINP, the aromatic ring is reduced to avoid a phthalate moiety (Scheme 4.6).

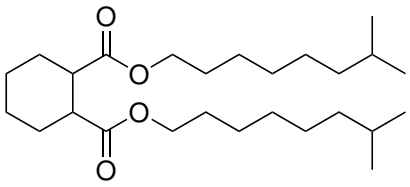

Scheme 4.6: Lewis structure of Hexamoll® DINCH (diisononyl cyclohexane-1,2-dicarboxylate).

Apart from this, many other plasticizers are currently on the market. Among these is still a range of *ortho*-phthalate-based products, such as DINP which is produced as Palatinol® N by BASF SE or as Jayflex™ by ExxonMobil Corp. DINP made up for nearly half of the 2017 plasticizer production according to a factsheet by *European Plasticisers*.[81] Meanwhile, the

highly disreputable DEHP is still produced and widely used.[82] Furthermore, trimelliate-based structures like Diplast® (Polynt S.p.A.) or adipate-based structures such as DEHA (bis(2-ethylhexyl) adipate), which is marketed as Plastermoll® DOA (BASF SE), are currently on the market.

Today, increasing efforts are focused on the production of not only the PVC itself starting from renewable resources or through recycling but also necessary additives like plasticizers. According to a 2021 press release, BASF launched a new plasticizer product line based on renewable resources using a 'biomass balance' approach.[83]

Furthermore, several academic examples for renewable plasticizers have been reported.[84] Chen *et al.* and He *et al.* reported recently on a plasticizer based on soy oil.[85,86] Other oil resources, such as waste frying oil[87,88], castor oil[89] or tartaric acid[90] have been used as well (Scheme 4.7). Moreover, the utilization of Cardanol, which can be obtained from cashew nutshells as an industrial waste product, is known. Cardanol was epoxidized to yield a performant plasticizer.[91,92]

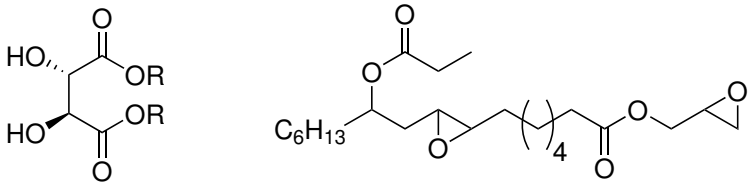

Zawada *et al.* Chen *et al.*

Scheme 4.7: Examples of bio-derived plasticizers based on tartaric acid[90] (left) and castor oil[89] (right) investigated in the literature.

4.2 Concept

This work aims to explore a new potential platform for sustainable and less toxic plasticizers for the application in PVC. The targeted structural motive contains a bicyclic oxo-bridged and twice ester-functionalized ring system. The cyclic compound can be obtained retrosynthetically from 2-methylfuran (**1**) in combination with maleic- or fumaric bis(2-ethylhexyl) esters (**2** and **5**). 2-Methylfuran (**1**), as well as maleic esters, can be obtained from a plant-based feedstock. Thus, the newly developed plasticizers will be potentially ecologically beneficial compared to petrochemical-based products such as

DINP or DINCH. Moreover, by avoiding a phthalate moiety, an improved toxicological profile is expected.

Starting from these green chemicals, different molecules related to the platform compound will be synthesized in this project (Scheme 4.8). While Plass[93] and Altemeier[94] worked on the synthesis of the *exo*-bicyclus **7** starting from maleic anhydride and 2-methylfuran, the focus of this work will be on the *endo*-**4** product. In contrast to the work of Plass[93], a different synthetic approach will be investigated. Due to the lower reactivity of maleates compared to maleic anhydrides, a catalytic route will be developed. Therefore, many additional aspects in the chemical process development must be considered. To reveal the structure-function relationship, both products as well as the non-methyl bearing *exo*-bicyclus **8** will be investigated in terms of performance in polyvinyl chloride by colleagues from the BASF SE.

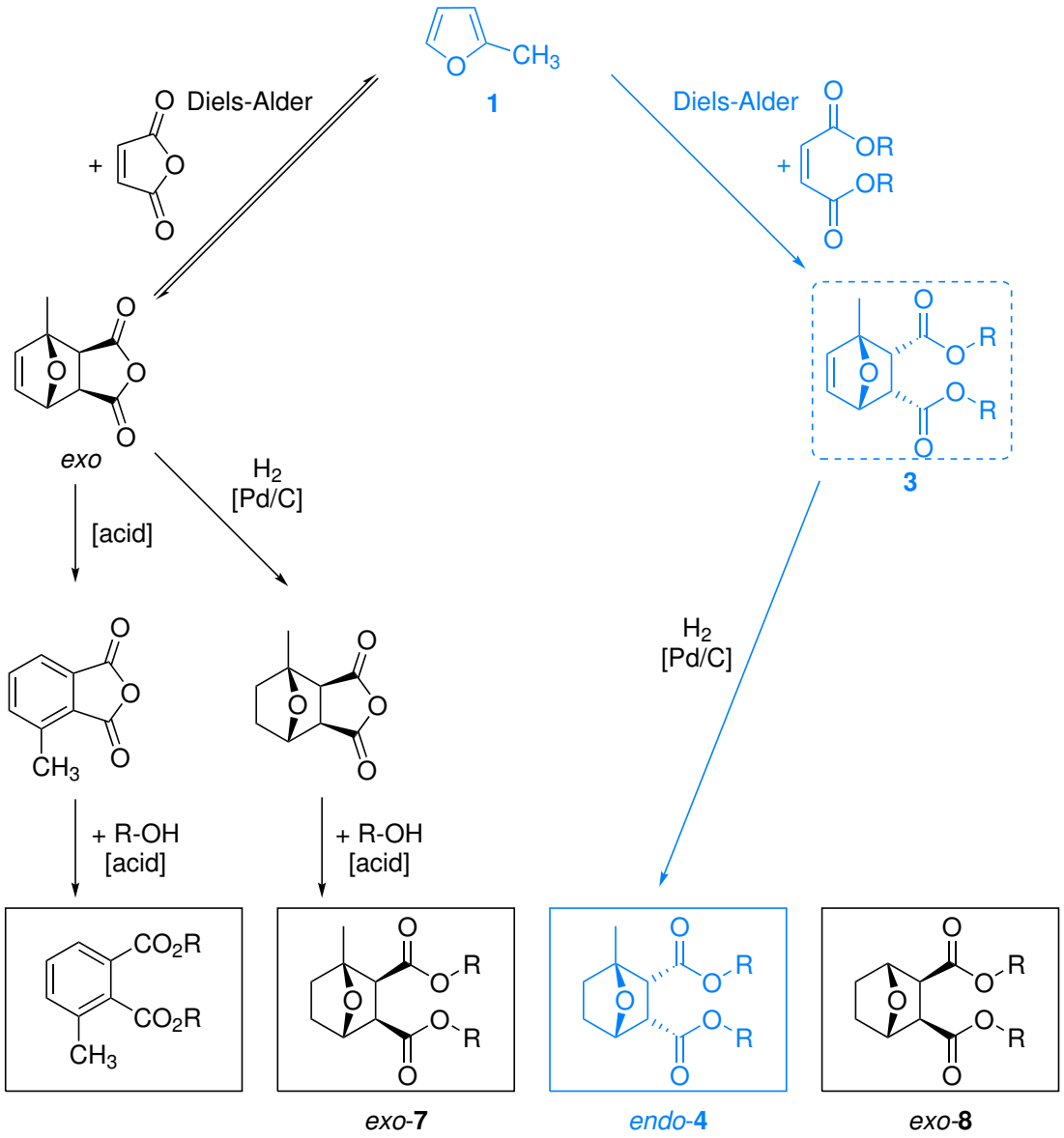

Scheme 4.8: Overview of the synthesized compounds in the BMBF-funded 'bioplasticizers' project. Highlighted blue route developed in this work while others were developed by Plass[93] and Altemeier.[94]

Additionally, this synthetic pathway will be converted into a new continuous process in order to increase the conversion and to control the selectivity to meet specific targets. Through more precise control over process parameters enabled by flow chemistry, this goal is targeted. This approach goes beyond the work of Plass and Altemeier.

4.3 Synthesis of Novel Plasticizers

4.3.1 Diels-Alder Reaction

The first plasticizer candidate **3** was synthesized in a Diels-Alder reaction (Scheme 4.9). To gain a deep insight into the reaction, catalysts, and reaction conditions were screened. Inspired by the work of Hayashi *et al.*[95], a number of Lewis acid catalysts were tested. Using the best catalyst, the reaction parameters, such as solvent and temperature were investigated. With the optimized conditions, the reaction was scaled up to 30 g-scale and then 300 g-scale. After having this efficient discontinuous batch process in hand, a continuous synthesis based on an immobilized catalyst was developed. A packed bed reactor was charged with immobilized Lewis acid and starting material solution was pumped over the catalyst bed. Finally, the applicability of the plasticizers **3** was evaluated based on the analysis carried out by colleagues at BASF SE. It should be noted, that the product **3**, as well as the hydrogenated form **4** are obtained as racemate. For the sake of readability, only one of the enantiomers will be shown in this chapter (Scheme 4.9).

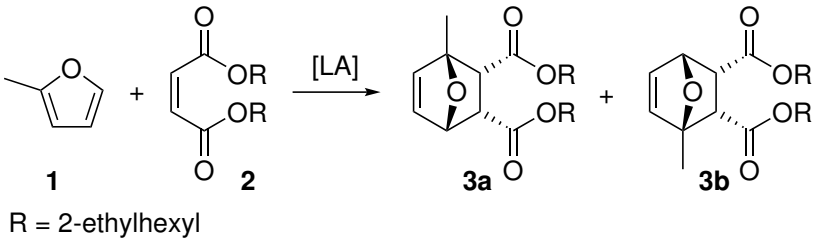

Scheme 4.9: Synthesis of the first plasticizer candidate **3** from 2-methylfuran (**1**) and bis(2-ethylhexyl) maleate (**2**). In this case, both possible enantiomers **3a** and **3b** are shown. LA, Lewis acid.

While Plass[93] focussed on the synthesis of an *exo*-isomer **7** of the plasticizer candidate, this work aims to investigate the synthesis of the corresponding *endo*-isomer **3**.

4.3.1.1 Reaction Optimization

The investigated Diels-Alder reaction of bis(2-ethylhexyl) maleate (**2**) and 2-methylfuran (**1**) to the bicyclic plasticizer candidate **3** was initially optimized on milliliter-scale in batch mode. Hayashi *et al.* reported that lanthanides are efficient catalysts for similar Diels-Alder reactions.[95] Inspired by their findings, a variety of lanthanides, as well as aluminium and titanium salts were investigated as catalysts in this work (Table 4.1). The reactions were carried out in dichloromethane at 0 °C for 24 h.

Table 4.1: Results of the Lewis acid screening for the Diels-Alder reaction of furan **1** and ester **2** to synthesize the plasticizer candidate **3**. Catalyst loading: 10 mol%.

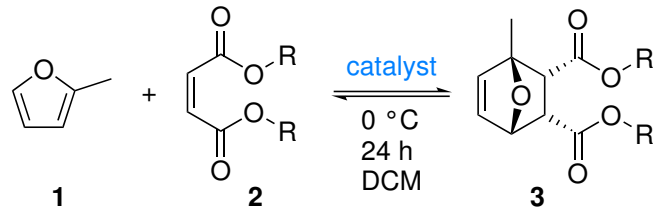

Entry	*Lewis acid*	*Conversion to **3** / %*	*Exo/endo selectivity*
1	$AlCl_3$	6	n.d.
2	$TiCl_4$	10	n.d.
3	$HfCl_4$	59 (48)	1:5
4	$Hf(OTf)_4$	2	n.d.
5	$Er(OTf)_3$[(a)]	70	1:6
6	$Er(OTf)_3$[(b)]	<1	n.d.
7	$La(OTf)_3$	< 1	n.d.
8	$Yb(OTf)_3$	38	1:4
9	$YbCl_3$	< 1	n.d.

[(a)] $Er(OTf)_3$ from Sigma Aldrich (LOT: MKBS5455V), [(b)] $Er(OTf)_3$ from BLDpharm (LOT: AGU604).

Erbium(III) triflate provided the highest conversion (70%) from the investigated set of Lewis acids. While the largest[96] investigated lanthanide triflate—lanthanum—produces only traces of the desired product, ytterbium triflate, which has a similar ionic radius to erbium, showed 38% conversion to **3**. Ytterbium chloride on the other hand only generated traces of the product. The group 4 metal chlorides of titanium(IV) (10%) and hafnium(IV) (49%, respectively 59% in a second experiment) could provide low to decent conversions. Using aluminium(III) chloride, a conver-

sion of 6% to the desired product **3** was detected. The two best-performing catalysts—$Er(OTf)_3$ and $Hf(OTf)_3$—provided a similar selectivity (*exo*/*endo*: 1:5–1:3) within the margin of analytical error. It could not be clarified why only the erbium(III) triflate purchased from Sigma Aldrich could yield the desired product, although both results were very reproducible (several experiments by different experimenters) with the corresponding catalyst batches.

For the reaction using the best catalyst (erbium(III) triflate), the conditions were further improved. Different reaction times, temperatures, and solvents were used. While the initial catalyst screening was conducted in dichloromethane, other more environmentally suitable options were applied. Initially, 5 vol% water was added to the reaction mixture to investigate the sensitivity against water content and moisture (Table 4.2). Only a moderate decrease (−21%) of the conversion to the desired product **3** was observed. This indicates a relatively high robustness of the reaction system against large quantities of water. It was therefore decided that dry conditions were not required for the synthesis. Moreover, the reaction was not accelerated through traces of water, which is also a known effect in literature. As environmentally better solvent options, acetonitrile (ACN) and methyl-*tert*-butyl ether (MTBE) were tested. Furthermore, the reaction was carried out in 2-methylfuran (**1**) as solvent (Table 4.2).

Table 4.2: Results of the solvent screening for the Er(III) triflate-catalyzed Diels-Alder reaction of furan **1** and ester **2** to synthesize the plasticizer candidate **3**. Cat. loading: 10 mol%. ACN, acetonitrile; DCM, dichloromethane; MTBE, methyl-*tert*-butyl ether.

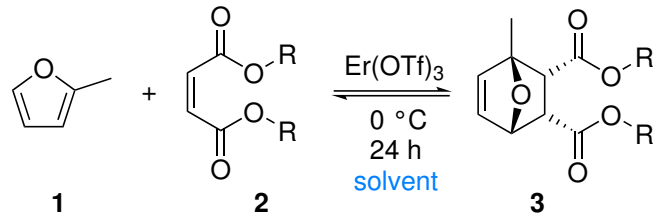

1 **2** **3**

Entry	*Solvent*	*Conversion to 3 / %*	*Exo/endo selectivity*
1	DCM	70	1:6
2	DCM + water (5 vol%)	49	1:6
3	ACN	< 1	n.d.
4	MTBE	< 1	n.d.
5	2-methylfuran, substr. conc.: 0.8 M, cat. loading: 6 mol%	86	1:9

The reaction proceeded best in furan **1** offering a conversion to the desired product of 86%, even with a lower catalyst loading (6 mol%), while in acetonitrile and MTBE only traces of the desired product were found (Table 4.2). In the next set of experiments, the effect of the reaction temperature and reaction time on the conversion and stereoselectivity was investigated using dichloromethane as solvent (Table 4.3).

Table 4.3: Results of the condition screening for the Er(III) triflate-catalyzed Diels-Alder reaction of furan **1** and ester **2** to synthesize the plasticizer candidate **3**. Catalyst loading: 10 mol%; DCM, dichloromethane.

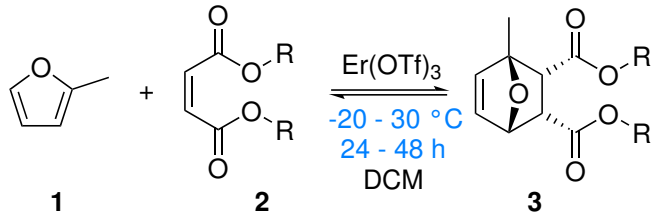

Entry	*Conditions*	*Conversion to **3** / %*	*Exo/endo selectivity*
1	0 °C, 24 h	70	1:6
2	−20 °C, 24 h	33	1:7
3	−20 °C, 48 h	47	1:7
4	30 °C, 24 h	33 (32)	1:3

Higher (30 °C) and lower (−20 °C) temperatures provided the same conversion to the desired *endo*-product **3** of 33% with a reaction time of 24 h. Doubling the reaction time increased the conversion to **3** by 15% for the reaction at −20 °C, which is an expected trend. The selectivity decreased with higher temperature: At −20 °C, a higher selectivity of 1:7 (*exo*/*endo*) was measured. High temperatures of 30 °C decreased the selectivity to 1:3 (*exo*/*endo*). The lower reactivity at 30 °C compared to 0 °C could be confirmed in an independent experiment, which was carried out as this tendency is unintuitive.

In a final optimization step, the catalyst loading was lowered to 6 mol%, and a concentration of 0.8 M maleate **2** was used in methylfuran **1** as solvent at 0 °C. Using these conditions, a conversion of 86% along with a selectivity of 1:9 *exo*/*endo* could be achieved (Table 4.2 Entry 6).

4.3.1.2 Scale-up

As a minimum of 30 g was required for the application test, the reaction was scaled up, and a purification method was established.

The reaction was first scaled up to 100 mL-scale in a jacked flask. After multiple batches, the reaction showed high reproducibility (conversion to

3 of 85%) without significant deviation of the conversion to the desired product **3** of a few percent. Even a scale-up to 1 L in a 2 L jacked glass reactor could be carried out without change of conversion to **3** (85%) or selectivity (*exo*/*endo*, 1:9).

While column chromatography proved tedious and only moderately successful, distillation turned out to be unsuitable. By flash column chromatography, a few grams of the desired product could be isolated and further analyzed.

4.3.1.3 Product Stability Investigation

To evaluate the applicability of the plasticizer candidate **3**, the stability of the compound was investigated. Product **3** was incubated at different temperatures for one day. In Figure 4.5, the NMR spectra indicating product instability are shown.

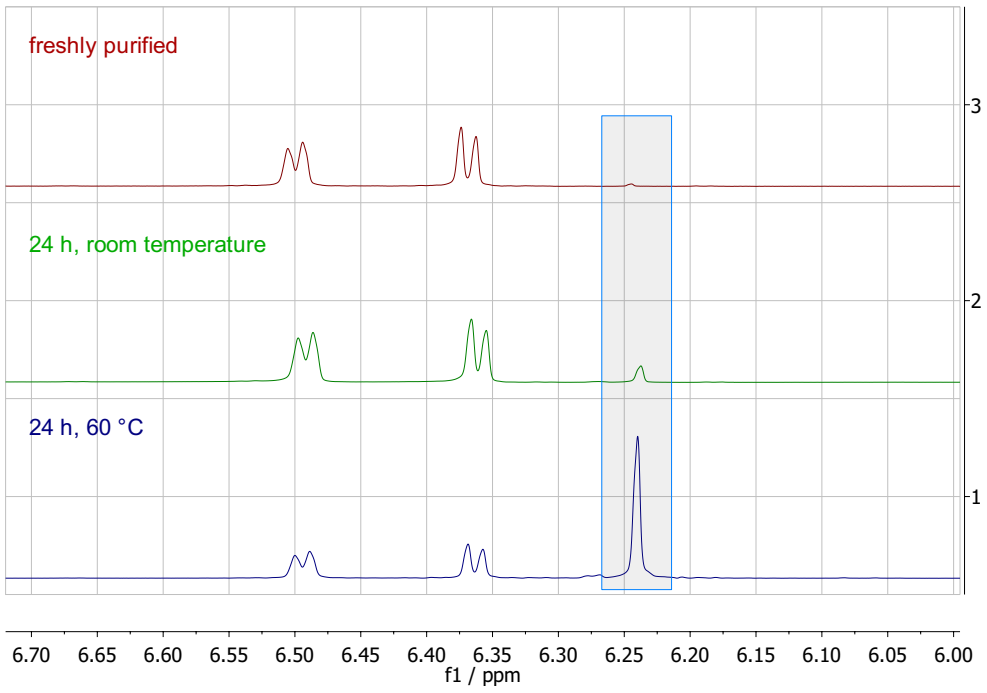

Figure 4.5: ^{1}H NMR spectra of plasticizer candidate **3**. Freshly purified compound (upper), and after 24 h incubation without solvent at room temperature (middle) or 60 °C (lower). Framed peaks indicate the decomposition product **2** (two protons). The two left doublets are related to the product **3** (each one proton).

The product decomposed *via* a *retro*-Diels-Alder reaction to maleate **2** and 2-methylfuran (**1**). As this decomposition is relatively quick, even at ambient temperatures, the product is not suitable for a long-term application as a plasticizer. Thus, a way for stabilization is required.

4.3.1.4 Synthesis of *tans*-Isomer

Analog to the synthesis of the *endo*-compound **3**, and completing the picture of the *endo*/*exo* comparison, the synthesis of a *trans*-configured product **6** was attempted (Scheme 4.10). In this case, bis(2-ethylhexyl) fumarate (**5**) and 2-methylfuran (**1**) were used as starting materials.

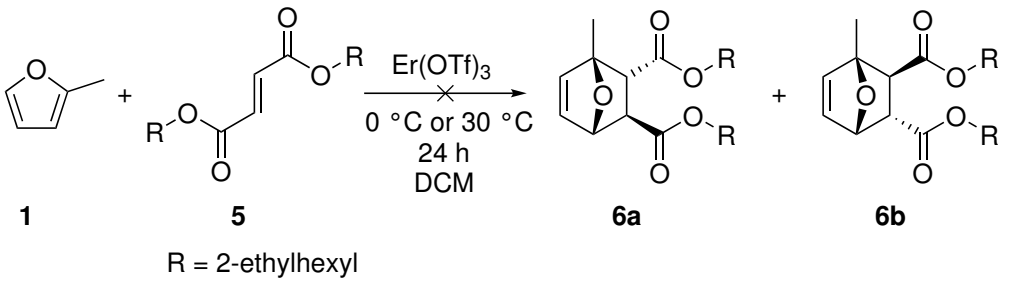

Scheme 4.10: Synthesis of plasticizer candidate **6** starting from bis(2-ethylhexyl) fumarate (**5**) and 2-methylfuran (**1**) in a Diels-Alder reaction. DCM, dichloromethane.

The same conditions as previously used for the synthesis of *endo*-**3** were applied; however, no conversion was observed at 0 °C. Also, the increase of the reaction temperature to 30 °C did not yield any product.

4.3.2 Hydrogenation

To stabilize the plasticizer candidate *endo*-**3**, a similar strategy as developed by Plass[93] for the synthesis of the *exo*-isomer **7** was used. By hydrogenation of the carbon-carbon double bond, the back reaction could be suppressed allowing for a stable compound (Scheme 4.11).

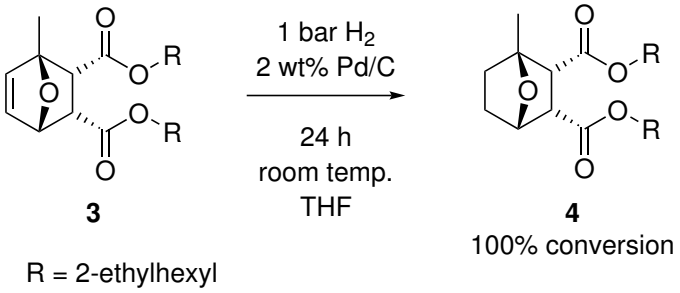

Scheme 4.11: Hydrogenation of plasticizer candidate **3** to gain the stable bicyclic plasticizer candidate **4**. THF, tetrahydrofuran.

The hydrogenation was carried out at room temperature for 24 h at 30 g-scale in tetrahydrofuran (THF) using palladium on carbon (2 wt%) as catalyst and 1 bar hydrogen atmosphere. After the catalyst was filtered off and the solvent was removed, full conversion was obtained. Since for the hydrogenation the crude product from the Diels-Alder reaction was used, both stereoisomers as well as the hydrogenated starting material, bis(2-ethylhexyl) succinate (**9**) were obtained. A ^{1}H NMR spectrum of the developed plasticiser **4** is shown in Figure 4.6.

A portion of the crude product was finally purified by column chromatography to yield product **4** with 45% and 99% purity (^{1}H NMR). However, a challenging separation of the desired product **4** from the succinate **9** turned out to be a bottleneck for the preparation of a larger 100 g-sample. Low reproducibility and yield—even using automated column chromatography with a suitable evaporative light scattering (ELS) detector—called for a different approach for the purification. Distillation was also for this compound not suitable due to the high boiling point.

Prior to further scale-up of the hydrogenation, the challenging separation of the succinate **9** was addressed by a change of the reaction sequence as presented in the following Subsection 4.3.3. After this solution was found, a more defined temperature profile was used during scale-up of the hydrogenation to 300 g. Initially, the reaction mixture was cooled to 0 °C for 3 h to prevent the *retro*-Diels-Alder reaction. Then, the reaction was resumed for 22 h at room temperature. Also in this case, full conversion of the starting material was observed with a purity of 97% according to ^{1}H NMR for the crude product. For this reaction, the starting material obtained from the *aza*-Michael step (Subsection 4.3.3) was used. In the crude product, residual 3% of succinate **9** originating from an initial impurity of fumarate

5 in the commercially available maleate **2** were observed. The product **4** was fully characterized *via* ^{1}H, ^{13}C, 2D NMR as well as high-resolution mass spectrometry.

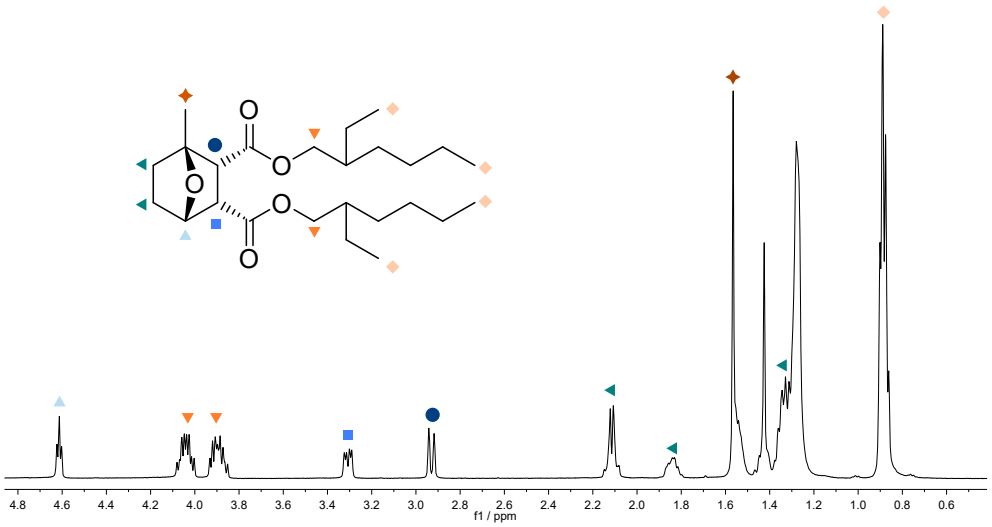

Figure 4.6: ^{1}H NMR spectrum of the developed plasticiser **4** with assignment of characteristic protons.

4.3.3 Process Sequence Optimization

To overcome this issue, the reaction sequence was changed. As in particular the removal of succinate **9** turned out to be challenging, its formation must be prevented. The major source of this compound is the hydrogenation of unreacted maleate **2**. Despite many efforts, the Diels-Alder synthesis only provided incomplete conversion. Thus, the maleate **2** had to be removed from the crude reaction mixture. One option was column chromatography, which is, however, time and material intensive. Therefore, a chemical way for the removal was chosen. As maleates can be considered as a Michael system, the related reactivity can be exploited to remove the compound from the crude mixture.

In this work, an *aza*-Michael addition was used to transform the maleate **2** into a polar amine compound, which can be removed easily by silica gel filtration (Scheme 4.12). As Michael additions tend to be highly selective for Michael systems, the intermediate plasticizer candidate **3** remained unaffected. A diamine nucleophile, 1,5-diaminopentane (**10**), was used in excess regarding the maleate **2**. Potentially, the bifunctional amine **10** could also react with two equivalents of maleate **2**.

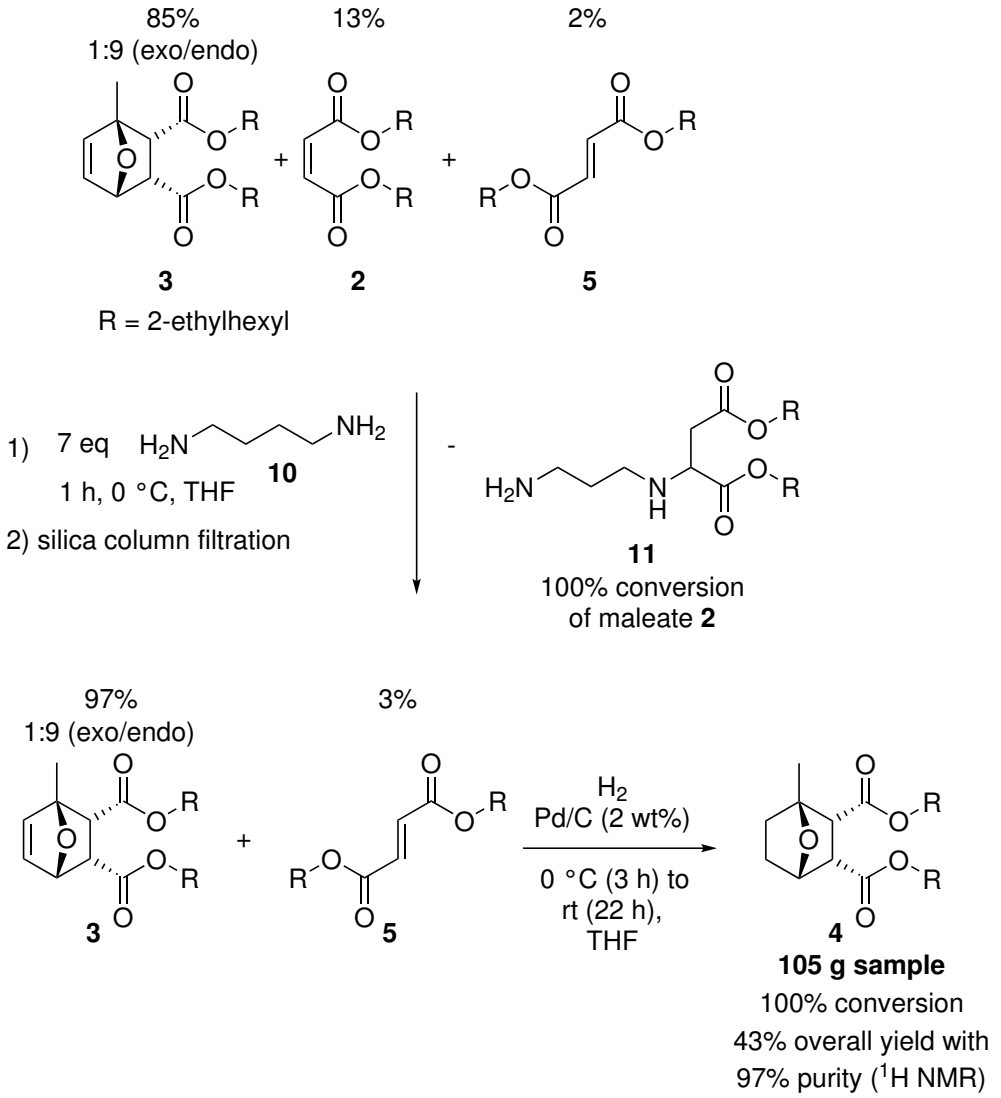

Scheme 4.12: Removal of remaining maleate **2** by *aza*-Michael addition of 1,5-diaminopentane (**10**) from the crude reaction mixture of the Diels-Alder reaction of maleate **2** and furan **1**. The percentages in the crude mixtures as determined by ^{1}H NMR are shown. THF, thetrahydrofuran.

Initial small scale test reactions with pure maleate **2** showed high to complete conversion. The plasticizer intermediate **3** was as expected not converted. Moreover, bis(2-ethylhexyl) fumarate (**5**) could also not be converted. Hence, the reaction was applied to the crude reaction mixture. Maleate **2** could be entirely removed from the mixture leaving only a mixture of polar amine **11**, intermediate plasticizer **3** as well as 3% fumarate **5** (originating from an impurity in the commercially available starting material) behind. The mixture was then filtered over a short silica column and hydrogenated as previously described to yield the desired product **4** as stereoisomer mixture with only 3% impurity of succinate **9**. Finally, the desired isomer **4** was isolated from the mixture in 97% purity and a yield

of 43% over all reaction steps by column chromatography to give a 105 g sample for performance tests.

4.3.4 Towards Continuous Synthesis

After the successful optimization of the reaction in batch mode, an attempt to develop a continuous process for the Diels-Alder reaction of furan **1** and maleate **2** was made. As these kinds of processes can lead to higher catalyst usage and more precise control of reaction parameters, an even more improved process can potentially be realized. Especially fine-tuning of the stereoselectivity of the Diels-Alder reaction to a specific target was of interest.

Continuous processes with heterogeneous catalysts can be realized by different process designs: Processes based on immobilized catalysts, and processes with mobile catalysts. As processing catalyst suspensions usually is challenging, a process based on an immobilized Lewis acid catalyst in a packed bed reactor was chosen for this reaction. Other aspects of this continuous reaction were further investigated in the Bachelor thesis of Diedrich.[97]

To immobilize the Lewis acid, an approach based on the so-called SILP technology (Supported Ionic Liquid Phase) was chosen.[98,99] In this technology, the catalyst is dissolved in ionic liquid, then silica support, as well as solvent, are added. After drying, the residual powder can be applied as a catalyst. The catalyst is dissolved in ionic liquid, which coats the silica gel particles. In this study, erbium(III) triflate along with an imidazolium-based ionic liquid with triflate anion ([bmim][OTf]) were chosen.

Inspired by a procedure published by Hagiwara *et al.*[100], and using the above-mentioned composition, a pale pink powder was obtained. This power was initially investigated in a batch reaction for benchmarking. Compared to similar experiments carried out with non-immobilized catalyst at 0 °C for 5 h in an excess of furan **1**, the conversion to the desired product was with 19% much lower (non-immobilized: 58%). With these results in hand, a continuous setup for an initial investigation was developed. A cotton-stoppered packed bed reactor was charged with the Er-SILP catalyst and starting material solution with an excess of furan **1** as solvent was pumped

over the bed at room temperature (Figure 4.7). The product solution was collected and analyzed by ^{1}H NMR. Later work of Diedrich explored also lower temperatures controlled by a custom-built reactor chiller and different continuous systems for the reaction.[97]

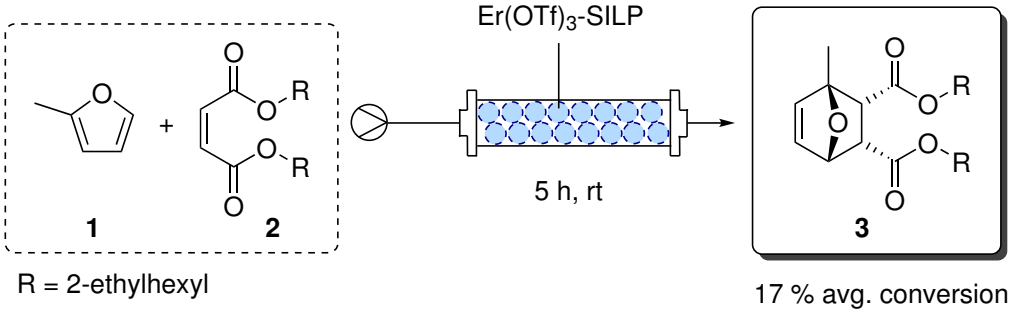

Figure 4.7: Continuous Diels-Alder reaction of maleate **2** and furan **1** in a packed bed reactor with an immobilized erbium(III) triflate catalyst. An excess of furan **1** was used as solvent. SILP, supported ionic liquid phase.

Compared to the batch mode, a similar conversion (average of 17%) to the desired product **3** was achieved. Over the course of the reaction, the first part of the catalyst bed turned slightly yellow. This was probably caused by impurities in the commercially available methylfuran **1**, which was not freshly distilled for this reaction. The impurity could not be isolated and identified.

In summary, the continuous flow approach was moderately performant; however, this flow reaction cannot be considered to be applicable with respect to closed-loop optimization due to the extremely long residence times. In the case of this Diels-Alder reaction, a parallel batch screening is more suitable for finding the optimal reaction conditions.

4.4 Plasticizer Performance Investigations

To complete the development of the novel plasticizer candidate, the synthesized samples were evaluated by colleagues at BASF SE for their suitability as an additive in PVC. Initially, physical parameters were determined to get a first impression of the applicability. Then, application tests of the compound in a soft-PVC formulation were carried out. The results of the investigations from the colleagues at BASF SE are presented below.

In particular, the comparison of the two stereoisomers *endo*-**4** and *exo*-**7**, as well as the non-methyl functionalized *exo*-**8** isomer is interesting in order to gain an insight into the structure-function relationship (Scheme 4.13). The *exo*-compound **7** and the norcantharidin-based **8** were synthesized by Plass.[93] Please note, that compounds **4** and **7** are racemic mixtures. Only one of the enantiomers is shown in this chapter to improve readability.

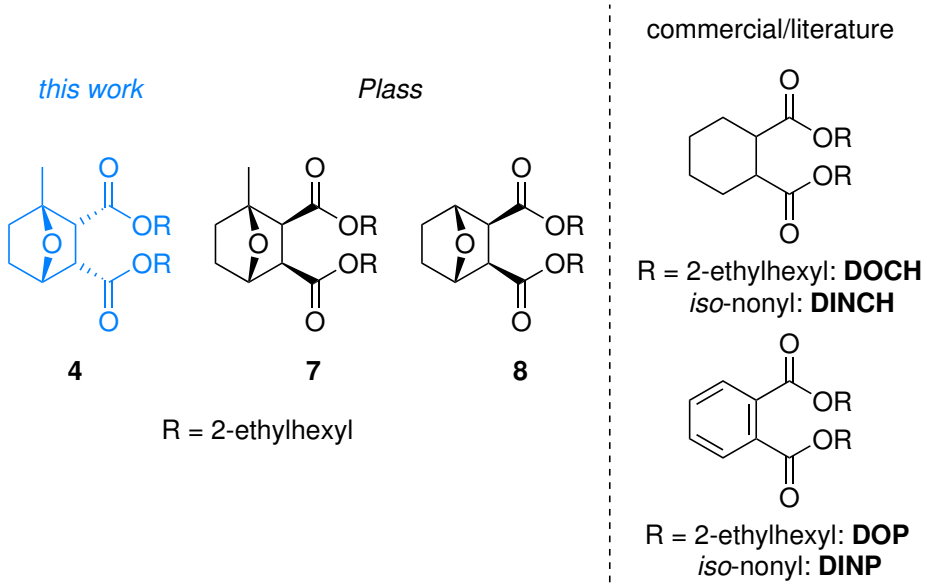

Scheme 4.13: Plasticizer compounds compared in this chapter. Left: In this work developed *endo*-compound **4** (highlighted in blue), and from Plass[93] synthesized *exo*-compounds **7** and **8**. Right: Commercial/literature-known plasticizers. DOCH, bis(2-ethylhexyl) cyclohexane-1,2-dicarboxylate; DINCH, diisononyl cyclohexane-1,2-dicarboxylate; DEHP, bis(2-ethylhexyl) phthalate; DINP, diisononyl phthalate.

First, the physical parameters were investigated (Table 4.4) by colleagues at the BASF SE. Important for the processability are the viscosity and the solution temperature. Viscosity can give an idea of whether the compounds can be easily transported in liquid form, while solution temperature represents the temperature at which the polymer can be dissolved in the plasticizer (for the details of the procedure for the determination see experimental details). This shows how easily a plastic/plasticizer formulation can be prepared. In both cases, lower numbers are generally better for processability.

Table 4.4: Some physical parameters of different plasticizers in comparison to the synthesized candidate **4**.

Parameter	*endo-**4***	*exo-**7***[93]	***8***[93]	*DINCH*	*DINP*
Density[(a)] / g·mL^{-1}	0.9808–0.9894	0.9810–0.9974	n.d.	0.9478	0.9722
Viscosity[(b)] / mPa·s	69.9–101.62	182.60–393	n.d.	50.00	72.20
Soln. Temp. [(c)] / °C	153-154	96	95	140	118

[(a)] DIN 51757, [(b)] DIN 51562, [(c)] solution temperature: BASF-Method. Values for **4** and **7** are given as a range of two different samples.

As one of the most important parameters, the solution temperature was investigated. In Figure 4.8, the solution temperatures of different plasticizers are compared. With a value lower than 100 °C, a compound is classified as *fast fuser*. These compounds very quickly form plastisols with PVC; therefore, they are considered to have good plasticizing activity.[78] Comparing both stereoisomers of the developed plasticizer candidates, a huge difference was found. While the performance of the *exo*-isomer **7**[93] is very good (96 °C), and can be classified as a fast fuser, the corresponding *endo*-isomer **4** had a much higher solution temperature (154 °C). The commercial/literature known products were in between the two configurations with temperatures ranging from 118 to 145 °C. The non-methylated compound **8**[93] performed with 95 °C similar to its methyl group-bearing counterpart **7**.[93]

From the combined data of Plass[93] and this study, a structure-function relationship could be concluded. The dramatic effect of the stereokonfiguration from *endo*-, and *exo*-compound can be explained by the three-dimensional structures. As *exo*-**7** has a 'flatter', more two-dimensional structure compared to *endo*-**4**, it can probably fit better between the polymer chains and therefore be dissolved more easily.

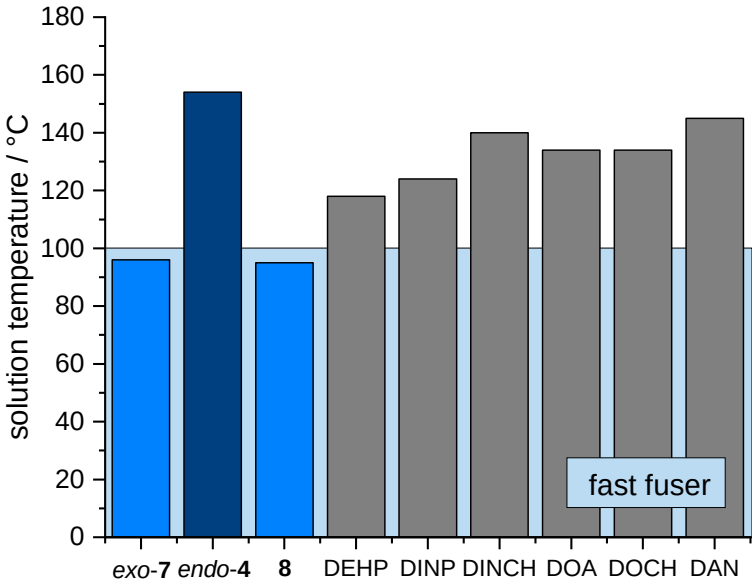

Figure 4.8: Solution temperatures of different plasticizers.

Furthermore, the viscosity was determined (Figure 4.9). A range of 69.9–101.6 mPa · s for two different samples of *endo*-**4** was observed. This is in the range of the commercial plasticizers (DINCH: 50.0 mPa · s, DINP: 72.2 mPa · s) and should not be problematic for technical processing. The *exo*-**7** on the other has a higher viscosity, which might be caused by impurities, as the range of 182.6–393 mPa · s is very high.[93] Thus, no clear structure-function relationship can be seen.

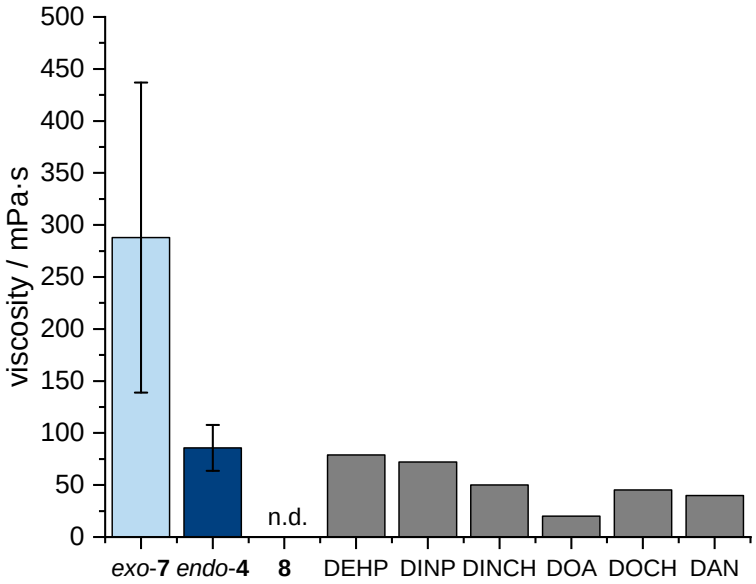

Figure 4.9: Viscosity of different plasticizers.

Other physical parameters like density, refractive indices or Pt/Co color were unremarkable and within the expected range.

As a next step in the investigation of the novel plasticizer, application tests were carried out by colleagues at the BASF SE. A soft-PVC foil was prepared with 100 parts PVC, 60 parts plasticizer, and 2 parts stabilizer and investigated by colleagues from the BASF SE.

A range of performance-related parameters were investigated (Table 4.5). Again, a comparison of the two stereoisomers with commercial plasticizers reveals the suitability and provides an indication of a structure-function relationship.

Table 4.5: Application test data of different plasticizers.

Parameter	*endo-**4***	*exo-**7**[93]*	***8**[93]*	*DINCH*	*DINP*
Efficiency / Shore A 15s[(a)]	83	76	75	80	78
Tensile stress at break / MPa[(b)]	9.7	8.8	7.5	8.6	7.2
Tensile strain at break / %[(b)]	332	268	266	334	351
Brittleness temperature[(c)] / °C	–27.5	1[(f)]	–10	–42.5	–35.0
Volatility[(d)] / %	5.51	3.35	2.59	2.48	1.34
HCl-resistance[(e)] / min	18.17	9.24	9.17	17.12	–

[(a)] DIN EN ISO 868, [(b)] DIN EN ISO 527 part 1 and 3, [(c)] BASF-method, [(d)] BASF-method, [(e)] Congo red test DIN EN 60811-3-2, [(f)] glass transition temperature according to ISO 6721-7.

As a value for the hardness of the soft-PVC formulation, the efficiency of the plasticizer is particularly important to determine its suitability. It is given as material hardness, which can, for example, be measured with a Shore durometer. Shore Type A measures the hardness using a hardened steel rod with exact specifications to diameter and cone angle, which applies a perpendicular force on the test object. The material hardness, given in a dimension-free unit, correlates with the indentation.

The efficiency is evaluated in comparison to the industry-standard DEHP, which measures 76 on the Shore A scale (Figure 4.10). One of the best-selling plasticizers today is DINCH, which performs not as good (80 Shore A); however, it is still preferred, as it does not contain a phthalate unit.

While both *exo*-isomers (**7**: 76; **8**: 75 Shore A) showed a good performance in the range of DEHP, the *endo*-isomer performed significantly worse (**4**: 83 Shore A). Again, this can be understood by the changed three-dimensional structure. The less the plasticizer suits between polymer chains, the less it can unfold its potential. Thus far, *endo*-candidate **4** is not well-suited to replace the commercial DINCH.

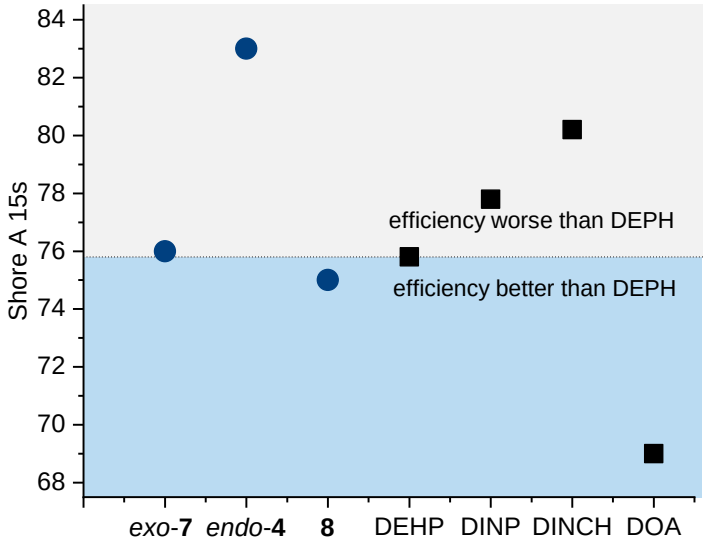

Figure 4.10: Efficiency (Shore A hardness) of different plasticizers.

Moreover, the flexibility of the PVC formulations was investigated by colleagues at the BASF SE. The tensile strain and stress at break as well as the modulus of elasticity at 100% elongation were determined. As observed before, the stereokonfiguration seems to have a great influence on the parameters. For example, the strain at break was for both *exo*-isomers similarly low (**7**: 268%; **8**: 266%), while *endo*-**4** performed on the same level as the commercial DINCH (334%). The tensile strain at break is shown in Figure 4.11.

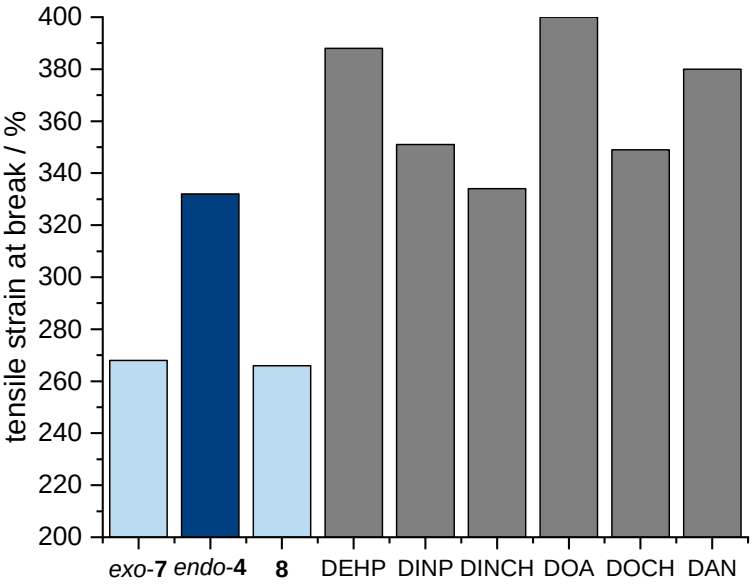

Figure 4.11: Tensile strain of different plasticizers.

Another important parameter, in particular, to evaluate the low-temperature performance, is the brittleness temperature. In detail, this is the temperature at which 50% of the specimens fail under the defined test conditions. For the investigation, the specimens are immersed into a liquid coolant and a force is applied until material failure.[78,101] Brittleness in an application must be avoided to ensure the functionality of the product over a wide temperature range.

All investigated bio-based plasticizers had a comparatively high brittleness temperature (*endo*-**4**: −27.5 °C; *exo*-**8**: −10 °C), while for *exo*-**7** only a glass transition temperature was measured (*exo*-**7**: 1 °C). In general, the glass transition temperature is comparative to the brittleness temperature.[101] Compared to the low-temperature performance of commercial plasticizers (DINCH: −42.5 °C; DINP: −35 °C), only the *endo*-isomer **4** is in a range of practical applicability. Both *exo*-isomers have a limited low-temperature performance and are not well suited for a number of products. In literature, a similar compound to *exo*-**7** was reported bridging the six-membered ring with a carbon-, instead of an oxygen atom. In this case, a brittleness temperature of −55 °C was determined, indicating a tremendous influence of the *oxo*-bridge.[102]

To complete the investigations related to the temperature application range, the volatility as an important measure for high-temperature applicability was investigated. This parameter describes the volatility of the plasti-

cizers in the soft-PVC foil at 130 °C for 24 h and is given in either loss of mass per foil area or relative loss of mass (%). The volatility of the *endo*-compound **4** (5.5%) was very high. Likewise, the corresponding *exo*-compound **7** had a relatively high value of 3.4% compared to the commercial compounds (DINCH: 2.5%; DINP 1.3%). Partly, the high volatility of the *endo*-compound **4** can be explained by its relatively low purity of 95%, since the impurities are mainly of lower molecular mass (bis(2-ethylhexyl succinate (**9**) and solvent residues). The difference to the commercial/literature known compounds are shown in Figure 4.12. From the plot of volatility against molecular mass, a relationship between the two parameters is suggested. This can be well understood, as lower molecular mass corresponds in general to a lower boiling point as well as higher volatility.

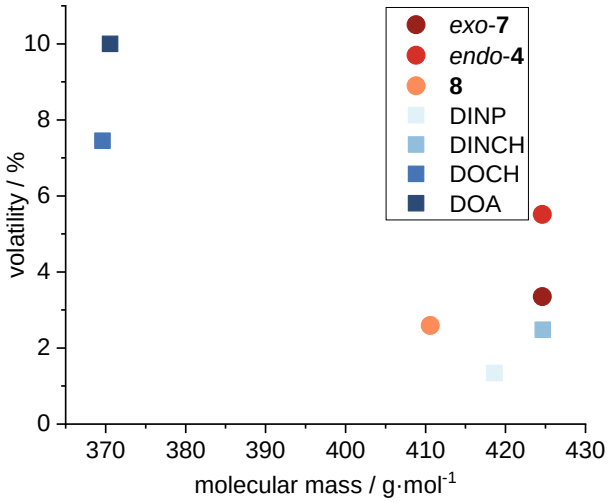

Figure 4.12: Volatility of different plasticizers against their molecular mass.

Furthermore, the soft-PVC stability was determined based on the HCl-resistance. While both *exo*-compounds **7** (9.3 min) and **8** (9.4 min) performed less well but still in an acceptable range, the *endo*-compound **4** performed well (18.3 min). The commercial plasticizer DINCH, for example, resisted for 17.3 min.

4.5 Summary & Outlook

In this project, a route for the synthesis of a novel sustainable plasticizer candidate was developed. The prepared sample was tested by BASF SE for its suitability as a plasticizer in PVC.

Starting from chemicals that can be obtained from renewable feedstocks, a process for the Diels-Alder synthesis of a first candidate was optimized to 85% product-related conversion. An efficient process starting from 2-methylfuran and bis(2-ethylhexyl) maleate based on erbium(III) triflate as a catalyst and without additional solvent was developed. As the product turned out to be moderately unstable under ambient conditions, a way for stabilization was required.

By hydrogenation of the remaining alkene in the bicyclic backbone, the *retro*-Diels-Alder reaction could be successfully prevented, and a stable compound could be obtained. Since approximately 100 g were required for in-depth application testing, a workup based on column chromatography, which yielded only a few grams per run, turned out to be a bottleneck for the final purification. In particular, the separation of a side-product from the hydrogenation reaction originating from an incomplete Diels-Alder reaction was challenging. To avoid tedious column chromatography, unreacted maleate was removed after the Diels-Alder reaction by a reaction with a diamine in an *aza*-Michael-Addition. This method led to the complete removal of the remaining starting material and finally to a product with 97% purity and 43% overall yield with a vastly simplified column chromatography.

A pysical and performance-related analysis of the synthesized material was carried out by colleagues at the BASF SE. While the efficiency, as well as the solution temperature of the novel plasticizer, were not suitable for a commercial product, the viscosity and HCl resistance were in the range of technical applicability. In addition, the volatility was comparatively high. The cold flexibility—a weak point of the corresponding *exo*-isomer—was not perfect but in an acceptable range for most applications. In summary, the synthesized compound can compete with commercial products in some areas and provides a promising platform for further investigations.

A comparison of *exo*- and *endo*-product revealed a strong difference in virtually every parameter. The *exo*-plasticizer is more two-dimensional compared to the *endo*-compound. While the in this work synthesized *endo*-compound had a significantly better low-temperature performance, the solution temperature and efficiency were worse compared to the opposite stereoisomer.

In the future, a mixture of both isomers might be investigated to improve the performance. Moreover, derivatization of the alkene function might lead to compounds replacing trimelliate-based structures.

4.6 Experimental

4.6.1 Chemicals & Equipment

All purchased chemicals were used in commercial grade unless noted otherwise. Chloroform-d1 (99.8% purity, with Ag) was purchased from Deutero. Purified water was used as deionized water (dH_2) or Millipore. If not noted otherwise, deionized water was used. Inert gases (N_2, 99.995%; Ar, 99.996%) and H_2 were supplied by Linde.

Equipment

Syringe pumps: Two-channel syringe pumps Fusion 200 or Fusion 4000 from Chemyx were used for the flow experiments.

Syringes: Gas-tight glass syringes from SGE purchased from Sigma Aldrich or VWR were used in several sizes.

Packed bed reactor: In-house built reactor with cotton-stoppered 5 mm ID glass tube.[103]

Tubing & Fittings: PFA tubing purchased from Techlab (0.8 mm ID). Fittings (PEEK or PFA) were purchased from Techlab.

Up-scale reactor: 1 L jacked glass reactor from Rettberg equipped with an overhead stirrer and tempered using a chiller.

4.6.2 Analytics

All NMR spectra were recorded on a Bruker Avance III 500 spectrometer (500 MHz) in chloroform-d1, referenced internally to the residual solvent

peaks in ppm (chloroform-d1: 7.26 ppm (s)), and analyzed using MestReNova. Chemical shifts σ are reported in ppm to the nearest 0.01 ppm. The multiplicity of ^{1}H signals are indicated as following: s = singlet, d = doublet, dd = doublet of doublet, t = triplet, q = quadruplet, m = multiplet, or combinations thereof. Coupling constants (J) are reported in Hz to the nearest 0.1 Hz.

Mass spectrometry:

Accurate mass nano-ESI measurements were performed using a Q-IMS-TOF mass spectrometer Synapt G2Si (Waters, Manchester, UK) in resolution mode, interfaced to a nano-ESI ion source. Nitrogen served both as the nebulizer gas and the dry gas for nano-ESI. Nitrogen was generated by a nitrogen generator NGM 11. Helium 5.0 was used as buffer gas in the IMS entry cell, nitrogen 5.0 was used for IMS separations. Argon served as collision gas for MS/MS experiments. 1,3-Dicyanobenzene was used as electron transfer reagent in ETD experiments. The MALDI source was equipped with a 2.5 kHz solid-state Nd:YAG laser at a wavelength of 355 nm. Samples were dissolved in acetonitrile and introduced by static nano-ESI using in-house pulled glass emitters.

Nano-ESI mass spectra were recorded using an Esquire 3000 ion trap mass spectrometer (Bruker Daltonik GmbH, Bremen, Germany) equipped with a nano-ESI source. Samples were dissolved in acetonitrile and introduced by static nano-ESI using in-housepulled glass emitters. Nitrogen served both as nebulizer gas and dry gas. Nitrogen was generated by a Bruker nitrogen generator NGM 11. Helium served as cooling gas for the ion trap and collision gas for MS^n experiments. The mass axis was externally calibrated with ESI-L Tuning Mix (Agilent Technologies, Santa Clara, CA, USA) as calibration standard. The spectra were recorded with the Bruker Daltonik esquireNT 5.2 esquireControl software by the accumulation and averaging of two single spectra. DataAnalysis^{TM} software 3.4 was used for processing the spectra.

4.6.3 Screening of the Synthesis of Racemic Bis(2-ethylhexyl) (1R*,2S*,3R*,4R*)-1-methyl-7-oxabicyclo[2.2.1]hept-5-ene-2,3-dicarboxylate (3) at 1 mL Scale

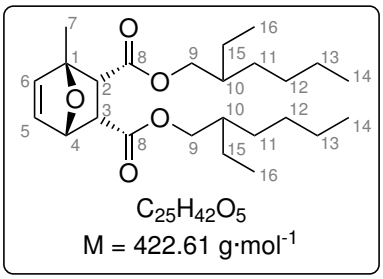

In a glass vial, DCM (500 μL) was cooled to 0 °C. 2-Methylfuran (**1**; 20 eq, 2.0 mmol, 177 μL), bis-(2-ethylhexyl) maleate (**2**; 1 eq, 0.10 mmol, 36.5 μL) and Lewis acid (0.02 mmol, 20 mol%) were added. The suspension was stirred for 24 h at 0 °C. The reaction mixture was quenched with aqueous $NaHCO_3$ solution (0.5 mL of a sat. aq. soln.), filtered using a syringe filter (PTFE, pore size 0.45 μm) and extracted with DCM (2 x 1 mL). The combined organic phases were dried over $MgSO_4$, and filtered using a syringe filter (PTFE, pore size 0.45 μm). The solvent was evaporated (40 °C, > 500 mbar) and the residual oil was analyzed *via* ^{1}H NMR spectroscopy.

^{1}H NMR (500 MHz, $CDCl_3$): δ [ppm] = 6.48 (dd, ^3J = 5.8, 1.6 Hz, 1H, C(5)*H*), 6.35 (d, ^3J = 5.7 Hz, 1H, C(6)*H*), 5.03 (dd, ^3J = 4.6, 1.7 Hz, 1H, C(4)*H*), 4.06–3.94 (m, 2H, C(9)*H*), 3.91–3.81 (m, 2H, C(9)*H*), 3.57 (dd, ^3J = 10.0, 4.5 Hz, 1H, C(3)*H*), 3.05 (d, ^3J = 10 Hz, 1H, C(2)*H*), 1.68 (s, 3H, C(7)*H*), 1.29–1.27 (m, 16H, C(11,12,13,15)*H*), 0.93–0.85 (m, 12H, C(14,16)*H*).

Table 4.6: Results of the Lewis acid screening for the Diels-Alder reaction of furan **1** and ester **2**.

Entry	*Lewis acid*	*LA mass / mg*	*Conversion to **3** / %*	*Exo/endo selectivity*
1	$AlCl_3$	2.7	6	n.d.
2	$TiCl_4$	2.1 µL	10	n.d.
3	$HfCl_4$	6.4	59 (48)	1:5
4	$Er(OTf)_3$[a]	12.3	70	1:6
5[97]	$Er(OTf)_3$[b]	[97]	<1	n.d.
6	$La(OTf)_3$	11.7	< 1	n.d.
7	$Hf(OTf)_3$	15.5	2	n.d.
8	$Yb(OTf)_3$	12.8	38	1:4
9	$YbCl_3$	6.8	< 1	n.d.

[a] $Er(OTf)_3$ from Sigma Aldrich (LOT: MKBS5455V), [b] $Er(OTf)_3$ from BLDpharm (LOT: AGU604).

Table 4.7: Results of the reaction condition screening for the Diels-Alder reaction of furan **1** and ester **2** catalyzed by $Er(OTf)_3$.

Entry	*Change from standard*	*Conversion to **3***	*Exo/endo selectivity*
1	no change	70	1:6
2	solv.: ACN	< 1	n.d.
3	solv.: DCM + water (5 vol%)	49	1:6
4	solv.: MTBE	< 1	n.d.
5	−20 °C	33	1:7
6	−20 °C, 48 h	47	1:7
7	30 °C	33 (32)	1:3
8	30 °C, substr. loading: 0.01 mmol	25	1:3
9	solv.: 2-methylfuran, substr. conc.: 0.8 M, cat. loading: 6 mol%	86	1:9

4.6.4 Synthesis of Racemic Bis(2-ethylhexyl) (1R*,2S*,3R*,4R*)-1-methyl-7-oxabicyclo[2.2.1]hept-5-ene-2,3-dicarboxylate (3) at 30 g Scale

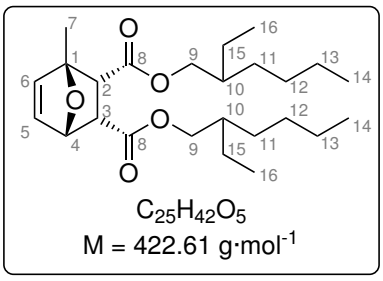

In a 100 mL jacked glass flask, 2-methylfuran (**1**; 10 eq, 0.85 mol, 75 mL), bis-(2-ethylhexyl) maleate (**2**; 1 eq, 85 mmol, 30 mL) and $Er(OTf)_3$ (5.1 mmol, 6.1 mol%, 3.102 g) were added. The yellow suspension was stirred for 24 h at 0 °C. The reaction mixture was quenched with aqueous $NaHCO_3$ solution (25 mL), the phases were separated, dried over $MgSO_4$, and filtered using filter paper. The solvent was removed (5 mbar, 40 °C) and analyzed by ^{1}H NMR (85% conversion to desired product, *exo/endo* = 1:9). Then, portions (up 5–7 g) were purified for further analysis using column chromatography (cyclohexane/ethyl acetate: 0–4% for 3 CV, 4% for 4 CV, 4–9% for 4 CV) and the fractions were analyzed with TLC. Product fractions were combined, and the solvent was removed. The product was analyzed *via* ^{1}H NMR spectroscopy.

^{1}H NMR (500 MHz, $CDCl_3$): δ [ppm] = 6.48 (dd, ^3J = 5.8, 1.6 Hz, 1H, C(5)*H*), 6.35 (d, ^3J = 5.7 Hz, 1H, C(6)*H*), 5.03 (dd, ^3J = 4.6, 1.7 Hz, 1H, C(4)*H*), 4.06–3.94 (m, 2H, C(9)*H*), 3.91–3.81 (m, 2H, C(9)*H*), 3.57 (dd, ^3J = 10.0, 4.5 Hz, 1H, C(3)*H*), 3.05 (d, ^3J = 10 Hz, 1H, C(2)*H*), 1.68 (s, 3H, C(7)*H*), 1.29–1.27 (m, 16H, C(11,12,13,15)*H*), 0.93–0.85 (m, 12H, C(14,16)*H*).

4.6.5 Synthesis of Racemic Bis(2-ethylhexyl) (1R*,2S*,3R*,4R*)-1-methyl-7-oxabicyclo[2.2.1]heptane-2,3-dicarboxylate (4) at 30 g Scale

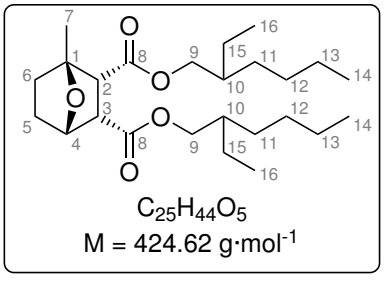

The crude product (**3**; 29.77 g) prepared according to the protocol described in Section 4.6.4 (85% conversion; starting from bis(2-ethylhexyl) maleate (30.08 g, 88.35 mmol)) was dissolved in THF (100 mL). Palladium on carbon (10 wt% Pd basis, 503.1 mg, 1.7 wt%, 0.62 mol%) was added. A hydrogen atmosphere was applied (1 bar) and the suspension was stirred for 24 h at room temperature. Then, the black suspension was

filtered and the solvent was removed from the clear yellow solution. The resulting oil (28.96 g) was purified portion-wise (each approx. 6 g) by column chromatography (cyclohexane/ethyl acetate: 0–4% for 3 CV, 4% for 4 CV, 4–9% for 4 CV) to give the desired product (**4**; corresponding to 45% yield, 99% purity ^{1}H NMR) as a colorless oil.

^{1}H NMR (500 MHz, $CDCl_3$): δ [ppm] = 4.59 (t, ^3J = 5.3 Hz, 1H, C(4)*H*), 4.13–3.94 (m, 2H, C(9)*H*), 3.94–3.79 (m, 2H, C(9)*H*), 3.29 (ddd, $^{3,3,4}J$ = 11.8, 5.1, 1.7 Hz, 1H, C(3)*H*), 2.91 (dd, $^{3,4}J$ = 11.8, 2.1 Hz, 1H, C(2)*H*), 2.16–2.01 (m, 2H, C(5,6)*H*), 1.89–1.75 (m, 1H, C(5)*H*), 1.55 (s, 3H, C(7)*H*), 1.54–1.49 (m, 2H, C(10)*H*), 1.46–1.37 (m, 1H, C(6)*H*), 1.37–1.18 (m, 16H, C(11,12,13,15)*H*), 0.93–0.80 (m, 12H, C(14,16)*H*).

^{13}C NMR (500 MHz, $CDCl_3$): δ [ppm] = 171.14 (C(8)), 171.03 (C(8)), 86.98 (C(1)), 78.33 (C(4)), 67.21 (C(9)), 67.01, 53.65 (C(2)), 50.50 (C(3)), 38.71 (C(10)), 32.17 (C(6)), 30.55–30.43 (C(Alk)), 29.08–28.95 (C(Alk)), 27.65 (C(5)), 23.94–23.75 (C(Alk)), 23.08 (C(Alk)), 20.99 (C(7)), 14.15 (C(14)), 11.04 (C(16)).

Accurate Mass MS (ESI, positive ions): $[C_{25}H_{44}O_5+Na]^+$ *m/z* (calcd) = 447.30810, *m/z* (exp) = 447.3077, deviation = 0.89 ppm.

4.6.6 Synthesis and Purification of Racemic Bis(2-ethylhexyl) (1R*,2S*,3R*,4R*)-1-methyl-7-oxabicyclo[2.2.1]hept-5-ene-2,3-dicarboxylate (3) at 300 g Scale

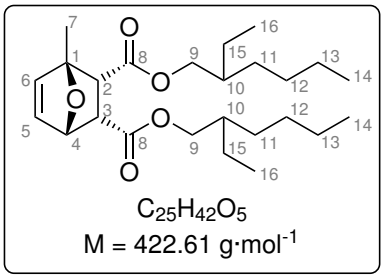

In a jacked reactor (2 L, glass) equipped with an overhead stirred and chiller, 2-methylfuran (**1**; 10 eq, 750 mL, 8.31 mol) was chilled to 0 °C. Then, bis(2-ethylhexyl) maleate (**2**; 1 eq, 276.7 g, 0.813 mol) was added and the yellow solution was stirred for 30 min. Erbium(III) triflate (50.7 mmol, 6 mol%, 31.17 g) was added to give a yellow solution which was stirred at 270 rpm at 0 °C for 22 h. Then, the reaction was quenched with saturated Na_2CO_3 solution (250 mL) to give a foamy

pink aqueous suspension and a yellow organic solution. The organic solution was separated, dried over $MgSO_4$, and filtered. Excess 2-methylfuran (**1**) was removed (10 mbar, 40 °C) to yield the product **3** as a yellow oil. The conversion to the desired product (85%) and selectivity (*endo*/*exo*: 1:9) were determined by ^{1}H NMR.

To the solution of crude product **3** (entire product from the previous step containing residual 13 mol% maleate **2**, and 2 mol% fumarate **5**) in THF (650 mL), 1,5-diaminopentane (50 mL, 0.43 mol) was added. The mixture was stirred at 400 rpm and 0 °C for 1.5 h. After filtration over silica gel (9 cm diameter, 7 cm height) the column was flushed with ethyl acetate (200 mL) and the solvent was removed (1 mbar, 30 °C). The conversion of bis(2-ethylhexyl) maleate (**2**) to the corresponding diamine (100%) was determined by ^{1}H NMR. Residual 2 mol% of fumarate **5** were observed in the crude product. The crude mixture was directly used in the following hydrogenation step.

^{1}H NMR (500 MHz, $CDCl_3$): δ [ppm] = 6.48 (dd, ^3J = 5.8, 1.6 Hz, 1H, C(5)*H*), 6.35 (d, ^3J = 5.7 Hz, 1H, C(6)*H*), 5.03 (dd, ^3J = 4.6, 1.7 Hz, 1H, C(4)*H*), 4.06–3.94 (m, 2H, C(9)*H*), 3.91–3.81 (m, 2H, C(9)*H*), 3.57 (dd, ^3J = 10.0, 4.5 Hz, 1H, C(3)*H*), 3.05 (d, ^3J = 10 Hz, 1H, C(2)*H*), 1.68 (s, 3H, C(7)*H*), 1.29–1.27 (m, 16H, C(11,12,13,15)*H*), 0.93–0.85 (m, 12H, C(14,16)*H*).

4.6.7 Synthesis of Racemic Bis(2-ethylhexyl) (1R*,2S*,3R*,4R*)-1-methyl-7-oxabicyclo[2.2.1]heptane-2,3-dicarboxylate (4) at 300 g Scale

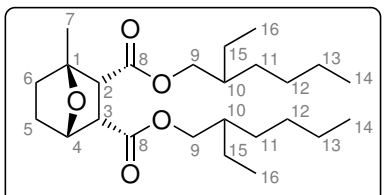

The crude product from the previous reaction was dissolved in THF (approx. 500 mL) and palladium on carbon (10 wt% Pd basis, 5 g, 2 wt%). A hydrogen atmosphere was applied (1 bar) and the mixture stirred at 400 rpm at 0 °C. The mixture was allowed to heat to room temperature after 3 h and stirred for a further 22 h. Periodically, the hydrogen bal-

loon was replaced. Then, the black suspension was filtered and the solvent was evaporated from the clear yellow solution. A portion (204.36 g) of the resulting oil (290.61 g) was purified by column chromatography (equilibration: 3 CV cyclohexane; gradient: cyclohexane/ethyl acetate: 0–3% for 2.5 CV, 3–4% for 7.5 CV, 4–5% for 3.0 CV, 5–6% for 0.7 CV) to give the desired product **4** as a colorless oil (105.1 g, 97% purity according to ^{1}H NMR, corresponding to a theoretical yield of 43% considering all reaction steps including the Diels-Alder and the *aza*-Michael steps).

^{1}H NMR (500 MHz, $CDCl_3$): δ [ppm] = 4.59 (t, ^{3}J = 5.3 Hz, 1H, C(4)*H*), 4.13–3.94 (m, 2H, C(9)*H*), 3.94–3.79 (m, 2H, C(9)*H*), 3.29 (ddd, $^{3,3,4}J$ = 11.8, 5.1, 1.7 Hz, 1H, C(3)*H*), 2.91 (dd, $^{3,4}J$ = 11.8, 2.1 Hz, 1H, C(2)*H*), 2.16–2.01 (m, 2H, C(5,6)*H*), 1.89–1.75 (m, 1H, C(5)*H*), 1.55 (s, 3H, C(7)*H*), 1.54–1.49 (m, 2H, C(10)*H*), 1.46–1.37 (m, 1H, C(6)*H*), 1.37–1.18 (m, 16H, C(11,12,13,15)*H*), 0.93–0.80 (m, 12H, C(14,16)*H*).

^{13}C NMR (500 MHz, $CDCl_3$): δ [ppm] = 171.14 (C(8)), 171.03 (C(8)), 86.98 (C(1)), 78.33 (C(4)), 67.21 (C(9)), 67.01, 53.65 (C(2)), 50.50 (C(3)), 38.71 (C(10)), 32.17 (C(6)), 30.55–30.43 (C(Alk)), 29.08–28.95 (C(Alk)), 27.65 (C(5)), 23.94–23.75 (C(Alk)), 23.08 (C(Alk)), 20.99 (C(7)), 14.15 (C(14)), 11.04 (C(16)).

Accurate Mass MS (ESI, positive ions): $[C_{25}H_{44}O_5+Na]^+$ *m/z* (calcd) = 447.30810, *m/z* (exp) = 447.3077, deviation = 0.89 ppm.

4.6.8 Synthesis of Racemic Bis(2-ethylhexyl) (1R*,2S*,3S*,4R*)-1-methyl-7-oxabicyclo[2.2.1]hept-5-ene-2,3-dicarboxylate (6)

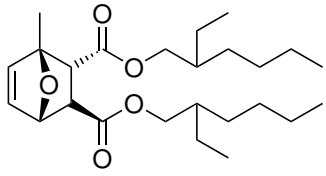

$C_{25}H_{42}O_5$
M = 422.61 g·mol^{-1}

In a 100 mL jacked glass flask, 2-methylfuran (**1**; 10 eq, 0.85 mol, 75 mL), bis-(2-ethylhexyl) fumarate (**5**; 1 eq, 85 mmol, 30 mL) and $Er(OTf)_3$ (5.1 mmol, 6.1 mol%, 3.102 g) were added. The yellow suspension was stirred for 24 h at 0 °C (or 30 °C). The reaction mixture was quenched with aqueous $NaHCO_3$ solution (20 mL), the phases were separated, dried

over $MgSO_4$, and filtered using filter paper. The solvent was removed ($\leq$ 10 mbar, 40 °C) and investigated by ^{1}H NMR ($\leq$ 1% conversion at either temperature). No further purification, isolation and detailed analysis were attempted.

4.6.9 Praparation of $Er(OTf)_3$ SILP

To prepare silica immobilized erbium catalyst, $Er(OTf)_3$ (755.29 mg) was mixed with [bmim][OTf] (1.025 82 g), silica gel (spherical for column chromatography, 9.996 42 g) and THF (10 mL). After stirring for 90 min at room temperature, the solvent was removed under reduced pressure to yield a pale pink powder. The powder was rinsed with Et_2O and dried in high vacuum (0.1 mbar) for 1 d. Powder (12.1801 g) was obtained resulting in a theoretical Er-loading of 0.06 $mg_{Er(OTf)_3} \cdot mg_{SiO_2}{}^{-1}$.

4.6.10 Synthesis of Racemic Bis(2-ethylhexyl) (1R*,2S*,3R*,4R*)-1-methyl-7-oxabicyclo[2.2.1]hept-5-ene-2,3-dicarboxylate (3) using $Er(OTf)_3$ SILP

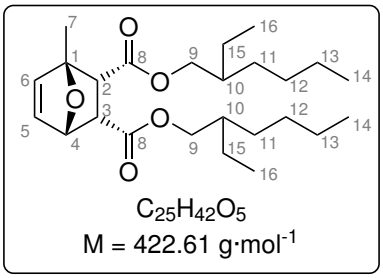

In a glass vial, 2-methylfuran (**1**; 10 eq, 8.5 mmol, 750 μL), bis-(2-ethylhexyl) maleate (**2**; 1 eq, 0.83 mmol, 287 μL) and either $Er(OTf)_3$ (0.051 mmol, 6.1 mol%, 31.3 mg) or $Er(OTf)_3{\cdot}SiO_2$ (0.05 mmol, 6.0 mol%, 530 mg, corresponding to 31.8 mg $Er(OTf)_3$) were added. The yellow suspension was stirred for 24 h at 0 °C. The reaction mixture was quenched with aqueous $NaHCO_3$ solution (1 mL), the phases were separated, dried over $MgSO_4$ and filtered using a syringe filter. The solvent was evaporated (50 °C, > 10 mbar) and the residual oil was analyzed *via* ^{1}H NMR spectroscopy. For the immobilized catalyst a conversion to the desired product **3** of 19% was obtained and for the non-immobilized 58%.

^{1}H NMR (500 MHz, $CDCl_3$): δ [ppm] = 6.48 (dd, ^3J = 5.8, 1.6 Hz, 1H, C(5)*H*), 6.35 (d, ^3J = 5.7 Hz, 1H, C(6)*H*), 5.03 (dd, ^3J = 4.6, 1.7 Hz, 1H, C(4)*H*), 4.06–3.94 (m, 2H, C(9)*H*), 3.91–3.81 (m, 2H, C(9)*H*), 3.57 (dd, ^3J = 10.0, 4.5 Hz, 1H, C(3)*H*), 3.05 (d, ^3J = 10 Hz, 1H, C(2)*H*), 1.68 (s, 3H, C(7)*H*), 1.29–1.27 (m, 16H, C(11,12,13,15)*H*), 0.93–0.85 (m, 12H, C(14,16)*H*).

4.6.11 Continuous Synthesis of Racemic Bis(2-ethylhexyl) (1R*,2S*,3R*,4R*)-1-methyl-7-oxabicyclo[2.2.1]hept-5-ene-2,3-dicarboxylate (3) using Er(OTf)$_3$ SILP

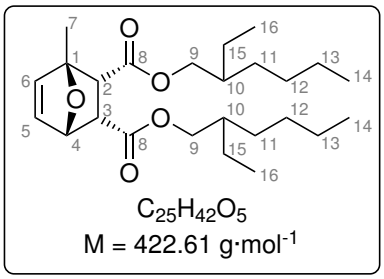

In a glass syringe, 2-methylfuran (**1**; 10 eq, 16.4 mmol, 1446 μL) and bis-(2-ethylhexyl) maleate (**2**; 1 eq, 1.60 mmol, 554 μL) were mixed. In a glass reactor (inner diameter 5 mm), a cotton layer (5 mm hight) followed by $Er(OTf)_3{\cdot}SiO_2$ (600 mg, corresponding to 36.0 mg $Er(OTf)_3$, 0.057 mmol) and a final cotton layer (5 mm height) were added. The reactor volume was determined volumetrically by injection of 2-methylfuran as 860 μL. The starting material solution was pumped using a syringe pump over the reactor bed with a flow rate of 0.172 mL $\cdot$ min^{-1} corresponding to a residence time of 5 h. One fraction was collected, the solvent was evaporated (50 °C, > 10 mbar) and the residual oil was analyzed *via* ^{1}H NMR spectroscopy (17% conversion to **3**). Over the reaction time, the first 1 mm of the reactor bed turned from colorless to orange. After the reaction was completed, the reactor bed was removed, extracted with dichloromethane and the residual oil after solvent evaporation was analyzed *via* ^{1}H NMR spectroscopy (similar results compared to collected fraction).

^{1}H NMR (500 MHz, $CDCl_3$): δ [ppm] = 6.48 (dd, ^3J = 5.8, 1.6 Hz, 1H, C(5)*H*), 6.35 (d, ^3J = 5.7 Hz, 1H, C(6)*H*), 5.03 (dd, ^3J = 4.6, 1.7 Hz, 1H, C(4)*H*), 4.06–3.94 (m, 2H, C(9)*H*), 3.91–3.81 (m, 2H, C(9)*H*), 3.57 (dd, ^3J = 10.0, 4.5 Hz, 1H, C(3)*H*), 3.05 (d, ^3J = 10 Hz, 1H, C(2)*H*), 1.68 (s, 3H, C(7)*H*), 1.29–1.27 (m, 16H, C(11,12,13,15)*H*), 0.93–0.85 (m, 12H, C(14,16)*H*).

4.6.12 Performance Tests of Plasticizer 4

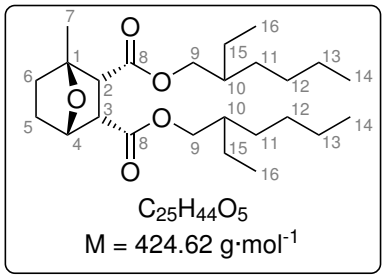

Two samples of plasticizer candidate **4** were sent to the BASF SE for in-depth analysis of the physical properties and performance tests. While the first sample (approx. 30 g) was not purified *via* the previously described *aza*-Michael route, the second sample (approx. 100 g was purified that way (see synthesis of 300 g sample).

Table 4.8: Physical data of candidate **4** determined by the BASF SE.

Entry	*Parameter*	*First sample*	*Second sample*
1	Molecular mass	424.62 g/mol	424.62 g/mol
2	Density[(a)]	0.9808 gcm^3	0.9894 gcm^3
3	Viscosity[(b)]	69.9 mPas	101.62 mPas
4	Pt/Co color[(c)]	n.d.	75
5	Refractive index[(d)]	1.4618 n_{20D}	1.4636 n_{20D}
6	Solution temperature[(e)]	153 °C	154 °C
7	Water content[(f)]	n.d.	0.029%
8	Acid number[(g)]	n.d.	0.086 mg_{KOH}/g
9	Purity (GC)	94.61 area%	94.85 area%

[(a)] Method: DIN EN ISO 868, description: mechanical oscillator, instrument: Paar DMA 48 Dig., [(b)] method: DIN 51562, description: rheometer, instrument: Paar MCR 101, [(c)] method: DIN ISO 6271, description: comparison with platium-cobald standards, instrument: Lange Lico 400, [(d)] method: DIN 51423, description: refractometer, instrument: Paar MCR 101, [(e)] method: BASF method (details see below), description: rheometer, instrument: Paar MCR 302, [(f)] method: DIN 51777 pt. 1, description: Karl-Fischer titration, instrument: Metrohm E 547 K.F. titrator, [(g)] method: DIN EN ISO 3682, description: direct titration, instrument: Metrohm titrator.

Table 4.9: Performance data of candidate **4** in PVC determined by the BASF SE.

Entry	*Parameter*	*Value*
1	Tensile stress at break [(a)]	21.1 MPa
2	Tensile strain at break[(a)]	332%
3	100% modulus[(a)]	9.7%
4	Shore A Hardness 15s[(b)]	83
5	Solution temperature[(c)]	154 °C
6	Brittleness temperature[(d)]	−27.5 °C
7	Volatility[(e)]	5.51%
		1.67 mg/cm^2
8	HCl-stability [(f)]	18.28 min

[(a)] Mechanical properties determined based on method: DIN EN ISO 527 pt. 1 and 3, description: 23 °C, 0.5 mm pressed plaques clamp speed 100 mm/min; instrument: Zwick BZ2.5/TH1S, [(b)] method: DIN EN ISO 868, description: 10 mm test specimen, readings 15 s; instrument: Hildebrand digital durometer, [(c)] method: BASF method (details see below), description: rheometer, instrument: Paar MCR 302, [(d)] method: BASF method, description: falling weight method, instrument: Heraeus Voetsch test chamber, [(e)] method: BASF method, description: heating at 130 °C for 24 h, instrument: Heraeus-oven, controlled airflow; [(f)] method: DIN EN 60811-3-2.

Measurement of the solution temperature

PVC plastisols were prepared from PVC (Vinoflex S7114, sieve fraction <100 μm, 5 parts), stabilizer (Reagens SLX/781, 0.1 parts) and plasticizer (**4**, 95 parts). The PVC was weighed in a PE beaker and pre-mixed with the liquid components in a metal bowl before it was transferred back to a PE beaker. Then, the mixture was homogenized at 2500 rpm for 150 s using a stirrer equipped with a dissolver disk (IKA RE-166 A, disk diameter: 40 mm). The obtained plastisol was confined air-free in a steel bowl in a desiccator under reduced pressure until no more or only very reduced bubble formation was observed and transferred in a PE beaker. After 30 min, the viscosity was determined using a heatable oscillating and rotational rheometer (Paar MCR 302) in a rotational test according to the following specifications:

Table 4.10: Specifications of the viscosity determination.

Entry	*Parameter*	*Value*
1	System	plate/plate 50 mm diameter
2	Shear rate	$10\,s^{-1}$
3	Gap width	0.25 mm
4	Start temperature	30 °C
5	Temperature profile	30–180 °C with 5 °C/min
6	Measuring points/duration	600/3 s

In the first step, the sample was tempered to 30 °C. The plastisol was sheared for 2 min with a rate of $10\,s^{-1}$. Then, the temperature profile as mentioned above was started. The viscosity was monitored as a function of temperature. At the viscosity maximum, the solution temperature was reached.

Closed-loop Optimization Platform

5

» *This chapter describes the development and application of a closed-loop optimization software platform featuring remote access, a user-friendly interface, as well as a performant optimization algorithm. By designing and developing customized online analytic solutions for gas chromatography and a modular reactor, a system for automated optimization of multistep flow processes with biocatalytic steps was created.* «

5.1 Theoretical Background

5.1.1 Digitalization in Chemistry

Chemistry evolved over many hundreds of years, and chemists developed an intuition for reactions and mechanisms. Today, technology has leaped forward and opened possibilities to relieve lab scientists of many laborious tasks, so they can focus on other challenges. Moreover, digital tools offer users to learn more from the gathered data.

While some tasks can be easily and reliably assigned to digital systems, other tasks, especially ones that require experience and creativity are still a challenge for automation. One of these tasks is, for example, the optimization of reactions. The development of synthetic routes is another example requiring experience and creativity. In the past years, tremendous progress has been made in computer-assisted synthesis planning, exploiting huge databases or machine learning algorithms.[104–108]

Repetitive tasks on the other hand can be automated in a very robust and simple way.[109,110] Many devices and systems have been automated, and chemists today do not want to miss the benefits of autosamplers in analytical devices, automated fraction collection, and computer-assisted data analysis.

Moreover, process analysis technologies (PAT) are enriching the chemistry by offering a deep insight into reactions. Mechanisms can be better understood[111] and kinetic profiling[112] offers a way of improvement and modeling based on data.

5.1.2 Closed-loop Optimization

Recently, the combination of lab automation, inline analytics, and process optimization within a single system has become an emerging field of research. In such systems, a chemical reaction can be improved fully automated. In this context, *closed-loop* systems offer a maximum degree of automation. They operate in a *loop* of (1) reaction, (2) analysis, and (3) improvement, to optimize a given reaction (Figure 5.1). It is commonly called *closed*, as no data must be included from external sources, and the system does not require input from an operator—the system is self-operating.

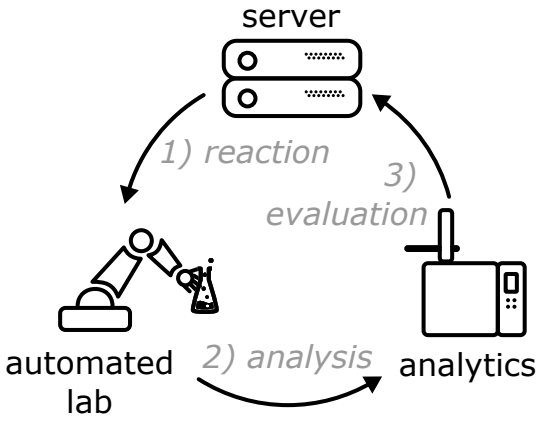

Figure 5.1: Steps of a closed-loop optimization system.

In particular, the combination with continuous synthesis is exciting, as it can be relatively easily automated and offer novel process windows compared to batch chemistry. Moreover, scale up of flow reactions is often

simpler compared to batch mode. For a more detailed introduction to flow chemistry, please see Section 6.1.2.

As flow reactions are typically run after each other (serial), iterative algorithms have proven to be highly suitable. In contrast, parallelization is a typical feature of batch screening (e.g. high-throughput screening). Therefore, different optimization algorithms are preferred taking the possibility to run many reactions simultaneously into account (Figure 5.2).

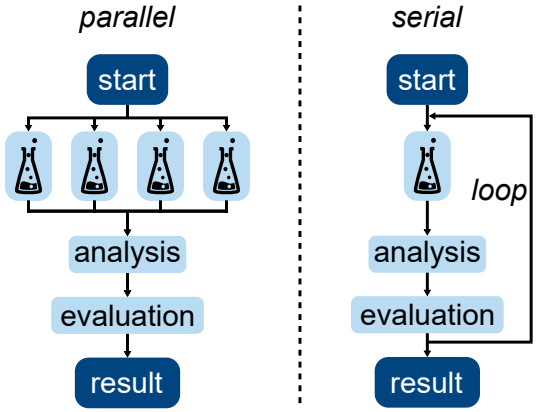

Figure 5.2: Schematic comparison of parallel and serial (closed-loop) optimization.

As in most real-world problems, we typically have no deep insight in the reaction system; therefore, the system cannot be exactly defined by a mathematical function. Thus, optimization methods based on differentiation (analytical methods) cannot be used, as they require knowledge of the exact or a model function. *Heuristic* methods (from Ancient Greek *heurískō*, "I find, discover"), attempt to find optimal conditions by approximation. Such approaches are often called "back-box" optimization. A trade-off between accuracy, completeness, and speed is inevitable. With heuristic methods, the best value the optimizer found is given, which does not necessarily mean it is the most optimal. In this context, a typical problem is that a local maximum was found instead of the global maximum.

In chemistry, trends are often not linear. Instead, often more complex behavior can be seen. Consider the example of the temperature dependency of the oxidation of an alcohol to an aldehyde: At low temperatures, the reaction proceeds very slowly. As the temperature is increased, initially, the conversion is, too. However, from a certain temperature on, an over-oxidation to the acid can occur, reducing the selectivity of the reaction. The resulting yield of the reaction has then a maximum at a temperature,

which is not at the maximum or minimum value of the process space (Figure 5.3).

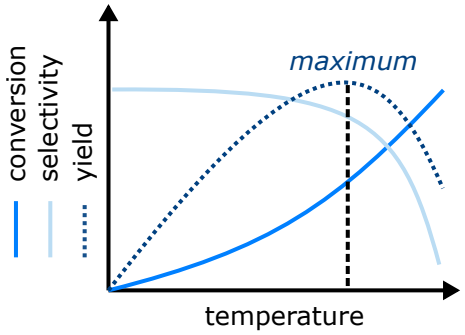

Figure 5.3: Visualization of the non-linear temperature dependency of conversion, selectivity, and the resulting yield of an imaginary reaction with a highlighted maximum of yield.

Therefore, algorithms like the Simplex—a classic approach for linear optimization—cannot be used. A prominent algorithm for solving these non-linear problems is the Downhill-simplex (or Nelder-Mead simplex), developed by the statisticians *J. Nelder* and *J. Mead* in the 1960th.[113] Due to its simplicity and robustness, the Nelder-Mead (NM) simplex is often applied for optimization problems. Examples can be found in a variety of applications ranging from baking bread[114] to nuclear reactor core design.[115] In chemical process optimization, this algorithm is frequently used as well.[116–119]

As the name indicates, Nelder and Mead used a simplex to perform the optimization. Simplices are special, n-dimensional geometrical polytopes with $n+1$ corners. Examples are triangles in two-, or tetrahedra in three-dimensional spaces. An in-depth explanation of the algorithm is given in Subsection 5.3.1. Since the optimization is based on geometry, only continuous numerical variables can be used (Figure 5.4).

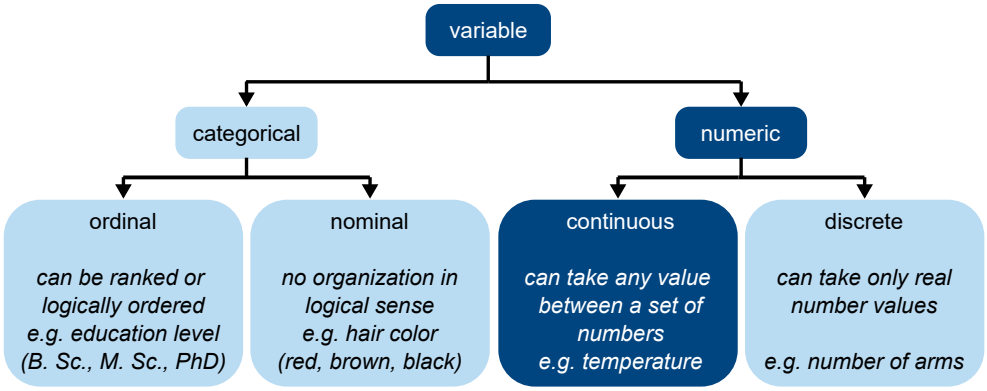

Figure 5.4: Classification of variables.

From the relevant evaluation parameters, like yield or throughput, typically an evaluation function is created.[120] The value of the function is maximized during the optimization by adjusting the optimization parameters—like temperature or residence time. Within the defined process space, these parameters can be changed. In Figure 5.5, an exemplary evaluation function for the evaluation parameters yield and throughput is shown. Each parameter is weighted by a factor (a or b) and normalized. The parameters are then additively combined to create the function. The function response is fed into the optimization algorithm to be maximized (or minimized depending on the implementation).

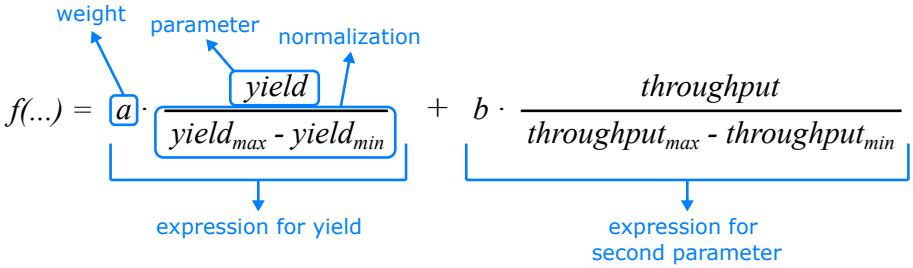

Figure 5.5: Exemplary evaluation function $f(...)$ for a closed-loop optimization using yield and throughput as parameters.

Besides the Nelder-Mead (NM) simplex (and modifications thereof), a number of other algorithms were applied in the past, as reviewed by Clayton *et al.*[121] One of the most well-established optimization methods is design of experiments (DoE; Figure 5.6). In this model-based approach, a set of experiments is calculated. This approach will identify the importance and influence of the studied parameters. Moreover, the interaction of different parameters can be investigated. Through statistical analysis, a model can be fitted, and a response surface can be plotted. Over the past years, this initially rigid design was modified to allow for more flexible applications. In particular, the combined investigation of continuous and categorical variables offers general applicability of this method. In academia as well as industry, DoE is well understood and readily applied.[122–124] For example, Santi *et al.* optimized an electrochemical reaction using this procedure, which enabled fast screening of several parameters, such as temperature, electrode material, current, flow rate, and concentration. Furthermore, Reizman and Jensen applied this technique in a continuous synthesis optimizing solvent and reaction conditions in real-time.[125]

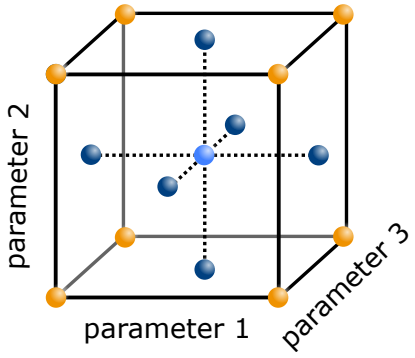

Figure 5.6: Illustration of a central composite design of experiments approach.

Alternative "black-box" algorithms to the Nelder-Mead simplex were applied as well. In combination with a DoE approach, the *steepest decent method* was used by the group of Jensen.[126,127] This algorithm is gradient-based and calculates from an initial local response surface, which was generated *via* DoE, the gradients. Along the trajectory, experiments are conducted until the result gets worse. Another local response surface is generated to determine the new direction or decide if the maximum was found.

Furthermore, the SNOBFIT (Stable Noisy Optimization by Branch and FIT) was frequently applied in self-optimizing systems. Compared to the NM simplex, the SNOBFIT is a global optimization algorithm with noise-handling. In this context, noise is random deviation in the experiment through inaccuracy or unknown factors. In contrast to the simplex, the noise does not lead to reduced optimization speed and the issue of premature termination not at the maximum. This higher confidence in finding the global maximum is one of the main advantages of this approach. Analog to the NM simplex, the algorithm requires no knowledge of the objective function describing the reaction system. By modeling the system with linear and quadratic surrogate functions, the optimum can be determined. Applying this system, Krishnadasan *et al.* could successfully develop a system for the self-optimized generation of nanoparticles.[128] Later, several groups successfully applied this concept to a wide range of reactions.[129–132]

Recently, multi-objective optimization approaches were applied.[133] This approach enabled the authors to simultaneously optimize for reactor productivity and environmental objectives (E-factor). A Bayesian optimization algorithm that aims to approximate a Pareto front was used to improve the

reaction. The Pareto front is the tradeoff curve of two conflicting parameters. It is generated by the value set where the improvement of one of the parameters leads to a reduction of the other. In their example, they created a Pareto front of space-time yield *versus* E-factor. This dataset allowed a simple reevaluation of the reaction if the targets were changed. Moreover, the group of Sasai applied a Gaussian optimization approach to an enantioselective organo-catalyzed Rauhut–Currier and [3+2] annulation to form a chiral spiro compound.[134]

Different closed-loop optimization platforms for flow chemistry were developed in the past. For example, Fitzpatrick *et al.* developed a platform for remote self-optimization exemplified on the synthesis of different active pharmaceutical ingredients.[119,120] This system enabled the authors to remotely control equipment around the world and optimize a reaction from a distance as far away as continents. A recent mini review by Mateos *et al.* summarizes the efforts in the area of self-optimizing flow platforms.[135]

5.2 Concept

To make process development more efficient and autonomous, this second chapter presents a closed-loop optimization platform. The platform is planned as a server-based system that provides the user with a simple user interface. This will allow chemists without programming skills to easily use the program for reaction optimization tasks. During this work, various devices will be modified or designed and built to meet the requirements for continuous and remote operation by the server.

Despite numerous published examples, no source code of a remote-controlled closed-loop platform was publicly available. Therefore, in this work such a software will be programmed from scratch, starting with modules for the optimization algorithm and the calculation of flow rates. The selected optimization algorithm is a Nelder-Mead simplex, the implementation of which is described in this chapter. At the start of the development, a local, script-based system will be developed. The reactions will be defined directly in the source code of the program. Python will be used as the primary programming language. After initial testing of the individual modules, a server-based system featuring remote access will be presented. This concept will

enable chemists without programming knowledge to use the optimization platform.

For the control of the reaction temperature, the development of a modular reactor concept is planned. This reactor will allow on the one hand remote temperature control by the control server and on the other hand simple manual control through an integrated touch screen.

Furthermore, the modification of a gas chromatograph as an online analysis instrument is described. For this purpose, a concept for continuous sampling will be developed and a driver will be programmed that remotely controls the chromatograph, communicates with the server, and evaluates the data. In addition to chromatography, a nuclear magnetic resonance spectrometer is planned to be integrated into the system.

A particular focus of this project will be on the ability to optimize reaction cascades involving biocatalytic reaction steps, which has not yet been described in the literature. In particular, the combination of continuous biocatalysis with closed-loop optimization will provide a previously unexplored perspective on biocatalysis. The developed platform will moreover form the basis for investigations of challenging aspects in chemical process optimization, such as multi-component reactions or optimization of ee values, and enable their rapid development.

5.3 Software Modules

At first, the optimization platform was developed with different modules: The optimization algorithm (Subsection 5.3.1) and the flow rate calculating modules (Subsection 5.3.2).

5.3.1 Optimization Algorithm

In this work, a Nelder-Mead (NM) simplex algorithm was used for the closed-loop optimization. The algorithm was programmed inspired by an open-source implementation.[136]

Algorithm Implementation In the following paragraph, the operations of the NM simplex algorithm are explained on a simplified mathematical basis. After the initialization (1), the experiments are ordered (2) and the centroid is calculated (3). Then, a new experiment is proposed by the transformation of the previous runs (4). The steps of ordering, centroid determination, and transformation are iterated as long as the termination conditions are not met (5).

1) Initialization

At the beginning, the corners of the first simplex are calculated. As the simplex has n+1 (n = number of dimensions) corners, this number of experiments is required. The initial guesses are distributed over the lower quadrants of the process space (Figure 5.7).[i] The first points were calculated with 1/2 and 1/4 of all parameters, respectively. The following points were determined with one parameter at 3/4, while the others remained at 1/4.

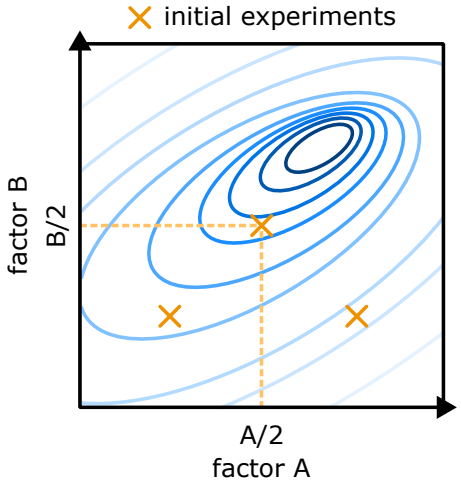

Figure 5.7: Illustration of the initial experiments for the Nelder-Mead simplex optimization distributed in the lower quadrant. The contour plot indicates a higher function value by a darker color.

i Other implementations might choose random initial conditions; however, this tends to make the system vulnerable to tediously small steps during the optimization. The method used in this work is based on the results of Fitzpatrick *et al.*[119]

2) Ordering

The experiments are then sorted by ascending function values (Figure 5.8).

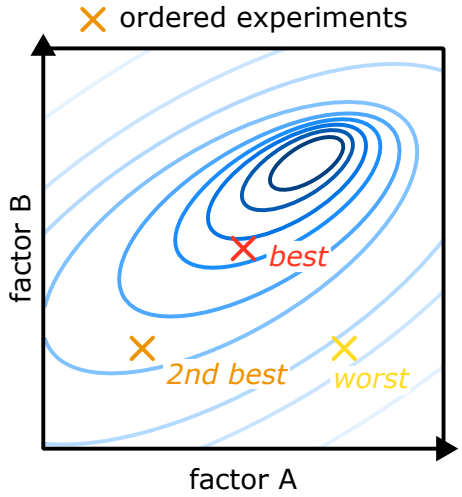

Figure 5.8: Illustration of the ordering of the experiments for the Nelder-Mead simplex optimization. The contour plot indicates a higher function value by a darker color. Yellow, worst experiment; orange, 2nd best; red, best experiment.

3) Centroid determination

Next, the centroid (mean value; x_c) is calculated considering all experiments (x_i) except the worst-performing one (x_w) as follows (Figure 5.9):

$$x_c = \frac{1}{n} \sum_{i \neq w} x_i \tag{5.1}$$

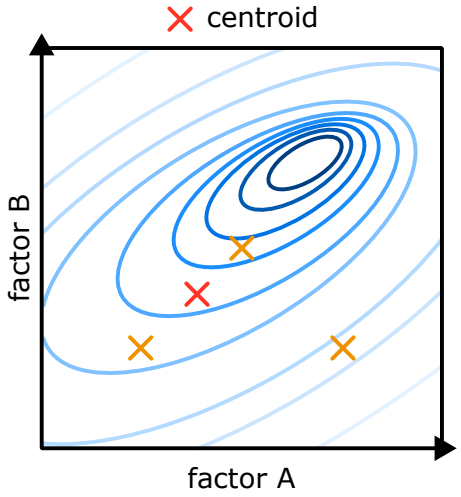

Figure 5.9: Illustration of the calculation of the centroid of the considered experiments for the Nelder-Mead simplex optimization. The contour plot indicates a higher function value by a darker color. Red, centroid of the two best experiments; orange, previously determined experiments (initial conditions from Figure 5.7).

4) Transformation

The transformation can happen in three ways: Reflection, expansion, or contraction.

4a) Reflection

In all cases, an initial reflection is performed (Figure 5.10). The idea is to move the next point away from the least-performing one. Therefore, the next value is calculated by reflecting the least-performing point x_w through the centroid x_c. The reflected point x_r is calculated with a reflection parameter α (usually equal to 1):

$$x_r = x_c + \alpha \cdot (x_c - x_w) \tag{5.2}$$

If the new point x_r is better than the second worst-performing point but not better than the best-performing point, the new point is added to the simplex and replaces the worst-performing one. Then, the next iteration is started from *2) Ordering*. Alternatively, an expansion or contraction procedure is performed—depending on the function value.[ii]

ii Other implementations make use of another operation called shrinking. Here, the simplex is contracted keeping only the best-performing point constant. However, this

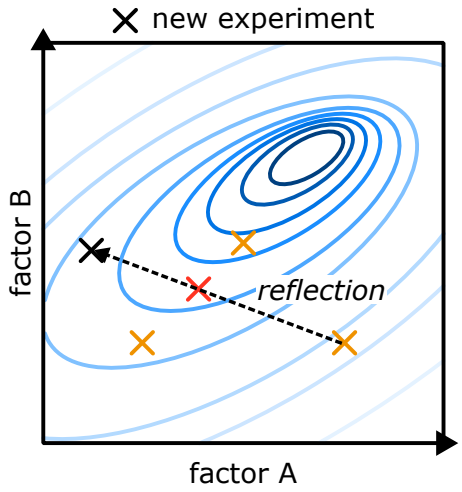

Figure 5.10: Illustration of the newly calculated experiment through reflection for the Nelder-Mead simplex optimization. The contour plot indicates a higher function value by a darker color. Dashed arrow, vector of the reflection; black cross, newly generated point; orange crosses, previous points; red cross, centroid.

4b) Expansion

If the reflected point is the best-performing point compared to the simplex, this direction is further explored. The vector from x_r to x_c is extended by the factor γ (in this work and commonly used, γ is 1.25):

$$x_e = x_c + \gamma \cdot (x_r - x_c) \tag{5.3}$$

In this implementation, the point with the worst-performance is replaced either by the reflected x_r or the expanded point x_e, depending on their performance. Other implementations might consider the extended point, regardless of whether it performs better.

4c) Contraction

In the case the reflected point performs worse than the second-worst point, the next experiment x_{con} is moved back along the vector from x_r to x_c and inward to the simplex with the parameter β (here 0.5):

operation is time-consuming as n (n = number of dimensions) new experiments are generated. For this reason, and because this process is rare, it is often omitted in the literature.

$$x_{con} = x_c + \beta \cdot (x_r - x_c) \tag{5.4}$$

This procedure happens in the case the algorithm moved in the wrong direction or passed the maximum. Again, the worst-performing point is replaced by the best new one.

5) Termination

Different options for termination are possible: (1) The *target* value of the system response might be reached: For example, a conversion of 100% was achieved. (2) A *limit* of experiments was reached. This option is particularly suitable if only limited resources (material or time) are available. Or (3), a *stable* response value was observed over a number of experiments. In this work, a maximum number of ten optimization iterations was used.

5.3.2 Flow Rate Calculation

To allow for adjustable reagent concentrations, catalyst loadings, phase ratios, and residence times, the substrate and dilution flow rates were calculated in a Python module. The phase ratio is only relevant for biphasic reaction systems and is defined here as the ratio of organic to aqueous volume.

The individual flow rates for the feeds were calculated based on the reactor volume, the current total flow rate, the desired reaction concentrations, and stock concentrations, as well as the phase ratio. When a biphasic system was selected, the total flow Q_{tot} was divided into organic Q_{org} and aqueous Q_{aq} flows according to the phase ratio PR:

$$Q_{org} = Q_{tot} \cdot PR \tag{5.5}$$

$$Q_{aq} = Q_{tot} - Q_{org} \tag{5.6}$$

If no phase ratio has been specified, a monophasic system was assumed. Based on desired substrate/catalyst concentrations c_i and the stock solutions $c_s(i)$, the flow rates Q_i for all compounds i (Q_i) in the corresponding

phase were calculated and subtracted from the total flow to obtain the remaining dilution streams $Q_{dil(org/aq)}$. They compensated for the reduced flow rate of the substrate compared to the flow rate required to achieve the total flow rate necessary for a given residence time.

$$Q_i = \frac{c_i}{c_s(i)} \cdot Q_{tot} \tag{5.7}$$

$$Q_{dil(org)} = Q_{org} - \sum_{i(org)} Q_i \tag{5.8}$$

During an optimization run, the reactor volume is considered to be constant. An illustration of the composition of the individual and combined flows in a process is shown in Figure 5.11.

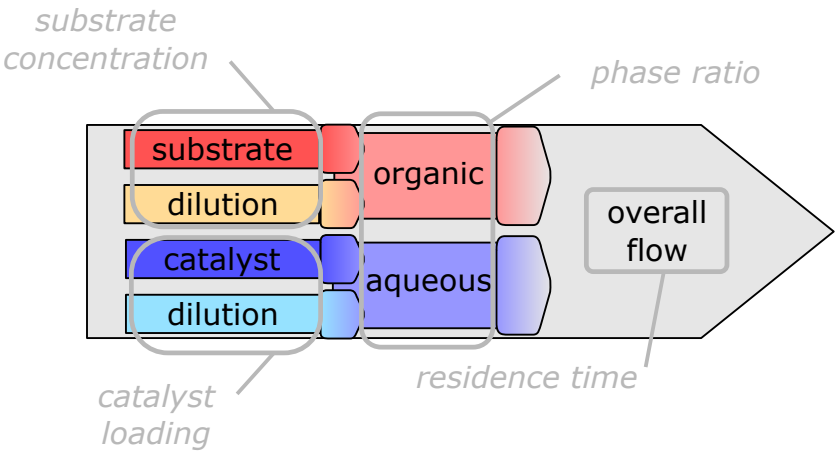

Figure 5.11: Visualization of the contributions of flow rates to the overall steam in a complex biphasic reaction system with substrate and catalyst. The adjustable parameters are shown in *italics*.

5.4 Closed-loop Optimization Platform

5.4.1 Local Implementation

For rapid development and testing purposes of the closed-loop optimization, a script-based approach was first developed. This was run locally on the stationary gas chromatograph computer to allow direct access to the gas chromatography system and its data. As communication with the analyti-

cal devices in particular proved challenging, this approach offered a simple solution to get the development of the single modules started.

However, some disadvantages could not be overcome due to the configuration of this particular PC. For example, remote access was not possible, and changes to the configuration of this PC's were limited. Nevertheless, this local implementation provided valuable initial insight into closed-loop systems and formed a solid and uncomplicated basis for further development. An overview of the concept of the local implementation is shown in Figure 5.12.

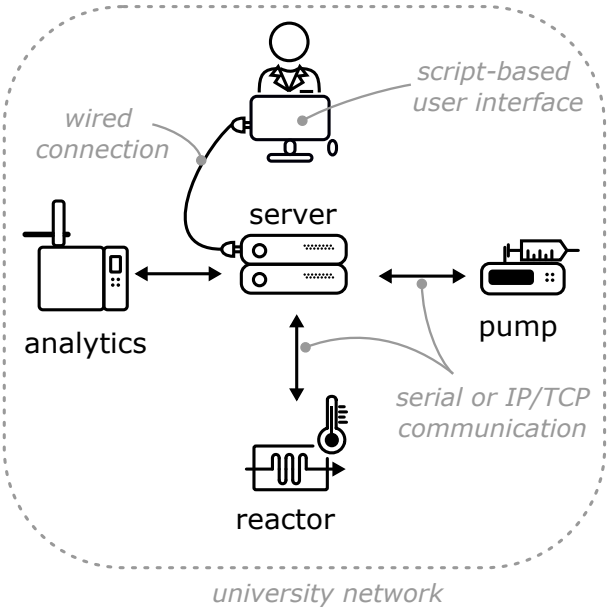

Figure 5.12: Schematic overview of the developed script-based closed-loop optimization system. TCP, transmission control protocol; IP, Internet protocol.

5.4.2 Server-based System

To further enhance usability, a server-based implementation of the optimization was developed. A user-friendly interface to set up and monitor a closed-loop optimization process was programmed. In the following, the implementation is described first. Instructions are then provided on how to use the system from the user's perspective. The system was named *sofalab* (Self-Optimizing Flow Apparatus).

Implementation The core of the system was the server, which was connected to all devices *via* serial or network connections within the university network. The user could connect to the system through a user-friendly user interface (UI) in the web browser. Thus, the users didn't have to install any software and could be virtually anywhere in the world—provided they had access to the Internet. Since the system operated only within the university network, a connection through a virtual private network (VPN) was required. A conceptual overview of the system is shown in Figure 5.13.

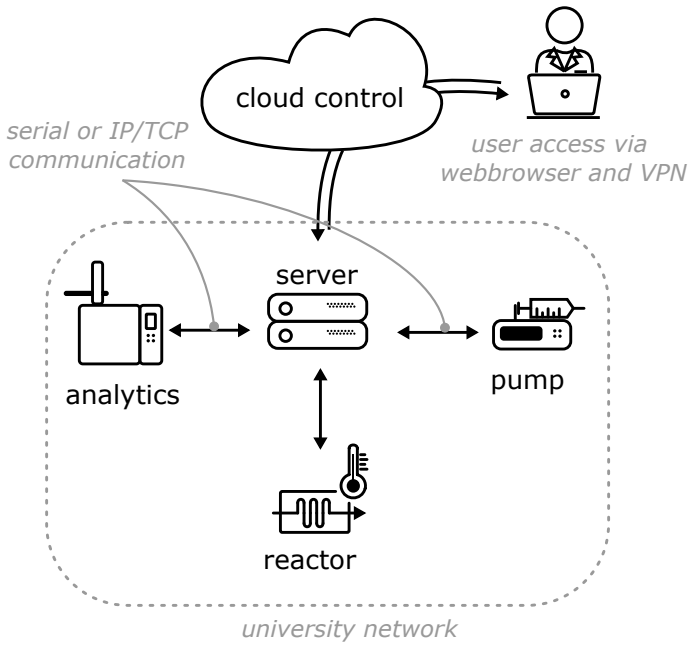

Figure 5.13: Schematic overview of the developed server-based closed-loop optimization platform *sofalab*. VPN, virtual private network; TCP, transmission control protocol; IP, Internet protocol.

A Python server based on the *flask* microframework was used in combination with a communication protocol based on *WebSocket* for the server-sided code. For the client-sided interface, a combination of typical programming with HTML, CSS, and JavaScript with the libraries *jQuery*, *Bootstrap 4*, and *SocketIO* was applied. These open-source libraries enabled rapid development without having to worry about many details and configurations.

The server was operated on a *Raspberry Pi* (either 4B or 3B) connected to the lab devices, such as pumps, reactor, and GC PC. To increase cybersecurity, the server was accessible only *via* the local network. Malicious users must therefore first gain access to the university network before having potential access to the server. In addition, the web application was protected by a simplistic user management system including password protection pro-

vided by the flask framework. Once the server was set up, the user could interact *via* the Internet browser with the server and initialize, set up, and monitor the optimization process. Figure 5.14 shows a simplified flowchart of the server-based software platform.

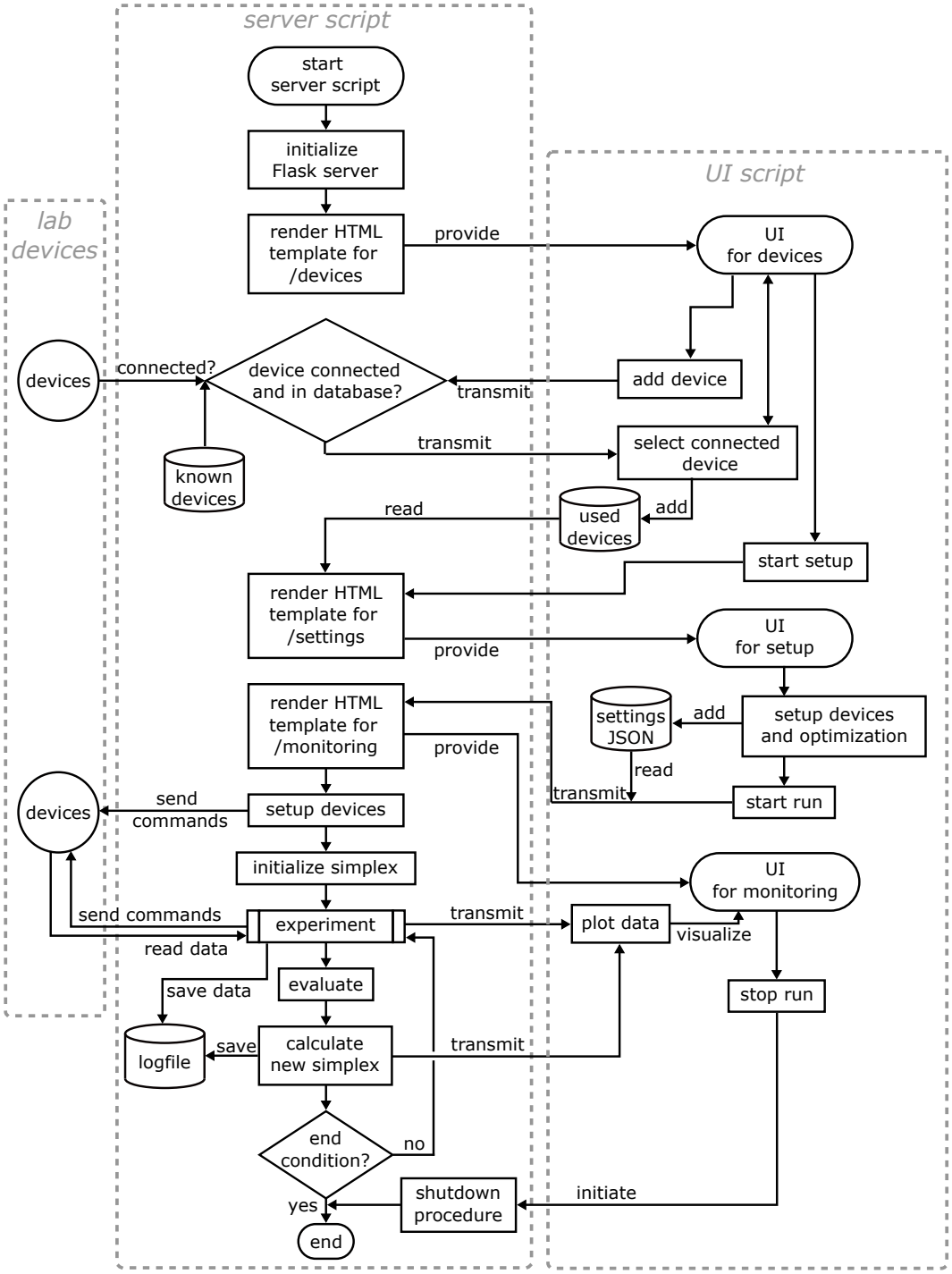

Figure 5.14: Simplified flowchart of the developed server-based closed-loop optimization platform *sofalab*. Flowchart is separated into three sections: Lab devices, server script, and UI script. UI, user interface; JSON, JavaScript Object Notation; HTML, Hypertext Markup Language.

The optimization platform can be divided into three sections: Lab devices, server script, and UI script. As the core of the program, the server script provided the user interface (UI) to the user, handled the communication to the user and devices, and processed the optimization algorithm and analytical data. Communication with the laboratory devices was based on their corresponding drivers and protocols, which allowed the server to interact with the "physical lab world". Through the web interface, the user could remotely interact with the server to se tup and monitor the optimization process.

The optimization experiments were started by powering up the connected devices and launching the server script. Moreover, the assisting scripts for the communication with the GC or NMR were started on the respective device-controlling computer. Initially, a `Flask` server was deployed, and the first page of the web user interface was delivered. The web interface was available only on the local network of the university under its IP address assigned to `port 5000`; therefore, a virtual private network (VPN) connection was required for outside connections. On this first page, the user could select the devices.

When a device was selected, a request was sent to the server to check if a device of this type (e.g. Fusion 4000 syringe pump) was connected. The server matched all connected devices with a database containing information about the available devices. This list was previously created manually and contains details about data which could be read from the connected device for unique identification (through device ID or manufacturer/product ID). Some similar devices, e.g. two syringe pumps Fusion 4000, could not be uniquely identified as the USB (Universal Serial Bus) identifiers were identical. To allow their identification as unique devices one of these pumps was connected *via* a serial to USB converter (Digitus DA-70167). The server then transmitted the information about the available devices to the user, who could then select and add them to the experiment.

In the next step, the user could issue the setup of the optimization run. The server received the command and rendered the subpage of the UI for the experiment and device settings. By reading the list of used devices in this run, it generated individual areas in the web interface: For example, if one syringe pump, one rector, and one NMR were connected, the interface elements were generated exclusively for these devices. This made the

user interface much more user-friendly and clearer compared to a page that always displays all possible devices. All settings made by the user were stored in a JSON (JavaScript Object Notation) on the client-side. The settings were submitted to the server when the user started the optimization run *via* the user interface.

The server then rendered a template for the monitoring subpage of the UI and initialized the devices by sending the respective commands to the physical devices. To start the optimization, the server initialized the simplex algorithm and calculated the initial experiments. This set of conditions for the first experiments was iteratively passed into the `experiment` subroutine. The server sent commands to the devices to start the reaction and read the collected analytical data. Transmission of the interpreted data and plotting on the user-side enabled real-time visualization of the process data. After the experiments were analyzed, the next iteration of the simplex algorithm was calculated. Moreover, the data was saved to a log file.

The server then examined whether the termination condition—a total number of ten optimization iterations—was fulfilled. If so, it ended the run. If not, the system jumped back into the `experiment` subroutine with the newly calculated conditions. In this loop, the user could trigger a manual stop *via* the user interface, which led to a shutdown sequence. This feature increased safety by allowing all devices to be shut down quickly and safely if the user needed to.

Application The above described closed-loop system was applied to the synthesis of octanal oxime (**14**) starting from octanal (**13**), and is presented in the following in the style of a user guide (Scheme 5.1).

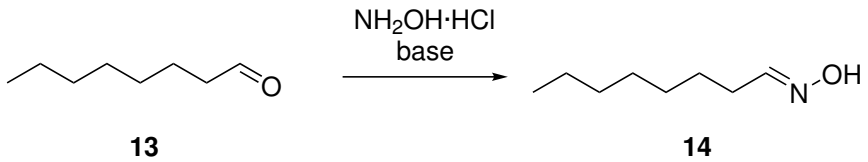

13 **14**

Scheme 5.1: Investigated condensation reaction of octanal (**13**) with hydroxylamine to form octanal oxime (**14**).

Four sections explain how to start the system, select devices, set parameters and devices, and monitor the system.

0. Start of the server & connect to the user interface

Firstly, the server (for example a Raspberry Pi 3B) must be powered on *via* the micro-USB connector and connected through an ethernet cable to the network. Wireless connection to the network is theoretically also possible, however, not as stable as a wired connection. Then, all devices are connected to the server using serial connections. In the case of network-devices—like the Spinsolve NMR—no connector needs to be plugged in. However, they also need to be powered on and connected to the network.

To start the optimization software, the script `server.py` must be started on the server. This can be done either locally *via* the connected touchscreen or remotely *via* Secure Shell (SSH). The script requires several packages and python version > 3.7.2 on the server-side. For detailed setup instructions and a list of dependencies, see Appendix B. On the client-side, any modern Web browser can be used, and nothing needs to be installed. The server script can be started with the following command in the bash (console):[iii]

```
nik@raspberrypi:/home/git/repos/weboptimisation/main $ python3 server.py
```

Moreover, the corresponding communication scripts on the respective analytical device must be started. In the case of the GC, the script `gcexe.py` must be started and the corresponding `...‣newfiles‣` folder should be cleared. Additionally, the GC program must be in the "batch measuring" window, as explained in Section 5.5.3 in more detail. As for the NMR, the script `nmr_client.py` must be started and the corresponding `...‣newfiles‣` folder should be cleared (Section 5.5.4). Furthermore, remote access to the Spinsolve software must be enabled.[iv]

iii Depending on the installation, `python3` or `python` must be typed for the correct selection of the Python version. The version can be checked with `python --version`.

iv In the case of the NMR, the IP address of the client and host may need to be adjusted in the source code of the `nmr_client.py`. On the server-side, the IP address can be assigned *via* the user interface once the function is fully implemented. On windows, the IP address can be determined by typing `ipconfig` into the Windows console, while the unix bash command is `ifconfig`.

1. Login & device selection

The user connects to the server *via* the web page by entering the IP address and port into the web browser: `127.xx.xxx.xx:5000`.[v] If the server is on the same machine (or by port forwarding), `loalhost:5000` can be used as well. Then, the login data will be requested (Figure 5.15).

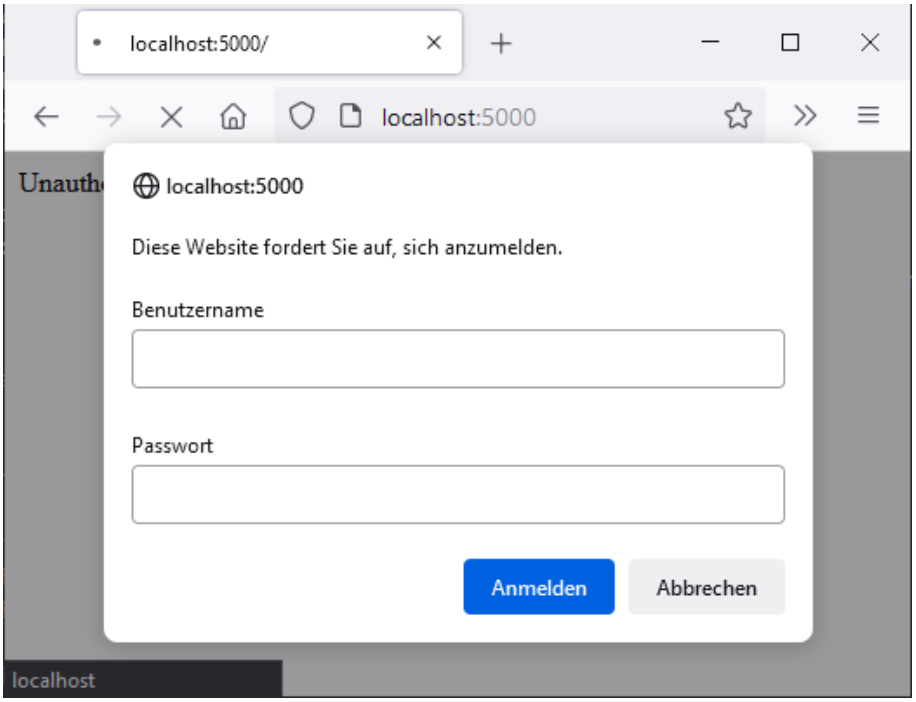

Figure 5.15: User login prompt (language selection of the login window is automatically done by the user's PC and corresponds to the system language).

The first step for the user is to select the desired devices. After clicking on Select devices, a list with all implemented devices drops down. The device can be selected and added by pressing the Add button (Figure 5.16).

v The IP address can be found out by entering `ifconfig` into the server bash.

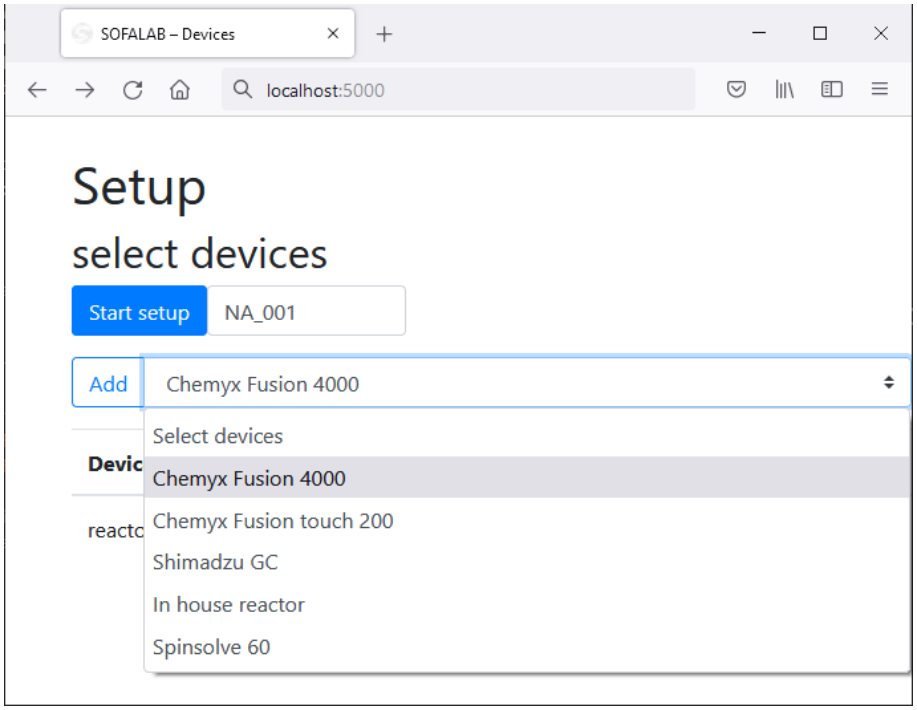

Figure 5.16: Window to select and add devices to the optimization experiment, select the experiment name, and start the setup.

A device can be selected from the list and added to the system. The server automatically checks which devices are connected and online.[vi] If there are multiple devices of the same type, a list is offered for selection (Figure 5.17). The devices can be added, and the required specifications of the connections are automatically assigned and saved. In the case that the device is not automatically recognized by the server, it can be added *via* the Cancel button, and the port can be assigned in the next step (2. Setup). Furthermore, the experiment name can be assigned.

vi The specification of the known devices can be found and modified in the `portlist.py` file.

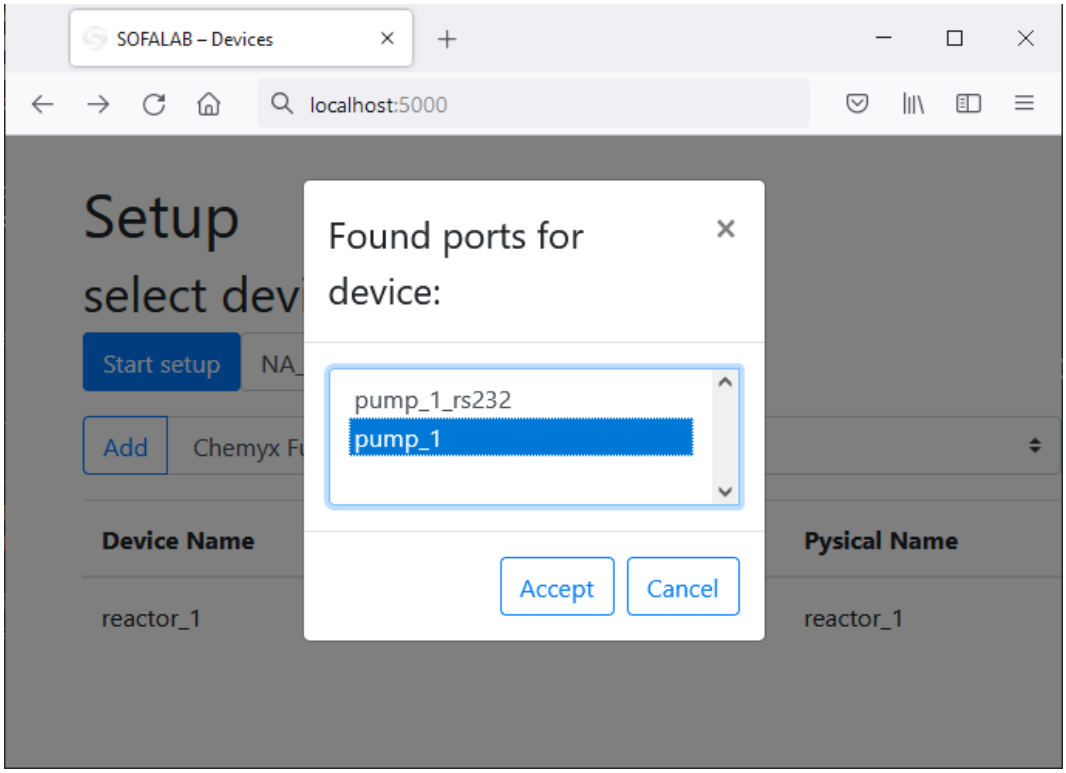

Figure 5.17: Prompt issued by the server that shows all connected devices matching the selected type (in this example, a syringe pump) and allows the user to select the desired device.

A click on Start setup signals the server to build and deliver the setup page.

2. Setup of the Parameters

For setting up the closed-loop optimization, the user is automatically directed to a settings page (Figure 5.18). The steps for the settings can be done in any order. The evaluation function must be defined. Based on this function, the system calculates the response value that is fed into the Nelder-Mead algorithm. For example, if the goal is to optimize the conversion, the function `yield` can be typed in. Clicking on the question mark opens a window with help on how to set up the evaluation function and which parameters are allowed. Further help is given in many places when the mouse cursor is moved over the input fields. All selected settings and devices can be added to the system by pressing the Add button.

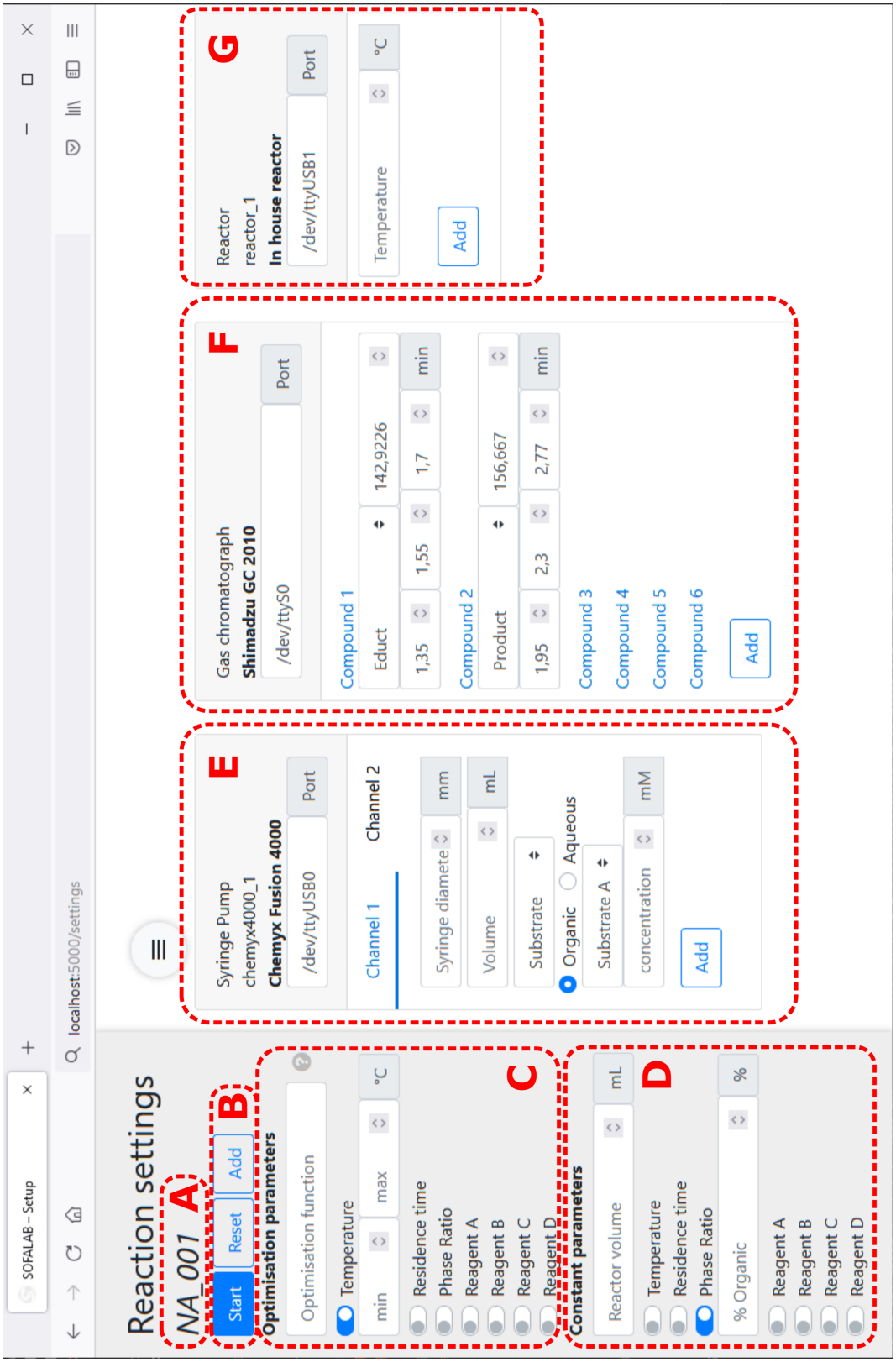

Figure 5.18: Settings subpage for setting up parameters and devices for an optimization experiment with *sofalab*. (A) experiment name, (B) interaction buttons, (C) evaluation function and variable parameters, (D) constant parameters, (E) setup window for a Chemyx fusion 4000 dual-channel syringe pump, (F) setup window for the gas chromatograph, (G) setup window for the reactor module.

Next, the optimization parameters are selected. The reaction parameters can be selected either as `optimization parameters`, allowing the system to adjust them in the defined range or as `constant parameters`. Constant values are not changed over the course of the optimization. Each variable parameter needs a maximum and a minimum value, while the constant parameters only require one value.

Moreover, the device settings can be chosen in the right part of the web interface. Each device is represented by a separate window ("card"). A number of devices are already included and can be set up. Please note, that the Spinsolve NMR must be set up manually (Section 5.5.4).

For example, a dual-channel syringe pump (Chemxy Fusion 4000) was integrated. The two channels can be selected with the corresponding slider and set up separately. The syringe diameter must be specified, as it is required for the correct adjustment of the syringe. If it was not specified, the syringe will use the last setting stored in the internal memory. Hovering the cursor over the input field shows a list of commonly used syringes and corresponding diameters. Moreover, the volume can be given. This is not mandatory, however, improves safety and functionality: With the volume indicated, the user can be notified when the syringe volume is depleted and the system will not start the next experiment automatically (Figure 5.19). This function calculates prior to each run if sufficient volume is available. If not, the user is notified *via* the user interface and can refill the reservoir. When the reservoir is refilled, the Refill button can be clicked, and the system will resume the optimization.

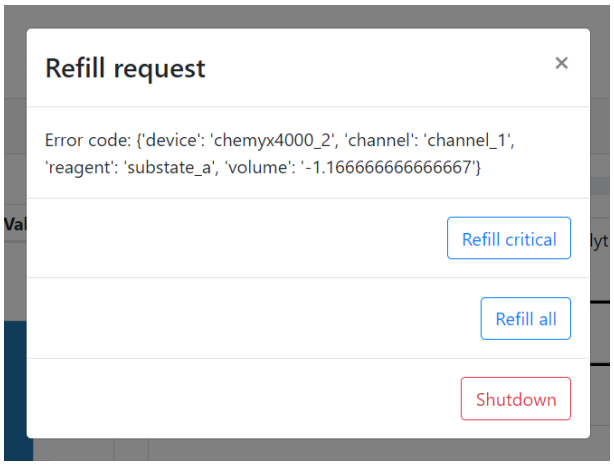

Figure 5.19: Solvent depletion notification in the user interface.

Furthermore, the role of the feed (substrate, dilution, or downstream) can be selected. Up to this point, the `downstream` option had not yet been implemented. It was planned as an option for a constant flow, independent of the concentration and residence time settings. The `substrate` option allows the selection of up to four substrates (A–D) for the optimization of complex reactions such as multi-component reactions. The `dilution` feed is used to compensate for the overall flow rate when lower concentrations are used (Subsection 5.3.2). If a biphasic system was selected (= when a phase ratio is specified), the phase (organic or aqueous) can also be selected.

In addition to the syringe pumps, the gas chromatograph must be set up. Up to six individual compounds can be tracked by the system. Each compound can be added separately. Specifications on expected retention times and calibration data can be added. Moreover, the compound's role in the reaction (educt, product, impurity, and product enantiomer) must be specified for the calculation of conversion and selectivity. To enable peak identification the retention time is defined with the maximum and minimum start of the peak, as well as the maximum end of the peak.

Similar settings can also be made for the NMR (Spinsolve 60): The expected range for the signal (in ppm) identification and integration can be defined for product and starting material. Additionally, the number of protons (or fluorines) at the observed position must be added for correct calculation. These settings must be done in the python source code (Section 5.5.4).

As for the reactor, no set up is required.

After all settings have been made and all devices have been physically set up, the Start button can be pressed. A loading screen appears until all devices are set up. For example, the syringe diameter is sent to the syringe pump and the algorithm is initialized.

3. Monitoring of the optimization run

After the setup screen disappears, the user is directed to the `/monitoring` subpage (Figure 5.20). On this page, the user can track the progress of the optimization, trigger an emergency stop, and monitor the reactor temperature/GC data.

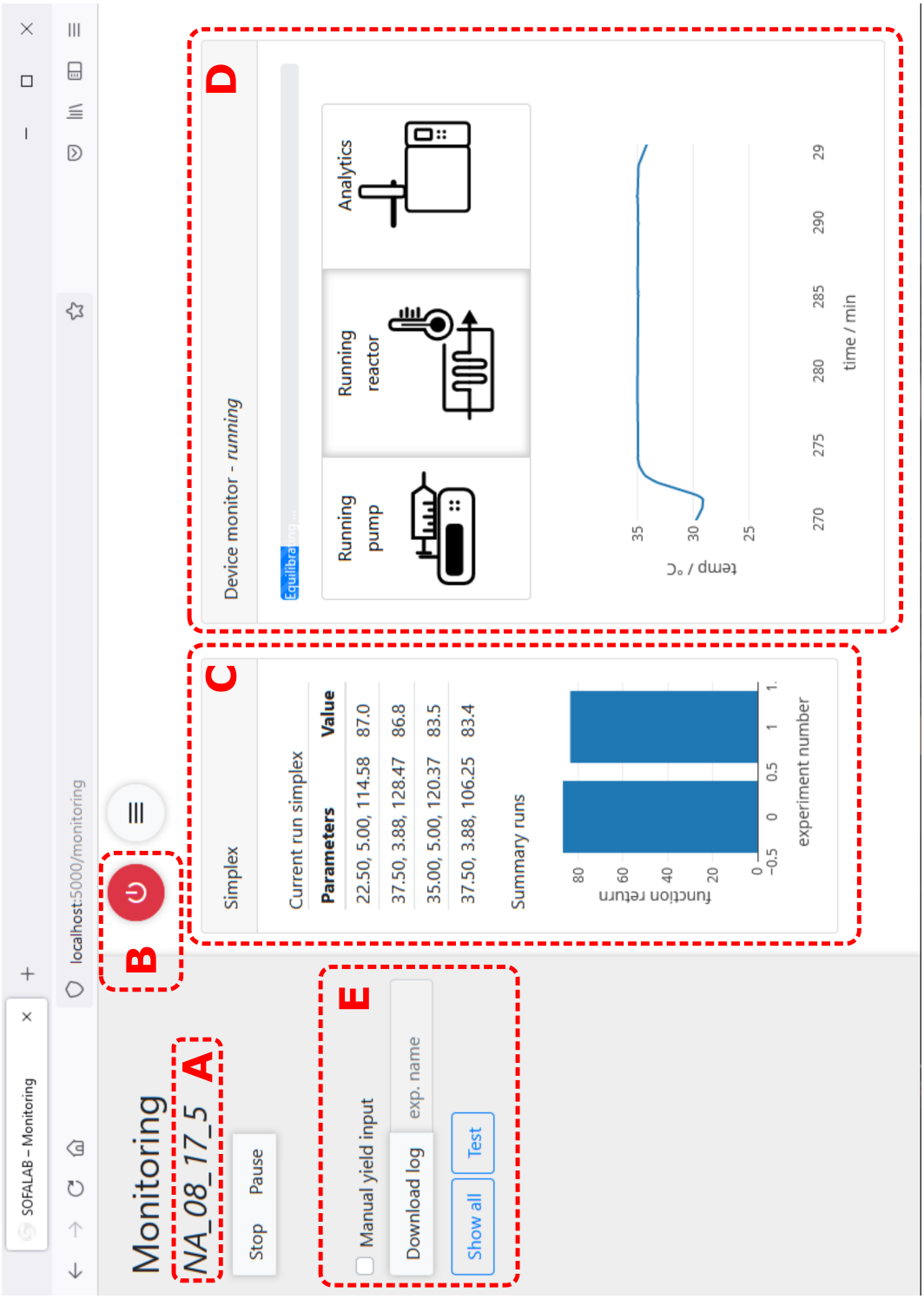

Figure 5.20: Monitoring page of *sofalab*. A: Reaction name, B: stop button to immediately shutdown the devices, C: current simplex values as parameters and function values, and a bar plot of the results, D: status bar with colored code and text-based information, and real-time temperature plot of the reactor.

The emergency stop button sends a command to the server that initiates a shutdown sequence during operation. This command cannot always be interpreted immediately; however, it is periodically checked whether a stop has been requested. The shutdown sequence sends stop commands to all pumps and reactors.

Not yet fully implemented are the stop and pause buttons. Once programmed, they can be used to stop or pause an optimization run after the current experiment.

In the `Simplex` window, current experiments of the optimization and a bar graph with the results of all runs are displayed. The current simplex experiments are the ones used by the algorithm for this step. During the initial four experiments, no data is shown.

The current operating status of the system is indicated by a colored bar in the `Device monitor` window. Different colors represent the operating status: Blue represents setup and equilibration, green a completed run, and red an error or shutdown. Additionally, text-based information is displayed in the bar as well. The width of the bar corresponds to the progress of the process.

The reactor temperature can be displayed by pressing the reactor symbol. A window opens with an interactive line graph of the temperature over a period of the last 30 min.[vii] The plot was created with Plotly[137], which offers some interactive functions like zooming or axis change (Figure 5.21).

vii Please note that the graph will not be updated while the system is waiting for analysis data. This can lead to unexpected lines when the next data point is plotted. Moreover, when reconnecting to the server, only the future data will be shown. No past data will be sent to the client.

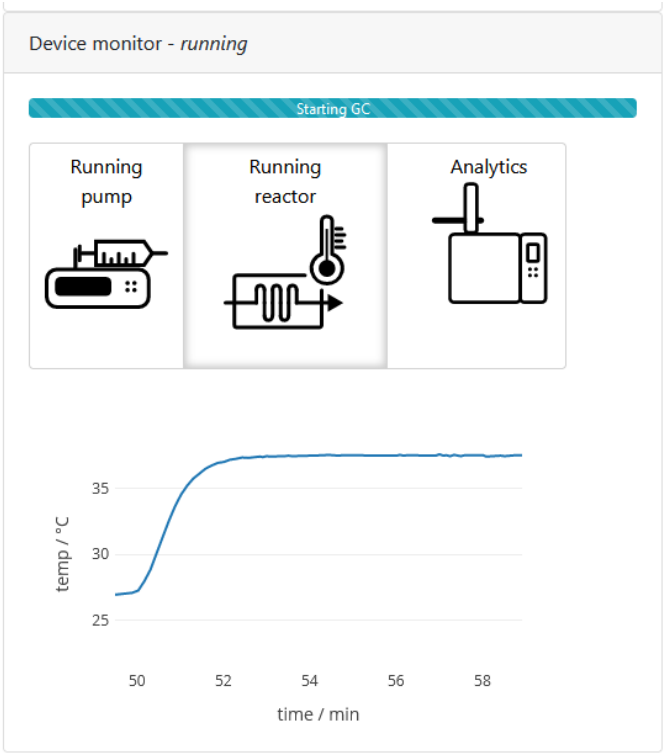

Figure 5.21: Real-time reaction temperature diagram and status bar in *sofalab*.

In addition, the GC chromatograms can be viewed by clicking on the gas chromatograph icon (Figure 5.22). The chromatograms are plotted in a stacked 3D graph. Since this plot was also created with Plotly, functions like zooming and rotating are available.

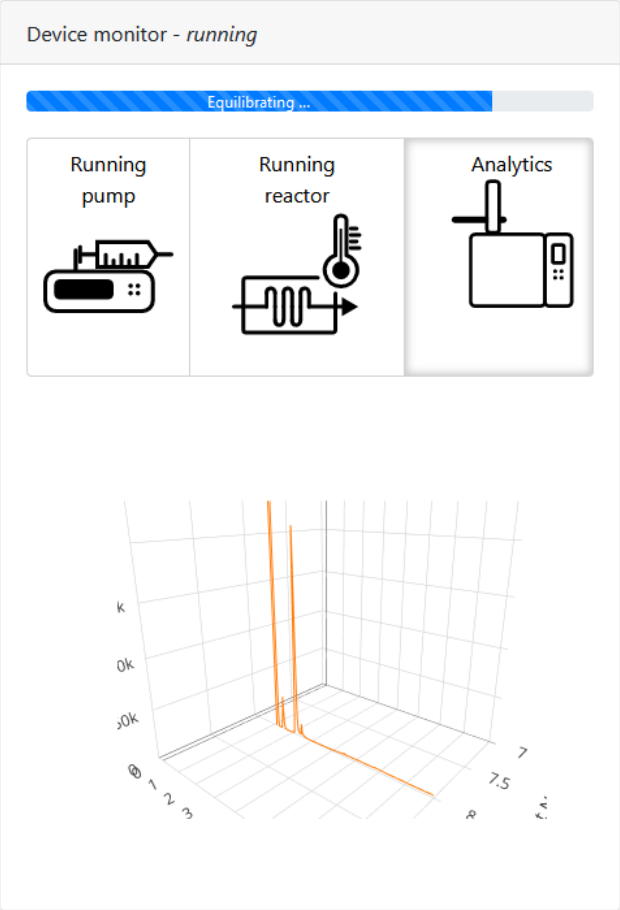

Figure 5.22: Stacked gas chromatograms and status bar in *sofalab*.

5.5 Hardware Modules

For the automated experimentation, some equipment was modified in order to meet the requirements. Other devices were designed and built from scratch to perfectly suit the intended purpose. The steps taken to modify the laboratory devices for use by the closed-loop optimization platform are presented below.

5.5.1 Reactor

Thermal control of a chemical process is one of the crucial aspects of reaction optimization. Many commercial options are available, but they tend to be expensive and often poorly customizable. One aim of this project

was therefore the development of a modular reactor concept for flow and batch reactions. The prototype was realized with the help of the in-house workshops. Three different versions were developed: First a prototype, then a four-unit, and a single-unit reactor. Reactors for both Schlenk tubes for batch experimentation as well as tubular flow reactors were designed. While the multi-unit reactor was intended for batch screening and multi-step flow reactions, the single-unit reactor was designed as a modular reactor system for closed-loop optimization and initial process development.

5.5.1.1 Design & Prototyping

Prototype For an initial prototype, the electronics were mounted on an aluminum plate to ease access. A reactor mounting consisting of four parts was designed to enclose Schlenk tubes (Figure 5.23): A base unit (A) for reaction temperature control with a removable aluminum holder for glass tubes (B), a reflux unit operated with tap water (C), and thermal insulation from the base unit by a PTFE insulating ring (D). The purpose of this prototype was to get a first impression whether the electronics were suitable and to have a platform to start the programming of a user interface and API (application programming interface).

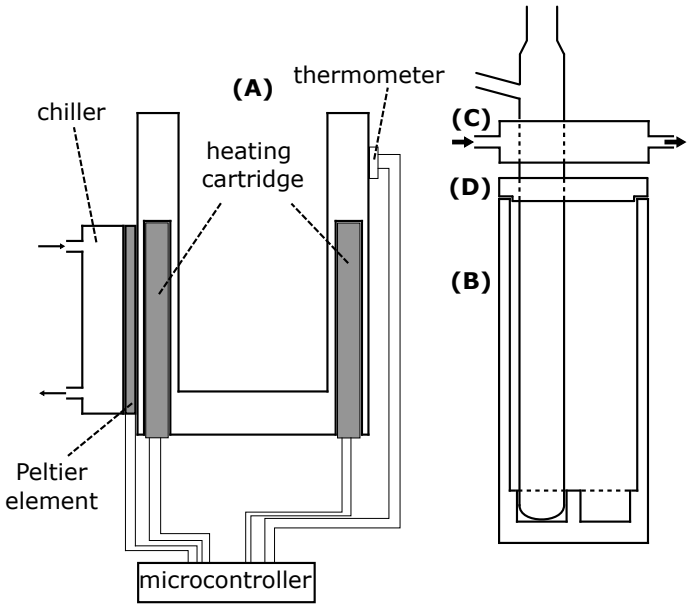

Figure 5.23: Cross-sectional view on the design for the prototype reactor system: (A) Base unit for temperature control, (B) aluminum holder for glass tubes, (C) reflux module, (D) PTFE insulating ring.

The prototype (Figure 5.24) was manufactured in-house by the electronics and mechanical workshops. The envisioned stirring solution has not yet been implemented to simplify the development.

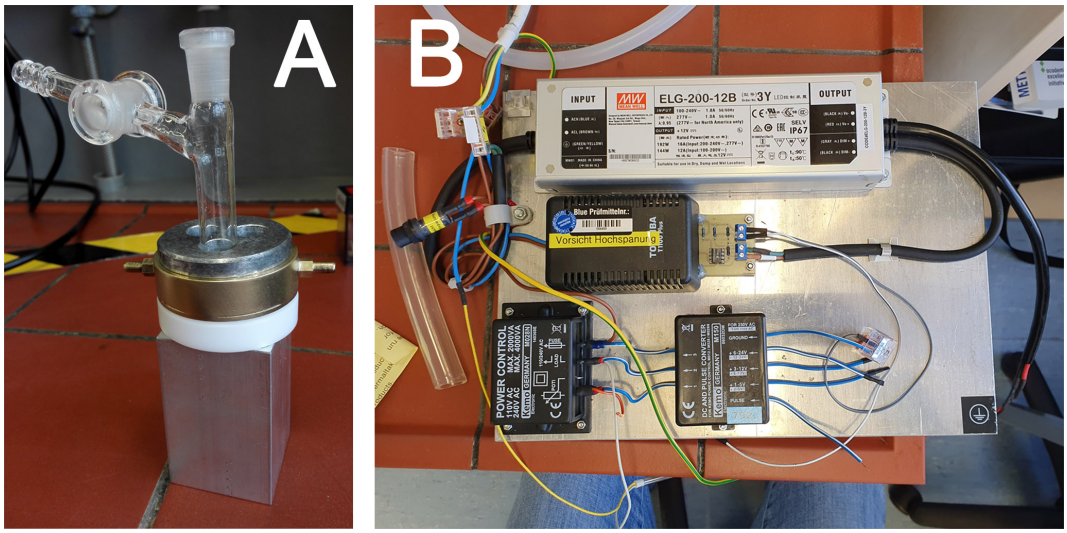

Figure 5.24: A: Prototype of the first generation reactor module. From bottom to top: Aluminum casing for steel mount (from commercial ChemiStation by EYELA), PTFE insulating ring, reflux cooling ring, stainless steel mount for glass tubes, and Schlenk-glass tube. B: Easily accessible electronic components for initial testing of the reactor system on an aluminum plate.

Four-unit Reactor After gaining some experience with the prototype, the next generation of the reactor system was developed. This system was planned as a multi-unit reactor. The design of the reactor consists of four identical subunits with a separate heater, cooler, and microcontroller. Thus, the system is scalable (more than four units are possible), and the individual units can be controlled *via* one single control computer.

After planning and CAD (computer-aided design), the system was built in the in-house mechanical workshop. The electronics were planned in cooperation with the electronics workshop, which also connected all the electronic parts. In Figure 5.25, the CAD of the system is shown.

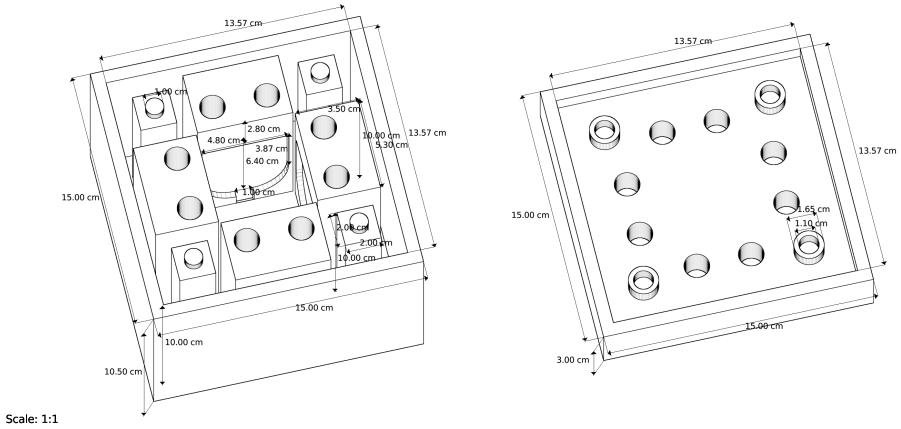

Figure 5.25: Computer-aided design of the four-unit reactor for batch screening and multi-step flow reactions by *Diedrich*.

A prototype was manufactured on the basis of the CAD (Figure 5.26). The system was designed as four individual units embedded in a single case containing the water-cooling solution to cool the Peltier elements and feed the reflux unit. The case was built from stainless steel plates, while the Schlenk tube holders were made from copper to improve heat transfer. Boreholes for temperature sensors and heating cartridges as well as a cavity for the Peltier elements were incorporated into each block. The copper blocks were thermally insulated from the enclosure by PTFE pads. However, it turned out that the copper blocks (each approximately 1 kg) had too high heat capacity for the previously selected electronics resulting in an insufficiently slow heating rate. Thus, a test block from aluminum was built as well, which worked flawlessly in combination with the electronics.

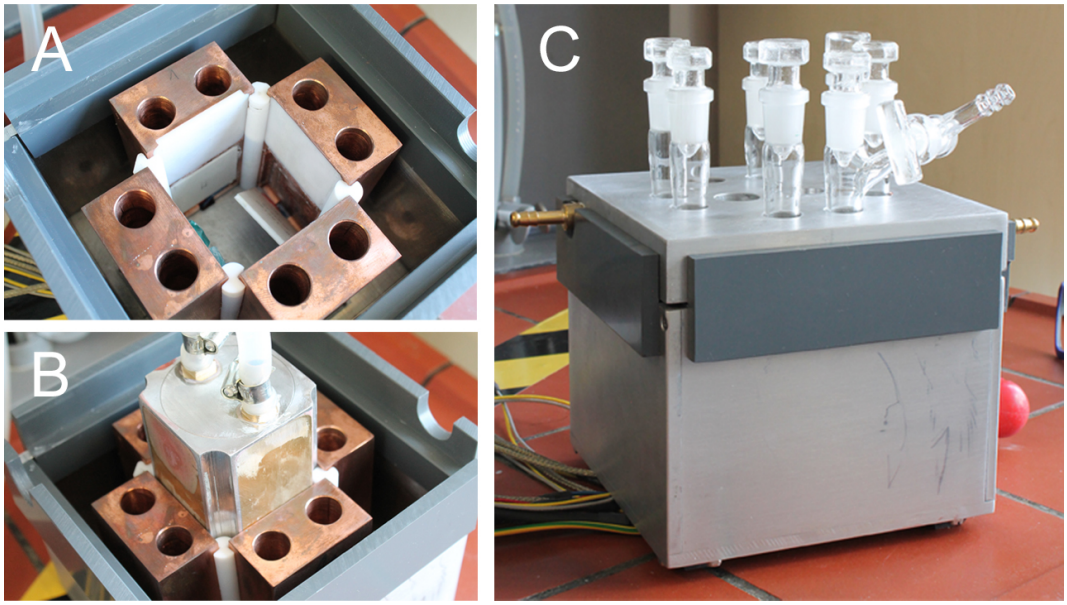

Figure 5.26: Four-unit reactor for batch screening, manufactured in the mechanical workshop. A: Copper holders for glass tubes in a steel case, B: chiller unit for Peltier cooling elements, C: fully assembled batch screening reactor equipped with reflux unit and glass tubes.

Modular Single-unit Reactor Since for most flow chemistry experiments only temperature control of one reactor element is required, a modular and more compact single-unit reactor was developed (Figure 5.27). The electronics and principle remained unchanged compared to the four-unit system. This reactor was designed from the ground up to be easy to operate, modular, and flexible. The system consisted of two elements: A case with temperature control electronics and a reactor unit with Peltier element, temperature sensor, and heating cartridge. The electronics for temperature control were built into a plastic case. Additionally, a PC CPU water cooler loop, which was used to cool the Peltier element, was installed in the case. To connect the reactor unit and control electronics, a 7-pin connector with a 1 m cable was used.[viii] Two pins were used respectively for the heating cartridge, the temperature sensor (Pt1000), and the Peltier element, while the remaining pin served as the protective earth (PE) for the reactor block. To ensure maximum flexibility, quick fittings were used to connect the CPU water block attached to the Peltier element to the cooling circuit in the electronics case. The cooling circuit consisted of a pump, tubing, heat exchanger, and a fan. Another fan was integrated into the back of the case

viii The design was later improved by Diedrich as a single connector has shown to be unreliable for the shared connection of sensor data and power for the heating cartridge. Instead, two separate connectors were used.

to ensure high air flow. User-friendly control of the system was provided by a touch screen mounted to the housing.

By using quick connectors for cooling water and electronics, a highly modular system was realized. Another reactor module, such as the temperature control of a packed bed reactor, can be designed with similar electronics and used interchangeably. However, since the PID controller parameters have been fine-tuned for the tubular reactor block, they may need to be adjusted if the thermal mass or thermal conductivity of the system changes significantly.

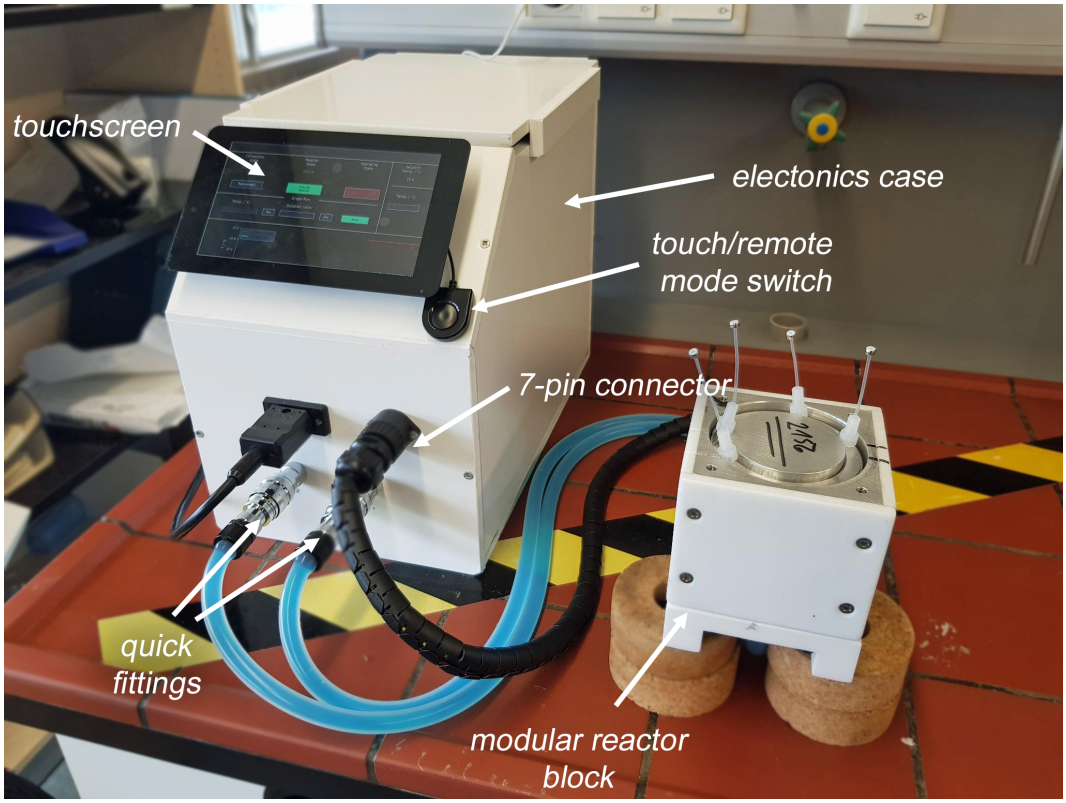

Figure 5.27: Single-unit modular reactor for batch and flow experimentation. Simple control *via* two modes (touchscreen or remote) selectable through a button. The touchscreen is driven by a Raspberry Pi and allows for easy use. Quick fittings and a 7-pin plug connect electronics in the case with the modular reactor block equipped with two tubular PFE reactors. The reactor block made of aluminum is encased in PTFE for thermal insulation.

5.5.1.2 Electronics & Programming

Prototype The electronics were mounted on a (grounded) aluminum plate so that all electronics were accessible for further testing and modifications. A combination of Peltier element (approx. 100 W) for cooling and heat-

ing cartridge (approx. 100 W) for heating provided temperature regulation. Both elements had a separate control circuit driven by an Arduino microcontroller that adjusted the output of the controllers with a PID controller.

Throughout the prototyping, different temperature sensors were used: A thermocouple and two different Pt1000 sensors, each with a matching sensor board from Adafruit. The temperature was fed into the microcontroller.

The heating cartridge was controlled by a power control unit (Kemo M240) in combination with a DC and pulse converter (Kemo M150), both of which were commercially available from Kemo. The power control unit was wired to the power supply and to the DC and pulse converter, which was also connected to the Arduino. A DC signal (0–5 V) for regulating the power output was provided by the microcontroller. The converter transformed this signal into a control signal for the potentiometric control input of the power controller, which was connected to the heating cartridge *via* the power output.

For the Peltier element, a commercially available LED driver by Mean Well Enterprises was used. Initially, an approx. 200 W driver was used (ELG-200-12B-3Y), which was eventually switched for a lower-powered device (ELG-150-12B-3Y; 6–12 V DC, constant current of 10 A). As this device required an input of 10 V analog DC, the analog 5 V output of the Arduino was doubled by a custom-build voltage doubler.

The Arduino code and parts of the Python control script were written by Diedrich during his occupation as lab assistant. A public PID controller library[138] was used to control the temperature. A simple script-based Python module was written for the prototype to test the functionality of the system. To enable communication between the microcontroller and the Python module, which was run on a Raspberry Pi, an API (Application Programming Interface) was implemented. Through serial communication, the microcontroller could be set up with different target temperatures and times, while the current status (temperature and operating status) could be read by the Python module. All temperature control operations were handled on the microcontroller level.

Four-unit Reactor The electronics, with the exception of the Raspberry Pi, were mirrored four times to create four separate temperature control areas. Additionally to the previously described electronics, an inrush current limiter was connected to the power supply to ensure a stable system. In particular, the LED drivers required high currents at startup, exceeding a standard circuit breaker's limit of 16 A.

A graphical user interface (GUI) based on the Tkinter GUI toolkit for Python was programmed for easy and user-friendly control of the system (Figure 5.28). The interface was programmed to provide complete control over all four reactor units without the need for programming skills.

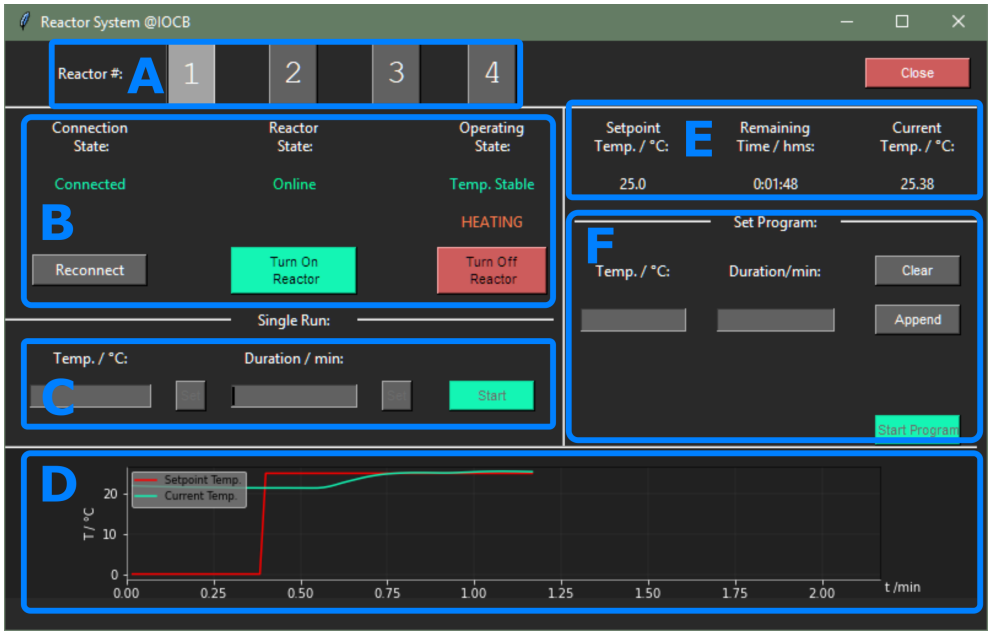

Figure 5.28: Graphical user interface (GUI) for the four-unit reactor system programmed with the Tkinter toolkit. Individual functions of the GUI are highlighted in blue. A: Reactor unit selector, B: basic controls and status indicators, C: single run settings, D: real-time temperature graph, E: current settings and system temperature, F: settings for temperature profile programming.

Two different operating modes were available: Single run and temperature profile program. While the single run allows operation for a specific time at a specific temperature, the temperature program mode provides multiple temperatures and time periods to create a complex temperature profile. For example, a reaction could be automatically thermally quenched after a certain reaction time. The real-time temperature plot was realized using the *matplotlib* library.[139]

After some testing at different temperatures and scenarios, it was found that the system operated unreliable at temperatures close to room temperature. Since the system had no information about the environment, the decision to heat or cool depended on a fixed value. As the room temperature in non-air-conditioned laboratories is far from constant, this caused the system to misbehave. To overcome this issue, a room temperature sensor was integrated into the system. Depending on the current room temperature, the system can decide whether heating or cooling is needed to reach the target.

Modular Single-unit Reactor A special focus of this system was versatility and user-friendliness. Another aspect was the interchangeability of the reactor module. Thanks to the use of a 7-pin connector and quick connectors for the water-cooling circuit, even technical amateurs can easily replace the module. Moreover, a switch for switching from touchscreen to remote mode was integrated. For this function, a USB peripheral switch (Anten US224-AT) was used, which allowed switching the USB port by clicking on an integrated button. The remote-control mode allowed the reactor system to be controlled *via* serial communication from another source through a USB cable, such as a closed-loop optimization system. Clicking the button, which was mounted on the outside of the case, changed the operating mode without the need to rewire the system.

As a protective measure, an inrush current limiter (Mean Well ICL-16L) was integrated into this system as well. The above-mentioned room temperature sensor (here Pt1000) was installed directly in the electronics housing. A PC water-cooling kit (Thermaltake) was used for the water-cooling of the Peltier element. The quick fittings were purchased from Alphacool and connected by silicone tubing to the CPU block, which was mounted on the Peltier element. For the power supply of the coolant pump and the fan, a power supply unit (12 V) was integrated into the electronics housing. Another power supply unit was integrated for the Raspberry Pi (5 V). A list of the components can be found in Appendix B.

System Stability Modifications After the development of the three reactor systems, modifications to the software were made to improve the useability. During remote operation by the closed-loop optimization system, it was

found that some temperature profiles were inefficiently controlled. For example, if a temperature 50 °C was selected first, while the room temperature was 30 °C. Immediately afterwards, a temperature of 40 °C was selected, which was higher compared to the room temperature; thus, the system tried to reach the temperature by heating. However, since the temperature of the system was already higher, it could not reach the temperature by heating, but only by heat dissipation to the surrounding air. This led to a very long equilibration time. To account for such scenarios, an optimization of the code was made. The microcontroller was programmed to periodically check whether the current temperature is above or below the target value and change the operating mode (heating or cooling) accordingly.

5.5.1.3 Outlook & Potential

In the future, this work can be used as a platform for the development of a multi-reactor screening system as well as a highly customizable single-unit reactor. Further improvements to the cooling solution could extend the system's temperature range—especially at low temperatures. This work provides a framework for modular reactors, such as packed bed reactors[97], using the same equipment. This allows chemists to design and integrate custom reactor solutions with only minimal knowledge of electrical engineering and programming. Moreover, a solution for the mixing of reaction solutions can be integrated using small motors equipped with magnets to allow individual magnetic stirring speeds in the multi-unit screening reactor. The material costs of the single-unit reactor are very low (below 1000 €) compared to commercial solutions (well over 10,000 €), while using mainly readily available "of-the-shelf" components.

5.5.2 Upstream and Pumps

During this work, many different pumps were used based on three different concepts. Discontinuous syringe pumps as well as continuous peristaltic and high-pressure HPLC pumps have been used for various purposes. Both the peristaltic and syringe pumps were based on serial communication. The respective serial commands and communication specifications can be found in the corresponding manuals. Python modules were written for different

pumps (Chemyx Fusion 4000 and 200, Ismatec Reglo ICC) to allow full remote access.

As syringe pumps are operating discontinuously from a reservoir, they tend to struggle to provide fresh feeding solution over a long time. The operation must be paused, and the syringe refilled or replaced. Furthermore, the tempering of the feed solution is difficult. This can be problematic, especially with unstable starting materials, such as sodium hypochlorite or whole-cell catalysts. Despite these major drawbacks, syringe pumps were essential for this work because of their unmatched precision at low flow rates.

To overcome at least the issue of temperature control of the feed solution, a syringe cooler was developed. The first version was based on ice-water-cooling. The syringe was placed in a hollow metal cooling jacked, which was supplied with coolant by a peristaltic pump. Until the water eventually equilibrated to room temperature, this solution worked fine. Later the syringe chiller was fed by a recirculating chiller.

5.5.3 Gas Chromatography

Often, analytical devices are operated with proprietary software, the hardware connections are inaccessible, and APIs are not provided. Therefore, their automation is usually difficult or impossible without the help of manufacturers. To avoid these issues, a relatively universal approach has been developed for remotely accessing analytical equipment and transmitting analytical data to an external device. This work focused on the application of a gas chromatograph (GC) for automated process analysis. Non-destructive hardware modifications and automation software were applied to make the chromatograph fit for a digitalized and interconnected laboratory.

5.5.3.1 Hardware Modifications

In this work, a Shimadzu GC 2010 system equipped with an AOC-20i autosampler was used. This system injects the sample using a syringe from a glass vial. The vial is placed on a sample holder that is moved in the x-axis. From the syringe, the sample is directly injected into the GC. To enable

continuous analysis with a GC, an automated method is required to bring the sample from the reaction mixture into the GC system.

In theory, there are different options to inject a sample. One option is to modify the injector. Instead of drawing the solution from a sample vial, a sample loop could be integrated to load the injection syringe. However, this option requires many modifications of the hardware and renders the machine unusable for standard operation. Therefore, in this work, a different method was chosen that requires as few changes as possible. A flow-through vial was designed to allow a continuous flow of the reaction solution through the sample vial. The reaction mixture was pumped *via* PFA tubing into the vial using the reaction pumps. In Figure 5.29, the flow-through vial assembly is shown.

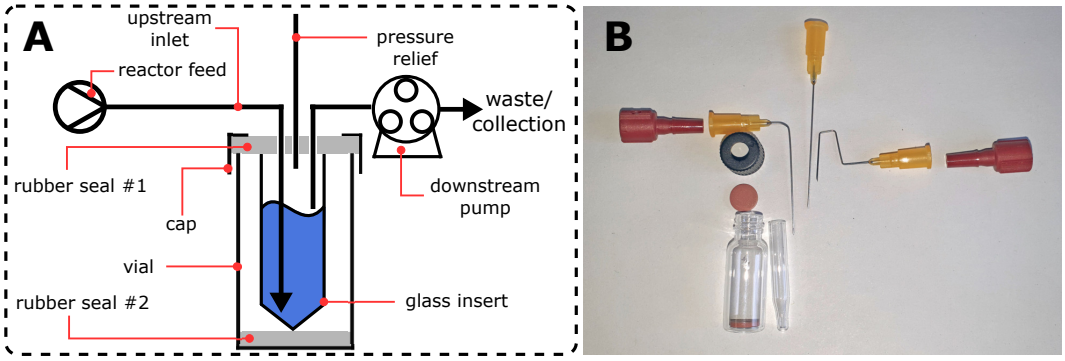

Figure 5.29: Flow-through vial for continuous gas chromatography. A: Scheme of the flow vial, B: individual parts used to build the flow-through vial.

A standard GC vial with a cap and rubber seal (#1) was used. Into this vial, a glass vial insert (200 μL) was placed on top of the spacer rubber seal (#2), which enables a rigid and tightly fixed construction. Three needles were inserted through the rubber seal. The inlet needle was placed at the bottom of the glass insert, the outlet needle at approximately three-quarters height, and the pressure relief above the outlet needle. A peristaltic pump was connected *via* PFA tubing to the outlet needle to keep the sample volume constant at the outlet height (Figure 5.29). The flow rate of the peristaltic pump was set to a higher flow rate as the overall reaction flow rate to ensure a constant sample level and to avoid leaking. This can create a negative pressure in the vial, which can have a negative effect on the reaction steam. By using the additional pressure relief needle, this effect can be avoided.

After some initial testing, the design of the flow vial solution was revised. Since the steel cannulas were not plane with the cap of the vial, in some cases, the autosampler lowered at an angle on the vial. This led to a bend of the needle of the sampler. To avoid this undesirable effect, a plastic vial was used instead (Figure 5.30). The feeds were introduced through a bore at the side of the vial.

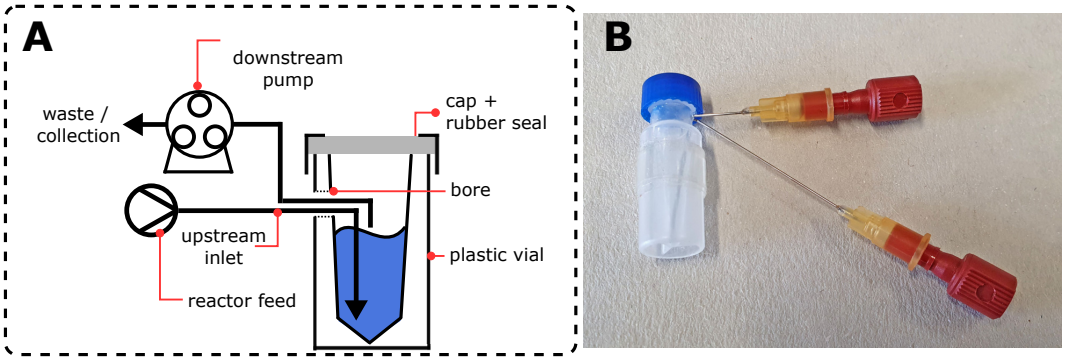

Figure 5.30: Second version of a flow-through vial for continuous gas chromatography. A: Scheme of the flow vial, B: assambled flow-through vial.

The vial was placed into the autosampler holder (Figure 5.31, step 1) and fixed with tape (Figure 5.31, step 2). A loop of the connecting PFA tubing with some additional tubing was fixed to the GC housing, since the autosampler moves and requires more tubing depending on the position (Figure 5.31, step 3). When preparing the machine, it is important to ensure that the tubing does not get caught by any moving part and that the vial setup including needles is at an appropriate height for the autosampler. The vial construction had to be at the same height as a standard vial to make sure that the autosampler could operate correctly.

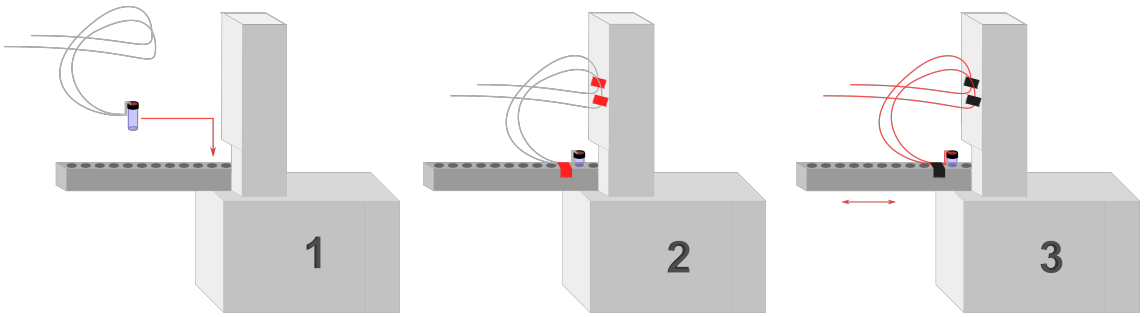

Figure 5.31: Steps to set up the GC. (1) Place the vial into one of the first autosampler holders, (2) fix tubing with tape, (3) check if sufficient tubing is available for the autosampler to safely move.

5.5.3.2 Instrument control

The next step was to remotely start the GC. Python modules for both local implementation (Subsection 5.4.1; start_gc.py, analyze.py) and server-based system (Subsection 5.4.2; gcexe.py) were programmed. After several initial attempts to control the chromatograph *via* the generic communication ports, another method was chosen that is potentially more widely applicable and much simpler. The proprietary Shimadzu software was controlled by a Python module (pywinauto), which can simulate keyboard input and mouse movement. This way, no modifications of the original software were required, which minimized development time, increased robustness, and reduced safety concerns (e.g. damages to injector or autosampler due to incorrect commands or timing). The general principle of the script is to start a batch measurement *via* the proprietary GC user interface using shortcuts. In this case: F5 for "start batch measurement".

Initially, a method for the measurement was set up on the GC instrument manually using the Shimadzu software. Virtually any GC analysis method can be selected. However, the shorter the measurement, the better for process control so that the delay from the analytics in the optimization loop can be minimized. The batch file must be saved prior to the automated control. Moreover, the target directory of result files is changed to the subdirectory `projectfolder‣newfiles‣` (Figure 5.32). This folder can be any directory, but it must be referenced in the automation code. For example, a folder on the Desktop can be used. Saving the files as .txt (csv; comma separated values) is mandatory, as the proprietary Shimadzu file format cannot be understood by the written Python script. Other file formats will be ignored by the analysis script. A tree structure for the project folder is shown in Figure 5.32.

Figure 5.32: Folder (tree) structure of the automated gas chromatography (GC) system on the GC control computer.

A flowchart of the script (start_gc.py) to automatically operate the chromatograph is presented in Figure 5.33. The measurement was started by the `start gc` subroutine, which will be explained in more detail in this paragraph. After that, the script monitored the `..‣newfiles‣` folder, and imported the raw GC data file (as text file) into the script. Finally, the data was analyzed using the `analyze file` subroutine, which is explained in more detail in the next subsection. In the case of the remote implementation (Subsection 5.4.2), the data was analyzed server-sided.

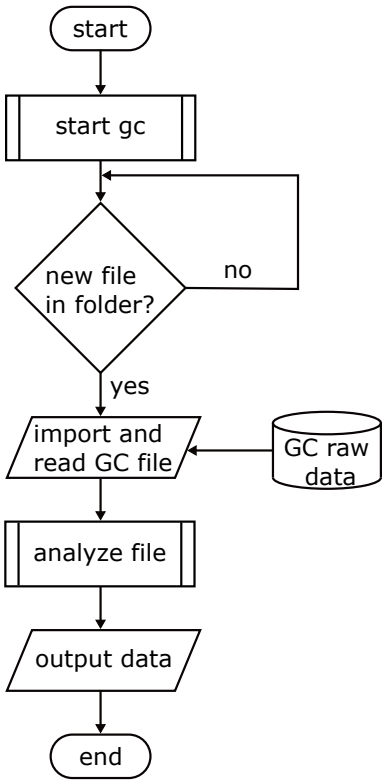

Figure 5.33: Flowchart of the script for automatic start and analysis of a gas chromatograph, with `start gc` and `analyze file` subroutines.

In the following, the code to start the GC measurement is shown. First, the module `pywinauto` is loaded. Then, the class `GC_control` is created. The function `start_batch` contains the code to execute the command to start the GC batch analysis. In lines 5–7 of the code, the Shimadzu GC program is defined, and the program window is selected in lines 8–11. Finally, the shortcut to start the batch measurement is executed in line 12.

```
1  from pywinauto import application
2
3  class GC_control:
4    def start_batch(self):
5      self.app.connect(
6        path = r"c:\GCSolution\Program\GCAnal.exe"
7        )
8      self.mainwin = self.app[
9        u"GC Real Time Analysis 1 (Instrument1 - Admin) -
10       [Batch Table - batchfilename.gcb]"
11       ]
12     self.mainwin.type_keys("{F5}")
```

The batch measurement was first checked manually to avoid unforeseen events. Pressing the shortcut key to start the batch measurement triggered the analysis without further need for confirmation by the user. After the measurement was completed, the GC program falls back into the "batch window", and is available for the next analysis. It is important to note that manual use of both the GC software and the system must be avoided to ensure smooth operation, as the Python script does not have in-build error correction and will not automatically detect other usage.

5.5.3.3 Data Transfer

Moving from a script-based (Subsection 5.4.1) to a remote server-based (Subsection 5.4.2) application required a method of data transfer between the GC operating computer and the server. Since Internet or network communication protocols could not be used for security reasons on this particular PC, a serial communication protocol was preferred. To enable remote use of the chromatograph, Python modules for receiving and sending data on both sides, server and GC automation module, were developed. An overview of the remote-control of the GC is shown in Figure 5.34.

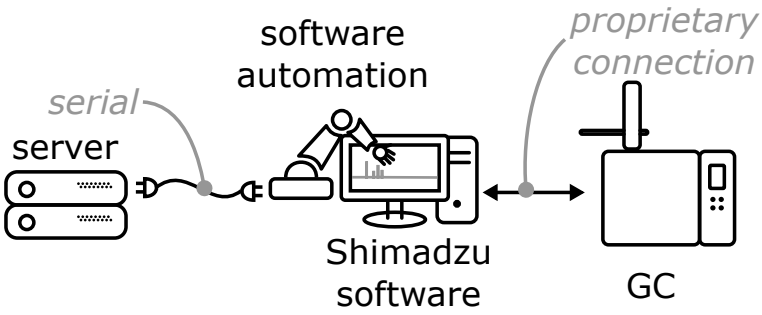

Figure 5.34: Illustration of the concept and communication protocols applied to remotely control the gas chromatograph (GC): Communication from the server to the software automation module on the GC control PC is realized *via* a serial protocol. Shimadzu's proprietary GC software is used by the automation software to provide access to the GC machine connected *via* the proprietary standard connectors from Shimadzu.

The server (Raspberry Pi) offered a simple way for communication with its GPIOs (General Purpose Input/Output). A 3.3V TTL (transistor-transistor logic) is used as the technical basis for the UART (universal asynchronous receiver-transmitter). After plugging in a connector cable and installing the driver on the Windows computer-side, the communication was established.

Considerations for the data transfer speed were made to avoid a high delay of the optimization operation caused by this communication. The rate of data transfer is given as baud rate (pulses per second), which in the case of a single voltage level (as in this case), correlates to bits per second (bit rate). A baud rate of more than 100,000 resulted in losses of transmitted packets, which would not necessarily lead to noticeably worse results thanks to the high sampling rate of the chromatograph (40 ms). However, data loss should be avoided in general, as the indicators for the start and stop of the data could also be lost, which would lead to an infinite loop in the script. A typical GC file (as .txt) for a 6 min GC method was 80 KB large, and, apart from some heading and padding, consisted of approximately 6000 lines of raw data. Each line consisted of a total of maximum 20 characters, which corresponds to 160 bits (in standard formatting). Therefore, the maximum total amount of sent data was approximately 1,000,000 bits. Considering a baud rate of 100,000, a theoretical maximum transfer time of 10 s was required. In practice, this time was approximately 5 s, as most lines contained less than 20 characters. This is sufficient considering an analysis time of 6 min. Thus, the data transfer-related delay can be neglected. For

more data-heavy applications like inline NMR with a sampling rate of a few seconds (max. 4 s), this would not be a suitable option.

On the side of the GC PC, a Python script was programmed to receive commands and send data. The script constantly scanned the assigned COM port (serial) for new commands.

The `start_GC` function triggered the batch measurement as described previously. Once the measurement was complete, the data was formatted and sent to the server. An indicator for the beginning of the data (`start_file`) was prepended, and `end_file` was appended to indicate the end of the data. The dataset is formatted as follows:

```
start_file
[time, signal]
  ...
end_file
```

When the data has been sent, the script returned to the "receive commands loop" and interpreted the incoming commands.

5.5.3.4 Data Processing

After the data was collected and sent to the server (in the case of the remote system), the raw GC data was analyzed. Peak picking, integration, and calculation of the conversion were implemented in a Python software module.

In the case of the local implementation, the analysis was done on the GC PC: First, the subdirectory containing the raw data (`projectfolder‣newfiles‣`) was searched for new .txt files. [ix] Figure 5.35 shows a flowchart for this process. A `while loop` with `newfile` as indicator ran as long as no new file was found. Inside the `while loop`, a `for loop` checked all files in a previously defined path `dir_path`, which corresponds to the `projectfolder‣newfiles‣` path defined earlier. The script ensured that the file was formatted correctly, and the file size exceeded a specified size. This specification to the file size was tailored to ensure that no files of a wrong analysis run were selected. For example, from a reset method, which

ix Here, file endings are case sensitive. For example, .TXT and .txt are not identical.

was in this case used to reset the GC parameters to the inital conditions. If a matching file was found, it was analyzed using the integration script.

Furthermore, within the `if` statement, the file was moved to another directory (`projectfolder‣processed‣`) to clear the `projectfolder‣newfiles‣` directory for the next measurement. For this purpose, the `rename` function from the `os` package was used. Finally, the `while` loop indicator was set to `True` to terminate the loop.

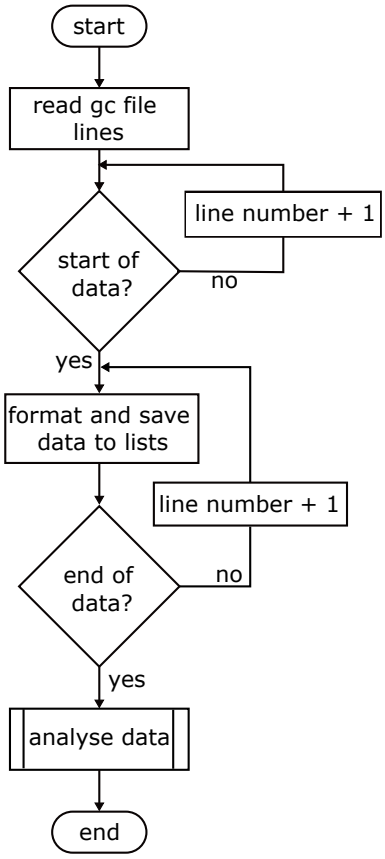

Figure 5.35: Flowchart of the first part of the `analyze_file` subroutine. The data is extracted from the raw gas chromatography data and prepared for further analysis.

Once the file was found, it was prepared and analyzed in the `analyze_file` subroutine shown in Figure 5.35. The raw data was first prepared for analysis, because it contains information beyond the time-signal data pairs. Thus, the data was trimmed to the data pairs only, and then transferred into x (time) and y (signal) data `lists`. In the case of the server-based system, the data was sent to the remote server *via* serial. For the local implementation, the data was passed into the analysis function. Now that the data was prepared, the data analysis script could search for peak beginnings and

ends. These were stored in `lists` that form the basis for the integration performed with the `scipy` module. A threshold for the minimum signal intensity of a peak was established based on an educated guess (prior manual analysis of the data) and iteratively fitted to a set of real-world test files. For the oximation of octanal (**13**) to octanal oxime (**14**), which is presented in Subsection 6.3.2, this value was 2500. The resulting integrals were stored in a `list`. As for the integration, different cases were included (Figure 5.36).

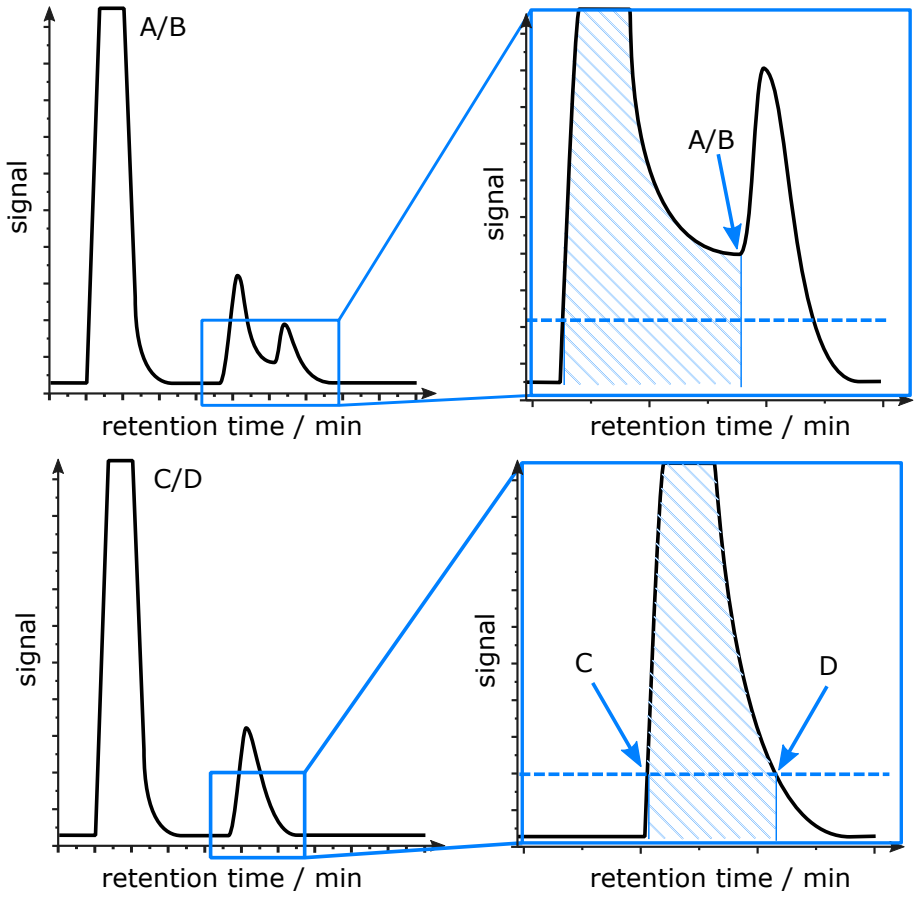

Figure 5.36: Scenarios (A–D) for integration of peaks in gas chromatography analysis. Upper part: Overlapping peak (A/B) with zoomed-in area and highlighted integration area. Lower part: Isolated peak (C/D) with zoomed-in area and highlighted integration area. Start and end of the integration area are marked with arrows.

Two potential scenarios were covered: The first scenario represents the case of an isolated peak (Figure 5.36, case C/D). Here, the beginning (C) and end (D) of the integration was determined by a combination of signal threshold and slope investigation. This is not possible in the second scenario of overlapping peaks (Figure 5.36, case A/B). In this case, the threshold investigation would yield an end after the second peak. An investigation based on

the change in sign of the slope successfully yielded the marked area, which is commonly used when investigating such patterns. Case A and B differ in that not two directly consecutive values are considered, but the value after the following one. In rare cases, the same signal intensity was measured for two consecutive x-values. In the case A, this led to an error in the script because the case for no change of the slope was not implemented as the number of peak starts and ends were mismatched. A flowchart describing this second part of the "analyze file" subroutine is given in Figure 5.37.

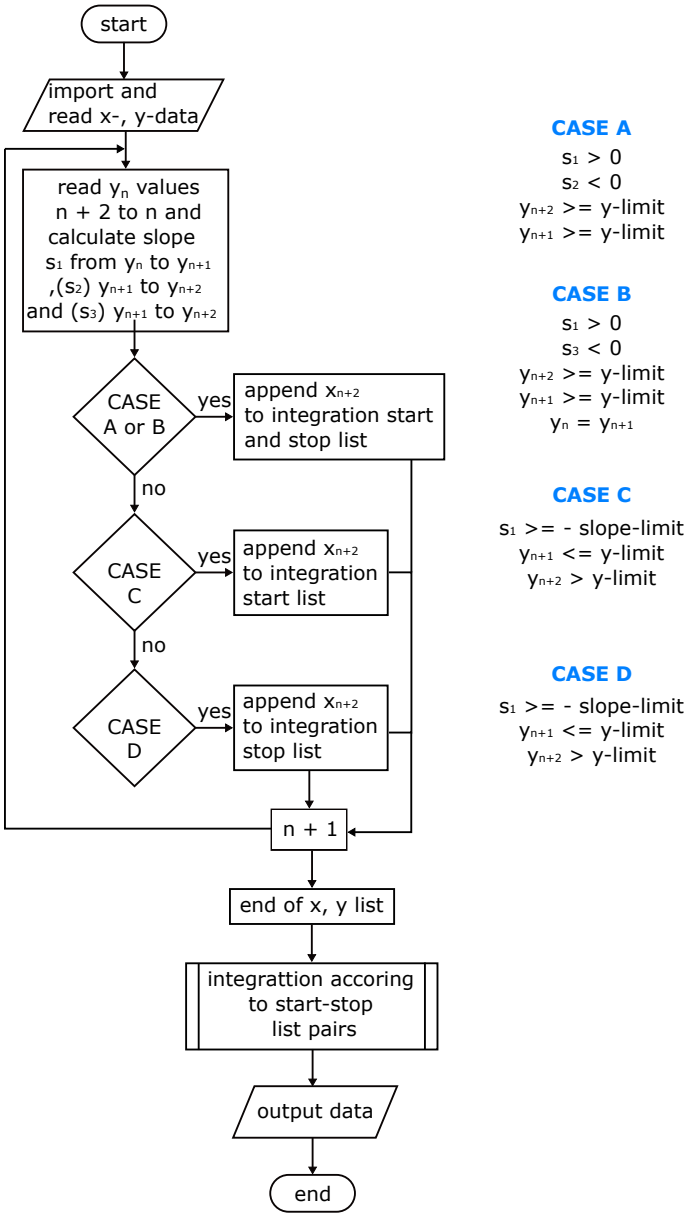

Figure 5.37: Flowchart of the `analyze_data` subroutine, imports x- and y-raw data (time, signal) from the gas chromatography analysis, identifies peaks according to different scenarios (case A–D), integrates each peak, and outputs the integrals. n, index of data pair; s_x, slope.

Based on the beginning and end of the integrals, lists of x- (time) and y- (signal) data was generated for each peak, which covered only the peak area. This data was then passed into a `scipy` integration function to give the absolute integrals. The integration was based on the cumulative trapezoidal rule. Other rules for integration were applied as well; however, no significant difference in area or computing time was found. Since the computation time was only in the millisecond range, no bottleneck is expected since the data was generated on a minute scale.

The signals were then analyzed, and a calibration was applied to quantify the obtained integrals. The calibration curves were previously measured manually to allow the calculation of the concentrations in the sample. An earlier version used "hard-coded" (written into the source code) input for peak identification. This was changed to allow for more dynamic analysis to an input *via* the web UI. To identify a peak, the user had to provide the system with some information: Minimum and maximum start of the peak, maximum end of the peak (all as retention time in minutes), as well as the role of the compounds in the reaction (starting material, product or side product) and the corresponding calibration data. The user input was formatted using JSON (JavaScript Object Notation) and did not need to be translated into Python. Two examples for compound data objects (formatted list of data; JSONs) are given below:

```
1  {'name': 'shimadzugc_1_c1', 'start_min': '1.51', '
    start_max': '1.55', 'end_max': '1.70', 'calibration': '
    142.92269622709955', 'role': 'educt'},
2
3  {'name': 'shimadzugc_1_c2', 'start_min': '1.95', '
    start_max': '2.30', 'end_max': '2.77', 'calibration': '
    156.66726065361453', 'role': 'product'},
```

To enable machine readability, the object (or in Python: dictionary) paired key-value pairs with the individual information: The `name` key was used to uniquely identify the device (gas chromatograph: `shimadzu_1`) and the compound number (`c1`); `start_min`, `start_max`, and `end_max` gave the retention times for peak characterization in minutes, while `calibration` contains the previously manually determined slope for calibration, and `role` allows to identify the role of the compound. This identification was needed for further calculation of the yield and selectivity. In the above-mentioned example (Subsection 6.3.2), line 1 corresponds to the octanal (**13**) peak in

the oximation to form octanal oxime (**14**), which is described by the entry in line 3.

The script returned the integrals as a list of absolute values as well as concentrations, which were calculated based on the calibration data. From these concentrations, the yield and selectivity were calculated. To calculate the GC yield, the concentration of the product was divided by the sum of all compounds and multiplied by 100. The yield could be used by the closed-loop system as a system response. Moreover, a calculation for ee values was implemented. For this purpose, two additional compound roles were defined: `product_enantiomer_1` and `product_enantiomer_2`.

Software Stability Modifications During the use and testing of the automated GC system, different issues came up. These problems were addressed by several modifications of the software. These modifications are explained in detail below.

1. Value Error

Over the course of several automated runs, it was found that in some cases the data could not be analyzed correctly. This error can potentially originate from different scenarios: Data transmission error, errors in controlling the Shimadzu software on the GC operating PC or poor data quality.

Whenever these errors occurred, a yield with the value `None` (in Python: undefined value) was returned. This resulted in an error in the entire optimization script that caused the system to shut down prematurely. A loop to catch this value error was written. The pseudo-code (code that explains in an easily readable way the function but cannot be interpreted by Python) is shown below.

```
1  while yield == None:
2    # start analysis script
3    # receive and analyze GC results
4    if yield == None:
5      # request restart of the analytics
6
7  # continue here only if yield is correctly set
```

The system remained in the `while` loop as long as the `yield` was not properly defined. Iteratively, the script requested a measurement from the GC system and analyzed the results. If the yield was `None`, the user was notified and could issue another measurement. In this case, user interaction was required, which was important to ensure the correct operation of the GC.

2) Low-quality Data

With this modification, most errors could be fixed. However, low-quality data remained problematic, at least in parts. In rare cases, it was observed that bubbles occurred in the flow-through GC vial attached to the chromatograph. They appeared to have occurred in the membrane separator and may be caused by partial degassing of the reaction mixture. These bubbles could be drawn from the sampling syringe leading to a very low sample concentration on the gas chromatography column. In this case, the quality of the analysis data was reduced because the signal to noise ratio was lower, and the signal intensity might be lower than the selected integration threshold. For example, in one case of an automated optimization run only the product peak was integrated leading to a wrong yield of 100% (Figure 5.38; experiment 3).

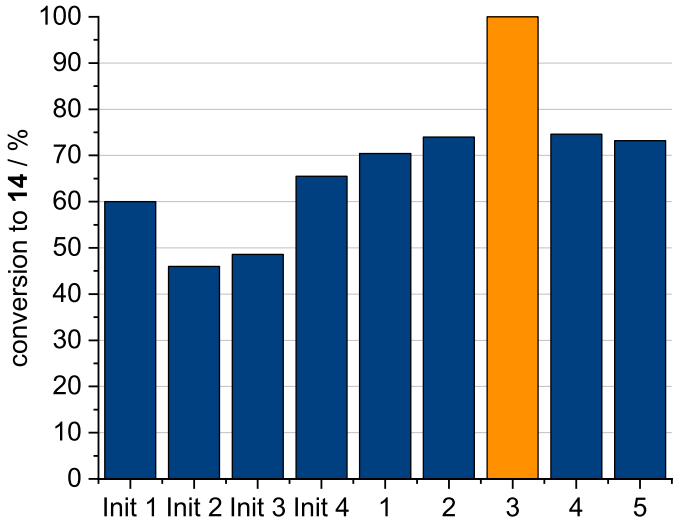

Figure 5.38: Exemplary results obtained from an automated run with four initial experiments and 5 optimization iterations. Conversion of the oximation of octanal (**13**) to octanal oxime (**14**) is shown. Highlighted conversion (orange) of run 3 shows a false result from the gas chromatography analysis, where a low sample concentration was caused by bubbles in the sample vial.

To account for such problems, a script was written and included into the analysis module. Based on current and previous data, the system calculated whether the total sum of the peak integral was in the usual range. To allow this comparison, the sum of all integrals for each measurement were stored in a `list`. The current analysis data was then compared against this list. The following equation (5.9) with j as the number of experiment, and i as the compound peak in chromatogram must be `True` to consider the measurement successful:

$$\sum^{i} \int peak_i > \frac{\sum^{j,i} \int peak_{j,i}}{j} \cdot 0.5 \tag{5.9}$$

Only if the sum of all integrals in the current measurement is greater than the average sum of all integrals in all past experiments times a factor (0.5), the equation is `True`. As product and starting material do not necessarily have the same signal intensities, a factor of 0.5 was introduced to allow for variations of the analysis.

If this test failed, the user was notified and could manually restart the analytics after revising the GC machine. As this approach is based on past data, it cannot work for the first measurement—this had to be checked manually.

3) Baseline Increase

In many cases, the baseline signal increased toward the end of the run as higher temperatures were reached. This resulted in an error during the integration of the peaks, as the peak beginnings and ends were mismatched. The rising baseline was misinterpreted as the beginning of a peak; however, a corresponding end was not found. This behavior originates from the integration threshold, which was required to reduce the noise during peak picking. A chromatogram with this behavior is shown in Figure 5.39.

This issue can be solved in several ways. In this work, the threshold was raised above the baseline threshold after a certain time to avoid the baseline being detected as a peak. The limits were coded into the GC analysis Python module. Alternative, and more complicated solutions, to delete the last entry if the ends and beginning were mismatched. In the future,

a more complex baseline analysis script could be included. By creating a mathematical model for the baseline, and subtracting this model from the data, improved results could be obtained.

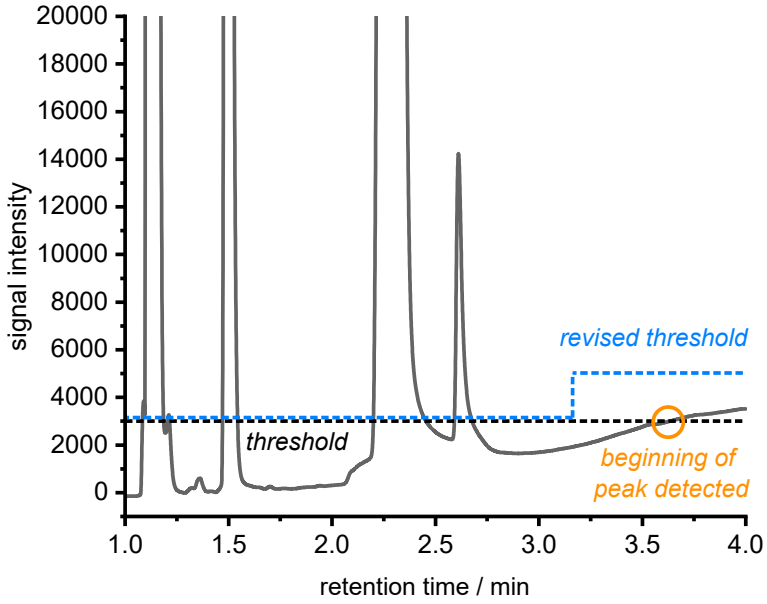

Figure 5.39: Exemplary gas chromatogram with integration thresholds (blue dashed line, revised; black dashed line, original) and highlighted (orange circle) misinterpreted peak.

4) Fixed-time Integration

When integrating a sample with a very low sample concentration of $< 5\,\mathrm{mM}$, the peak picking Python function had difficulty identifying the peak due to a low signal-to-noise ratio. The slope detection was triggered when the noise was too high and prematurely ended the integration area of the peak. Thus, one single peak was split into multiple integrals leading to a wrong result (Figure 5.40). This problem was addressed by the implementation of a fixed-time integration. To realize this, the integration areas were defined, and the automatic peak identification was overwritten manually. To this point, this type of integration has been tested and coded into the analysis module. In the future, a selection of the integration method could be integrated into the user interface.

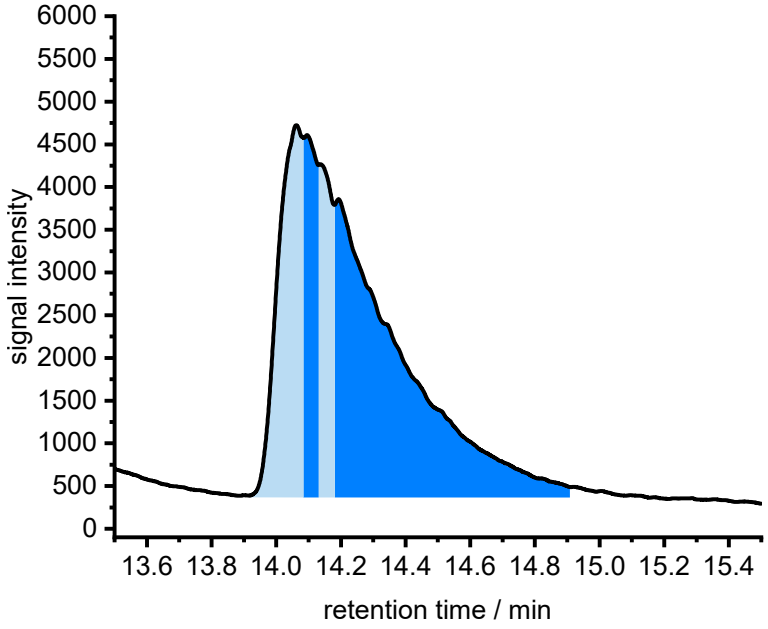

Figure 5.40: Exemplary gas chromatogram with a low signal-to-noise ratio. Integration areas are highlighted in blue.

5.5.4 Nuclear Magnetic Resonance Spectroscopy

For another project—the self-optimization of multi-component reactions[140]—a nuclear magnetic resonance spectrometer (NMR) was implemented into the system as well. A 60 MHz system from Magritek (Spinsolve 60) was used for this purpose. The development can be divided into four major parts: Hardware control, communication, data interpretation, and implementation in sofalab.

Hardware Control To enable remote and automated control of the machine, a Python driver was written and implemented into the closed-loop platform. The Spinsolve software offers an API (Application Programming Interface), which can be used to control the device using TCP/IP (Transmission Control Protocol/Internet Protocol) communication *via* `socket`, which is a popular Python library. The term "socket" is also used for a communication end-point. After remote access to the proprietary software was enabled, predefined commands could interact with the software. The corresponding commands can be found in the manual.

Data Transfer The communication for the hardware control was already predefined, but there was no integrated option to send the analytical data back to the server. Thus, a channel for communication based on the same protocols was implemented. Compared to the previously described GC communication, other aspects were important. As the system was connected to the university network, protocols based on the IP (Internet Protocol) were available. In addition, much higher data throughput was expected compared to the GC, as the sampling rate for the NMR can be as low as 4 s. This rate of data is very close or even exceeds the limits of the previously described serial-based protocol.

For the data transfer, a `socket` was provided by the sofalab server and the NMR PC connected as a client to it. A scheme of the communication is shown in Figure 5.41.

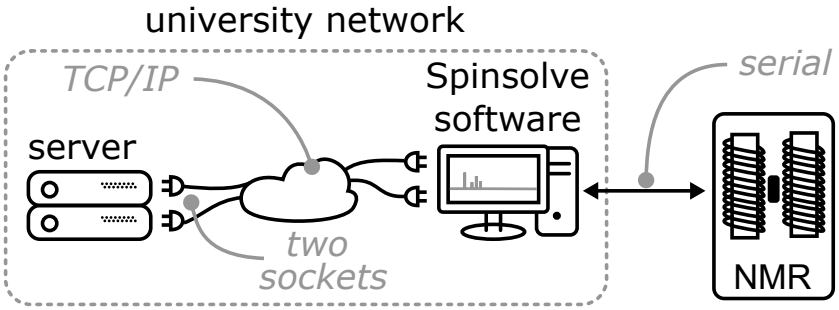

Figure 5.41: Communication protocols applied to remotely control the nuclear magnetic resonance spectrometer (NMR). Two communication ports (sockets) are used for data and command transfer *via* the university network. TCP, transmission control protocol; IP, Internet protocol.

Data Analysis Both ^{19}F and ^{1}H NMR are available and could be analyzed similarly. The NMR machine saved recorded data automatically in different file formats. One of which was the universal file format `JCAMP-DX`[141] containing the FID (free induction decay) data and some instrument/measurement metadata. This file format was analyzed using an open-source Python package called `NMRglue`.[142,143] Firstly, the data was prepared, and data points were stored in a complex `numpy array`. In this array, the real and imaginary parts of the FID (Free Induction Decay) signal were stored. Then, zeros were filled in to the given array size to allow automatic analysis. After the Fourier transformation, the imaginary part of the data was deleted. This mathematical operation transformed the signal obtained in the time domain into the frequency domain and was pioneered by the Nobel Prize-winning chemist *R. R. Ernst*. All of the operations could be done

easily with predefined functions of the `NMRglue` package. However, when it came to the automatic interpretation of the metadata, additional calculations (without the NMRglue module) had to be performed. For example, the carrier frequency was not correctly interpreted. According to contributions[144] on the development platform of the module, the metadata can be read and interpreted as in the following to allow conversion to a ppm scale (from frequency domain). Please note that these calculations are specific to the used Spinsolve 60 device. Other devices might not require them.

The carrier frequency CAR can be calculated by subtracting the absolute frequency for the 0 ppm position SF from the given base frequency $BF1$. To convert the units, this value is multiplied by 1 E6 (Equation 5.10).

$$CAR = (BF1 - SF) \cdot 10^6 \tag{5.10}$$

Also, the spectral width sw of the spectrum was converted. For this, the spectral width given in the meatadata (SW) is multiplied by the absolute frequency for the 0 ppm position SF (Equation 5.11).

$$sw = SW \cdot SF \tag{5.11}$$

Having these values calculated, the unit conversion was performed yet again by the `NMRglue` module. This spectral data on a ppm scale was analyzed by integration of the signals. Two different options for integration were tested: Simpson's rule (also: parabolic rule) and the trapezoidal rule. The approaches differ in the way how the curve over the integral is estimated. In the case of the trapezoidal rule, it is a linear model, while Simpson's rule is based on a parabolic curve. Usually, Simpson's rule offers better results, which comes at the cost of higher computing power compared to the trapezoidal rule.[145] Analyzing a real-world ^{1}H NMR dataset for integration using Simpson's rule resulted in a conversion of 68.532 18%, while the result from the trapezoidal rule was only insignificantly different (68.532 21%) with only a fraction of one percent difference (0.000 03%). Manual integration using MestreNova, resulted in 68.20% applying the integration tool and 68.68% using the multiplet analysis tool. Here, the main difference can be attributed to a small shoulder tip, which is integrated in the first

case, but not in the second. Compared to the automated integration, similar results were obtained (deviation of 0.33% or 0.15%). Both Python integration methods took 0.01 ms to compute the integrals from the NMR spectrum and were thus much less "expensive" than the previous Fourier transformation (calculated on a notebook with Core i7-7700HQ). Even on a "low-performance" system like the Raspberry Pi (model 4), this computing demand is insignificant. Therefore, considering the maximum sampling rate by the NMR (0.25 Hz), the choice of rule for integration is irrelevant.

The Python module for server-sided calculation of the conversion can feed the calculated data directly into the optimization algorithm as a response value. In the future, a more sophisticated approach based on indirect hard modeling could further improve the applicability of the system.

Implementation For another project, the NMR was implemented in the server. The code can be found in `server_alina.py`. For the first experiments, the NMR specifications were "hard-coded" into the server source code. They are given in lines 10, 11 and 16,17 (line 62 of server_alina.py) and must be set manually (not possible via the web UI):

```
1  tempnewdev = {
2    "name":"nmr_1",
3    "category":"analytic",
4    "type":"nmr",
5    "host_ip":"xx.xx.xxx.xx",
6    "port":13000,
7    "compounds":
8      [
9        {"name":"nmr_1_c2",
10       "stop":"-71.85",
11       "start":"-72.5",
12       "protons":"1",
13       "role":"product"},
14
15       {"name":"nmr_1_c1",
16       "start":"-71.85",
17       "stop":"-71.6",
18       "protons":"1",
19       "role":"educt"}
20     ]
21   }
```

After starting the experiment, the system continuously measured ^{19}F NMR spectra in a 60 s interval for five residence times. These spectra were prepared and interpreted to determine the NMR yield. While the first three residence times were considered as equilibration, the results of the remaining two residence times were collected in a `list`. The average of these yields was returned as the reaction yield. Moreover, the raw .dx files were saved in the directory `projectfolder‣logfiles‣EXPERIMENT_NAME‣data_nmr` for later manual analysis and documentation.

5.6 Summary & Outlook

In summary, a remotely controlled, self-optimizing continuous synthesis platform was successfully developed. Initially, the laboratory equipment was prepared and drivers for remote-control were written to enable remote and continuous operation. For the optimization, a Nelder-Mead algorithm was implemented. Then, a local, script-based system was developed for initial testing of the devices and the optimization algorithm. After successful results, the system was enriched by a server-based approach.

A number of devices have been added to allow inline analysis and control over flow rates and reaction temperature. A gas chromatograph (GC) and a nuclear magnetic resonance (NMR) spectrometer were included as analytical options. Modifications for inline analysis at the instrument level and a driver for automated control and communication were developed for the GC. Additionally, a Python module for analysis and interpretation of the data was programmed for the determination of the conversion as well as the enantioselectivity. As a second option, a benchtop NMR was included as an inline option with a high sampling rate.

In order to control the temperature efficiently (0–140 °C), a modular reactor system was designed, developed, and built. Moreover, a four-unit reactor for batch screening was developed. The modular reactor featured simple offline control using an included touchscreen, and interchangeable reactor units. In the future, many different reactors units, such as packed bed reactors, may be included.

The server-based platform enabled users to remotely set up and monitor the reaction optimization process. Server-sided, Python was used as the main programming language. A server microframework (Flask) was used for rapid development. On the client-side, a combination of HTML, JavaScript, and CSS allowed the user to interact with the system without the need for knowledge in programming. Popular programming frameworks (Bootstrap, Plotly, SocketIO) were used for efficient development. In total, well over 6000 lines of code were programmed, excluding comments, pre-existing modules, and frameworks (Figure 5.42). More than half of the software was written in Python.

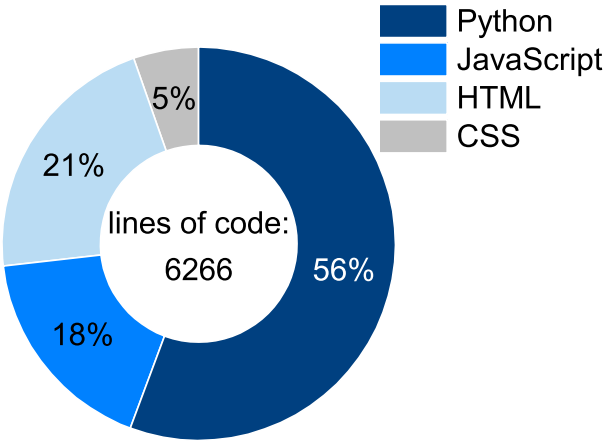

Figure 5.42: Lines of code and percentage of languages written for *sofalab* excluding pre-existing libraries.

Since a modular design philosophy was followed in programming the server system, new devices and functions can be implemented relatively quickly. Moreover, various optimization algorithms can be integrated in the future. The platform can potentially enrich the work of chemists by relieving them of tedious, repetitive tasks. At the same time, more reliable results as well as efficient and resource-saving synthesis planning can be realized. In the future, the developed platform could form the basis for more advanced optimization tasks.

6 Chemoenzymatic Continuous Nitrile Synthesis

» In this chapter, a chemoenzymatic reaction cascade for the synthesis of alkyl nitriles was translated into a flow process. A reaction optimization was carried out partially or fully automated, based on the previously described technology. Parts of this project were the result of a cooperation with the University of Cambridge, UK. «

6.1 Theoretical Background

6.1.1 Nitrile Synthesis

Nitriles represent an important functional group in a variety of chemicals. Not only does this moiety readily appear in drugs such as Vildagliptin but also in bulk chemicals like butyronitrile or acrylonitrile (Figure 6.1).[146]

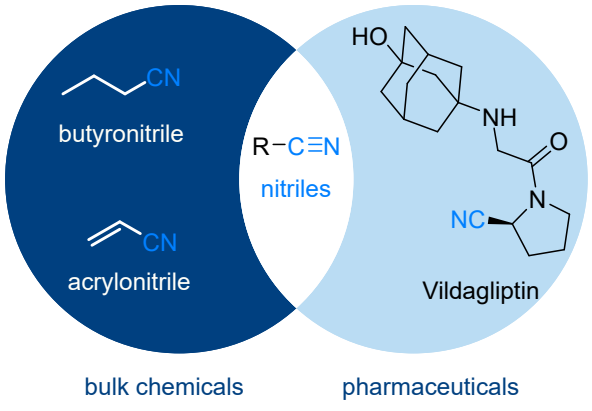

Figure 6.1: Examples of industrially relevant molecules containing nitrile groups.

Today, a wide range of reactions are available to synthesize aliphatic nitriles. Many of them—like hydrocyanation—require highly toxic starting materials. Others demand very harsh conditions, resulting in an environmentally unfriendly process. An overview of some classic pathways is shown in Scheme 6.1 .

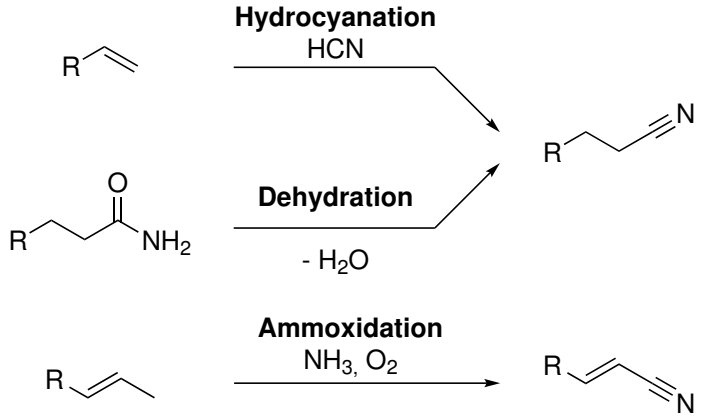

Scheme 6.1: Commonly applied routes for the synthesis of aliphatic nitriles. R = alkyl.

The metal-catalyzed hydrocyanation of olefins is known since the 1950th.[147] Moreover, α,β-unsaturated carbonyl compounds have been converted into nitriles as well.[148] DuPont developed an industrial process for the production of polymer precursors based on this reaction.[149] However, all of these reactions have a toxic compound in common—hydrogen cyanide. Only recently, less toxic yet very expensive options to replace cyanides have been explored.[150]

The SOHIO process is one of the prime examples of industrial-scale ammoxidation.[151] On multi-million ton-scale, propylene, ammonia, and oxygen react under high temperature and pressure to acrylonitrile. Today, also biomass is suggested for the production of acrylonitrile.[152] Moreover, improvements towards greener protocols for ammoxidation have been made.[153]

Furthermore, the dehydration of aliphatic amides, for example, using sodium borohydrate[152] or silanes[154] has shown to be a suitable route to nitriles. The Beller group recently presented a general catalytic protocol for this reaction.[155,156]

To overcome the sustainability concerns of these classic methods, the Gröger group developed recently a multi-step process involving biocatalysis. In the aldoxime dehydratase (Oxd)-catalyzed dehydration of oximes, aliphatic

nitriles can be formed under ambient conditions (Scheme 6.2).[157–160] A first example of this reaction catalyzed by OxB-1 from *Bacillus* sp. was reported by Asano *et al.*[161] This reactivity was furthermore exploited in a nitrile synthesis with an Oxd found in *Rhodococcus* YH3-3 by Kato *et al.*[162] Later, several other Oxds from different species have been found, like the OxdB from *Bacillus* sp. Through cascade reactions starting from either renewable fatty acids[163] or petrochemical-based alkenes[164] efficient routes to nitriles have been developed based on these enzymes.

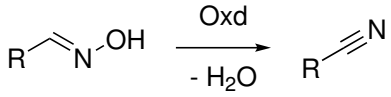

Scheme 6.2: Oxd-catalyzed dehydration of an aldoxime to the corresponding nitrile. R, alkyl; Oxd, aldoxime dehydratase.

Hinzmann *et al.* could show, that the Oxd-catalyzed oxime dehydrogenation can be run at a very high substrate loading of $1.4\,\mathrm{kg}\cdot\mathrm{L}^{-1}$ in buffer.[159] The substrate had to be added portion-wise to keep the mixture stirrable. An impressive catalyst efficiency of $23\,\mathrm{g_{prod}}\cdot\mathrm{g_{wcm}^{-1}}$ regarding the wet cell mass (wcm) was achieved. However, Oxds have proven to be labile against organic solvents.[165] As organic solvents can simplify processes tremendously, the issue of incompatibility was addressed using a range of techniques. Immobilization of the whole-cells in superabsorber was used to make Oxds usable in organic solvents. In our recent study, we could show that the conversion of octanal oxime in a cyclohexane/superabsorber system could be improved to 99% compared to the corresponding cyclohexane/buffer system (9%).[165] This superabsorber system was then also applied in a packed bed reactor.

Moreover, Bago Rodriguez *et al.* could show that pickering emulsions represent a further technology to run the oxime dehydration in biphasic media.[166] Different parameters were optimized to yield a catalyst formulation with a very high interface area, which increased the conversion. In contrast to typical biphasic whole-cell reaction systems, the positive effect of the silica particles on the catalyst stability enabled efficient recycling.

Besides these process design-related improvements, enzyme engineering has been frequently applied to enhance the abilities of the catalysts.[167,168] Since this would go beyond the scope of this work, this topic will not be discussed in detail.

6.1.2 Flow Chemistry

General Introduction

Although flow chemistry is an emerging field of research today, this area has been known and researched for decades. But only today, commercial devices are readily available and manufactured by many companies around the globe. As suddenly many laboratories have access to these technologies, the research has been stimulated and still flourishes. As proven by many books, countless articles, and dedicated journals, flow chemistry has become a crucial part in modern chemical process development.

But what factors make flow chemistry so popular? Besides the benefits of continuous production, better heat and mass transfer enable new process windows. Previously impossible reactions have been realized in microreactors thanks to improved process control. Furthermore, small reactor volumes make these kinds of processes inherently safer compared to batch mode.

Besides these advantages, there are also drawbacks. Compared to batch mode, the equipment tends to be much more expensive and less versatile. While a flask can be used for the reaction as well as, for example, for crystallization, a microreactor usually only serves as a reactor. Downstream processes are often carried out in dedicated devices. Moreover, processing heterogeneous mixtures can sometimes be incredibly challenging or nearly impossible. Lastly, long reaction times tend to decrease the efficiency of flow processes as mixing is not as good, and accurate material supply can become challenging to control. Figure 6.2 shows a summary of the general benefits and drawbacks of flow and batch chemistry.

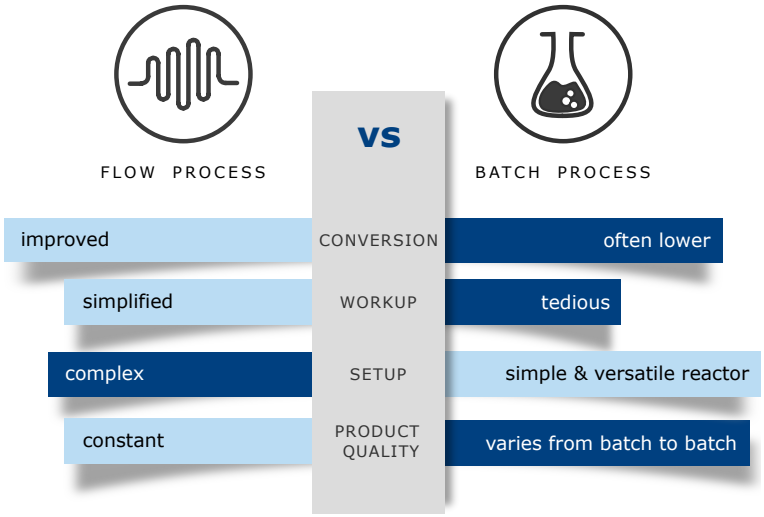

Figure 6.2: Comparison of benefits and drawbacks of batch *vs* flow processes (modified from Adebar *et al.*[169]).

Today, there is a number of concepts for continuous reactors. The most basic flow process uses a *plug flow reactor* (PFR). In this setup, a tube or pipe is used as a reactor for fluid or gas-phase chemistry. Starting materials are continuously pumped into the tube, react inside, and the product leaves the system at the outlet. From a theoretical view, this plug flow process can be imagined as an arrangement of infinite infinitesimal small discontinuous batch reactors (Figure 6.3). Thus, under ideal conditions—perfect heat- and mass transfer—both processes will perform identical, as kinetics and thermodynamics remain unchanged.

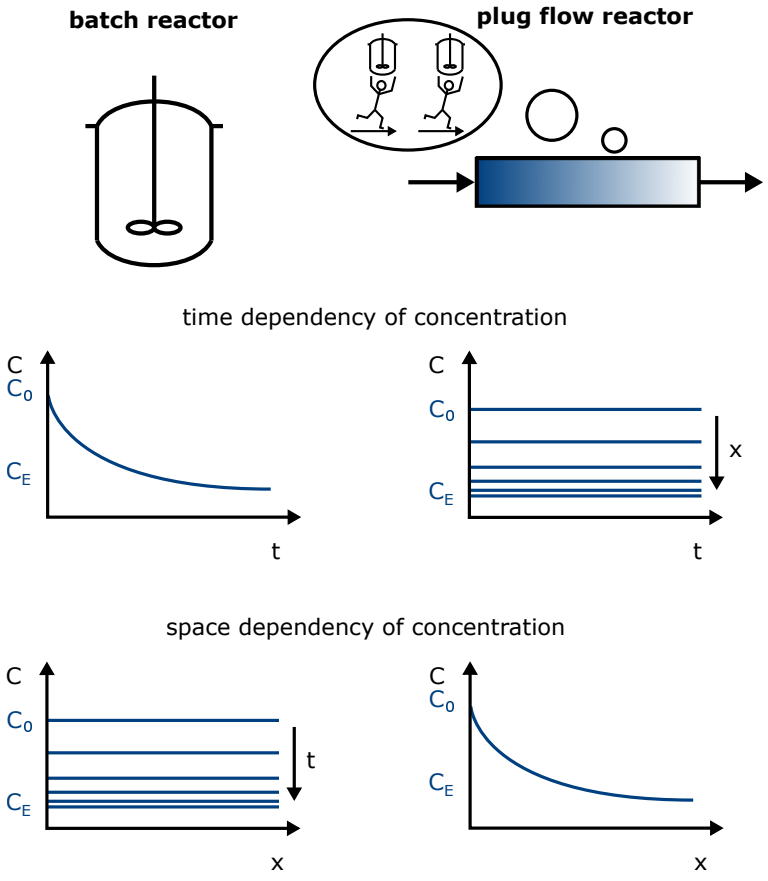

Figure 6.3: Comparison of batch and plug flow reactors in terms of substrate consumption in dependence of time and space. c_0, start concentration; c_E, end concentration; x, reactor length (adapted from Adebar *et al.*[103]).

Moreover, *packed bed reactors* have proven to be powerful tools in synthesis. Often, a catalyst bed is packed into a tubular system, and starting material is continuously pumped over the bed. Thanks to this integrated catalyst recycling, highly efficient processes can be realized. In particular for long reaction times, *continuously stirred tank reactors* have shown to be a good combination of batch- and flow processes. Besides these basic examples, there are many more (advanced) concepts for the continuous production of chemicals.

Biphasic flow systems often offer advantages over monophasic ones. In flow processes, these systems can perform much better due to a larger interface area and more rapid mixing compared to batch. A straightforward way to realize increased interphase areas is the use of a segmented flow. In most cases, organic and aqueous solutions are combined in a Y- or T-mixer to produce alternating segments which are led into a reactor. For example, Schachtner *et al.* described a liquid-liquid system for the nitration of xy-

lidines. This reaction mixture was then separated and fed into a reduction unit to produce the corresponding amine in a telescoped process.[170] The same group previously presented a study on the scale-up of an acyl azide synthesis in a number of different homogeneous and biphasic systems.[171] The importance to maintain good mixing while scaling up the channel diameter was pointed out as crucial. In contrast, this aspect is far less important for homogeneous systems. The group of Kappe could show that the mixing of biphasic reactions can be further increased through the integration of a packed bed reactor filled with inert material.[172] This static mixer allowed a very fine dispersion of the aqueous phase depending on the static material. Many more studies applying[173–177] and investigating[178] segmented flow processes have been conducted in the past years.

Taking the concept of fine droplet dispersion to the maximum, pickering emulsions can generate very high interface areas. These stabilized emulsions were investigated in continuous flow mode, for example, by Zhang *et al.* (Figure 6.4).[179]

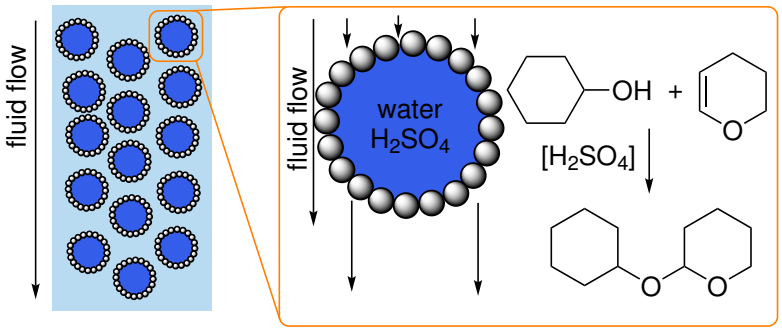

Figure 6.4: Exemplary continuous flow system using sulfuric acid in a pickering emulsion as catalyst for the condensation of aliphatic alcohols with alkenes.[179]

Moreover, many segmented flow systems in packed-bed reactors were reported. For instance, an immobilized Pd-catalyzed Suzuki coupling with a liquid-liquid system pumped over a catalyst bed[180] or a biphasic oxidation of alcohols by immobilized TEMPO[181] were developed. Abolhasani *et al.* used an oscillating three-phase flow system to improve the mixing.[182,183] Particularly interesting is the finding of the authors that no equilibration time was needed to ensure stabilization of flow velocities and reagent concentrations. Thus, different reaction times could be used without the need for adjusting the flow rate and reactor length, potentially rendering this system ideal for rapid closed-loop optimization.

Furthermore, fluorous solvent systems were used as recyclable catalyst-containing phase, for example, for Lewis-acid catalyzed reactions, reaching a TON of over 9800 in a bench-scale reactor in an esterification reaction.[184]

A different technology was described by Kendall *et al.* They used a high-throughput film-shear flow reactor for highly efficient ozonolysis of alkenes.[185] Yet another technique is based on the use of a Taylor vortex flow reactor (Figure 6.5).[186] The authors additionally investigated segmented-flow systems and observed that larger tube diameters decrease the reaction rate in such systems. Furthermore, the segments depended on the tube diameter as well as the pump mechanism. A syringe pump, which generally delivers very constant flow rates, was considered to be the best pumping method. With the Taylor vortex flow approach, they could reach even higher conversions compared to segmented flow mode.

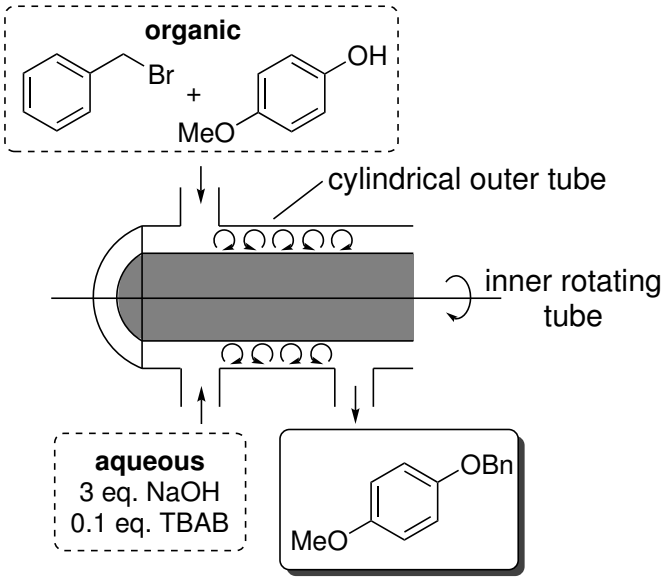

Figure 6.5: Taylor vortex flow reactor for the biphasic benzylation of an aromatic alcohol by Kendall *et al.*[185] TBAB, tertrabutylammonium bromide.

Not only liquid-liquid systems have been reported but also gas-liquid reactions are very popular. Schachtner *et al.* reported on a low-cost setup for an oxygen-organic photocatalytic oxidation.[187]

Many tools have been developed to allow for the efficient processing of biphasic reactions[188]: For example, a miniature continuously stirred tank reactor, which was applied for liquid-liquid C-C bond formation.[189] In particular, phase separation was intensively investigated, as this technique provides a

powerful tool for downstream processing. Besides membrane separators[190], also gravity-based systems were reported.[191,192]

Continuous production generally allows to avoid reactor downtimes, for example, for cleaning and recharging, thus time and workforce can be saved. This leads to an overall production cost reduction. But time savings are not the key aspect why regulatory agencies like the European Medicines Agency (EMA) or the U.S. Food and Drug Administration added continuous manufacturing to their guidelines.[193,194] In this pharmaceutical context, continuous product quality is a key element. As no separate batches with varying results are prepared, the product quality is often considered to be more reliable. The absence of human intervention in a continuous process can furthermore reduce human errors and dangerous situations. In conjunction with automation and process analytical technology (PAT), highly stable and safe processes can be realized. The group of Kappe realized a multi-step process with four complementary analytical online tools: Nuclear magnetic resonance-, infrared- and ultraviolet/visible spectroscopy in combination with a high-performance liquid chromatography system.[195]

But also on a reaction level, flow processes can make a difference. Generally, higher mass- and heat transfer can be realized leading to novel process windows.[196,197] Through rapid mixing and short diffusion paths, the mass transfer can be improved compared to batch.[198] By overheating solvents far above their boiling points, conditions unreachable by batch reactors can be generated safely.[199] With specially designed reactors, the mass transfer can remain constant while scaling up the reaction.[200] This leads to a very quick process development path from early screening-scale to ton-scale production. Commercial products have been realized, among others, by Corning (Figure 6.6) and Little Things Factory.

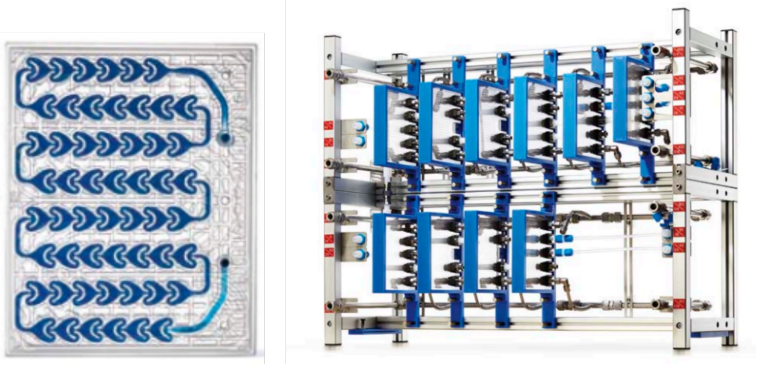

Figure 6.6: Corning™ G1 glass chip reactor. Left: Single glass chip reactor, right: assembly of multiple reactors.

Small reaction volumes, high heat transfer, and the possibility to generate toxic intermediates *in situ* make flow processes inherently safer compared to their batch counterparts.[201–204] The enormous benefit of heat transfer in flow processes was impressively demonstrated by Rebrov *et al.* in their system for an ammonia oxidation reaction.[205] They have operated this highly exothermal process at an adiabatic temperature of 1400 °C at a reactor temperature of only 318 °C at the first reactor part, and 332 °C at the reactor outlet. This example illustrates the heat transfer capacities in microstructured reactors.

Flow Biocatalysis

For flow biocatalysis, many of these benefits do not play a major role. The improved heat transfer and safe processing are not necessarily beneficial for biocatalysis, as reactions are usually operated at ambient temperatures, and most catalysts are neither explosive nor toxic. Nevertheless, continuous product delivery and rapid mass transfer are relevant for these syntheses.

By using a high-performance countercurrent chromatography system, the groups of Wirth and Allemann were able to improve the yield of a terpene synthesis by the factor three to 94%.[197] It outperformed even a segmented flow approach, proving the importance of high mass transfer for fast biocatalytic reactions.

While biocatalysts are usually harmless, (co)substrates sometimes can be highly toxic. For example, Brahma *et al.* developed a hydroxynitrile lyase-catalyzed nitrile synthesis using hydrogen cyanide in a multi-step flow process (Scheme 6.3). Through the use of microreactor technologies, the related risk could be effectively minimized.[206]

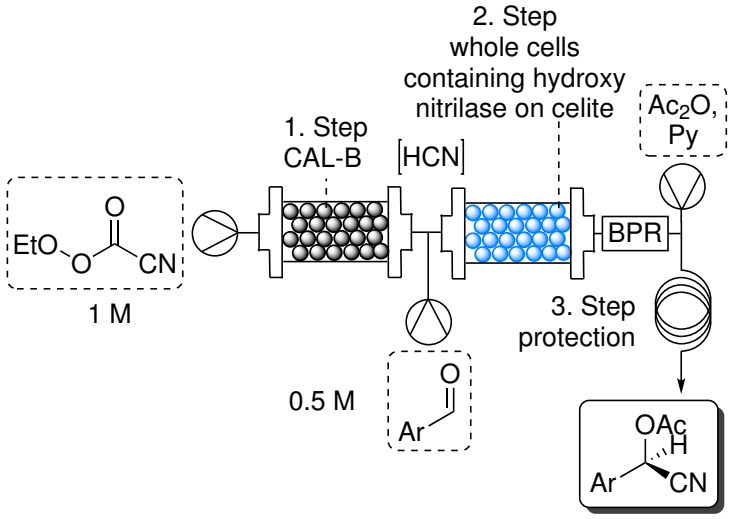

Scheme 6.3: Reaction sequence for the synthesis of aliphatic nitriles starting from either renewable fatty acids or alkenes *via* hydroformylation as reported by Brahma *et al.*[206] (adapted from Adebar *et al.*[207]). BPR, back pressure regulator; Py, pyridine.

Our group could recently show that not only the reaction can be improved through continuous synthesis but also downstream processes can be simplified.[208] Illustrated on the example of an ADH (alcohol dehydrogenase)-catalyzed dehydrogenation of acetophenone, it was shown that emulsification and phase separation are much better when performing the reaction in a segmented flow mode. In these experiments, the conversion compared to batch mode was similar. Analogous findings were previously described by Karande *et al.*[209]

The sheer number of reviews that have mushroomed in the past years proves the importance of flow biocatalysis to chemical process design.[207,210–219] Four major concepts for conducting these continuous syntheses crystallized from many studies. By far the most widely applied principle is the immobilization of catalysts on a solid support, which is then loaded into a packed bed reactor. Besides loose carrier materials, the reactor itself was used as a support for the biocatalysts resulting in a wall-coated reactor. Moreover, enzymes have been used readily in liquid-liquid segmented flow systems. In contrast to the previous methods, the catalyst is continuously pumped through the reactor. Thus, catalyst degradation is less problematic allowing for a very stable process. Meanwhile, the catalyst efficiency is usually much lower. Contrary to all these examples, a biofilm reactor can exploit the unique characteristic of catalyst regeneration through living cells. Either in cycles or continuously, the catalyst-containing whole-cells can be reproduced

inside of the reactor allowing for a theoretically infinite process without the need for catalyst preparation. The presented concepts are summarized in Figure 6.7.

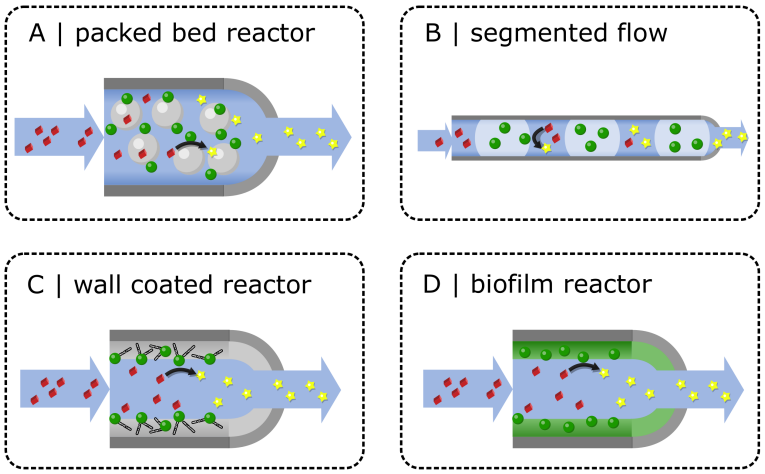

Figure 6.7: Overview of commonly applied reactor concepts for continuous whole-cell catalysis (adapted from Adebar *et al.*[207]). Green sphere, catalyst; red cube, substrate; yellow star, product.

Multi-step Flow Processes

As mentioned earlier, one major advantage of flow chemistry over batch processes is the possibility to combine multiple steps into one process.[220–223] With this strategy, labile intermediate products can be directly processed without the need for storage and tedious isolation. Moreover, incompatible reaction cascades can be realized. But not only the synthesis can be carried out continuously: Recently, the continuous manufacturing of multiple drugs in a compact, reconfigurable system starting from raw chemicals, and finishing with the drug in a tablet formulation, was reported.[224,225] This renders flow chemistry an ideal partner for other continuous manufacturing steps. A schematic comparison of multi-step batch and flow chemistry is shown in Figure 6.8. Flow chemistry enables several reaction steps within one continuous process without the need for separate operation steps. Thus, workforce and downtimes can be reduced, allowing a more economical production.

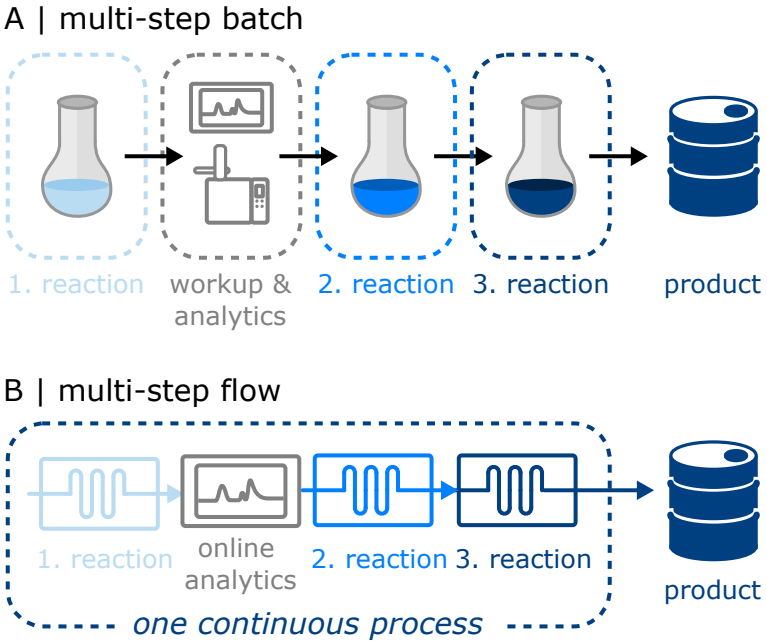

Figure 6.8: Schematic overview of multi-step batch vs. flow chemistry with one exemplary intermediate workup/analytics step.

Through a combination of bio- and chemocatalysis, highly efficient and sustainable syntheses have been realized in the past years.[226–228] Examples can be found in the combination of metal-catalyzed cross-coupling and enzymatic reduction by Burda *et al.*, and the combination of photo- and enzymatic catalysis by the groups of Zhao and Hartwig.[229,230]

This fruitful fusion can be realized in flow processes as well, as they offer new means for combining these often incompatible catalytic worlds.[216] One, rather classic, example is the dynamic kinetic resolution in continuous flow. Here, biocatalysts for the resolution are frequently combined with chemocatalysts for racemization. But also other reaction concepts have been reported—like the combination of a phenolic acid decarboxylase with a Pd-catalyzed cross-coupling by Grabner *et al.*[231] Moreover, Döbber *et al.* developed a process for epoxide formation based on the combination of an alcohol dehydrogenase with a subsequent basic epoxidation.[232] Furthermore, continuous multi-enzyme cascades have become popular over the last years.[233–239]

6.2 Concept

The aim of this project is the development of a continuous process for the synthesis of aliphatic nitriles starting from renewable feedstocks. A previously described[163] multi-step batch process for the synthesis of octanenitrile will be transferred into a flow process (Figure 6.9). Beginning from the aliphatic alcohol, which can be obtained from renewable fatty acids, an aldehyde will be generated by organo-catalyzed oxidation. Subsequently, the intermediate product will be converted into the corresponding aldoxime to finally yield the desired nitrile in a biocatalytic step.

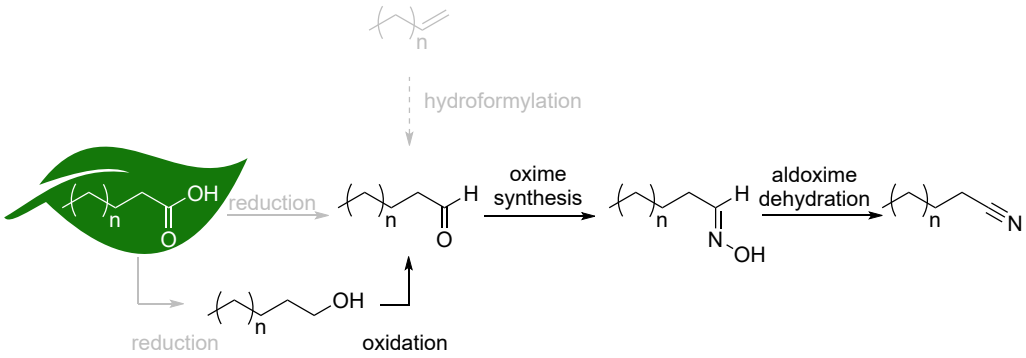

Figure 6.9: Reaction sequence for the synthesis of aliphatic nitriles starting from either renewable fatty acids or alkenes *via* hydroformylation.

To accomplish this goal, the separate reactions will be individually brought into continuous processes and optimized. The optimization will be achieved using the previously described closed-loop system. Finally, the processes will be combined in a multi-step flow process.

Along the way, different approaches to continuous whole-cell catalysis will be investigated and compared. A focus will be on process stability and reliability, which is crucial, in particular, for closed-loop optimization. While both microreactor technologies and biocatalysis are matured technologies in the synthesis of active pharmaceutical ingredients (APIs), in this work their applicability to bulk chemical preparation will be investigated.

6.3 Synthesis of Alkyl Nitriles from Renewables

6.3.1 TEMPO-catalyzed Oxidation

Theory & Concept Different protocols for the selective oxidation of alcohols to the corresponding aldehydes have been reported. Chromium salts have been frequently used in the past, but alternatives were needed due to their high toxicity.[240] Moreover, the Swern oxidation is commonly applied; however, due to unfavorable reaction conditions not ideal.[241] Only recently, this reaction could be performed at room temperature in a continuous flow reaction.[242]

A powerful and cost-effective alternative was found in the TEMPO-catalyzed oxidation using simple oxidants. TEMPO (2,2,6,6-tetramethylpiperidin-1-yl)oxyl) is a stable nitroxyl radical, which is accessible from ammonia and acetone.[243] Today, the Anelli-type TEMPO-catalyzed oxidation using mild conditions of 0–15 °C and hypochlorite as an oxidant in a biphasic system is a popular protocol (Scheme 6.4).[244,245] Finding a generally applicable alternative solvent to the commonly used dichloromethane is a remaining challenge to render this process sustainable.[246]

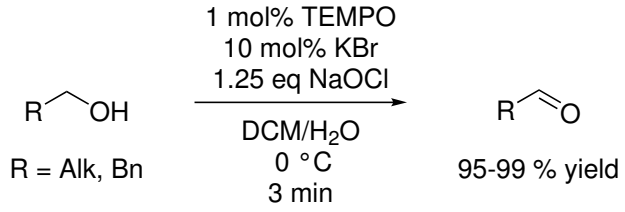

Scheme 6.4: Anelli-type TEMPO-catalyzed oxidation of primary alcohols to aldehydes at mild reaction conditions.[244] TEMPO, 2,2,6,6-tetramethylpiperidin-1-yl)oxyl; DCM, dichloromethane.

The catalytic cycle of the TEMPO-catalyzed oxidation of primary alcohols to aldehydes under acidic or neutral conditions begins with a single electron transfer (SET) of the nitroxyl radical **A1** to a secondary oxidant (e.g. NaOCl).[247] The generated oxoammonium species **A2** reacts with the alcohol **B** in a concerned, but asynchronous oxidation *via* the transition state **A3**. Firstly, a hydride is transferred from the alcohol **B** to the electrophilic oxygen atom of **A2**. Then, a proton is transferred from the alcohol to the now basic nitrogen atom of **A3** to form the hydroxylammonium **A4** under

release of the desired product **C**. This can be reoxidized to regenerate the active catalyst **A2**. Hamlin *et al.* suggested this mechanism based on theoretical and experimental data.[247] In Scheme 6.5, a simplified version of the mechanism is shown.

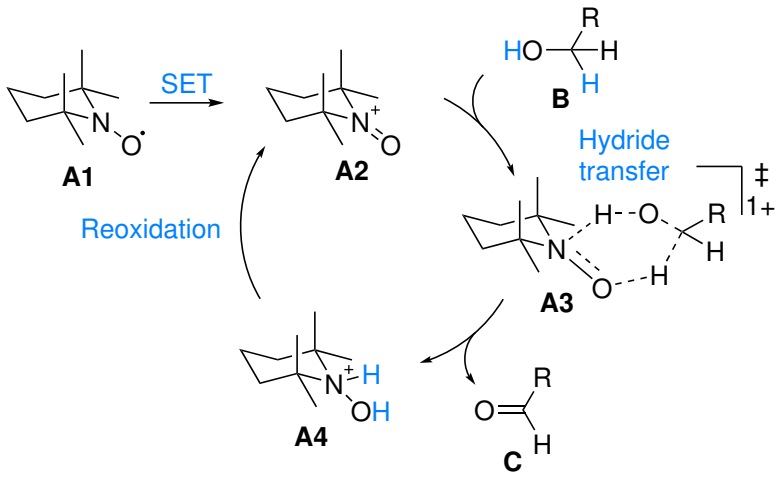

Scheme 6.5: Simplified mechanism of the TEMPO-catalyzed oxidation of primary alcohols to aldehydes under acidic or neutral conditions as suggested by Hamlin *et al.*[247] SET, single electron transfer; R, alkyl, benzyl.

The Anelli-type oxidation is already known as a continuous process: The group of McQuade performed the reaction using immobilized TEMPO in a packed bed reactor.[181] High stability of the catalyst-bed was found by the authors, enabling recycling of the system. Leduc and Jamison reported on a biphasic system using cheap bleach as an oxidant, which provided complete conversion of a wide range of alcohols within 5–30 min residence time.[248] To precisely adjust the pH of the hypochlorite solution inline, Vanoye *et al.* introduced a carbon dioxide steam.[249]

Greene *et al.* developed a system with Cu(I) as co-catalyst using oxygen as an oxidant with a short residence time of only 5 min.[250] Moreover, hypervalent iodine can act as an oxidant, as reported by the group of Wirth.[251] Yet another oxidant was used by Hill-Cousins *et al.* for the development of a general procedure: Electrons from a microfluidic electrolytic cell.[252]

Results & Discussion Being the first reaction in the three-step synthesis of nitriles, the TEMPO-catalyzed oxidation of 1-octanol (**12**) to octanal (**13**) was investigated with regard to its suitability in a self-optimized multistep flow process. As both, organic reagents and inorganic salts are used

in the reaction, a liquid-liquid segmented flow system was chosen. Sodium hypochlorite proved to be a suitable oxidant in previous studies by Hinzmann *et al.*[246] In their study, also an alternative to the commonly used solvent dichloromethane (DCM) was found in alkyl nitriles. Based on a well-established system of the catalyst TEMPO in dichloromethane and water, a flow process was developed. Parts of the experiments were carried out by Warkentin during his research internship.

For the continuous reaction, a two-channel syringe pump was connected *via* a Y-piece to a PFA coil reactor (0.5 mL, 0.8 mm ID). The reactor was tempered using a water bath. At the outlet, the reaction mixture was collected and quenched. To quench the reaction, initially, HCl solution was used. However, this produced octyl octanoate as an undesired side product. Thus, a different method based on a $Na_2S_2O_3$ solution was used and validated. An organic DCM solution containing the starting material **12** (overall concentration 0.76 M) and 0.25 mol% TEMPO was filled into one syringe, and an aqueous solution containing 1.1 eq. NaOCl and 5 mol% $NaHSO_4$ into the other. A schematic overview of the setup can be seen in the upper part of Figure 6.12. The syringe pump was switched on, and periodically the organic phase of the collecting vial was analyzed *via* GC. A fresh quenching vial was attached after the analytics. The reaction was carried out at 0 °C for a residence time of 30 min.

Especially, high NaOCl concentrations have shown to be challenging, as the hypochlorite quickly decomposes and produces chlorine gas. Using bleach (13% aq. solution) instead of higher concentrated hypochlorite solution improved the stability somewhat; however, a minor gas formation was still observed in the syringe (Figure 6.10).

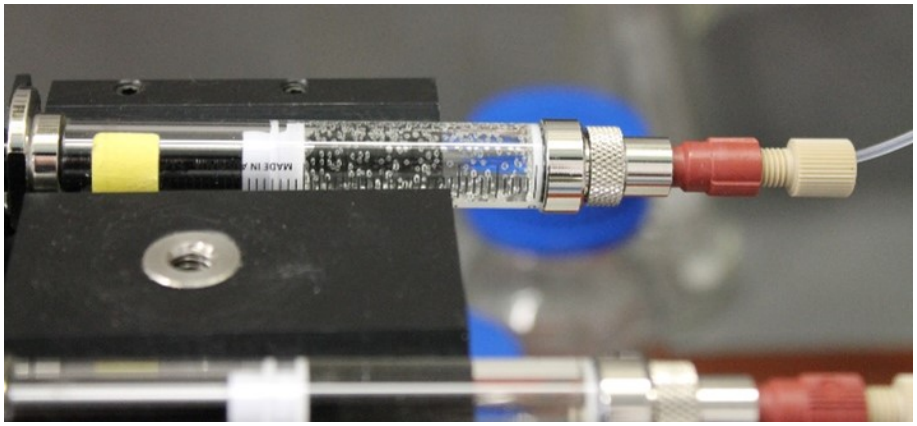

Figure 6.10: Gas formation by decomposition of aqueous NaOCl solution in a syringe.

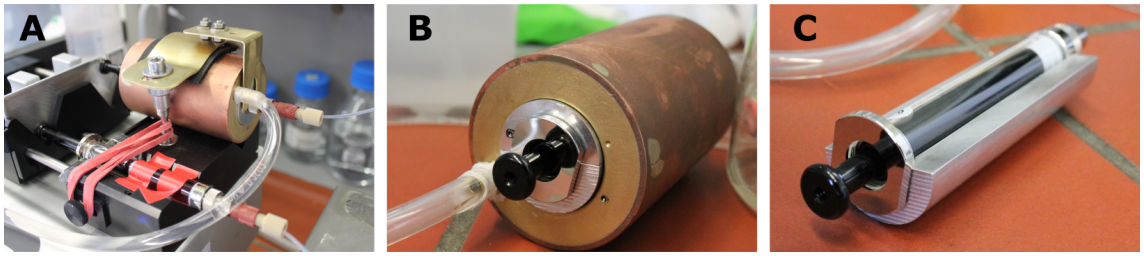

Figure 6.11: Developed syringe chiller. A: Chiller mounted on a syringe pump with cooling water supply; B: syringe and syringe mounting inside a hollow brass cylinder; C: syringe and one half of the aluminium mounting.

The decomposition of the oxidant also affected the product formation, as lower conversion was observed over the time of the process (Figure 6.12). To avoid this issue, a syringe chiller was developed and attached to the syringe pump to avoid decomposition (Figure 6.11). The chiller consisted of a hollow brass cylinder with an aluminium mounting for the syringe. A peristaltic pump was used to pump water (0 °C) through the chiller. Alternatively, a recirculating chiller with *iso*-propanol was used. By applying the syringe chiller, a much more stable reaction could be realized (Figure 6.12).

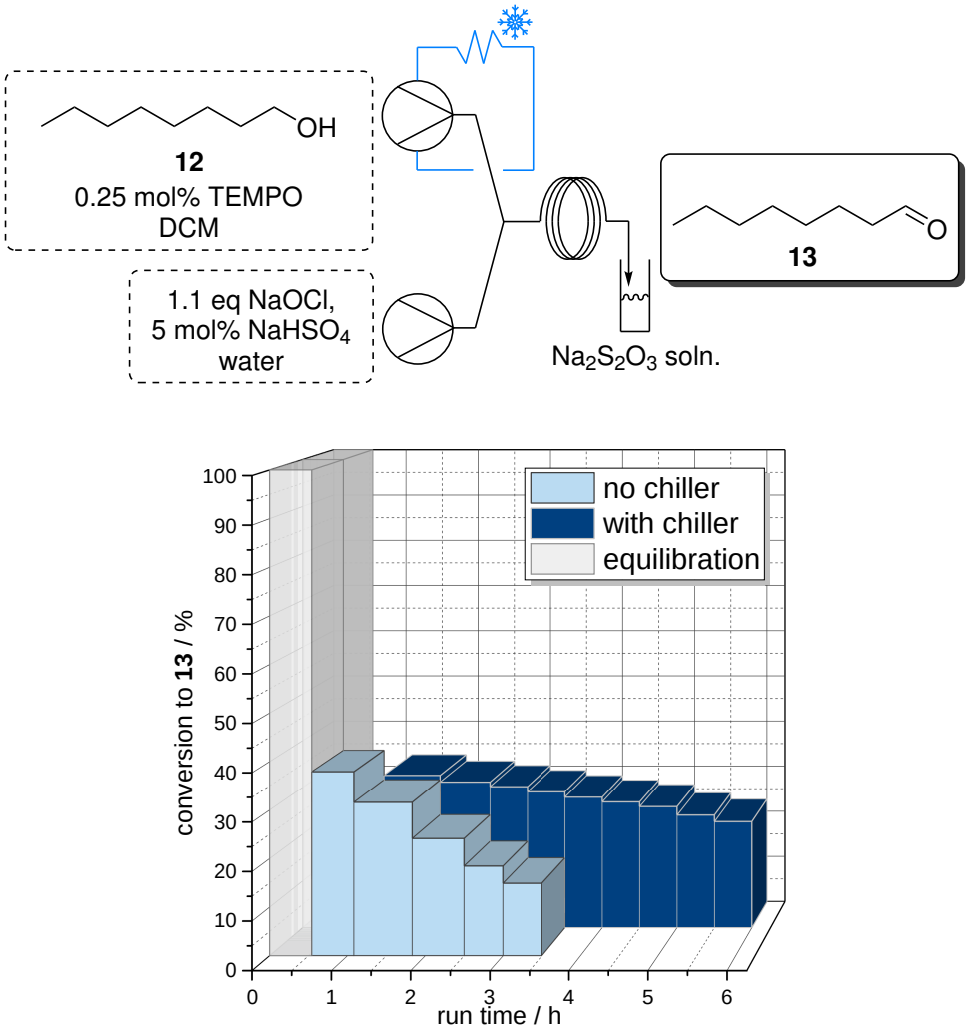

Figure 6.12: Schematic setup (upper part) and results for the conversion to octanal (**13**) of the TEMPO-catalyzed oxidation of 1-octanol (**12**) using a DCM/aqueous segmented flow system with or without syringe chiller (at 0 °C). Residence time = 30 min, temperature = 0 °C, overall concentration starting material = 0.76 M. DCM, dichloromethane; TEMPO, 2,2,6,6-tetramethylpiperidin-1-yl)oxyl.

Furthermore, experiments revealed the need for freshly prepared hypochlorite solution to ensure correct concentrations. Using fresh NaOCl solution (1.1 eq), even with half of the residence time, the conversion to the desired product **13** could be improved to an average of 87% (Figure 6.13).

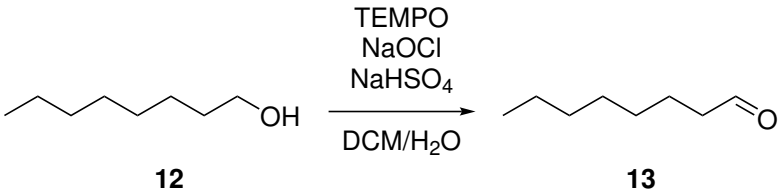

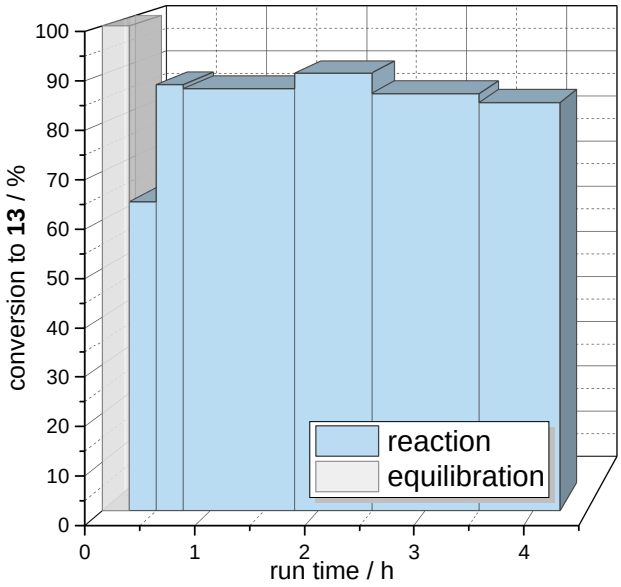

Figure 6.13: Schematic reaction (upper part) and results for the conversion to octanal (**13**) of the TEMPO-catalyzed oxidation of 1-octanol (**12**) using a DCM/aqueous segmented flow system with syringe chiller (at 0 °C) and freshly prepared NaOCl solution. Residence time = 15 min, temperature = 0 °C, overall concentration starting material = 0.76 M. DCM, dichloromethane; TEMPO, 2,2,6,6-tetramethylpiperidin-1-yl)oxyl.

In conclusion, two aspects have shown to be crucial for a reliable and stable continuous process. Firstly, the oxidant solution must be chilled in the reservoir to avoid decomposition. An in-house developed syringe chiller has proven to be a suitable tool in this context. Alternatively, a continuous pump, such as a HPLC pump or a peristaltic pump could be used to draw the solution from a chilled reservoir. This method would reduce the complexity of the setup; however, rather high flow rates (ideally $>0.1\,\mathrm{mL}\cdot\mathrm{min}^{-1}$) would be required to ensure a uniform segmented flow. Besides this, the NaOCl solution must be freshly prepared, as it readily decomposes, even when stored at lower temperature (8 °C). This gas formation and the change of the oxidant concentration destabilized the process. Thus, for further experiments towards self-optimized processes, these aspects are important to consider in the experimental setup. Nevertheless, the process seems to be suitable for a multi-step flow process.

6.3.2 Oxime Synthesis

Theory & Concept Analog to the previously described oxidation, a continuous process for the oximation of the product **13** from the TEMPO-catalyzed oxidation of 1-octanol (**12**) will be developed. Using commercial octanal (**13**), a segmented flow process for the condensation with hydroxylamine to yield octanal oxime (**14**) will be applied. Again, this work is based on previous batch investigations by Hinzmann *et al.*[163] As this reaction is known to be very robust, fast, and clean, it represents the ideal synthesis to test the self-optimizing platform. In the following three paragraphs, the implementation of a continuous flow system for the reaction, its manual algorithm-assisted optimization, and finally a fully automated closed-loop optimization are described. This step-wise procedure will be carried out in parallel to the work towards the closed-loop system (Chapter 5) as a reliable and predictable standard reaction system for testing.

The reaction to form aldoximes is well known for many years.[253] By releasing water, the hydroxylamine reacts readily with a ketone or aldehyde to the oxime or aldoxime, respectively.

The condensation of hydroxylamine and an aldehyde or ketone proceeds *via* a sequential addition-elimination mechanism (Scheme 6.6).[69] Initially, the carbonyl compound is activated by a proton. The electrophilic carbonyl carbon atom is then attacked by the nucleophilic nitrogen atom of the hydroxylamine to form an adduct. After deprotonation of the nitrogen and protonation of the oxygen, water is eliminated in an E1 step. Finally, the product is generated by deprotonation of the hydroxyiminium species to give the aldoxime.

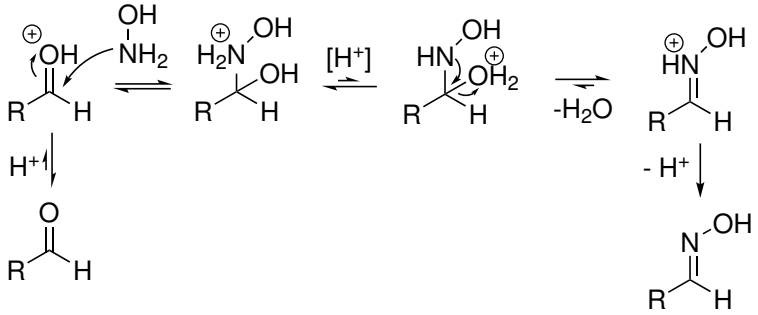

Scheme 6.6: Mechanism of the condensation of hydroxylamine and an aldehyde *via* addition-elemination.[69]

Results: Flow Reaction To find a suitable setup and process parameters, the reaction was initially carried out in flow mode without online analysis or algorithm-based optimization.

A similar setup compared to the previously described oxidation was used (Figure 6.14; upper part). On a two-channel syringe pump, two syringes with either organic solution containing the aldehyde **13** (overall concentration 50 mM) or aqueous solution containing hydroxylamine hydrochloride and sodium carbonate were mounted. The aqueous solution was prepared in a measuring flask and sonicated for 5–20 min to reduce gas bubbles. Both feeds were combined in a Y-mixer to give a segmented flow which was led into a PFA coil reactor (0.8 mm ID, 1 mL). The reaction mixture was then collected in a glass vial containing HCl solution for quenching. Previous validation of this quenching method showed only a low reactivity of 4% conversion to the oxime **14** within 30 min reaction time. Initially, a residence time of 30 min, a temperature of 30 °C, and an excess of 1.5 eq hydroxylamine hydrochloride along with 0.75 eq of sodium carbonate were chosen as reaction parameters.

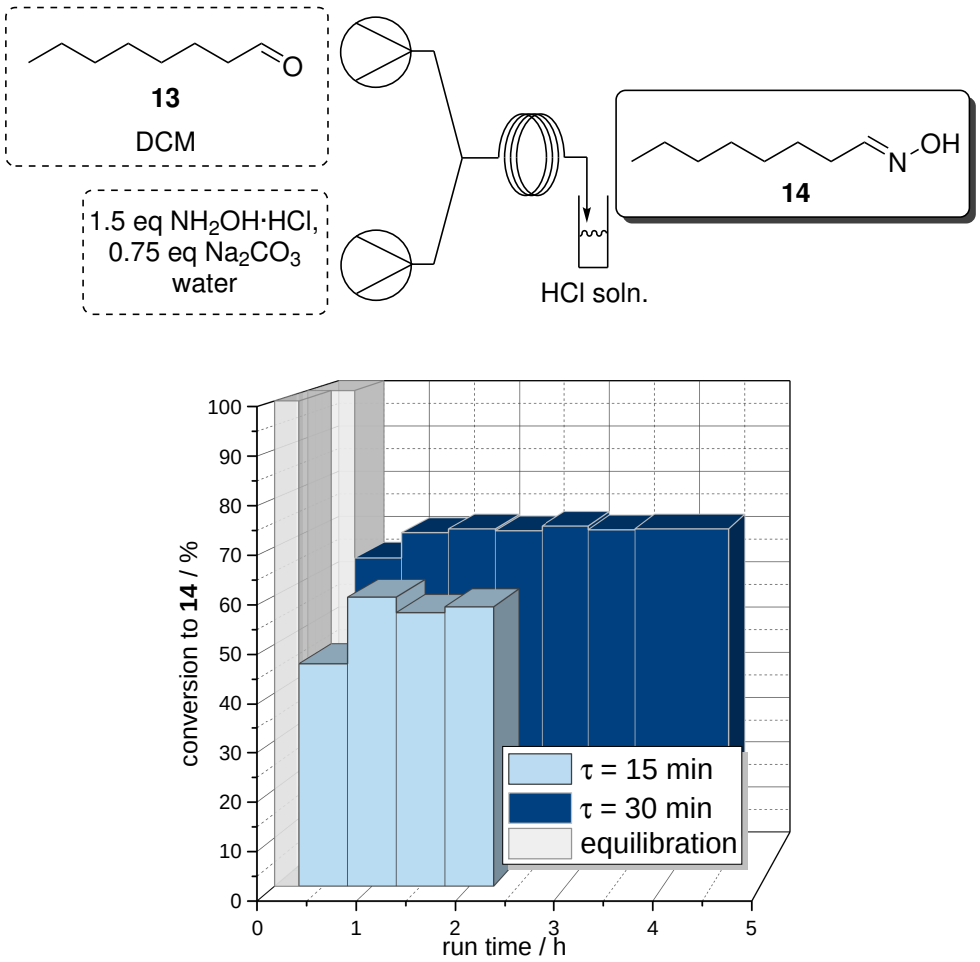

Figure 6.14: Schematic setup (upper part) and results for the conversion to octanal oxime (**14**) of the condensation of hydroxylamine and octanal (**13**) using a DCM/aqueous segmented flow system with different residence times. Temperature = 30 °C, overall concentration starting material = 50 mM. DCM, dichloromethane.

As shown in Figure 6.14, a very stable average conversion to oxime **14** of 70% could be achieved over an investigated period of 4.5 h. In the next experiment, a shorter residence time of 15 min was used. This led to an average conversion of 58% over an investigated period of 2.5 h. As expected, the longer residence time improves the conversion. Furthermore, octanenitrile (**15**) was investigated as solvent option (Figure 6.15). As DCM is not a suitable option for the following biocatalytic step, this solvent offers a viable option to combine both steps without a solvent switch. This solvent has already shown to be suitable for the entire reaction cascade from alcohol **12** to the nitrile **15**.[163] For the product isolation, no solvent must be removed and wasted, as the product from the cascade is at the same time the solvent.

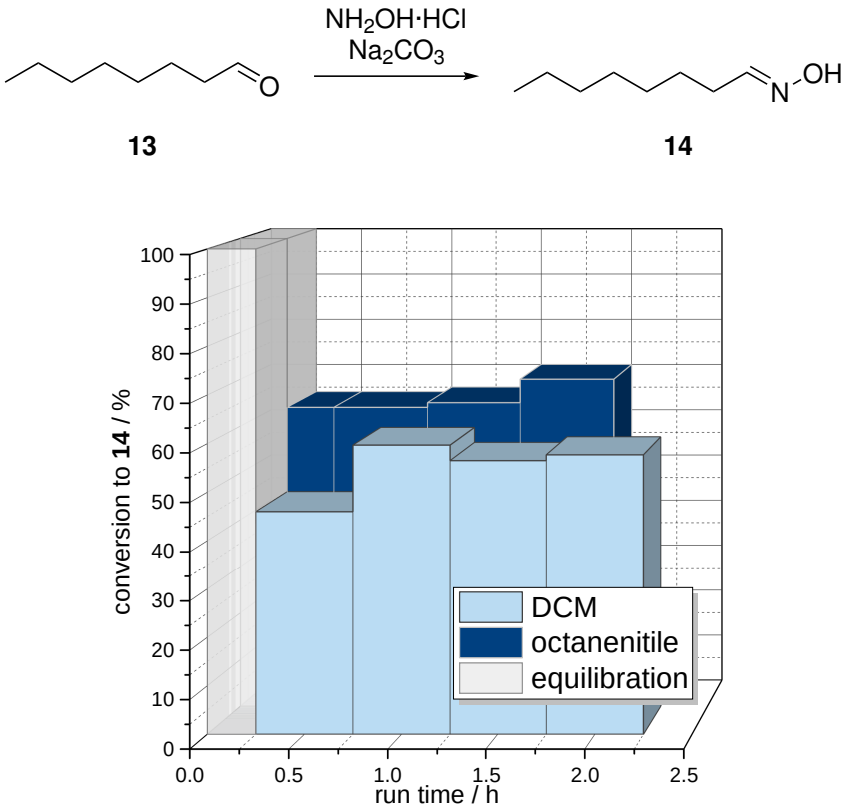

Figure 6.15: Schematic reaction (upper part) and results for the conversion to octanal oxime (**14**) of the condensation of hydroxylamine and octanal (**13**) using an aqueous/organic segmented flow system with either dichloromethane or octanenitrile (**15**) as solvent. Temperature = 30 °C, residence time = 15 min, overall concentration starting material = 50 mM. DCM; dichloromethane.

Compared to the equivalent process using dichloromethane, the average conversion to **14** was with 66% slightly higher (plus 8%) using octanenitrile (**15**) as solvent. Thus, a potential alternative to DCM was found and seemed to be suitable for the multi-step process. A drawback was the challenging GC-based analytics, as the peaks for the solvent might overlap the other compounds. For these reactions, a membrane separator was connected to the reactor tube. Thus, no quenching of the reaction solution was required. The organic feed was collected fractionated and analyzed with GC.

Different bases to replace sodium carbonate were investigated as well. As carbonates release CO_2 when protonated, bubbles were formed in the reservoir which can led to an unreliable feed. A short residence time of 12.8 min, a reaction temperature of 25 °C, and 1 eq of hydroxylamine was used for the tests.

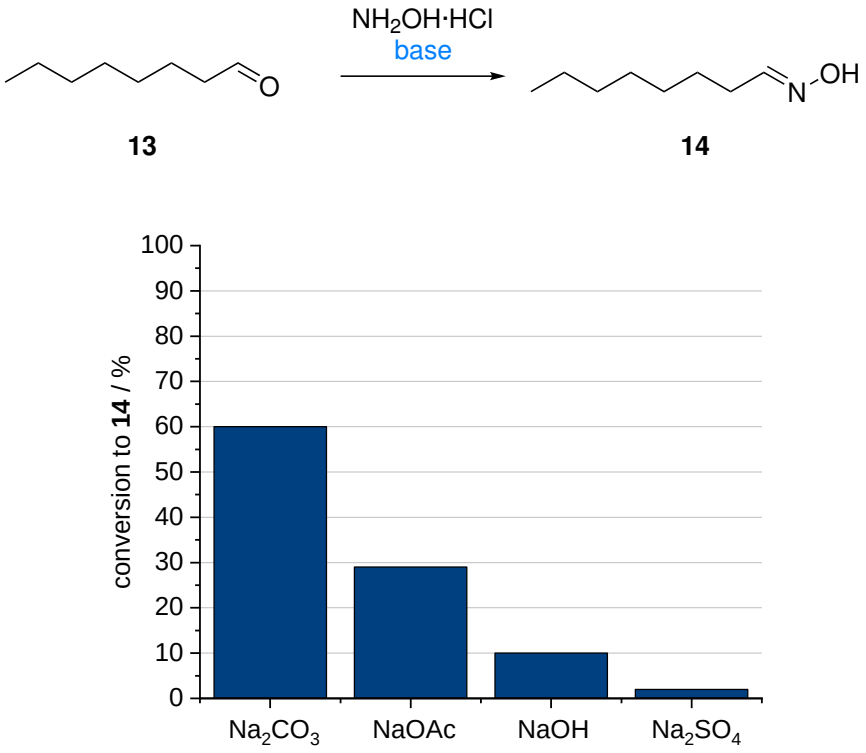

Figure 6.16: Schematic reaction (upper part) and results for the average conversion to octanal oxime (**14**) of the condensation of hydroxylamine and octanal (**13**) using a DCM/aqueous segmented flow system with different bases (1 eq). Temperature = 25 °C, residence time = 12.8 min, 0.99 eq hydroxylamine, overall concentration starting material = 50 mM. DCM, dichloromethane.

While sodium carbonate provided a conversion to the desired oxime **14** of 60%, the other bases did not even reach half of this conversion (Figure 6.16). The best alternative base was sodium acetate, which showed a conversion to **14** of 29%. Thus, no suitable alternative base was found. To cope with the gas formation using the carbonate, the aqueous solution was sonicated to remove the dissolved gas and bubbles. This procedure worked well enough to provide a stable flow of aqueous solution from the syringe pump for a range over at least several hours.

Results: Manual Algorithm-assisted Optimization After the continuous reaction was established, the setup remained widely unchanged. A membrane separator was used for the reactions instead of a quenching method. This approach improved the reliability of the results and was suitable for closed-loop optimization. These manual experiments were carried out to investigate the algorithm and modify it for an application in a closed-loop

system. The experiments were carried out by Marquardt during his research internship.

For the optimization, a Nelder-Mead algorithm was used (Section 5.3.1). A local implementation of the program was used to calculate the reaction conditions (Section 5.4.1). Three numeric continuous parameters were used for the optimization. First, the reaction temperature in a range of 20–40 °C, second, the residence time from 2–30 min, and lastly, the equivalents of hydroxylamine from 0.9–1.25 eq. As base and hydroxylamine concentration are coupled parameters, the equivalents of the base were controlled in dependency of the hydroxylamine in a range of 0.45–0.63 eq. To improve the membrane separator's performance, a back pressure regulator (BPR) with 0.34 bar was attached to the aqueous outlet. Later results showed that also a short, narrow PFA tube (0.25 mm ID, 30 cm length) could be used, as the BPR did not always provide reliable results. Highly important was the wetting of the hydrophobic membrane with an organic solvent prior to application.

The parameters for the four initial experiments were calculated by the algorithm, and the system was set up manually. For each reaction, a fresh solution was prepared. The initial experiments showed a conversion to octanal oxime (**14**) of 38–64%.

The results of the experiments are summarized in a smoothed surface plot (Figure 6.17), while the raw data can be found in the experimental Section 6.5.5.2. In total, 13 experiments were carried out to give an impression of the optimization algorithm.

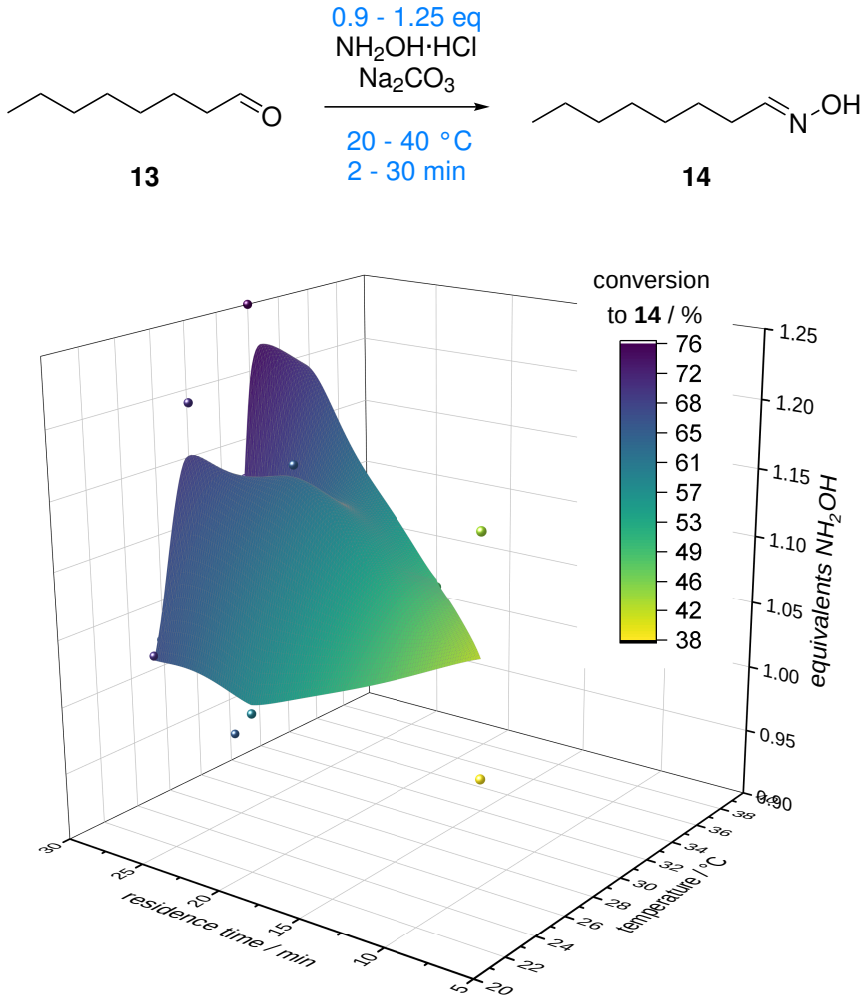

Figure 6.17: Schematic reaction (upper part) and smoothed surface plot for the algorithm-assisted optimization of the conversion to octanal oxime (**14**) of the condensation of hydroxylamine and octanal (**13**) using a DCM/aqueous segmented flow system. Single datapoints are shown as colored spheres. Temperature = 20–40 °C, residence time = 2–30 min, 0.9–1.25 eq hydroxylamine, overall concentration starting material = 50 mM. Surface plotting parameters in OriginPro, soothing: Factor to increase total the number of points = 10 000, parameter for tge smoothing = 0. DCM, dichloromethane.

The best results were obtained in the 13th experiment (9th optimization iteration; Figure 6.17). In general, the algorithm tended towards the maximum of all parameters (temperature, equivalents hydroxylamine, and residence time). This behavior within the defined chemical space was expected from previous experience with the reaction system and is plausible from a chemical standpoint. From the average conversion to the oxime **14** of the initial experiments (48%), an improvement of 28% within 9 experiments was gained.

During the optimization, repeatedly the limits of the chemical space were reached (Figure 6.18).

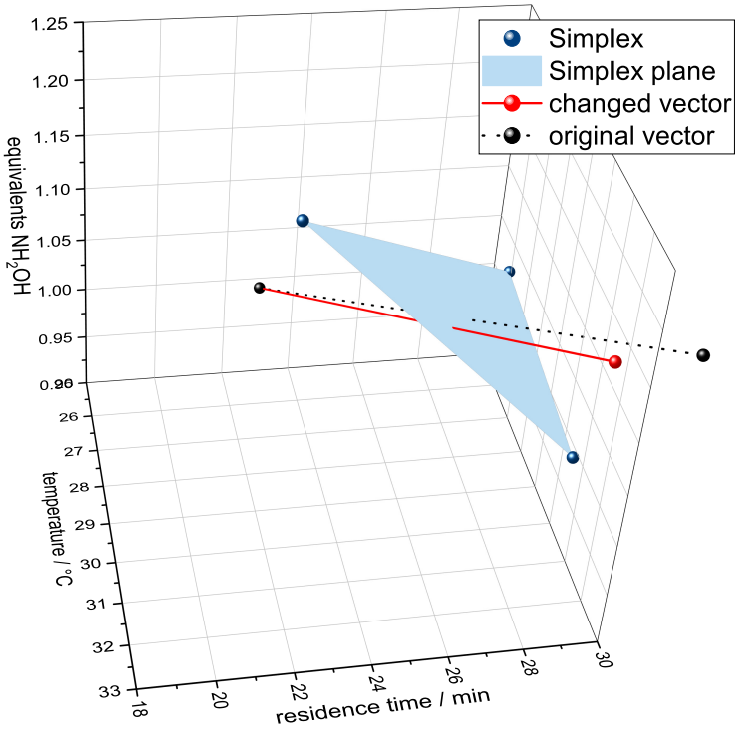

Figure 6.18: Exemplary data for a parameter limit (maximum residence time of 30 min) during the Nelder-Mead optimization. Blue dots: experiments spanning the blue plane; black dots: experiments for the reflection through the plane; black dotted line: original vector calculated by the algorithm; red line: modified vector by resetting the maximum parameter (residence time).

The algorithm has been programmed to set the parameter to the maximum allowed value when a limit was reached. For example, if the algorithm suggested based on the reflection a residence time of 32 min, an additional check for the limits (2–30 min) set back the residence time to the limit of 30 min. However, as the Nelder-Mead simplex is based purely on geometry, this might affect its performance, as the vector is changed. An alternative approach would be to limit the length of the optimization vector instead, to preserve the geometry. Both cases are in particular for an extension (Section 5.3.1) of the vector critical.

Automated Closed-loop Optimization After the reaction was established and the remote closed-loop optimization software (Section 5.4.2) was developed, the octanal oxime (**14**) synthesis was optimized automatically. Simi-

lar reaction conditions as in the previous experiments were used. To ensure compatibility in a future multistep flow process, the solvent was changed to dimethyl carbonate (DMC). Since this solvent is also compatible with the subsequent biocatalytic nitrile formation, no solvent switch within the process is required.

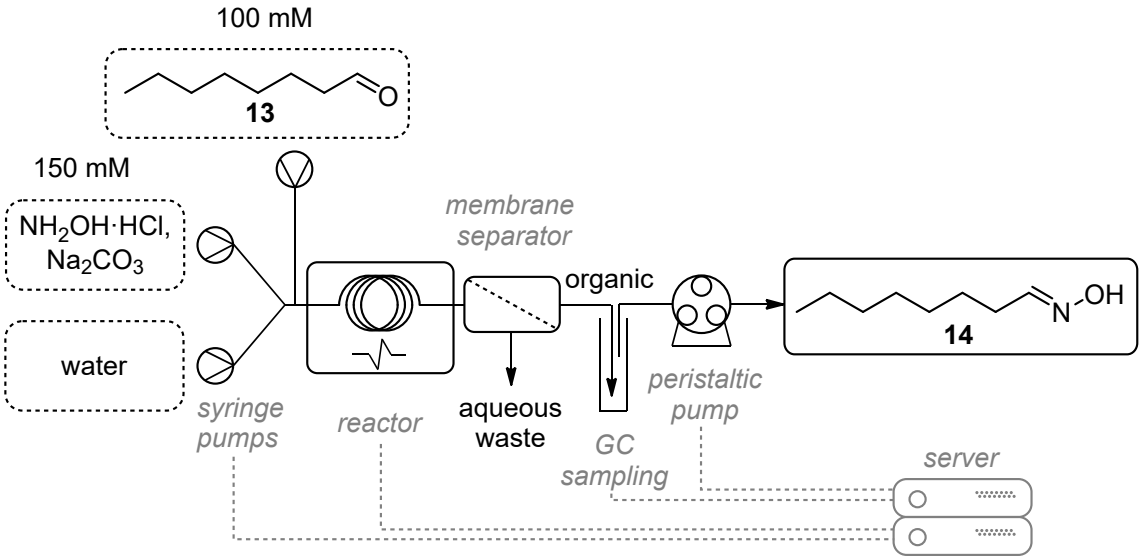

Figure 6.19: Schematic setup of the closed-loop optimized synthesis of octanal oxime (**14**) starting from octanal (**13**).

The setup was similar to the previous paragraph (Figure 6.19). One two-channel syringe pump was connected *via* USB, while the other was connected *via* the RS-232 port and a serial-to-USB converter. This was done to allow for unique identification of the devices. One syringe (25 mL) containing aqueous hydroxylamine (150 mM) and sodium carbonate (75 mM), and a dilution feed with water (25 mL) were combined in a Y-piece. The remaining port of the Y-piece was connected to another T-piece, which was connected to the organic feed (25 mL) containing octanal (100 mM) in dimethyl carbonate. Finally, the reactor was connected to the T-piece as well.

The previously described four-unit reactor (Section 5.5.1.1) was used to control the temperature the 1 mL coil reactor (PFA, 0.8 mm ID). A membrane separator equipped with a hydrophobic membrane was used to separate the biphasic system. The inline sampling GC vial described in Section 5.5.3 was connected to the organic stream of the separator and to a peristaltic pump. The peristaltic pump outlet was led into a glass flask for waste collection.

All devices were connected to the server and set up according to Paragraph 5.4.2. As the optimization function, the conversion to the desired oxime **14** was selected. Optimization parameters were temperature (15–45 °C), hydroxylamine concentration (75–150 mM), and residence time (0.5–5 min). The reactor volume (1 mL), the phase ratio (50% organic) and the aldehyde concentration (100 mM) were set as constant parameters.

Then, the optimization was started from the user interface. The reaction was successfully optimized to 94% within 8 optimization iterations starting from the worst initial experiment of only 68% (Figure 6.20). The optimization completed in 6 h.

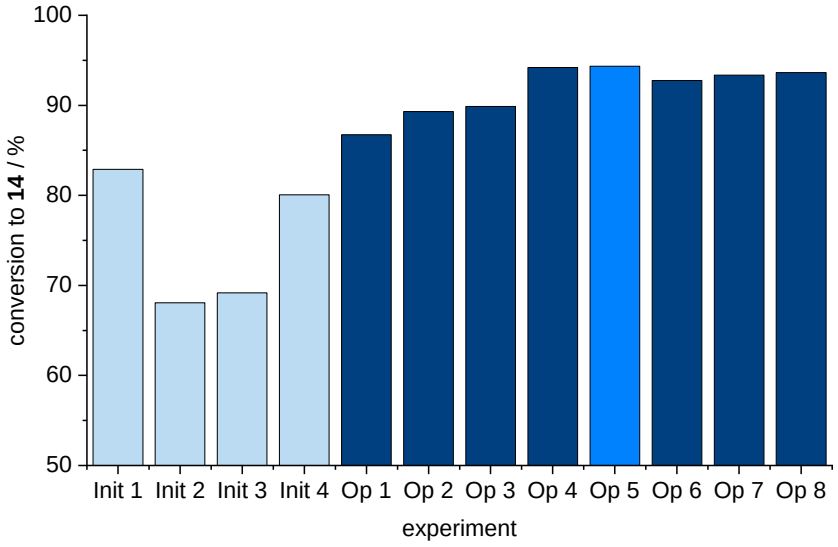

Figure 6.20: Results of the closed-loop optimized synthesis of octanal oxime (**14**) from octanal (**13**). The best experiment (Op 5) is highlighted. Light blue or Init, initial experiments; darker blue or Op, optimization runs.

After the initial four experiments were completed, a reflection was carried out yielding the best result so far. Thus, an expansion was the next step (Figure 6.21).

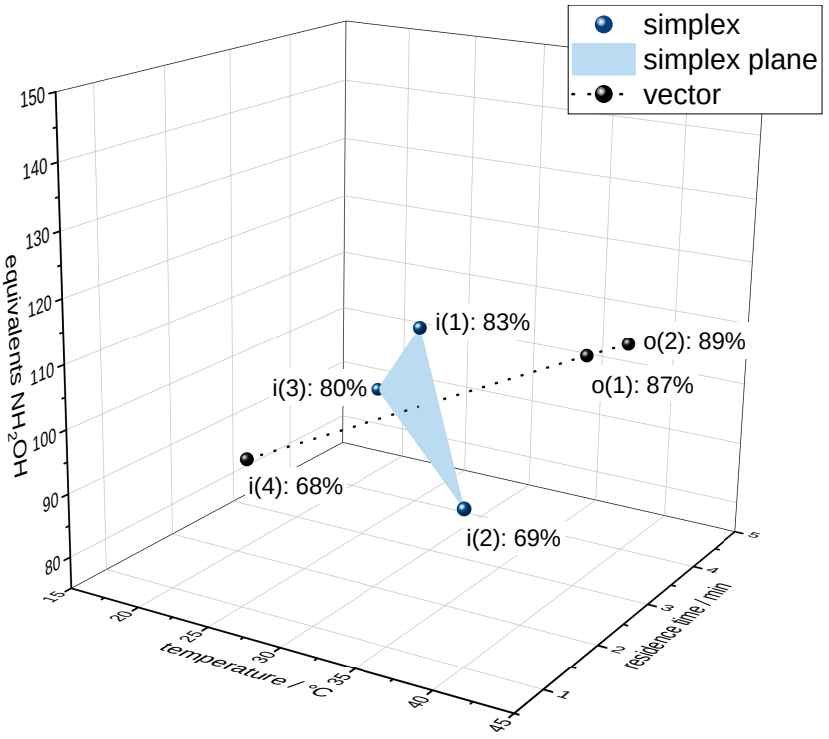

Figure 6.21: Conversion to **14** of the closed-loop optimized synthesis of octanal oxime (**14**) from octanal (**13**) for the first (reflection) and second (expansion) optimization iterations. i(x), initial experiments; o(x), optimization runs.

Two further reflection operations resulted in the best experiment in this optimization run. A conversion to **14** of 94% was reached using a reaction temperature of 23.8 °C, a maximized residence time of 5 min, and a hydroxylamine concentration of 115.6 mM. Afterwards, the algorithm explored higher concentrations and different temperatures. However, within the margin of error, the results were very similar with 93–94% conversion to the desired product **14**.

6.3.3 Biocatalyzed Oxime Dehydration

The reaction sequence to sustainable nitriles is completed by a bio-catalyzed oxime dehydration. In literature, this reaction is already well described.[162] Recently, also a continuous application using superabsorber-immobilized *E. coli* containing OxdB in a packed bed reactor was described.[165] In the past, not only packed bed reactors but also plug-flow systems or wall-coated reactors have been used extensively for flow biocatalysis. However, as packed bed reactors tend to lose activity over time, alternatives will be investigated

in this work. To avoid loss of activity, which especially in a self-optimizing system might cause troubles, a system where fresh catalyst is continuously provided is desired. Instable catalysts won't allow for the isolation of effects of changed parameters, as the catalyst activity changes over time. If that loss would be linear, it is theoretically possible to include the degradation into the optimization algorithm. However, the degradation is certainly depending on many factors like temperature and operation time, which are changed during the optimization procedure. This makes the implementation of such a 'correction factor' extremely challenging.

Segmented flow systems have shown to be particularly suited for this challenge of fresh catalyst supply. The catalyst is introduced with an aqueous buffer stream and can be easily removed by continuous phase separation after the reaction is completed. This system has shown to be suitable for ADH-catalyzed reductions, where mass transfer could be enhanced[209] and the downstream process simplified.[208] Based on these results, two segmented flow systems for whole-cell catalysis will be developed in this work. First, a system based on superabsorber-immobilized whole-cells will be developed. Then, another system without immobilization will be investigated. This system was further analyzed by studies of two reactions conducted by Nastke and Löwe.[169]

6.3.3.1 Fluid Heterogeneous Catalysis in Segmented Flow

Introduction & Concept Since a multi-step flow process heavily relies on the connection of reaction steps, preferably without change of the solvent system, an option to run the bio-catalysed reaction in organic or biphasic solvent systems is needed. However, the application of whole-cell catalysts in organic media has shown to be a major challenge in biocatalytic process design.

In this work, an apparently impossible system exploiting whole-cell catalyst stabilization by hydrogel immobilization combined with continuous catalyst supply will be developed (Figure 6.22). Instead of using the superabsorber as granulate loaded into a packed bed reactor, it will be ground into a fine powder. After absorption of an aqueous buffer system containing whole-cells, a fluid catalyst formulation will be obtained. This viscous catalytic gel will then be applied in a segmented flow system. Previously, this system

was described in more detail for isolated enzymes.[103] Based on the literature, in this work, a continuous process for the OxdB-catalyzed dehydration of octanal oxime (**14**) will be developed.

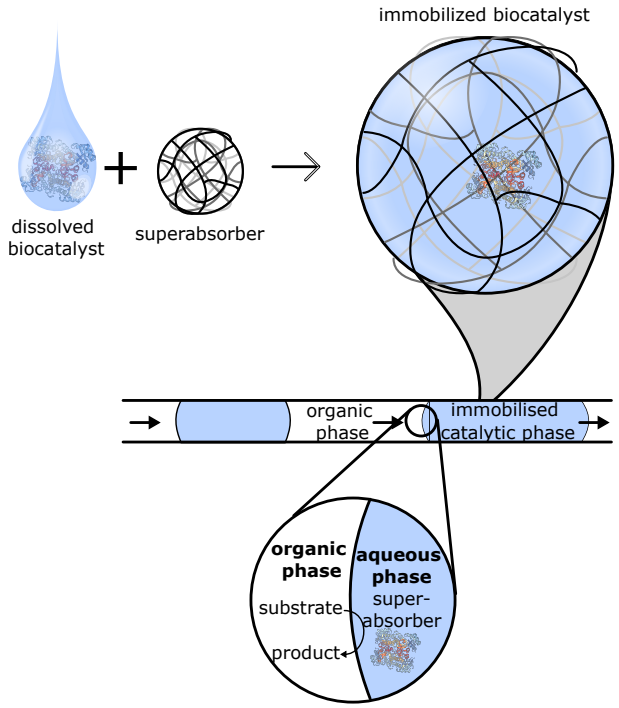

Figure 6.22: Illustration of the superabsorber/organic segmented flow system with immobilized enzyme (from Adebar *et al.*[254]).

In this study, catalyst recycling will not be investigated as process stability was the crucial aspect of a telescoped self-optimized process. Potentially, this recycling could be accomplished by separating and recycling the catalyst-containing aqueous phase into the process.

Results & Discussion The catalytic hydrogel was prepared by absorption of a PPB-buffered aqueous suspension containing wet whole-cells with overexpressed OxdB. Powdered superabsorber ($< 100\,\mu$m, $20\,\mathrm{mg \cdot mL^{-1}}$) was added to the aqueous suspension and vigorously stirred for one minute. This hydrogel was transferred into a syringe and connected to a Y-mixer (1 mm ID). A syringe containing octanal oxime (**14**) dissolved in cyclohexane was also connected to the mixer. Both syringes were mounted on a syringe pump. A tubular reactor (PFA, 0.8 mm ID) was connected to the remaining port of the Y-mixer and led into a stirred vial containing HCl-solution to quench the reaction. The quenching was previously validated to terminate the reaction. For GC analysis, multiple fractions were collected in

quenching vials, the phases were separated, and the organic crude product solution was analyzed *via* GC. The reactor coil was tempered using a water bath to 30 °C. An illustration of the reaction setup is shown in the upper part of Figure 6.24.

In a first run, a residence time of 30 min along with a catalyst loading of $33\,mg_{wcm} \cdot mL^{-1}$ was used. An average conversion of 54% with a very low average absolute deviation of 0.9% was obtained considering the data after 1.5 h (2 residence times equilibration). The low deviation indicates a very stable process. Despite its gel-like consistency, the catalyst formulation could form relatively uniform segments (Figure 6.23).

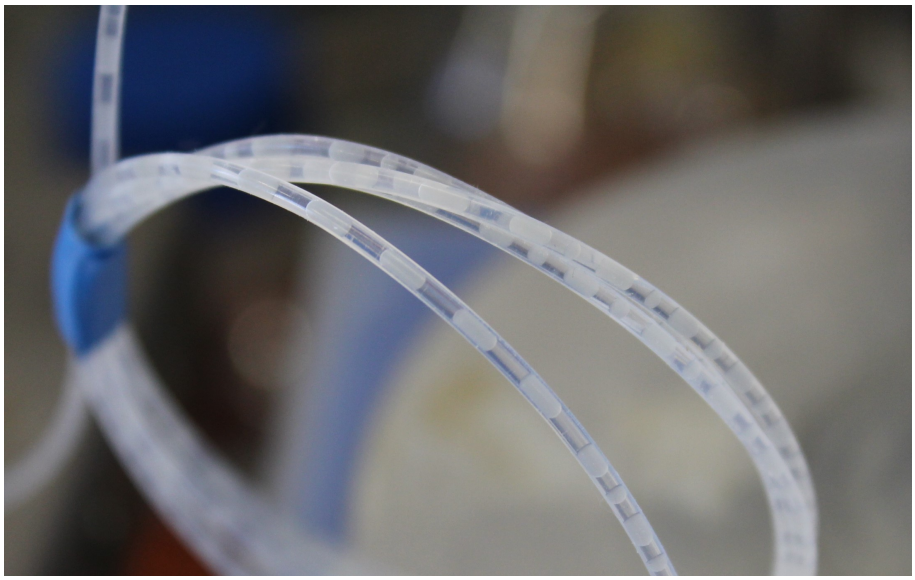

Figure 6.23: Segments of superabsorber/cyclohexane segmented flow system.

After this initial success, and to prove the system's general applicability for high performant biocatalytic systems, the process was further optimized. The superabsorber was ground finer ($< 80\,\mu m$ *vs.* $< 100\,\mu m$) and a wider tube diameter (1 mm) was used. Furthermore, the catalyst loading was increased to $250\,mg_{wcm} \cdot mL^{-1}$. Using the optimized conditions, an average conversion of 90% was obtained (Figure 6.24).

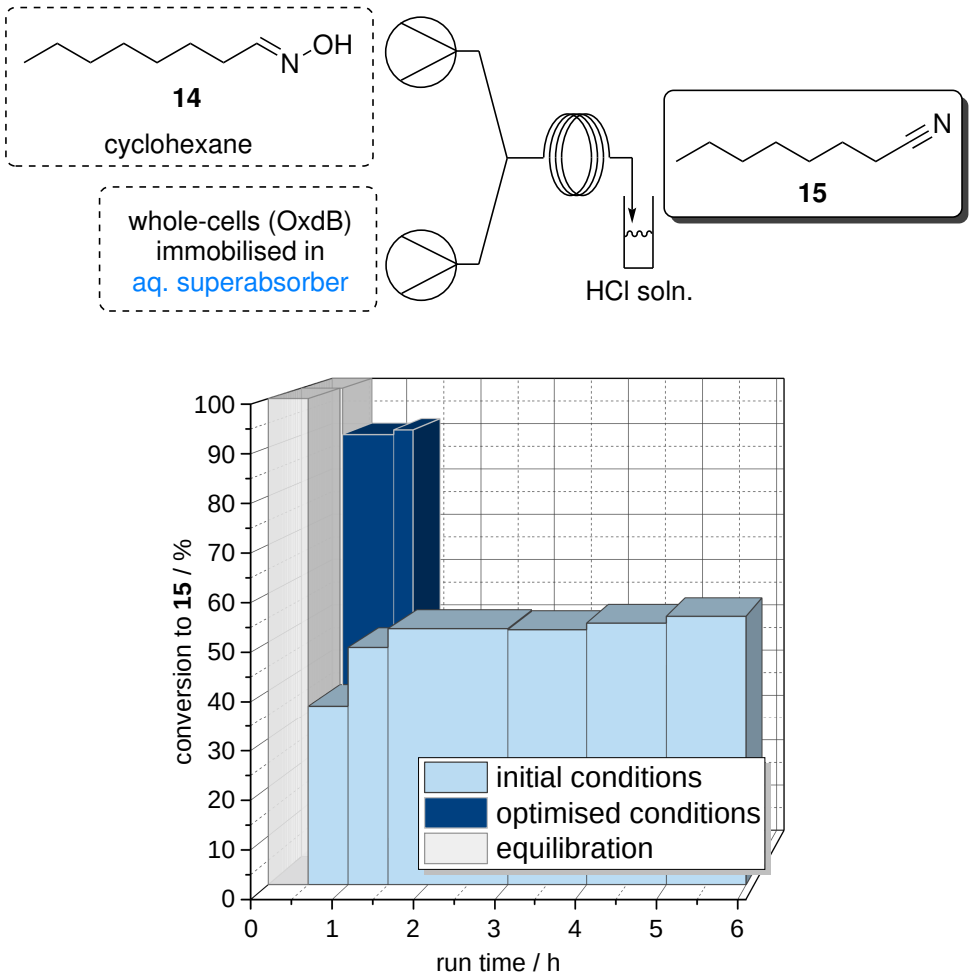

Figure 6.24: Schematic setup (upper part) and results for the conversion to octanenitrile (**15**) of the OxdB-catalyzed dehydration of octanal oxime (**14**) using a superabsorber/organic segmented flow system. Residence time = 30 min, temperature = 30 °C, cat. loading 33 $mg_{wcm} \cdot mL^{-1}$ and for optimized process = 250 $mg_{wcm} \cdot mL^{-1}$, overall concentration starting material = 50 mM. OxdB, aldoxime dehydratase from *Bacillus* sp.

Based on the average conversion, the volumetric productivity was calculated. For the initial process 7.6 $g \cdot h^{-1} \cdot L^{-1}$ was achieved, while the optimization offered a 70% higher productivity of 12.9 $g \cdot h^{-1} \cdot L^{-1}$. The catalyst productivity in product mass per catalyst mass was calculated as 0.16 $g_{prod} \cdot g_{cat}^{-1}$ for the reaction with lower catalyst loading.

For product isolation, the phases can be easily separated by gravity. No emulsification or precipitation was observed. However, continuous extraction using a membrane separator would be challenging, as the hydrogel probably blocks the membrane.

After the principle of superabsorber-immobilized segmented flow was already shown to be applicable for enzyme-catalysis[103], in this work it could be successfully extended to whole-cell catalysis. This concept potentially broadens the scope of whole-cell biocatalysis in organic media, in particular, that of solvent-labile catalytic systems. Especially, the simple immobilization method and application along with the high process stability render this process a viable alternative to packed bed reactors.

6.3.3.2 Whole-cell Segmented Flow

Introduction & Concept After the first successful development of a continuous process for the whole-cell catalyzed oxime dehydration, another concept was developed. This even more simple method compared to the superabsorber/organic flow was developed to increase compatibility for the reaction in a multi-step flow process. By skipping the immobilization completely and relying on an aqueous/organic segmented flow, the reaction mixture can be easily processed downstream. However, the compatibility of the whole-cell catalyst and the organic solvent is much more critical in this system.

To prove this system's suitability for the OxdB-catalyzed dehydration of octanal oxime (**14**), test reactions were carried out in batch and flow. Eventually, the conditions were optimized to yield an efficient process.

Results & Discussion Initially, batch experiments were carried out to set a benchmark for the reaction. A biphasic system of PPB buffer and cyclohexane was used. The reaction temperature was set to 30 °C and a reaction time of 30 min was chosen. The substrate was dissolved in the organic solvent to give a 100 mM solution. Compared to literature[159], where the substrate was added stepwise and processed in a suspension, this loading is relatively low. As the substrate can only be applied as a solution in this continuous process, the concentration could not be further increased due to limited solubility. Inspired by Buehler *et al.*,[209] the influence of an additive, Tween 20, was investigated.

The batch reaction without additive in 1 mL scale showed only a low conversion of 13%, while the addition of Tween 20 (approx. $2\,\mathrm{mg}\cdot\mathrm{mL}^{-1}$) im-

proved the conversion to 32%. By making the substrate more accessible to the catalyst, and presumable also stabilizing the catalyst, the additive showed a positive impact on the reaction. Under the selected conditions, no foam formation was observed; however, both reactions suffered severely under emulsification. The resulting emulsion with an interlayer proved to be challenging to separate.

A 10 mL scale batch reaction was carried out to determine the yield. The reaction was stirred for 3.5 h to give an emulsion which was centrifuged and separated to yield the product in 39%. After two times repeated centrifugation and separation, more product could be isolated (25% yield), which proves the importance of the tedious workup to give high yields. Combining all downstream steps, a yield of 64% (95% purity) could be obtained, while the conversion was 99%. For the extraction, 20 mL organic waste was created, corresponding to half of the total waste solvent volume.

With these non-satisfactory results in hand, the reaction was transferred into flow mode. A similar setup as in the superabsorber/organic system, consisting of a two-channel syringe pump, a PFA coil reactor (0.8 mm ID, 1 mL reactor volume), and a vial with HCl-quench solution, was chosen (Figure 6.25, upper part). In contrast to the previous flow experiments, the whole-cells were not immobilized but used as a suspension in PPB buffer. Reactions with and without added Tween 20 were carried out. To ensure the comparability of batch and flow reactions, the same conditions were chosen. The results of both flow reactions are shown in Figure 6.25.

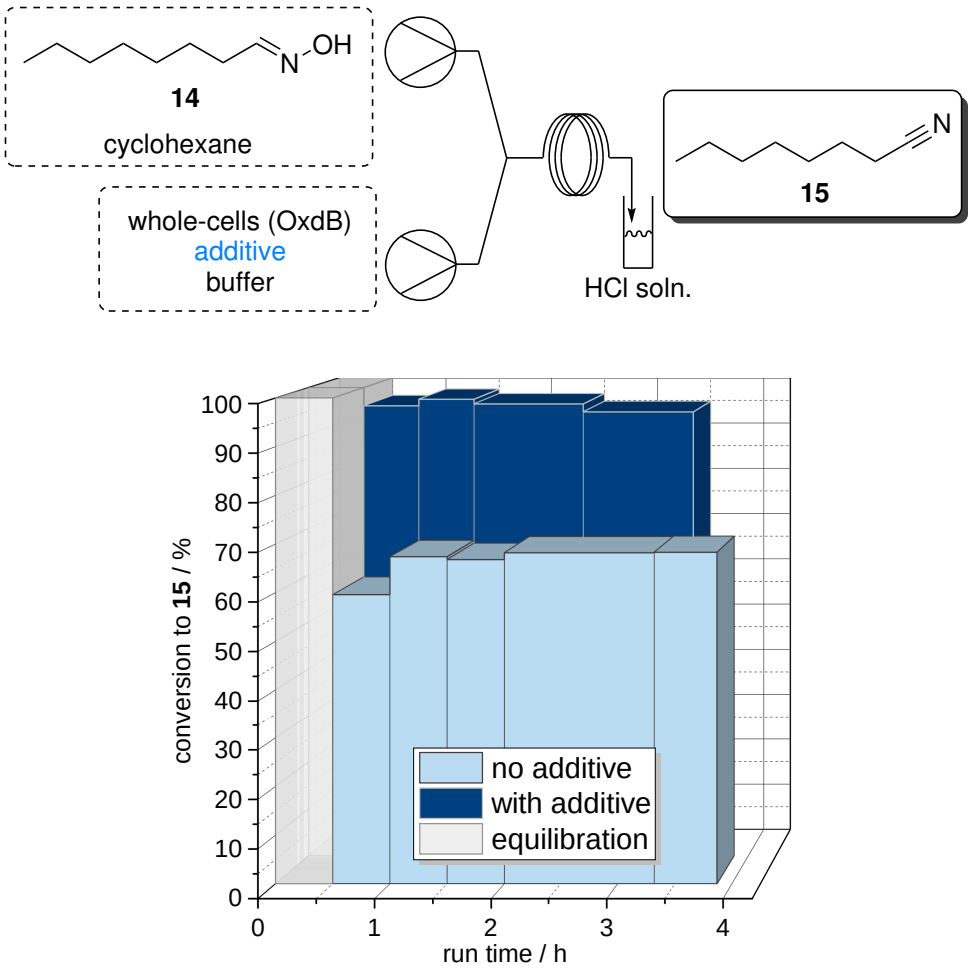

Figure 6.25: Schematic setup (upper part) and results for the conversion to octanenitrile (**15**) of the OxdB-catalyzed dehydration of octanal oxime (**14**) using a cyclohexane/aqueous segmented flow system. Residence time = 30 min, temperature = 30 °C, cat. loading 33 $mg_{wcm} \cdot mL^{-1}$, overall concentration starting material = 50 mM. With (1.3 $mg \cdot mL^{-1}$) and without additive (adapted from Adebar *et al.*[169]).

For the reaction without additive, an average conversion to the desired nitrile **15** of 68% was observed, which is a fivefold increase compared to the batch reaction. By using the additive, the conversion to **15** could be nearly completed with an average of 96%. This is a tremendous increase compared to the batch reaction (plus 64%). The results for batch- and flow mode reactions are shown in Figure 6.26.

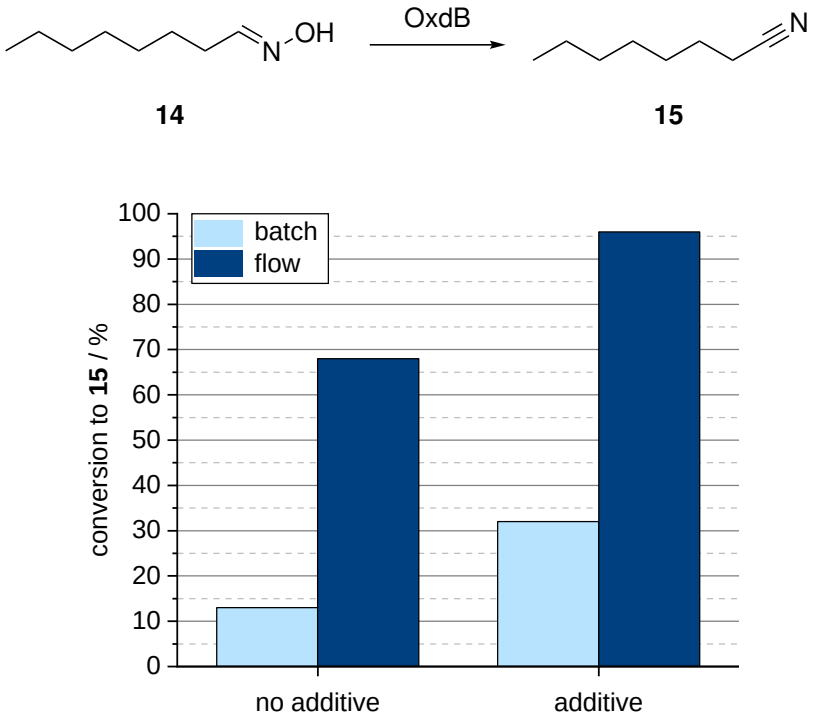

Figure 6.26: Schematic reaction (upper part) and results for the conversion to octanenitrile (**15**) of the OxdB-catalyzed dehydration of octanal oxime (**14**) using a cyclohexane/aqueous segmented flow and batch system, respectively. Residence time = 30 min, temperature = 30 °C, cat. loading 33 $mg_{wcm} \cdot mL^{-1}$, overall concentration starting material = 50 mM. With and without additive (1.3 $mg \cdot mL^{-1}$; adapted from Adebar *et al.*[169]).

Most remarkably, is not the improved conversion but the simplified downstream process of this flow synthesis compared to the batch approach. Virtually no emulsification and near-perfect phase separation were obtained from the outlet of the flow reactor (Figure 6.27). No centrifugation and repeated extraction were needed, reducing the time and costs for downstream processing to a minimum.

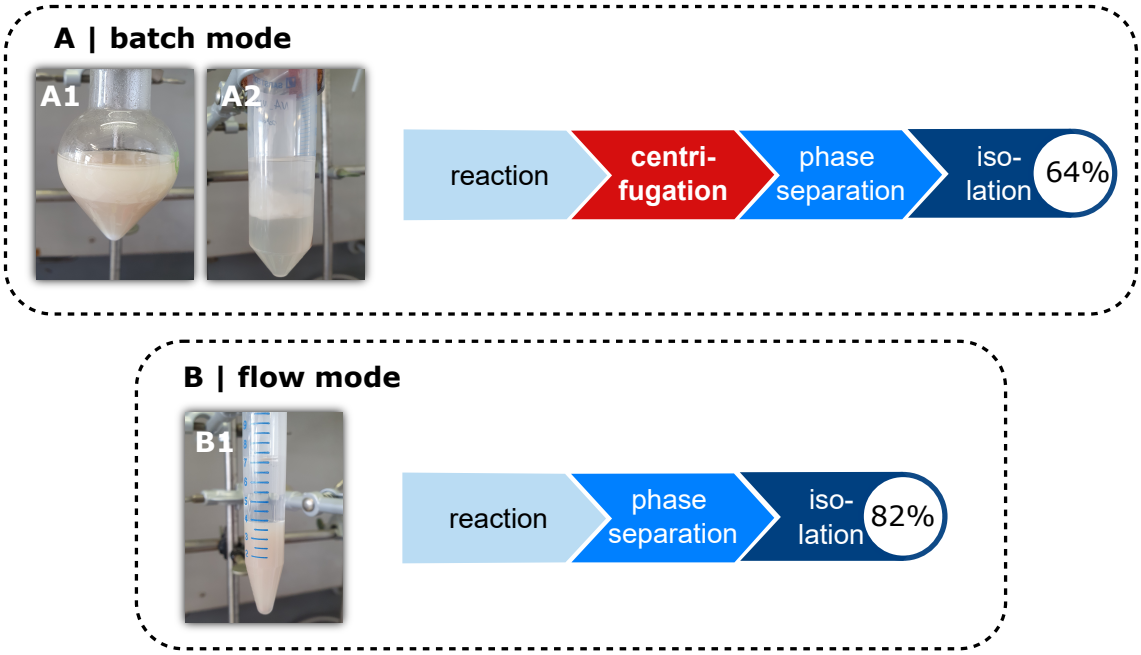

Figure 6.27: Pictures, scheme, and isolated yields of the downstream process for the liquid-liquid segmented flow whole-cell catalyzed dehydration of octanal oxime (**14**) in comparison to batch mode. A1: Batch mixture after reaction, A2: batch mixture after centrifugation, B1: mixture after flow reaction (modified from Adebar *et al.*[169]).

This improved downstream process can also be put in numbers. The isolated yield was with 82% significantly higher than the batch reaction (64%). Thanks to the reduced solvent waste, this process is furthermore much more sustainable. With the best conditions, a productivity of $12.5\,\mathrm{g}\cdot\mathrm{h}^{-1}\cdot\mathrm{L}^{-1}$ was calculated. This is similar to the superabsorber-based system. When it comes to the catalyst productivity, however, the buffer segmented flow system outperforms the previously superabsorber-based with a more than doubled product formation per amount of used catalyst (0.16 vs $0.38\,\mathrm{g_{prod}}\cdot\mathrm{g_{cat}^{-1}}$).

One critical aspect is the stability of the catalyst suspension. After several hours, the cell suspension settled and a gradient appeared in the syringe (Figure 6.28). This might lead to unreliable results, as the catalyst concentration from the feed varies over time.

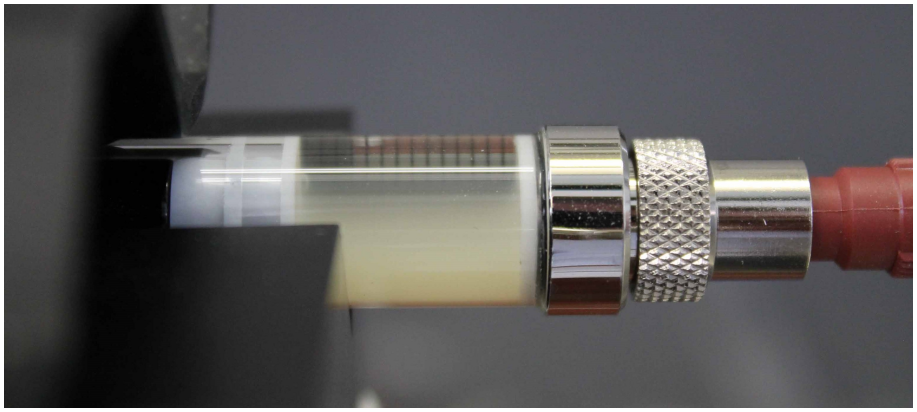

Figure 6.28: Sedimentation of the OxdB-containing whole-cell buffered suspension after 7 h process run time in a syringe.

There are several possibilities to avoid this issue. The most simple solution would be the use of a stirring bar inside of the syringe to continuously resuspend the mixture. Alternatively, a peristaltic pump could be used to draw solution from a stirred (and chilled) reservoir. However, a peristaltic pump has shown to deliver fluid not perfectly stable, especially, at low flow rates ($<0.1\,\mathrm{mL}\cdot\mathrm{min}^{-1}$). In this case, a HPLC pump is not an option, as the pump's chambers would probably block from the whole-cells. Shaking the syringe by a shaker plate did not yield a sufficient resuspension. An ultrasound treatment of the syringe would possibly improve the suspension; however, the catalyst-containing whole-cells would be disrupted.

In summary, a highly efficient process for the OxdB-catalyzed dehydration of octanal oxime (**14**) was developed. It outclasses the batch mode in many aspects. Not only could the conversion be increased fivefold but also the downstream process was improved a lot leading to an 18% increase of conversion while saving time and resources at the same time. Compared to the previously described superabsorber-based approach, the buffer-based system offers simpler integration of standard flow chemistry downstream tools, such as a membrane separator. Furthermore, time and material are saved without immobilization. This renders the process optimal for multi-step synthesis combining biocatalysis and an organic transformation requiring organic solvent.

6.4 Summary & Outlook

In this project, three individual steps of a reaction cascade to octanenitrile were translated successfully from batch to flow mode.

Initially, the TEMPO-catalyzed oxidation of 1-octanol to octanal was investigated in flow mode. The unstable starting material sodium hypochlorite proved to be particularly challenging to process. To overcome this issue, which occurred when syringe pumps were used, a syringe cooler was developed and successfully applied. An initial process design was tested using a DCM/water segmented flow system and provided an average conversion of up to 87% to the desired product.

After this initial success, the second reaction in the cascade, the oximation of the aldehyde, was investigated. This reaction was used as a benchmark and test system for the developed closed-loop optimization platform (Chapter 5). Different solvents, bases, and reaction times were tested in manual flow experiments to gain insight into the reaction. The reaction was then optimized manually in an algorithm-assisted approach using a segmented dichloromethane/water segmented flow system. Here, the reactions were performed manually, while the Nelder-Mead simplex suggested the reaction conditions. After 13 experiments (9th optimization iteration), the reaction was optimized to 76% conversion to the desired nitrile.

Finally, the reaction optimization was fully automated applying sofalab. The solvent was replaced with dimethyl carbonate to ensure compatibility with the other reactions in a potential reaction cascade. The automated system optimized the conversion to the desired product to a maximum of 94% within 5 optimization iterations, starting from the worst initial experiment of 68%. Temperature, hydroxylamine concentration, and residence time were used as the optimization parameters. These results demonstrate the opportunities enabled by this self-optimization platform.

Two different continuous approaches were developed for the bio-catalyzed oxime dehydration. First, an approach based on a mobile immobilized aqueous phase in a segmented hydrogel/organic flow system was investigated. Since the used aldoxime dehydratase (OxdB) is known to be solvent labile, this combination of immobilized and thus stabilized catalyst and continuous

supply of fresh catalyst for the reaction provided an option for stable flow processes. Especially with a view to closed-loop optimization, this aspect is crucial. Under optimized conditions (250 mg catalyst wet cell mass per mL; 30 min residence time), an average conversion of 90% to the desired nitrile was achieved.

Alternatively, a segmented flow system without any immobilization was investigated. In contrast to the previous synthesis, whole cells in a buffer solution were used. This system not only outperformed the batch approach by fivefold conversion to the desired product, but also the previously developed immobilization-based approach. By using an additive (Tween 20), the conversion reached an average of 96% within 30 min using only $33\,\mathrm{mg_{wcm}} \cdot \mathrm{mL}^{-1}$. Most notable, however, was the simplified downstream process. In the case of the liquid-liquid system, a simple phase separation after the reaction gave the product with 82% isolated yield, while for the batch mode several steps of centrifugation and separation were required to obtain only 64% isolated yield. This strong effect was possible due to a greatly reduced emulsification of the reaction mixture.

In the future, the optimization platform can also be used to optimize the other reaction steps—the TEMPO-catalyzed oxidation and the bio-catalyzed aldoxime dehydration. All three reaction steps can be telescoped to form an efficient flow process with only phase separation as downstream steps (Scheme 6.7). After successful optimization of the individual reaction steps to equally high substrate loadings, the combination offers high potential for an efficient, continuous, and sustainable nitrile synthesis. However, this was beyond the scope of this work.

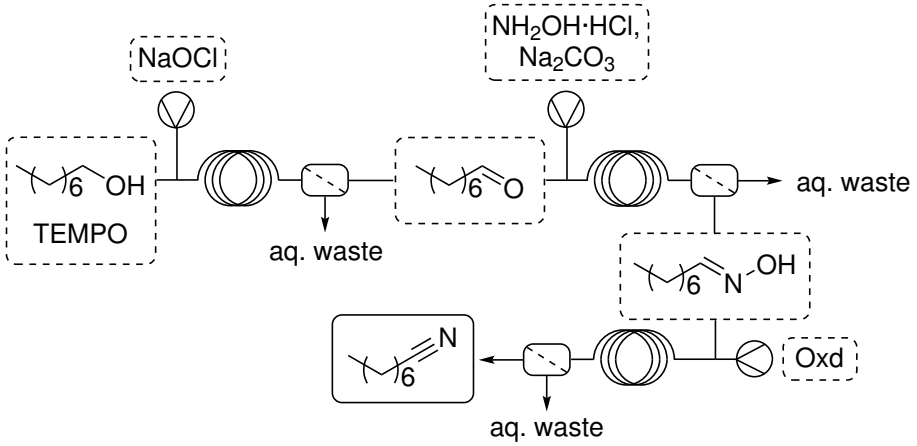

Scheme 6.7: Proposed multistep flow process for the synthesis of aliphatic nitriles starting from aliphatic alcohols. Oxd, aldoxime dehydratase; TEMPO, 2,2,6,6-tetramethylpiperidin-1-yl)oxyl.

6.5 Experimental

6.5.1 Analytics

All NMR spectra were recorded on a Bruker Avance III 500 spectrometer (500 MHz) in chloroform-d1, referenced internally to the residual solvent peaks in ppm (chloroform-d1: 7.26 ppm (s)), and analyzed using MestReNova. Chemical shifts σ are reported in ppm to the nearest 0.01 ppm. The multiplicity of ^{1}H signals are indicated as following: s = singlet, d = doublet, dd = doublet of doublet, t = triplet, q = quadruplet, m = multiplet, or combinations thereof. Coupling constants (J) are reported in Hz to the nearest 0.1 Hz.

GC analysis was made using a GC-2010 Plus by *Shimadzu*, with an AOC-20i autoinjector, a flame ionization detector (FID) and N_2 carrier gas. Conversions were determined based on calibration measurements of the compounds.

Method:
Column: chiral BGB-174 (0.25 mm ID, 0.25 μm film, 30 m length) by *BGB Analytik AG*.
Column oven temperature program: 140 °C for 1 min, 140 °C to 200 °C with 20 °C $\cdot$ min^{-1}, 200 °C for 1.5 min.

Settings: SPL1: 200 °C, pressure: 175.2 kPa, total flow: 203 mL · min^{-1}, column flow: 1.98 mL · min^{-1}, linear velocity: 46.9 cm · s^{-1}, purge flow: 3.0 mL · min^{-1}, split ratio: 100, injection volume: 1 μL, FID: 220 °C.
Retention times: Octanal (**13**) 1.8 min, 1-octanol (**12**) 2.0 min, octanal oxime (**14**) 2.4 min, octanenitrile (**15**) 2.7 min, octanoic acid (**16**) 3.0 min.

6.5.2 Chemicals & Equipment

For all experiments, deionized water was used unless noted otherwise. The starting materials were purchased in commercial quality and used without further purification.

6.5.3 Preparation of OxdB from *Bacillus* sp. OxB-1 Whole Cells

Parts of the OxdB from *Bacillus* sp. OxB-1 whole cells were gratefully obtained from Alessa Hinzmann and prepared according to literature, and the activity was found to be as reported according to a test reaction.[165]

The gene for the aldoxime dehydratase from *Bacillus* sp. OxB-1 (OxdB) was cloned into a pUC18 vector using HindIII and PstI restriction sites. Whole cells containing OxdB from *Bacillus* sp. OxB-1 were prepared according to literature[165] and stored as whole cell suspension at 4 °C. The activity of the whole cells was tested in reactions according to the literature.

6.5.4 TEMPO-catalyzed Oxidation of 1-Octanol (12)

6.5.4.1 Validation of the Quenching Method

Method A $NaHSO_4 \cdot H_2O$ (0.32 mmol, 4.4 mg) was dissolved in NaOCl·5 H_2O (13 %w/w, 1.7 M aq. soln.; 0.43 mmol, 250 μL). TEMPO (0.1 μmol, 0.15 mg) and 1-octanol (**12**; 0.39 mmol, 61 μL) were dissolved in DCM (to 1 mL). A third solution of $Na_2S_2O_3$ (1.4 mmol, 134 mg) in water (500 μL)

was prepared. All solutions were mixed in a glass vial and stirred for 10 min at 0 °C. For GC analysis, the reaction mixture was diluted with ethyl acetate (400 µL) and a sample of the organic phase (50 µL) was filtered over a silica plug (1–2 cm in a cotton-stoppered glass pipet). The silica plug was washed with ethyl acetate (1 mL) and the crude mixture was analyzed *via* GC.

Method B $NaHSO_4 \cdot H_2O$ (61 µL) was dissolved in NaOCl·5 H_2O (13 %w/w, 1.7 M aq. soln.; 0.43 mmol, 250 µL). TEMPO (0.1 µmol, 0.15 mg) and 1-octanol (**12**; 0.39 mmol, 61 µL) were dissolved in DCM (to 1 mL). A third aqueous HCl solution (10 %w/w, 500 µL) was prepared. All solutions were mixed in a glass vial and stirred for 10 min at 0 °C. For GC analysis, the reaction mixture was diluted with ethyl acetate (400 µL) and a sample of the organic phase (50 µL) was filtered over a silica plug (1–2 cm in a cotton-stoppered glass pipet). The silica plug was washed with ethyl acetate (1 mL) and the crude mixture was analyzed *via* GC.

Method C $NaHSO_4 \cdot H_2O$ (61 µL) was dissolved in NaOCl·5 H_2O (13 %w/w, 1.7 M aq. soln.; 0.43 mmol, 250 µL). TEMPO (0.1 µmol, 0.15 mg) and 1-octanol (**12**; 0.39 mmol, 61 µL) were dissolved in DCM (to 1 mL). A third aqueous malonic acid solution (1.4 mmol, 150 mg in 500 µL water) was prepared. All solutions were mixed in a glass vial and stirred for 10 min at 0 °C. For GC analysis, the reaction mixture was diluted with ethyl acetate (400 µL) and a sample of the organic phase (50 µL) was filtered over a silica plug (1–2 cm in a cotton-stoppered glass pipet). The silica plug was washed with ethyl acetate (1 mL) and the crude mixture was analyzed *via* GC.

GC: Octanal (**13**) 1.8 min, 1-octanol (**12**) 2.0 min, octanal oxime (**14**) 2.4 min, octanenitrile (**15**) 2.7 min, octanoic acid (**16**) 3.0 min.

Table 6.1: Results of the quenching experiments for the TEMPO-catalyzed oxidation of 1-octanol (**12**) to octanal (**13**). Results are shown in percentage as appearing in crude reaction mixture analyzed by GC.

Entry	*Method*	*Percentage in crude mixture / %*			
		*aldehyde **13***	*alcohol **12***	*acid **16***	*ester **17***
1	A	0%	100%	0%	0%
2	A[(a)]	71%	29%	0%	2%
3	B	1%	82%	0%	17%
4	B[(a)]	77%	18%	1%	4%
5	C	1%	95%	0%	3%
6	C[(a)]	74%	0%	23%	2%

[(a)] Higher NaOCl concentration (0.7 mmol, 115 mg from a 34 %w/w aq. soln.).

6.5.4.2 Synthesis of Octanal (13) in DCM Batch

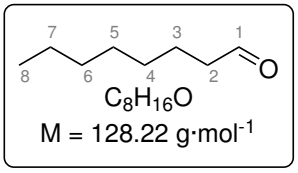

TEMPO (0.23 mol%, 0.013 mmol, 2.0 mg) and $NaHSO_4 \cdot H_2O$ (4.4 mol%, 0.25 mmol, 35 mg) were dissolved in DCM (5 mL) in a round bottom flask and chilled to 0 °C. NaOCl·5 H_2O (1.1–2.1 eq) was added. 1-Octanol (**12**; 1 eq, 5.1 mmol, 0.8 mL) was added drop-wise. The mixture was stirred for 2 h at 0 °C. To quench the reaction, aqueous HCl solution (2 mL of a 10 %w/w soln.) was added. Water (3 mL) was added until the solid was dissolved. Phases were separated and the aqueous layer was extracted with DCM (2 x 5 mL). The combined organic phases were washed with sat. NaCl soln. (2 x 15 mL), dried over $MgSO_4$ and filtered using filter paper. After the solvent was removed under reduced pressure, the crude product mixture was obtained as a colorless liquid and analyzed by GC.

GC: Octanal (**13**) 1.8 min, 1-octanol (**12**) 2.0 min, octanal oxime (**14**) 2.4 min, octanenitrile (**15**) 2.7 min, octanoic acid (**16**) 3.0 min.

Table 6.2: Results of the TEMPO-catalyzed oxidation of 1-octanol (**12**) to octanal (**13**). Results are shown in percentage as appearing in crude reaction mixture analyzed by GC.

Entry	*NaOCl*	*Percentage in crude mixture / %*		
		*aldehyde **13***	*alcohol **12***	*acid **16***
1	1.1 eq (5.7 mmol, 0.93 g)	93%	3%	4%
2	2.1 eq (13 mmol, 2.1 g)	54%	1%	45%

6.5.4.3 Synthesis of Octanal (13) in Aqueous/DCM Batch

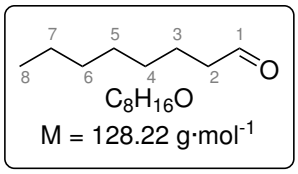

TEMPO (0.25 mol%, 0.013 mmol, 2.0 mg) and $NaHSO_4 \cdot H_2O$ (4.9 mol%, 0.25 mmol, 35 mg) were dissolved in DCM (2.1 mL) and water (2.1 mL) in a round bottom flask and chilled to 0 °C. Upon addition of NaOCl·5 H_2O (1.1 eq, 5.7 mmol, 0.94 g) a yellow suspension was obtained. 1-Octanol (**12**; 1 eq, 5.1 mmol, 0.8 mL) was added drop-wise to give first a red and then colorless suspension. For reaction control, a sample of the organic phase (30 μL) was filtered over a silica plug (1–2 cm in a cotton-stoppered glass pipet), flushed with ethyl acetate (2 mL) and directly analyzed *via* GC. The mixture was stirred for 1.5 h at 0 °C. To quench the reaction, aqueous HCl solution (2 mL of a 10 %w/w soln.) was added. Phases were separated and the aqueous layer was extracted with DCM (1 x 5 mL). The combined organic phases were dried over $MgSO_4$ and filtered using filter paper. After the solvent was removed under reduced pressure, the crude product mixture was obtained as a colorless liquid and analyzed by GC.

GC: Octanal (**13**) 1.8 min, 1-octanol (**12**) 2.0 min, octanal oxime (**14**) 2.4 min, octanenitrile (**15**) 2.7 min, octanoic acid (**16**) 3.0 min.

Table 6.3: Results of the TEMPO-catalyzed oxidation of 1-octanol (**12**) to octanal (**13**). Results are shown in percentage as appearing in crude reaction mixture analyzed by GC.

Entry	*Reaction time*	*Percentage in crude mixture / %*		
		*aldehyde **13***	*alcohol **12***	*acid **16***
1	15 min	77%	18%	5%
2	1 h	65%	19%	16%
3	1.5 h	60%	8%	32%

6.5.4.4 Synthesis of Octanal (13) in Aqueous/DCM Segmented Flow

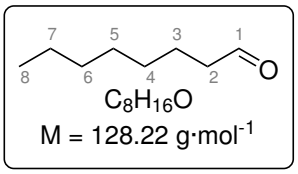

The setup consisted of a two-channel syringe pump, two short tubes (PFA, 10 cm, 0.8 mm ID) with fittings connected to a Y-mixer (PEEK, 0.51 mm ID), which was connected to a reactor tube (PFA, 0.5 mL, 0.8 mm ID). The temperature was controlled by a water bath. For the organic solution, 1-octanol (**12**; 7.6 mmol, 1.2 mL) and TEMPO (0.25 mol%, 0.019 mmol, 3.1 mg) were dissolved in DCM (to 5 mL). For the aqueous solution, freshly prepared NaOCl·5 H_2O (5 mL of a 13 %w/w, 1.7 M aq. soln. corresponding to 8.5 mmol, 1.1 eq) and $NaHSO_4 \cdot H_2O$ (2.0 mol%, 0.15 mmol, 54.2 mg) were mixed. Both solutions were transferred into syringes (5 mL, S.G.E., gas tight), attached to the syringe pump, and connected to the Y-piece. The aqueous solution was additionally chilled with a syringe chiller (0 °C). The reaction solution was collected in a glass vial containing $Na_2S_2O_3$ (0.5 mL of a 1 M aq. soln.) for quenching of the reaction. To start the reaction, the syringe pump was set up ($0.0083\,\mathrm{mL \cdot min^{-1}}$) corresponding to a residence time of 30 min. For GC analysis, the reaction mixture was diluted with ethyl acetate (400 μL) and a sample of the organic phase (50 μL) was filtered over a silica plug (1–2 cm in a cotton-stoppered glass pipet). The silica plug was washed with ethyl acetate (1 mL) and the crude mixture was analyzed *via* GC.

GC: Octanal (**13**) 1.8 min, 1-octanol (**12**) 2.0 min, octanal oxime (**14**) 2.4 min, octanenitrile (**15**) 2.7 min, octanoic acid (**16**) 3.0 min.

Table 6.4: Results of the TEMPO-catalyzed oxidation of 1-octanol (**12**) to octanal (**13**). Results are shown in percentage as appearing in crude reaction mixture analyzed by GC. Changed conditions: Not freshly prepared NaOCl solution, without syringe chiller.

Entry	*Run time*	*Percentage in crude mixture*			
		aldehyde ***13***	*alcohol* ***12***	*acid* ***16***	*ester* ***17***
1	33–65 min	38%	59%	<1%	3%
2	65–110 min	32%	65%	<1%	3%
3	110–150 min	24%	73%	<1%	3%
4	150–180 min	18%	79%	<1%	3%
5	180–210 min	14%	83%	<1%	2%

Table 6.5: Results of the TEMPO-catalyzed oxidation of 1-octanol (**12**) to octanal (**13**). Results are shown in percentage as appearing in crude reaction mixture analyzed by GC. Changed conditions: Not freshly prepared NaOCl solution, with syringe chiller.

Entry	*Run time*	*Percentage in crude mixture*			
		aldehyde ***13***	*alcohol* ***12***	*acid* ***16***	*ester* ***17***
1	33–65 min	20%	78%	<1%	2%
2	65–110 min	32%	65%	<1%	3%
3	110–150 min	31%	66%	<1%	3%
4	150–180 min	30%	67%	<1%	3%
5	180–210 min	29%	69%	<1%	2%
6	210–240 min	28%	69%	<1%	3%
7	240–270 min	26%	71%	<1%	3%
8	270–300 min	24%	73%	<1%	3%
9	300–330 min	22%	75%	<1%	3%
10	330–360 min	23%	75%	<1%	3%

Table 6.6: Results of the TEMPO-catalyzed oxidation of 1-octanol (**12**) to octanal (**13**). Results are shown in percentage as appearing in crude reaction mixture analyzed by GC. Changed conditions: Freshly prepared NaOCl solution, with syringe chiller, residence time = 15 min.

Entry	*Run time*	*Percentage in crude mixture*			
		*aldehyde **13***	*alcohol **12***	*acid **16***	*ester **17***
1	15–30 min	64%	34%	<1%	2%
2	30–45 min	88%	8%	1%	3%
3	45–107 min	87%	8%	2%	3%
4	107–150 min	90%	6%	2%	1%
5	150–210 min	86%	10%	2%	2%
6	210–255 min	84%	12%	2%	2%

Table 6.7: Results of the TEMPO-catalyzed oxidation of 1-octanol (**12**) to octanal (**13**). Results are shown in percentage as appearing in crude reaction mixture analyzed by GC. Changed conditions: Not freshly prepared NaOCl solution, solution volume each = 2 mL, syringe = 2.5 mL, residence time = 5 min.

Entry	*Run time*	*Percentage in crude mixture*		
		*aldehyde **13***	*alcohol **12***	*ester **17***
1	5–10 min	40%	59%	1%
2	10–15 min	36%	63%	1%
3	15–20 min	35%	64%	1%
4	20–25 min	35%	64%	1%
5	25–30 min	33%	65%	2%
6	30–35 min	33%	65%	2%

Table 6.8: Results of the TEMPO-catalyzed oxidation of 1-octanol (**12**) to octanal (**13**). Results are shown in percentage as appearing in crude reaction mixture analyzed by GC. Changed conditions: Not freshly prepared NaOCl solution, solution volume each = 2 mL, syringe = 2.5 mL, residence time = 5 min, reaction temperature = 30 °C.

Entry	*Run time*	*Percentage in crude mixture*		
		*aldehyde **13***	*alcohol **12***	*acid **16***
1	5–10 min	38%	59%	3%
2	10–15 min	37%	60%	3%
3	15–20 min	37%	60%	3%
4	20–25 min	35%	62%	3%
5	25–30 min	33%	64%	3%
6	30–35 min	32%	65%	3%

Table 6.9: Results of the TEMPO-catalyzed oxidation of 1-octanol (**12**) to octanal (**13**). Results are shown in percentage as appearing in crude reaction mixture analyzed by GC. Changed conditions: Not freshly prepared NaOCl solution, residence time = 15 min, without syringe chiller.

Entry	*Run time*	*Percentage in crude mixture*		
		aldehyde ***13***	*alcohol* ***12***	*acid* ***16***
1	15–30 min	46%	52%	2%
2	30–45 min	45%	52%	3%
3	45–60 min	42%	55%	3%
4	60–75 min	40%	57%	3%
5	75–90 min	38%	59%	3%
6	90–105 min	36%	62%	2%

6.5.5 Synthesis of Octanal oxime (14)

6.5.5.1 Synthesis of Octanal oxime (14) in Segmented Flow

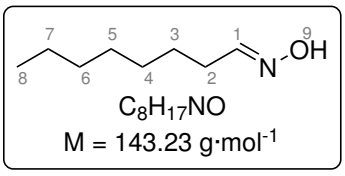

The setup consisted of a two-channel syringe pump, two short tubes (PFA, 10 cm, 0.8 mm ID) with fittings connected to a Y-mixer (PEEK, 0.51 mm ID), which was connected to a reactor tube (PFA, 1 mL, 0.8 mm ID). The temperature was controlled by a water bath. For the organic solution, octanal (**13**; 1 eq, 0.50 mmol, 78.1 μL) was dissolved in DCM (to 5 mL). The aqueous solution was prepared by dissolving hydroxylamine hydrochloride (1.5 eq, 0.75 mmol, 55.1 mg) and sodium carbonate (0.75 eq, 0.37 mmol, 39.7 mg) in water (to 5 mL). Both solutions were transferred into syringes (5 mL, S.G.E., gas tight) and attached to the syringe pump. The reaction solution was collected in a glass vial containing HCl solution (0.5 mL of a 1 M aq. soln.) for quenching of the reaction. To start the reaction, the syringe pump was set up (1–2 mL $\cdot$ h^{-1}) corresponding to a residence time of 15–30 min. Multiple fractions were collected and analyzed. For the GC sample, organic phase of the reaction mixture (50 μL) was diluted with ethyl acetate (100 μL) and filtered over a silica plug (1–2 cm in a cotton-stoppered glass pipet). The silica plug was washed with ethyl acetate (1 mL) and the crude mixture was analyzed *via* GC. For se-

lected reactions, also the aqueous phase was extracted with ethyl acetate (200 μL) and analyzed *via* GC.

GC: Octanal (**13**) 1.8 min, 1-octanol (**12**) 2.0 min, octanal oxime (**14**) 2.4 min, octanenitrile (**15**) 2.7 min, octanoic acid (**16**) 3.0 min.

Table 6.10: Results of the condensation of octanal (**13**) and hydroxylamine in DCM/buffer segmented flow to octanal oxime (**14**). Results are shown in percentage appearing in crude reaction mixture analyzed by GC. Residence time = 30 min.

Entry	*Run time*	*Percentage in crude mixture (extracted)*[a] */ %*	
		*aldehyde **13***	*oxime **14***
1	0–1 h	35 (10)	65 (90)
2	1–1.5 h	30 (29)	70 (71)
3	1.5–2 h	29 (n.d.)	71 (n.d.)
4	2–2.5 h	30 (15)	70 (85)
5	2.5–3 h	29 (13)	71 (87)
6	3–3.5 h	30 (12)	70 (88)
7	4–4.5 h	29 (27)	71 (73)

[a] Extracted from the aqueous phase and analyzed *via* GC.

Table 6.11: Results of the condensation of octanal (**13**) and hydroxylamine in DCM/buffer segmented flow to octanal oxime (**14**). Results are shown in percentage appearing in crude reaction mixture analyzed by GC. Residence time = 15 min.

Entry	*Run time*	*Percentage in crude mixture (extracted)*[a] */ %*	
		*aldehyde **13***	*oxime **14***
1	15–45 min	54 (19)	46 (81)
2	45–75 min	40 (20)	60 (80)
3	75–105 min	42 (28)	58 (72)
4	105–135 min	42 (37)	58 (63)

[a] Extracted from the aqueous phase and analyzed *via* GC.

Table 6.12: Results of the condensation of octanal (**13**) and hydroxylamine in DCM/buffer segmented flow to octanal oxime (**14**). Results are shown in percentage appearing in crude reaction mixture analyzed by GC. Solvent = octanenitrile.

Entry	*Run time*	*Percentage in crude mixture / %*	
		*aldehyde **13***	*oxime **14***
1	15–30 min	36	64
2	30–60 min	36	64
3	60–90 min	35	65
4	90–120 min	30	70

Table 6.13: Results of the condensation of octanal (**13**) and hydroxylamine in DCM/buffer segmented flow to octanal oxime (**14**). Results are shown in percentage appearing in crude reaction mixture analyzed by GC. Base = NaOAc (0.99 eq, 0.99 mmol, 81.23 mg); a membrane separator (Dolomite equipped with a hydrophobic membrane) was used instead of the quenching method.

Entry	*Run time*	*Conversion to oxime **14***
1	0.6–1 h	29%
2	1–1.3 h	29%
3	1.3–1.7 h	28%
4	1.7–2.3 h	29%
5	2.3–2.8 h	30%
6	2.8–3.3 h	29%

Table 6.14: Results of the condensation of octanal (**13**) and hydroxylamine in DCM/buffer segmented flow to octanal oxime (**14**). Results are shown in percentage appearing in crude reaction mixture analyzed by GC. Base = NaOH (0.99 eq, 0.99 mmol, 49.5 μL of a 2 mol $\cdot$ L^{-1} aq. soln.); a membrane separator (Dolomite equipped with a hydrophobic membrane) was used instead of the quenching method.

Entry	*Run time*	*Conversion to oxime **14***
1	0.5–0.8 h	9%
2	0.8–1 h	11%
3	1–1.3 h	9%
4	1.3–1.6 h	10%
5	1.6–1.9 h	9%

Table 6.15: Results of the condensation of octanal (**13**) and hydroxylamine in DCM/buffer segmented flow to octanal oxime (**14**). Results are shown in percentage appearing in crude reaction mixture analyzed by GC. Base = Na_2SO_4 (0.50 eq, 0.50 mmol, 71 mg); a membrane separator (Dolomite equipped with a hydrophobic membrane) was used instead of the quenching method.

Entry	*Run time*	*Conversion to oxime **14***
1	0.4–0.8 h	3%
2	0.8–1.2 h	5%
3	1.2–1.5 h	2%
4	1.5–1.7 h	2%
5	1.7–1.9 h	2%

6.5.5.2 Algorithm-assisted Optimization of the Synthesis of Octanal oxime in Segmented Flow

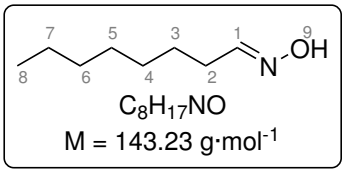

The setup consisted of a two-channel syringe pump, two short tubes (PFA, 10 cm, 0.8 mm ID) with fittings connected to a Y-mixer (PEEK, 0.51 mm ID), which was connected to a reactor tube (PFA, 1 mL, 0.8 mm ID). Temperature (20–40 °C) was controlled by a water bath. A membrane separator (Dolomite equipped with a hydrophobic membrane) was attached to the outlet of the reactor and from both phases fractions were collected in glass vials. For the organic solution, octanal (**13**; 1.0 eq, 1.0 mmol, 171 μL) was dissolved in DCM (to 10 mL). The aqueous solution was prepared by dissolving hydroxylamine hydrochloride (0.9–1.25 eq) and sodium carbonate (0.45–0.63 eq) in water (to 5 mL). From each solution, 5 mL were transferred into syringes (5 mL, S.G.E., gas tight), attached to the syringe pump and connected to the Y-piece. To start the reaction, the syringe pump was set up corresponding to a residence time of 2–30 min. Multiple fractions were collected and analyzed *via* GC.

GC: Octanal (**13**) 1.8 min, 1-octanol (**12**) 2.0 min, octanal oxime (**14**) 2.4 min, octanenitrile (**15**) 2.7 min, octanoic acid (**16**) 3.0 min.

Table 6.16: Results of the 1st step for the algorithm-assisted optimization of the condensation of octanal (**13**) and hydroxylamine in DCM/buffer segmented flow to octanal oxime (**14**). The conversion was calculated based on the percentage of compounds appearing in crude reaction mixture analyzed by GC. Temperature = 30 °C; residence time = 16 min; $NH_2OH{\cdot}HCl$ (1.08 eq, 1.08 mmol, 75.1 mg); Na_2CO_3 (0.54 eq, 0.54 mmol, 57.2 mg).

Entry	*Run time*	*Conversion to oxime **14***
1	0.4–0.7 h	38%
2	0.7–0.9 h	50%
3	0.9–1.6 h	50%
4	1.6–2.0 h	50%
5	2.0–2.4 h	49%

Table 6.17: Results of the 2nd step for the algorithm-assisted optimization of the condensation of octanal (**13**) and hydroxylamine in DCM/buffer segmented flow to octanal oxime (**14**). The conversion was calculated based on the percentage of compounds appearing in crude reaction mixture analyzed by GC. Temperature = 25 °C; residence time = 9 min; $NH_2OH{\cdot}HCl$ (1.16 eq, 1.16 mmol, 80.7 mg); Na_2CO_3 (0.58 eq, 0.58 mmol, 61.4 mg).

Entry	*Run time*	*Conversion to oxime **14***
1	0.4–0.6 h	56%
2	0.6–0.7 h	47%
3	0.7–0.9 h	46%
4	0.9–1.0 h	46%
5	1.0–1.2 h	46%
6	1.2–1.4 h	46%

Table 6.18: Results of the 3rd step for the algorithm-assisted optimization of the condensation of octanal (**13**) and hydroxylamine in DCM/buffer segmented flow to octanal oxime (**14**). The conversion was calculated based on the percentage of compounds appearing in crude reaction mixture analyzed by GC. Temperature = 25 °C; residence time = 23 min; $NH_2OH{\cdot}HCl$ (0.99 eq, 0.99 mmol, 68.8 mg); Na_2CO_3 (0.50 eq, 0.50 mmol, 53.1 mg).

Entry	*Run time*	*Conversion to oxime **14***
1	0.6–1.0 h	56%
2	1.0–1.3 h	58%
3	1.3–1.7 h	54%
4	1.7–2.3 h	58%
5	2.3–2.8 h	58%
6	2.8–3.3 h	58%

Table 6.19: Results of the 4th step for the algorithm-assisted optimization of the condensation of octanal (**13**) and hydroxylamine in DCM/buffer segmented flow to octanal oxime (**14**). The conversion was calculated based on the percentage of compounds appearing in crude reaction mixture analyzed by GC. Temperature = 25 °C; residence time = 9 min; $NH_2OH{\cdot}HCl$ (1.16 eq, 1.16 mmol, 68.8 mg); Na_2CO_3 (0.58 eq, 0.58 mmol, 61.4 mg).

Entry	*Run time*	*Conversion to oxime **14***
1	0.4–0.6 h	56%
2	0.6–0.7 h	47%
3	0.7–0.9 h	46%
4	0.9–1.0 h	46%
5	1.0–1.2 h	46%
6	1.2–1.4 h	46%

Table 6.20: Results of the 5th step for the algorithm-assisted optimization of the condensation of octanal (**13**) and hydroxylamine in DCM/buffer segmented flow to octanal oxime (**14**). The conversion was calculated based on the percentage of compounds appearing in crude reaction mixture analyzed by GC. Temperature = 28 °C; residence time = 23 min; $NH_2OH{\cdot}HCl$ (1.16 eq, 1.16 mmol, 80.6 mg); Na_2CO_3 (0.58 eq, 0.58 mmol, 61.5 mg).

Entry	*Run time*	*Conversion to oxime **14***
1	0.5–0.9 h	49%
2	0.9–1.2 h	57%
3	1.2–1.4 h	64%
4	1.4–2.0 h	65%
5	2.0–2.4 h	65%
6	2.4–2.7 h	65%
7	2.7–3.1 h	64%
8	3.1–3.5 h	64%

Table 6.21: Results of the 6th step for the algorithm-assisted optimization of the condensation of octanal (**13**) and hydroxylamine in DCM/buffer segmented flow to octanal oxime (**14**). The conversion was calculated based on the percentage of compounds appearing in crude reaction mixture analyzed by GC. Temperature = 30.5 °C; residence time = 30 min; $NH_2OH{\cdot}HCl$ (0.99 eq, 0.99 mmol, 68.9 mg); Na_2CO_3 (0.50 eq, 0.50 mmol, 53.0 mg).

Entry	*Run time*	*Conversion to oxime **14***
1	0.7–1.3 h	39%
2	1.3–2.6 h	67%
3	2.6–2.9 h	69%
4	2.9–3.3 h	69%
5	3.3–3.6 h	68%

Table 6.22: Results of the 7th step for the algorithm-assisted optimization of the condensation of octanal (**13**) and hydroxylamine in DCM/buffer segmented flow to octanal oxime (**14**). The conversion was calculated based on the percentage of compounds appearing in crude reaction mixture analyzed by GC. Temperature = 25.9 °C; residence time = 30 min; $NH_2OH{\cdot}HCl$ (1.02 eq, 1.02 mmol, 70.7 mg); Na_2CO_3 (0.51 eq, 0.51 mmol, 54.1 mg).

Entry	*Run time*	*Conversion to oxime* ***14***
1	0.7–1.2 h	73%
2	1.2–2.4 h	67%
3	2.4–2.8 h	65%
4	2.8–3.3 h	65%
5	3.3–3.8 h	63%
6	3.8–4.3 h	63%

Table 6.23: Results of the 8th step for the algorithm-assisted optimization of the condensation of octanal (**13**) and hydroxylamine in DCM/buffer segmented flow to octanal oxime (**14**). The conversion was calculated based on the percentage of compounds appearing in crude reaction mixture analyzed by GC. Temperature = 25.4 °C; residence time = 30 min; $NH_2OH{\cdot}HCl$ (1.01 eq, 1.01 mmol, 70.1 mg); Na_2CO_3n(0.51 eq, 0.51 mmol, 54.17 mg).

Entry	*Run time*	*Conversion to oxime* ***14***
1	1.0–1.5 h	64%
2	1.5–2.0 h	67%
3	2.0–2.5 h	70%
4	2.5–3.0 h	69%
5	3.0–3.8 h	69%
6	3.8–4.5 h	68%

Table 6.24: Results of the 9th step for the algorithm-assisted optimization of the condensation of octanal (**13**) and hydroxylamine in DCM/buffer segmented flow to octanal oxime (**14**). The conversion was calculated based on the percentage of compounds appearing in crude reaction mixture analyzed by GC. Temperature = 31.5 °C; residence time = 30 min; $NH_2OH{\cdot}HCl$ (1.12 eq, 1.12 mmol, 77.5 mg); Na_2CO_3 (0.56 eq, 0.56 mmol, 59.7 mg).

Entry	*Run time*	*Conversion to oxime **14***
1	0.8–1.3 h	87%
2	1.3–2.3 h	70%
3	2.3–2.8 h	70%
4	2.8–3.3 h	70%
5	3.3–3.8 h	69%
6	3.8–4.3 h	69%

Table 6.25: Results of the 10th step for the algorithm-assisted optimization of the condensation of octanal (**13**) and hydroxylamine in DCM/buffer segmented flow to octanal oxime (**14**). The conversion was calculated based on the percentage of compounds appearing in crude reaction mixture analyzed by GC. Temperature = 30.3 °C; residence time = 30 min; $NH_2OH{\cdot}HCl$ (0.92 eq, 0.92 mmol, 64.0 mg); Na_2CO_3 (0.46 eq, 0.46 mmol, 48.5 mg).

Entry	*Run time*	*Conversion to oxime **14***
1	0.8–1.3 h	58%
2	1.3–2.1 h	61%
3	2.1–2.6 h	63%
4	2.6–3.1 h	64%
5	3.1–3.6 h	64%
6	3.6–4.2 h	64%

Table 6.26: Results of the 11th step for the algorithm-assisted optimization of the condensation of octanal (**13**) and hydroxylamine in DCM/buffer segmented flow to octanal oxime (**14**). The conversion was calculated based on the percentage of compounds appearing in crude reaction mixture analyzed by GC. Temperature = 28.1 °C; residence time = 30 min; $NH_2OH{\cdot}HCl$ (1.19 eq, 1.19 mmol, 82.5 mg); Na_2CO_3 (0.60 eq, 0.60 mmol, 63.5 mg).

Entry	*Run time*	*Conversion to oxime **14***
1	0.8–2.0 h	69%
2	2.0–2.4 h	68%
3	2.4–2.9 h	68%
4	2.9–3.4 h	68%
5	3.4–3.9 h	72%
6	3.9–4.4 h	74%

Table 6.27: Results of the 12th step for the algorithm-assisted optimization of the condensation of octanal (**13**) and hydroxylamine in DCM/buffer segmented flow to octanal oxime (**14**). The conversion was calculated based on the percentage of compounds appearing in crude reaction mixture analyzed by GC. Temperature = 34.2 °C; residence time = 30 min; $NH_2OH{\cdot}HCl$ (1.18 eq, 1.18 mmol, 82.3 mg); Na_2CO_3 (0.59 eq, 0.59 mmol, 62.7 mg).

Entry	*Run time*	*Conversion to oxime **14***
1	0.8–1.2 h	61%
2	1.2–2.4 h	66%
3	2.4–2.9 h	72%
4	2.9–3.4 h	72%
5	3.4–3.9 h	73%
6	3.9–4.6 h	72%
7	4.6–5.4 h	70%
8	5.4–6.0 h	71%
9	6.0–6.4 h	73%

Table 6.28: Results of the 13th step for the algorithm-assisted optimization of the condensation of octanal (**13**) and hydroxylamine in DCM/buffer segmented flow to octanal oxime (**14**). The conversion was calculated based on the percentage of compounds appearing in crude reaction mixture analyzed by GC. Temperature = 32 °C; residence time = 30 min; $NH_2OH{\cdot}HCl$ (1.25 eq, 1.25 mmol, 86.9 mg); Na_2CO_3 (0.63 eq, 0.63 mmol, 66.8 mg).

Entry	*Run time*	*Conversion to oxime **14***
1	0.7–1.1 h	64%
2	1.1–2.3 h	75%
3	2.3–2.8 h	77%
4	2.8–3.3 h	76%
5	3.3–3.8 h	76%
6	3.8–4.4 h	76%

6.5.5.3 Closed-loop Optimization of the Synthesis of Octanal oxime (14) in Segmented Flow

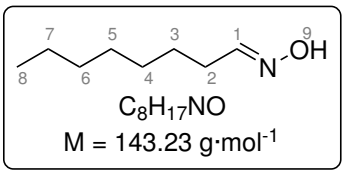

The setup consisted of two two-channel syringe pumps. For the first solution, hydroxylamine hydrochloride (522 mg, 7.52 mmol) and sodium carbonate (398 mg, 3.78 mmol) were dissolved in water (to 50 mL). A portion (25 mL) was filled into a glass syringe (25 mL, S.G.E. gas tight) and mounted on the syringe pump. The syringe was connected to a Y-piece *via* PFA tubing. A syringe (25 mL, S.G.E. gas tight) filled with water was connected to the other port of the Y-piece. The remaining port was connected to a T-piece. A syringe (25 mL, S.G.E. gas tight) containing 25 mL of a solution of octanal (**13**; 646 mg, 5.03 mmol) in dimethyl carbonate (to 50 mL) was connected to the T-piece as well. The remaining port was connected to a tubular reactor (PFA, 1 mL, 0.8 mm ID) which was tempered using a custom-built reactor (Paragraph 5.5.1.1). A membrane separator (Dolomite equipped with a hydrophobic membrane) was attached to the outlet of the reactor and the aqueous stream was collected in a glass flask. The organic stream was led into a custom-built flow GC vial (Subsection 5.5.3). The outlet of this vial was connected to a peristaltic pump (Ismatec Reglo ICC) and led into a glass flask.

The reaction was set up using sofalab (Section 5.4.2). Temperature (15–45 °C), concentration of hydroxylamine in the aqueous stream (75–150 mM), and residence time (0.5–5 min) were used as optimization parameters. The conversion (yield in sofalab) was used as the optimization function. The reactor volume (1 mL), phase ratio (50% organic), and octanal concentration (**13**; 100 mM) were set as constant parameters. The system was started, and after 12 experiments, the system was manually stopped.

GC: Octanal (**13**) 1.8 min, 1-octanol (**12**) 2.0 min, octanal oxime (**14**) 2.4 min, octanenitrile (**15**) 2.7 min, octanoic acid (**16**) 3.0 min.

Table 6.29: Results of the closed-loop optimization of the condensation of octanal (**13**) and hydroxylamine in DMC/buffer segmented flow to octanal oxime (**14**). The conversion was calculated based on the percentage of compounds appearing in crude reaction mixture analyzed by GC and is given to high accuracy to enable following of the decisions of the algorithm. Init, initialization experiment; Op, optimization experiment.

Experiment	*Temperature / °C*	*Residence time / min*	*Concentration NH_2OH / mM*	*Conversion to oxime **14***
Init 1	30.0	2.75	112.5	82.89%
Init 2	22.5	1.63	93.4	68.07%
Init 3	37.5	1.63	93.4	69.18%
Init 4	37.5	1.63	93.4	80.08%
Op 1	37.5	3.88	106.3	86.73%
Op 2	39.4	4.16	107.8	89.32%
Op 3	23.8	5.00	115.6	89.86%
Op 4	22.0	5.00	118.4	94.19%
Op 5	38.4	4.06	132.0	94.35%
Op 6	40.4	4.09	136.8	92.77%
Op 7	36.6	5.00	126.3	93.35%
Op 8	25.3	5.00	143.3	93.64%

6.5.6 Whole-cell Catalysis in Segmented Flow

6.5.6.1 Synthesis of Octanenitrile (15) in Buffer/cyclohexane Batch Mode

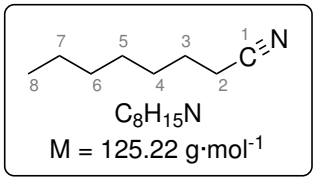

In a glass vial, whole-cells containing OxdB (100 μL of a 333 mg $\cdot$ mL^{-1} wet cell mass suspension in PPB (50 mM, pH 7)) were suspended in PPB buffer (900 μL of 50 mM, pH 7). A solution of octanal oxime (17.3 mg, 0.1 mmol, $c_{organic}$: 100 mM) in cyclohexane (to 1 mL) was added at 30 °C. The reaction mixture was stirred for 2 h with a magnetic stirring bar (400 rpm) at 30 °C. The reaction was monitored by GC analysis of diluted organic phase (20 μL) of the reaction mixture with ethyl acetate (100 μL).

GC: Octanal (**13**) 1.8 min, 1-octanol (**12**) 2.0 min, octanal oxime (**14**) 2.4 min, octanenitrile (**15**) 2.7 min, octanoic acid (**16**) 3.0 min.

Table 6.30: Results of the OxdB-catalysed dehydration of octanal oxime (**14**) in a cyclohexane/buffer batch system. Results are shown in percentage as appearing in crude reaction mixture analyzed by GC.

Entry	*Reaction time*	*Conversion to nitrile **15***
1	15 min	6%
2	30 min	13%
3	1 h	27%
4	2 h	51%
5	4 h	79%

Table 6.31: Results of the OxdB-catalysed dehydration of octanal oxime (**14**) in a cyclohexane/buffer batch system. Results are shown in percentage as appearing in crude reaction mixture analyzed by GC. Changed conditions: Addition of Tween 20 (1.3 mg) to aqueous phase.

Entry	*Reaction time*	*Conversion to nitrile **15***
1	5 min	4%
2	15 min	15%
3	30 h	32%
4	1 h	57%
5	1 h 45 min	85%

6.5.6.2 Synthesis of Octanenitrile (15) in Buffer/cyclohexane 10 mL Scale Batch Mode

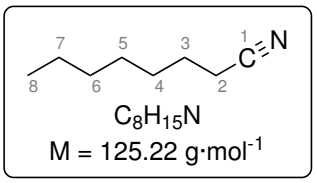

In a 50 mL pear-shaped flask, whole-cells containing OxdB* (2 mL of a 333 mg · mL^{-1} suspension in PPB (50 mM, pH 7)) were suspended in PPB buffer (8 mL of 50 mM, pH 7) and Tween 20 (17.4 mg) was added. A solution of octanal oxime (**14**; 145.1 mg, 1.01 mmol, $c_{organic}$: 101 mM) in cyclohexane (to 10 mL) was added at 30 °C. The reaction mixture was stirred for 3.25 h with a magnetic stirrer (600 rpm) at 30 °C. The poorly separated suspension was centrifuged (10 000 x g, 1 min) and the phases were separated. The solvent from the organic phase was evaporated to give the desired product (**15**; 49.4 mg, 39%) as a colorless liquid. The aqueous phase was two times extracted with cyclohexane (each 10 mL) and centrifuged (20 000 x g, 20 min). From the combined organic phases, the solvent was removed under reduced pressure and the product was obtained as a colorless liquid (**15**; 31.8 mg, 25%). The product was analyzed *via* GC and ^{1}H NMR analysis. The combined product (**15**; 81.2 mg) was obtained in 64% yield (with 95% purity determined by ^{1}H NMR) and the conversion was determined to be 99%.

GC: Octanal (**13**) 1.8 min, 1-octanol (**12**) 2.0 min, octanal oxime (**14**) 2.4 min, octanenitrile (**15**) 2.7 min, octanoic acid (**16**) 3.0 min.

*The wet-cell mass loading is higher compared to the other reactions in this chapter since the activity for the freshly prepared whole-cell catalyst was found to be lower. Activities have been compared to a test reaction and accordingly adjusted.

6.5.6.3 Synthesis of Octanenitrile (15) in Buffer/cyclohexane Segmented Flow

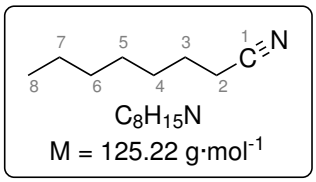

A syringe pump was connected to a Y-mixer (0.5 mm ID), which was connected to a tubular reactor (PFA, 0.8 mm ID, 1 mL). Reaction temperature (30 °C) was controlled by a water bath. For the organic solution, octanal oxime (**14**; 0.5 mmol, 71.5 mg, $c_{organic}$: 100 mM) was dissolved in cyclohexane (to 5 mL). For the aqueous solution, wet cells containing OxdB (500 μL of a 333 mg $\cdot$ mL^{-1} suspension in PPB (pH 7, 50 mM)) were suspended in PPB buffer (pH 7, 50 mM, to 5 mL). The reaction solution was collected in glass vials containing HCl solution (2 M aq. soln., 0.5 mL) for quenching of the reaction. To start the reaction, the syringe pump was set up (1 mL $\cdot$ h^{-1}, residence time: 30 min). For GC analysis, reaction mixture (20 μL) was diluted with ethyl acetate (100 μL) and analyzed *via* GC.

GC: Octanal (**13**) 1.8 min, 1-octanol (**12**) 2.0 min, octanal oxime (**14**) 2.4 min, octanenitrile (**15**) 2.7 min, octanoic acid (**16**) 3.0 min.

Table 6.32: Results of the OxdB-catalysed dehydration of octanal oxime (**14**) in cyclohexane/buffer segmented flow. Results are shown in percentage appearing in crude reaction mixture analyzed by GC. Conditions: Addition of Tween 20 (6.6 mg) to aqueous phase.

Entry	*Run time*	*Conversion to nitrile **15***
1	0.5–5 h	96%
2	1–1.5 h	98%
3	1.5–2.5 h	97%
4	2.5–3.5 h	95%

Table 6.33: Results of the OxdB-catalysed dehydration of octanal oxime (**14**) in cyclohexane/buffer segmented flow. Results are shown in percentage appearing in crude reaction mixture analyzed by GC. Conditions: No addition of Tween 20.

Entry	*Run time*	*Conversion to nitrile **15***
1	0.5–1 h	70%
2	1–1.5 h	67%
3	1.5–2 h	67%
4	2–3.3 h	68%
5	3.3–3.9 h	68%

6.5.7 Fluid Heterogeneous Catalysis in Segmented Flow

6.5.7.1 Synthesis of Octanenitrile (15) in Superabsorber/cyclohexane Segmented Flow

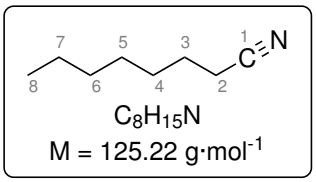

The setup consisted of a two-channel syringe pump, two short tubes (PFA, 10 cm, 0.8 mm ID) with fittings connected to a Y-mixer (PEEK, 0.51 mm ID), which was connected to a reactor tube (PFA, 0.5 mL, 0.8 mm ID). Fractions were collected in a glass vial containing quenching solution (2 M HCl solution, 400 μL). The reaction temperature was controlled with a bather bath. For the organic solution, octanal oxime (**14**; 0.2 mmol, 28.7 mg) was dissolved in cyclohexane (to 2 mL). For the aqueous solution, wet cells containing OxdB (200 μL of a 333 mg $\cdot$ mL^{-1} suspension in PPB(pH 7, 50 mM)) was diluted with PPB (pH 7, 50 mM, to 2 mL) in a small glass vial. Then, the aqueous solution was immobilized by adding the liquid to superabsorber powder (Evonik Favor SXM 9155, 20 mg $\cdot$ mL^{-1}, particle size $< 100\,\mu$m) while intensely mixing with a small spatula. The reaction solution was collected in a glass vial containing HCl solution (2 M aq. soln., 0.5 mL) for quenching of the reaction. To start the reaction, the syringe pump was set up (0.5 mL $\cdot$ h^{-1}, residence time = 30 min). For GC analysis, the reaction mixture was diluted with ethyl acetate (400 μL) and a sample of the organic phase (50 μL) was filtered over a silica plug (1 to

2 cm in a cotton-stoppered glass pipet). The silica plug was washed with ethyl acetate (1 mL) and the crude mixture was analyzed *via* GC.

GC: Octanal (**13**) 1.8 min, 1-octanol (**12**) 2.0 min, octanal oxime (**14**) 2.4 min, octanenitrile (**15**) 2.7 min, octanoic acid (**16**) 3.0 min.

Table 6.34: Results of the OxdB-catalysed dehydration of octanal oxime (**14**) in cyclohexane/buffer segmented flow. Results are shown in percentage as appearing in crude reaction mixture analyzed by GC.

Entry	*Run time*	*Percentage in crude mixture*	
		*oxime **14***	*nitrile **15***
1	0.5–1 h	63%	37%
2	1–1.5 h	51%	49%
3	1.5–3 h	47%	53%
4	3–4 h	47%	53%
5	4–5 h	46%	54%
6	5–6 h	45%	55%

Table 6.35: Results of the OxdB-catalysed dehydration of octanal oxime (**14**) in cyclohexane/buffer segmented flow. Results are shown in percentage appearing in crude reaction mixture analyzed by GC. Change from standard conditions: 25 mg · mL^{-1} superabsorber, residence time = 30 min.

Entry	*Run time*	*Percentage in crude mixture*	
		*oxime **14***	*nitrile **15***
1	10–20 min	69%	31%
2	20–30 min	68%	32%
3	30–40 min	61%	39%

Table 6.36: Results of the OxdB-catalysed dehydration of octanal oxime (3) in cyclohexane/buffer segmented flow. Results shown in percentage appearing in crude reaction mixture analyzed by GC. Change from standard conditions: $20\,\mathrm{mg} \cdot \mathrm{mL}^{-1}$ superabsorber, superabsorber particle size: $< 80\,\mu\mathrm{m}$, $250\,\mathrm{mg_{wcm}} \cdot \mathrm{mL}^{-1}$, reactor: Inner diameter 1 mm, 1 mL, residence time = 30 min.

Entry	*Run time*	*Percentage in crude mixture*	
		oxime ***14***	*nitrile* ***15***
1	0–32 min	-	-
2	52–72 min	10%	90%
3	72–87 min	9%	91%

7 Chemoenzymatic Continuous Flow Dynamic Kinetic Resolution

This project on dynamic kinetic resolution of secondary alcohols in a continuous manner was developed in a collaboration project with Osaka University, Japan. A major challenge of this project was the suppression of side product formation. To solve this problem, an innovative type of gradient packed bed reactor was developed. The application of this concept successfully minimized the side product formation, and the reactor showed very high efficiency.

7.1 Theoretical Background

Since chirality in small molecules was discovered by *Jean-Baptiste Biot* in 1815 and its role in vital metabolic processes was revealed[255,256], the desire to synthesize enantiopure compounds grew among chemists. Chirality manifests itself in multiple ways, be it the minty smell of (*R*)-(−)-carvone and the smell of caraway seeds of the opposite (*S*)-(+) enantiomer[257] or drug effectiveness, which is often closely related to a specific enantiomeric configuration.[258] However, this synthetic dream did not come true until the early twentieth century when first enantioselective reactions were discovered.[259]

Theoretically, there are three different methods to obtain chiral molecules.[260] First, one can start from a *chiral pool* of molecules, which already contains the stereo information and therefore does not have to be introduced. The second approach, starting from prochiral molecules, includes *asymmetric catalysis*. Third, a racemic mixture of molecules can be purified by *kinetic*

resolution or crystallization to yield one specific enantiomer. Starting from a *chiral pool* limits further synthesis, as this chiral center has to be protected in follow-up chemistry. Asymmetric catalysis is often very expensive and limited to a narrow substrate scope. However, kinetic resolution also has a drawback as the conversion is limited to a maximum of half the starting material.

To overcome this limitation, *dynamic* kinetic resolution (DKR) was developed. The concept and a simplified reaction are shown in Scheme 7.1. The underlying principle combines kinetic resolution with simultaneous racemization of the starting material. While kinetic resolution provides the desired product (*S*)-**B** from the starting material (*S*)-**A** with a high reaction rate k_1, the reaction of the corresponding (*R*)-**A** is much slower (rate k_2). Thus, very high enantioselectivity can be achieved. From the remaining (*R*)-enantiomer, the other enantiomer can be regenerated *via* racemization.[261]

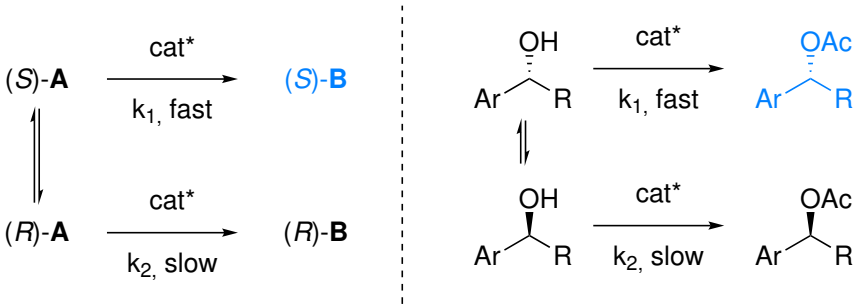

Scheme 7.1: Left: Concept of dynamic kinetic resolution (DKR). Right: Simplified exemplary DKR of an alcohol to the corresponding enantiopure product (adapted and modified from Ward *et al.*).[261]

A number of reviews have highlighted the achievements and importance of this asymmetric synthesis.[262–264] Often, highly selective biocatalysts such as lipases are used for kinetic resolution. In recent years, lipase B from *Candida antarctica* (CAL-B) has been frequently applied.[265,266] Meanwhile, chemocatalysts are very popular for racemization. Often, Pd, Fe, Ir, or Ru catalysts are used.[267–269]

The synthesis of secondary alcohols is highly important because they are common functional groups in drugs and natural products, such as the natural product (–)-rosemarinecine[270,271] or Formoterol[272], which is used as a bronchodilator (Scheme 7.2). In recent years, the group of Akai worked intensively on this topic, especially on the combination of lipases with vanadium-based catalysts.[273–277]

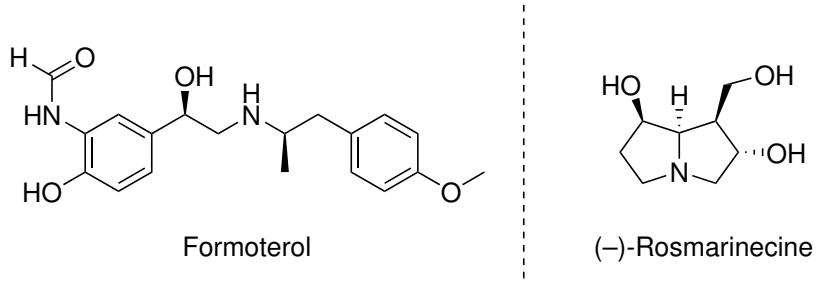

Scheme 7.2: Examples of molecules with chiral secondary alcohol moieties: Formoterol and (–)-rosmarinecine.

A reaction mechanism for the racemization using immobilized vanadium species was proposed in the literature (Scheme 7.3).[275] The racemic alcohol **A** is attacked by an *oxo*-vanadium species in mesoporous silica to form the cationic intermediate **B**. As this cationic species is in equilibrium with the corresponding alcohol **A**, the enantiomers are racemized. The (*R*)-**A** enantiomer is then converted to the acetate (*R*)-**C** by a lipase. As an unwanted side reaction, the attack of a nucleophilic alcohol **A** on the electrophilic cation **B** yields ether **D**.

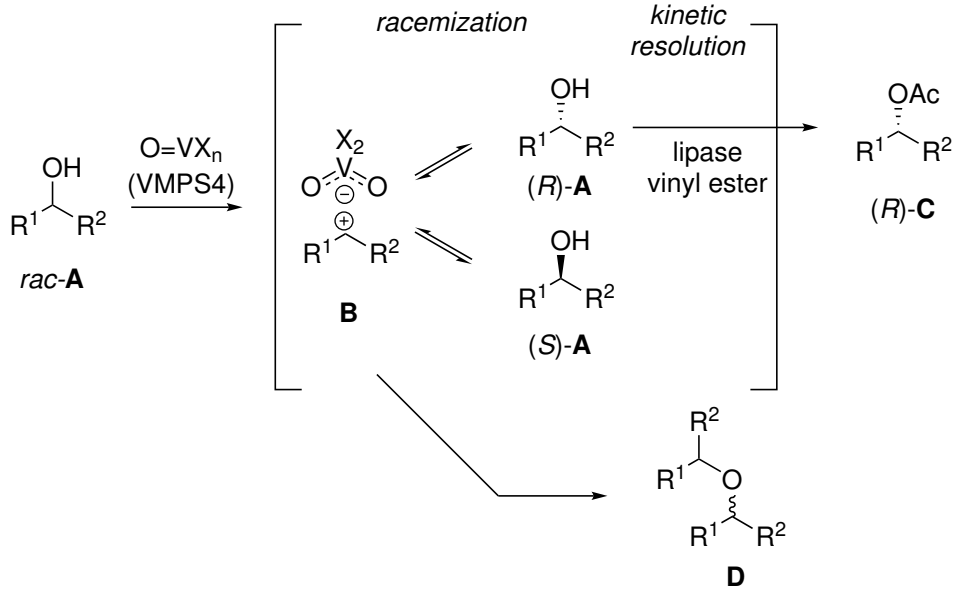

Scheme 7.3: Dynamic kinetic resolution of a secondary alcohol enabled by an immobilized vanadium catalyst (VMPS4) and a lipase (CAL-B; adapted and modified from Higashio *et al.*).[278] R^1, vinyl, benzyl; R^2, methyl, ethynyl; X, siloxyl.

7.2 Towards Continuous Flow Dynamic Kinetic Resolution

The goal of this project is the translation of a batch process for the dynamic kinetic resolution of allylic or benzylic alcohols developed by the group of Akai[273] into a continuous flow process. As a model substrate, alcohol **18** will be used (Scheme 7.4).

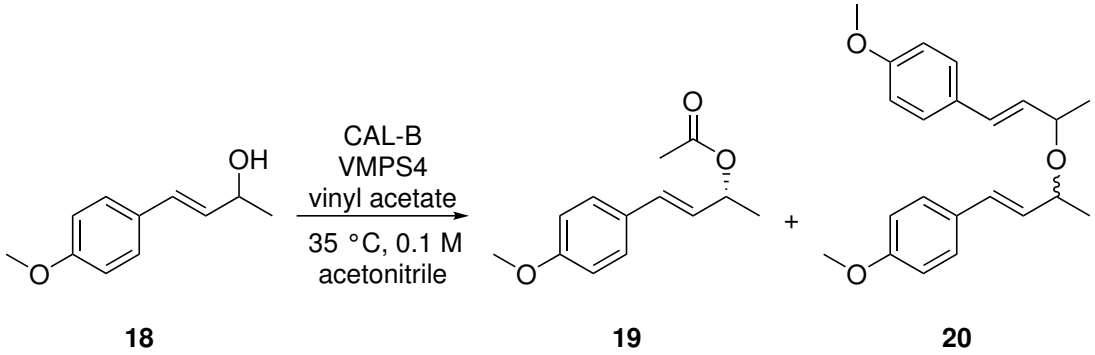

Scheme 7.4: Dynamic kinetic resolution of alcohol **18** to acetate (*R*)-**19** and side product **20**.

Preliminary research performed by the Akai group revealed a major issue when conducting the reaction in a packed bed reactor (Figure 7.1). As the catalyst concentration within the packed bed was increased in comparison with the batch mode, an undesired side reaction occurred.

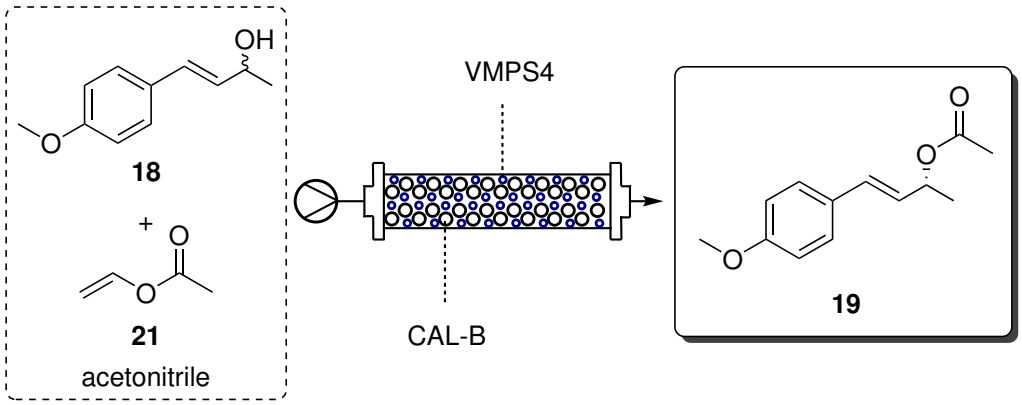

Figure 7.1: Schematic setup of the continuous flow dynamic kinetic resolution of alcohol **18** to acetate (*R*)-**19**.

To avoid this side reaction, in this study, both processes—kinetic resolution as well as racemization—will be initially investigated separately. After

initial experiments with a mixed bed reactor, a solution to the side product formation will be developed by designing the catalyst bed in a gradient manner.

7.2.1 Lipase-catalyzed Acylation

First, the acylation of (*R*)-**18** using vinyl acetate (**21**) as acetyl donor and lipase CAL-B as catalyst was investigated in a packed bed reactor. The starting material **18** was synthesized according to literature.[276] A range of residence times from 0.5 to 5 min was used. An Omnifit® column was used as the packed bed reactor and the temperature was maintained at 35 °C by a high-performance liquid chromatography column oven. The starting material **18** solution had a concentration of 0.1 M in acetonitrile.

As for the setup, a packed bed reactor was charged with a homogeneous mixture of immobilized CAL-B and silica or DualPore silica, respectively. The reaction mixture was pumped with a syringe pump over the catalyst bed, which was placed in a column oven. After an equilibration time equal to three residence times, to ensure steady state, a fraction was collected and analyzed.

Table 7.1: Lipase-catalyzed kinetic resolution of alcohol (*rac*)-**18** in a packed bed reactor using vinyl acetate **21** as acetyl donor.

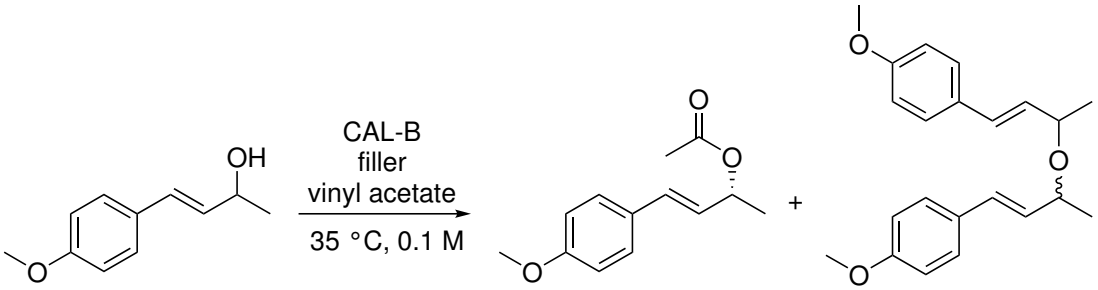

18 **19** **20**

Entry	*Residence time / min*	*Flow rate / mL min^{-1}*	*Percentage in crude mixture (ee-value)*[a]	
			*acetate (R)-**19***	*alcohol **18***
1	0.5	1.64	16% (99.9 %ee)	84%
2	1	0.82	26% (99.9 %ee)	72%
3	1.5	0.62	31% (99.9 %ee)	67%
4	2	0.41	38% (99.8 %ee)	60%
5	5	0.164	49% (99.7 %ee)	51%

[a] Determined by HPLC and ^{1}H NMR.

As shown in Table 7.1, the conversion to (*R*)-**19** proceeded completely within 5 min residence time with very high ee values of > 99 %ee. Therefore, a fast process should not be limited by the kinetic resolution of alcohol **18**. Furthermore, no traces of the undesired side product **20** were detected. This finding suggests that the racemization catalyst causes the side product formation.

7.2.2 Vanadium-catalyzed Racemization of Chiral Alcohols

Next, the vanadium-catalyzed racemization of an enantiomerically enriched starting material solution was investigated (Table 7.2). The same setup and conditions described in the previous subsection was used; however, the catalyst CAL-B was replaced by VMPS4. A range of residence times from

2 to 20 min was used. An optimal catalyst ratio was derived by comparing the reaction rates of racemization and kinetic resolution.

Table 7.2: Vanadium-catalyzed racemization of enantiomerically enriched alcohol (*S*)-**18** in a packed bed reactor.

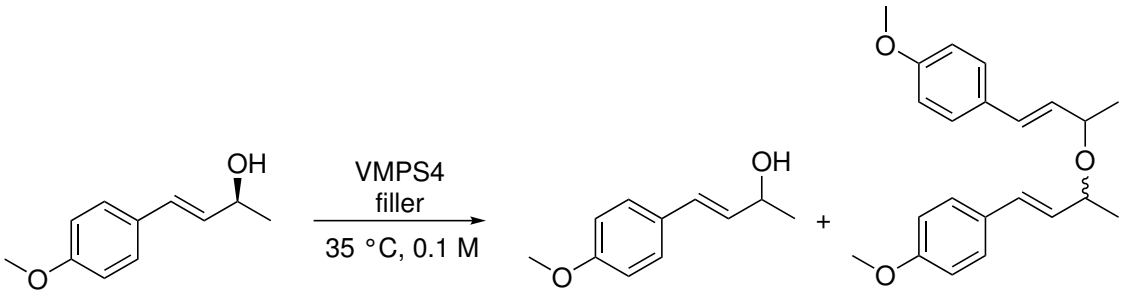

(*S*)-**18** *rac*-**18** **20**

Entry	*Residence time / min*	*Flow rate / mL min^{-1}*	*Percentage in crude mixture (ee-value)*[a]	
			*alcohol **18***	*ether **20***
1	2	0.45	72% (42 %ee)	28%
2	5	0.18	55% (18 %ee)	45%
3	10	0.09	36% (n.d.)	64%
4	20	0.045	38% (n.d.)	80%

[a] Determined by HPLC and ^{1}H NMR.

As expected, the racemization suffered under the formation of side product **20**. Within 5 min, the alcohol was nearly racemized (18 %ee); however, 45% of alcohol **18** was converted to ether **20**. Again, the reaction was found to be quite fast, facilitating an efficient DKR process.

7.2.3 Dynamic Kinetic Resolution

After the single processes were investigated, the dynamic kinetic resolution of the racemic alcohol could be studied. Different filler materials as well as reactor concepts were used and evaluated. For all reactions, the same conditions as previously were used: A reaction temperature of 35 °C and a substrate concentration of 0.1 M in acetonitrile.

7.2.3.1 Mixed Bed Reactor

Initially, both heterogeneous catalysts were mixed with a filler material, which was needed to adjust the reactor volume and reduce the void volume in the reactor bed to prevent particle movement and separation. Two filler materials, silica for column chromatography and DualPore silica, were tested.

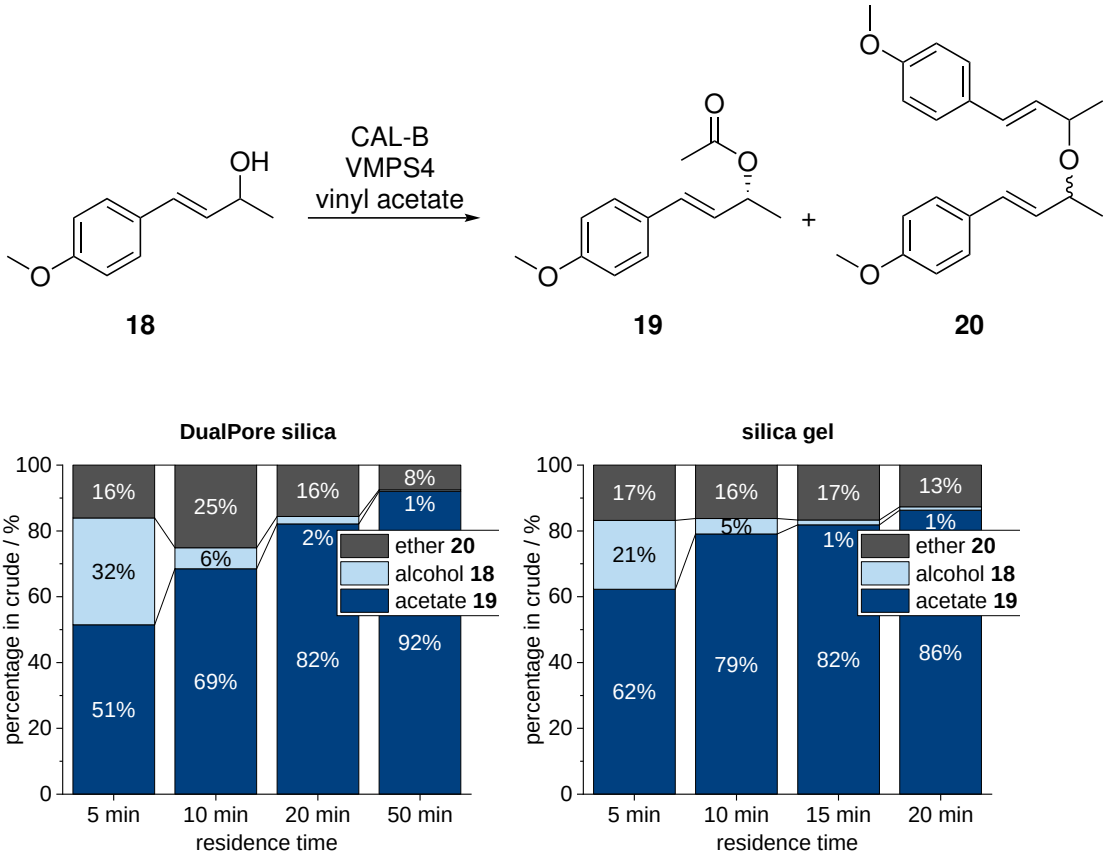

Figure 7.2: Comparison of the effect of filler materials on the dynamic kinetic resolution of alcohol (*rac*)-**18** to acetate (*R*)-**19**. Percentages of each compound in the crude reaction mixture with the use of either DualPore silica (left) or silica for column chromatography (right) as determined by ^{1}H NMR.

It was observed, that the conversion to acetate (*R*)-**19** was slightly higher in the case of silica as filler material. For example, when using a residence time of 5 min, the conversion was 10% higher (Figure 7.2) in the reaction using silica than in that using DualPore silica. However, one major issue using DualPore silica was the inhomogeneity of the catalyst bed as VMPS4 and DualPore silica were separated from CAL-B (Figure 7.3) by the fluid stream. Therefore, no reproducible results were obtained, as can be seen

in the irregular trend of ether formation under different residence times (Figure 7.2, left).

Figure 7.3: Particle separation of DualPore silica and CAL-B after a reaction (approximately 5 h operating time).

In the case of silica, this issue was not observed. Additionally, a test using colorized silica (SiO_2·$CuSO_4$), showed that the simulated catalyst bed was stable in terms of separation (Figure 7.4).

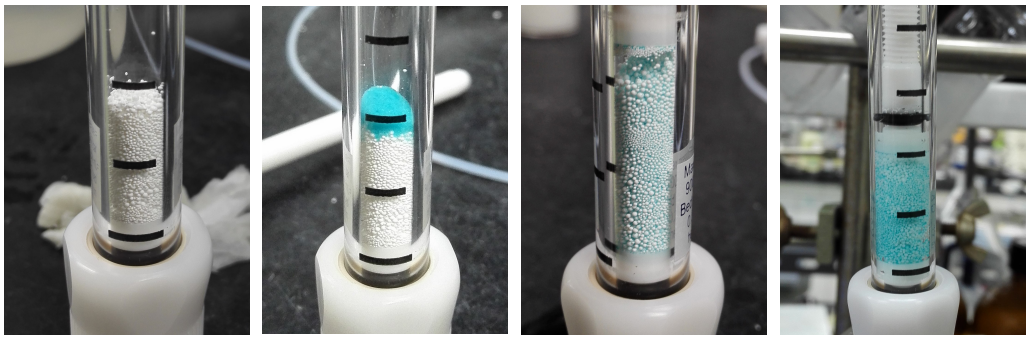

Figure 7.4: Simulation of a packed bed reactor using CAL-B and $SiO_2 \cdot CuSO_4$. 1: Filling of CAL-B. 2: Filling of silica. 3: Mixing of catalyst bed by shaking. 4: After packing the reactor bed tightly and flushing the reactor with approximately 10 mL solvent at different flow rates.

Because the catalyst ratio influences the side product formation, different ratios were tested. VMPS4:CAL-B ratios ranging from 1:3 to 1:9 were used at different residence times. For each catalyst ratio, a reactor was packed, then different residence times were screened by adjusting the flow rate. The experiments were performed in a random order, to avoid unwanted effects of factors such as the catalyst degradation.

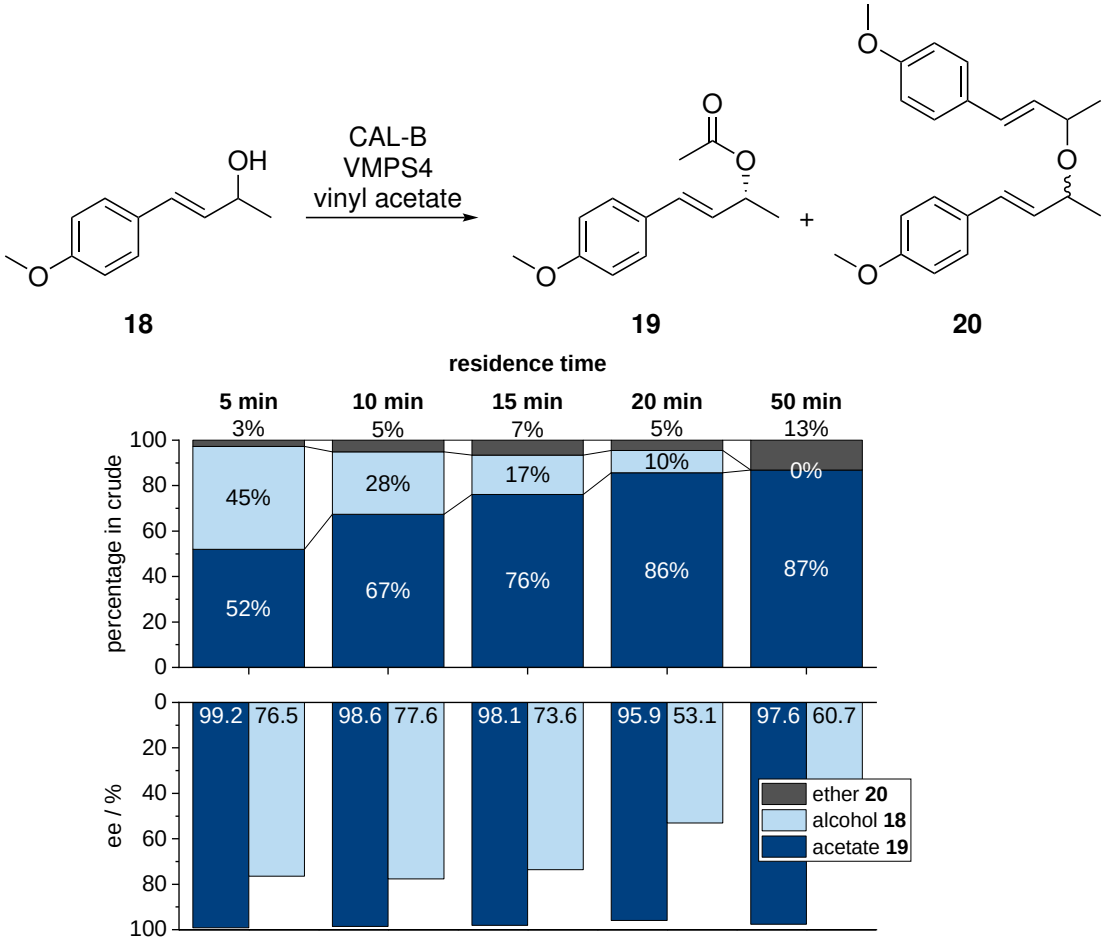

Figure 7.5: Percentage of compounds in the crude mixture and corresponding ee values for different residence times of the dynamic kinetic resolution of alcohol (*R*)-**18** using a homogeneously packed bed reactor with a catalyst ratio of 1:9 (33 mg VMPS4, 300 mg CAL-B).

Figure 7.5 shows that the conversion is strongly dependent on residence time. With longer residence time, the proportion of the desired product (*R*)-**19** increased from 52 to 87%, whereas the ee value of the desired product slightly decreased from 99.2 to 97.6 %ee. Furthermore, more complete racemization of alcohol **18** was observed. However, the formation of the unwanted ether **20** also increased from 3% to 13%.

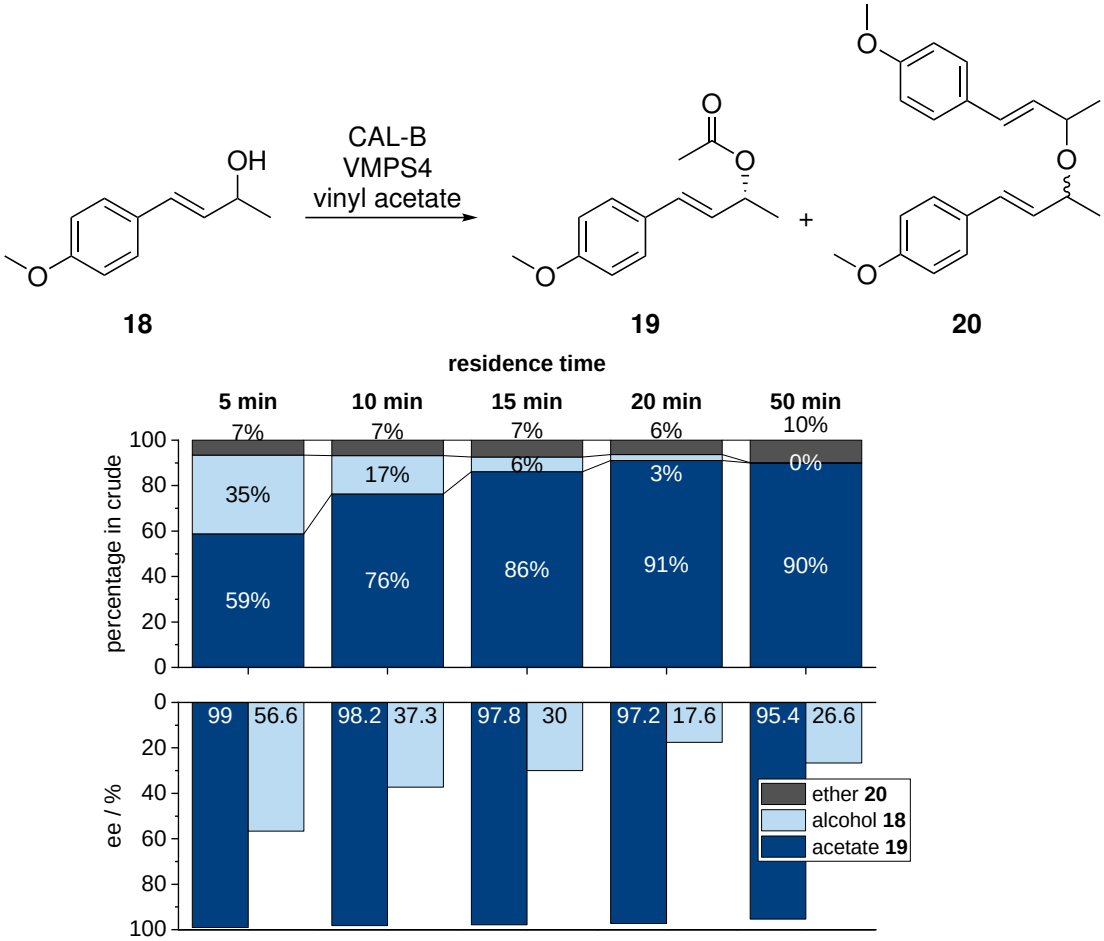

Figure 7.6: Percentage of compounds in the crude mixture and corresponding ee values for different residence times of the dynamic kinetic resolution of alcohol (*rac*)-**18** using a homogenously packed bed reactor with a catalyst ratio of 1:6 (50 mg VMPS4 and 300 mg CAL-B).

Increasing the quantity of VMPS4 in the mixed bed reactor raised both the conversion to the desired product (*R*)-**19** and the undesired product **20** (Figure 7.6). Moreover, the selectivity decreases slightly, and the racemization appeared to be more complete.

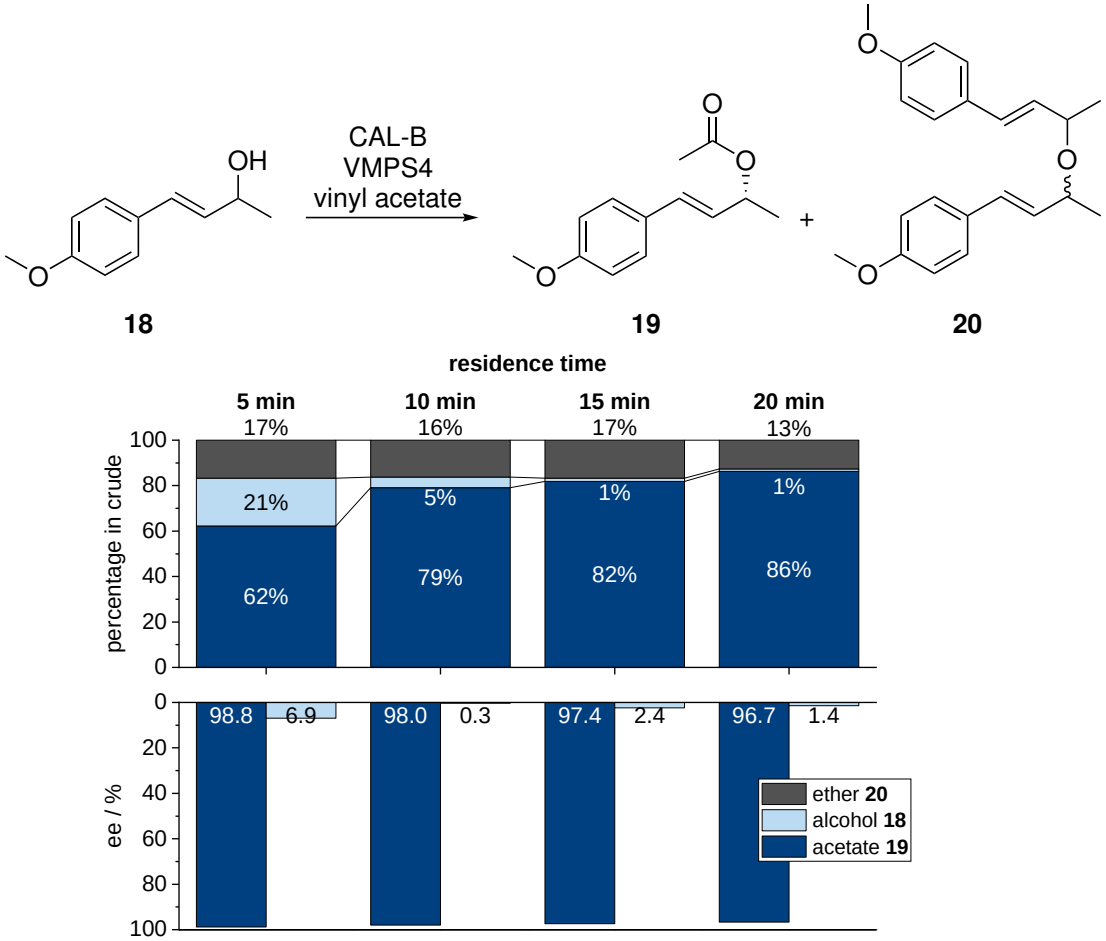

Figure 7.7: Percentage of compounds in the crude mixture and corresponding ee values for different residence times of the dynamic kinetic resolution of alcohol (*rac*)-**18** using a homogeneously packed bed reactor with a catalyst ratio of 1:3 (100 mg VMPS4 and 300 mg CAL-B).

As seen in Figures 7.5–7.7, the conversion to acetate (*R*)-**19** proceeded faster for higher VMPS4 loadings, probably owing to the higher rate of racemization of alcohol **18**. Moreover, the formation of ether **20** increased (up to 14%). Both results can be explained by the increased VMPS4 concentration on the catalyst bed. The lowest quantity of ether **20** formed under short reaction time of 5 min and a very low loading of VMPS4. However, a 62% conversion to acetate (*R*)-**19** is not sufficient for an efficient process. By increasing the residence time to 20 min, a conversion to acetate (*R*)-**19** of 86% was achieved, with formation of only 13% ether **20**.

7.2.3.2 Gradient Packed Bed Reactor

In theory, a decreasing gradient of the VMPS4-to-CAL-B ratio would be ideal to prevent the formation of ether **20** and still ensure an efficient process. With this design, the concentration of the cationic intermediate **B** can be minimized during the reaction.

This effect can be well understood with a view on kinetics based on a simplified reaction scheme (Scheme 7.8). For the product formation (Scheme 7.8 a), the reaction rate r is dependent on the concentration of alcohol **A** as well as water to regenerate the alcohol. However, the diffusion of cleaved water is presumably slower compared to the reaction; therefore, it is immediately available for the reaction. Thus, the concentration of water in the reaction equation can be neglected. With respect to the side product formation, the reaction rate depends on two molecules of alcohol **A**, one for the cation **B** formation and one for the ether formation.

This theory suggests that the side product formation depends more on the alcohol concentration. Following this argumentation, the racemization, rather than the kinetic resolution, should be limiting to the reaction. In theory, a very low quantity of the racemization catalyst should minimize the side product formation. However, such a process would take a long reaction time and is not suitable. Nevertheless, to exploit this theory, a gradient can be designed to initially ensure a rapid kinetic resolution and subsequently facilitate efficient racemization.

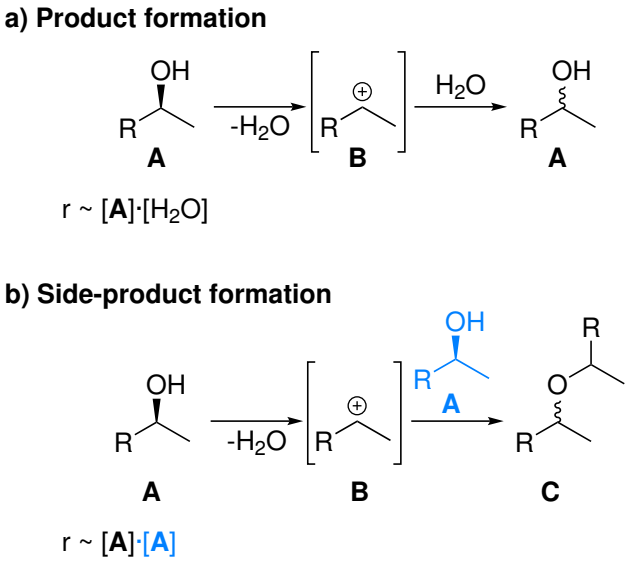

Figure 7.8: Simplified reactions in context of the VMPS4-catalyzed racemization to form the product (racemized alcohol) or side product (ether **C**) from the alcohol **A** over the cationic intermediate **B**.

Therefore, a reactor was filled with three layers of catalyst mixtures with increasing catalyst ratios. In the first experiment, a combination of the previously tested ratios (1:9, 1:6, 1:3; VMPS4:CAL-B) were used, resulting in an average ratio of 1:5. The setup is illustrated in Figure 7.9.

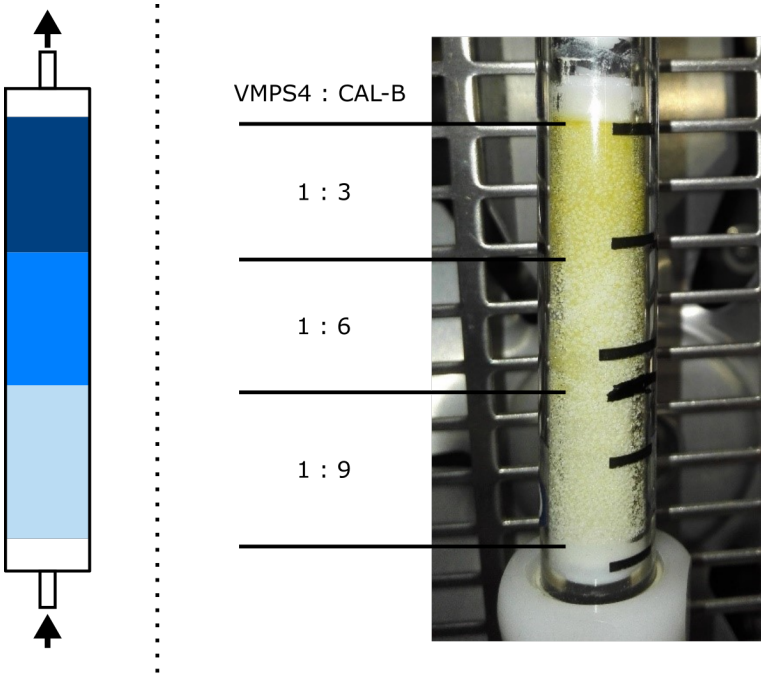

Figure 7.9: Three-layered packed bed reactor with VMPS4 and CAL-B. Left: Schematic of the setup. Right: Photo of the reactor.

In comparison with the closest ratio tested in a homogeneously packed bed (1:6) the conversion to acetate (*R*)-**19** was increased by 7% and the conversion to ether **20** decreased by 2%. Moreover, the racemization of alcohol **18** appeared to be faster with the gradient packed bed (13 %ee vs. 37 %ee; Figure 7.10).

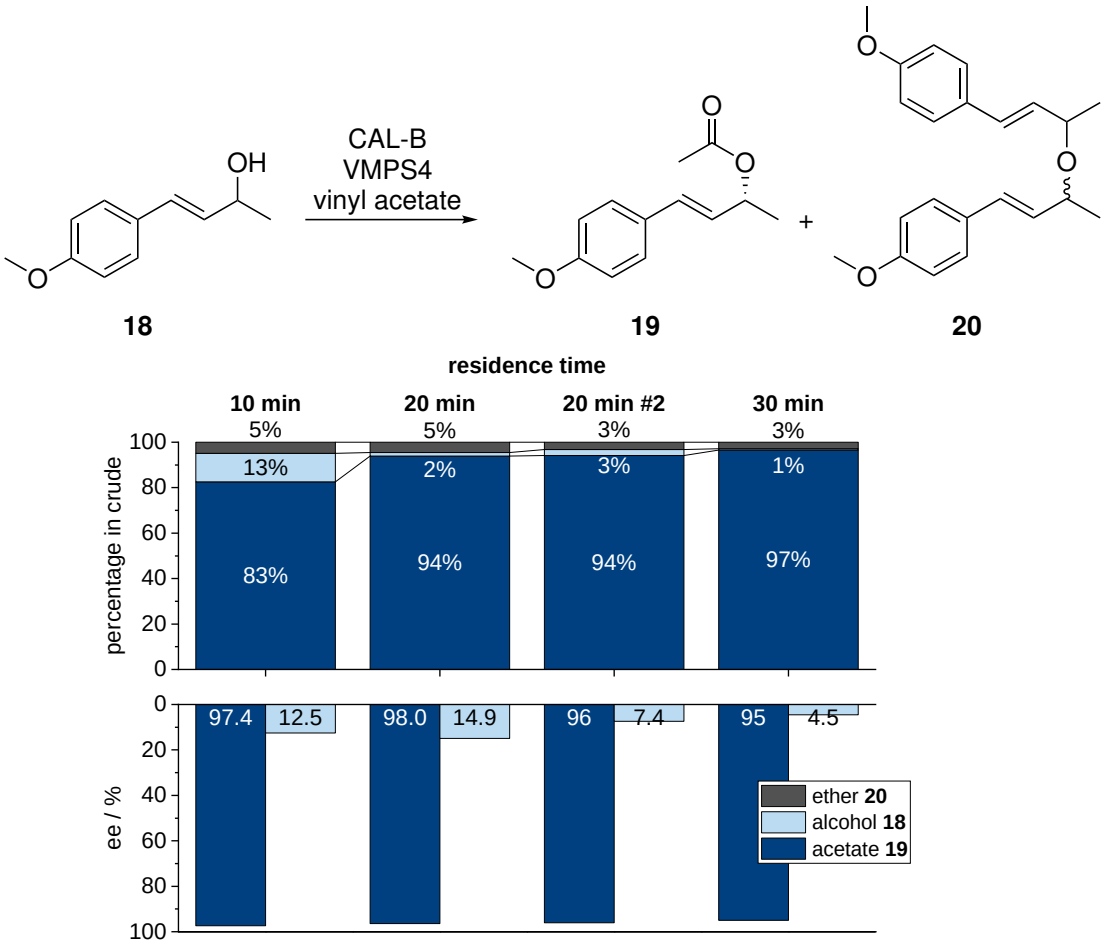

Figure 7.10: Percentage of compounds in the crude mixture and corresponding ee values for different residence times of the dynamic kinetic resolution of alcohol (*rac*)-**18** using a three-layer packed bed reactor (1:9, 1:6, 1:3; VMPS4:CAL-B) with an average catalyst ratio of 1:5.

Furthermore, the reproducibility of the reactor was tested by repeating the first experiment (20 min residence time) at the end of the screening set. It was observed that both results were identical, considering analysis error. Furthermore, the gradient of VMPS4 could be observed visually and did not appear to change during the reaction. Therefore, the reaction system is considered to be stable over the entire run time.

Since the ee values of the alcohol **18** were very low, the racemization should not be the limiting factor of the reaction system forming acetate (*R*)-**19**. Therefore, VMPS4 loading may be lowered further to minimize the side product formation. In the following experiment based on these findings, a four-layer reactor (1:40, 1:9, 1:6, 1:4; VMPS4:CAL-B) with an average ratio of 1:7 was used. The reaction was performed with a residence time of 30 min.

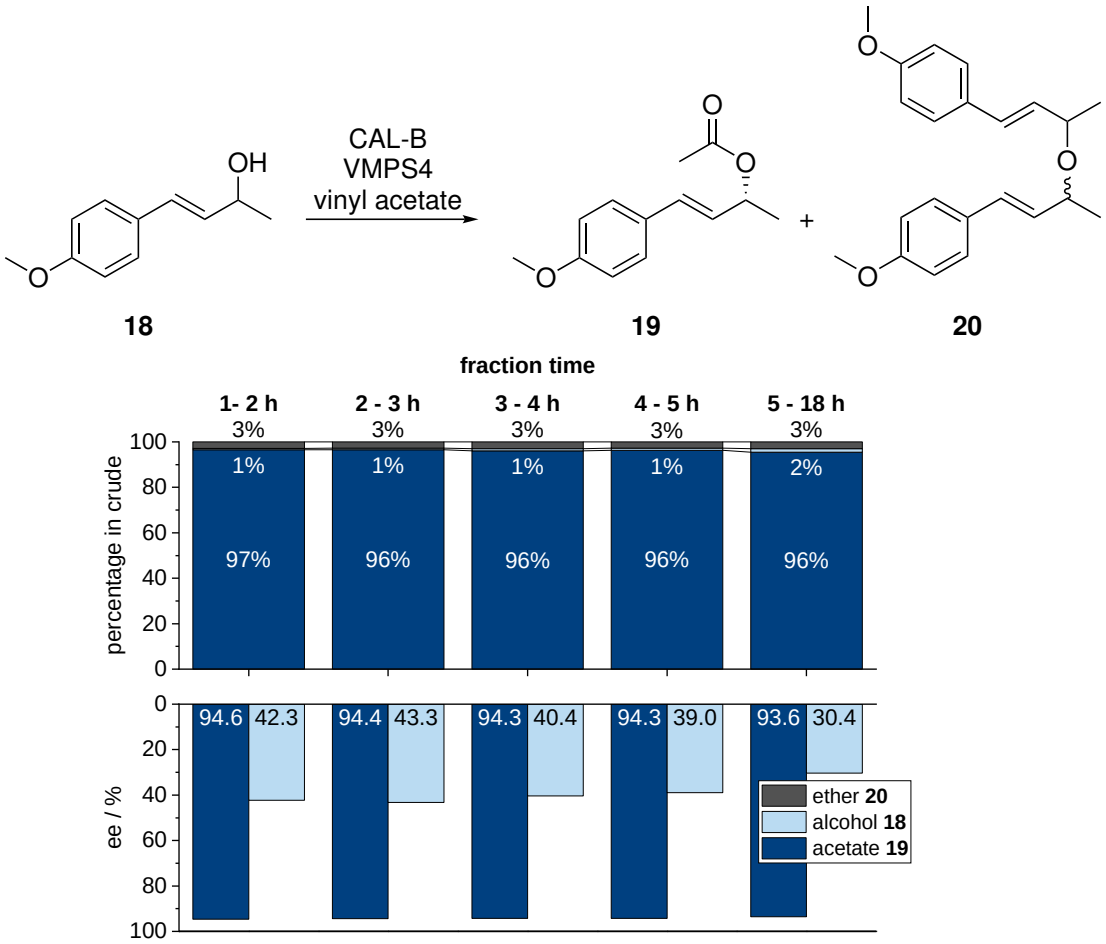

Figure 7.11: Percentage of compounds in the crude mixture and corresponding ee values of the dynamic kinetic resolution of alcohol (*rac*)-**18** using a four-layer packed bed reactor (1:40, 1:9, 1:6, 1:4; VMPS4:CAL-B) with an average catalyst ratio of 1:7 for different collected fractions.

As shown in Figure 7.11, the conversion to acetate (*R*)-**19** is stable at 96% for at least more than 18 h with formation of only 3% ether **20**, and traces of leftover alcohol **18** were observed. Compared to the previously investigated gradient reactor, a 30% lower VMPS4 loading was used, which provided the same results except for approximately 40% higher ee values for the traces of

remaining alcohol **18**. However, the ee values of acetate **19** were relatively low (94%), which can be explained by the relatively high residence time.

Furthermore, the effect of different reaction temperatures was investigated.

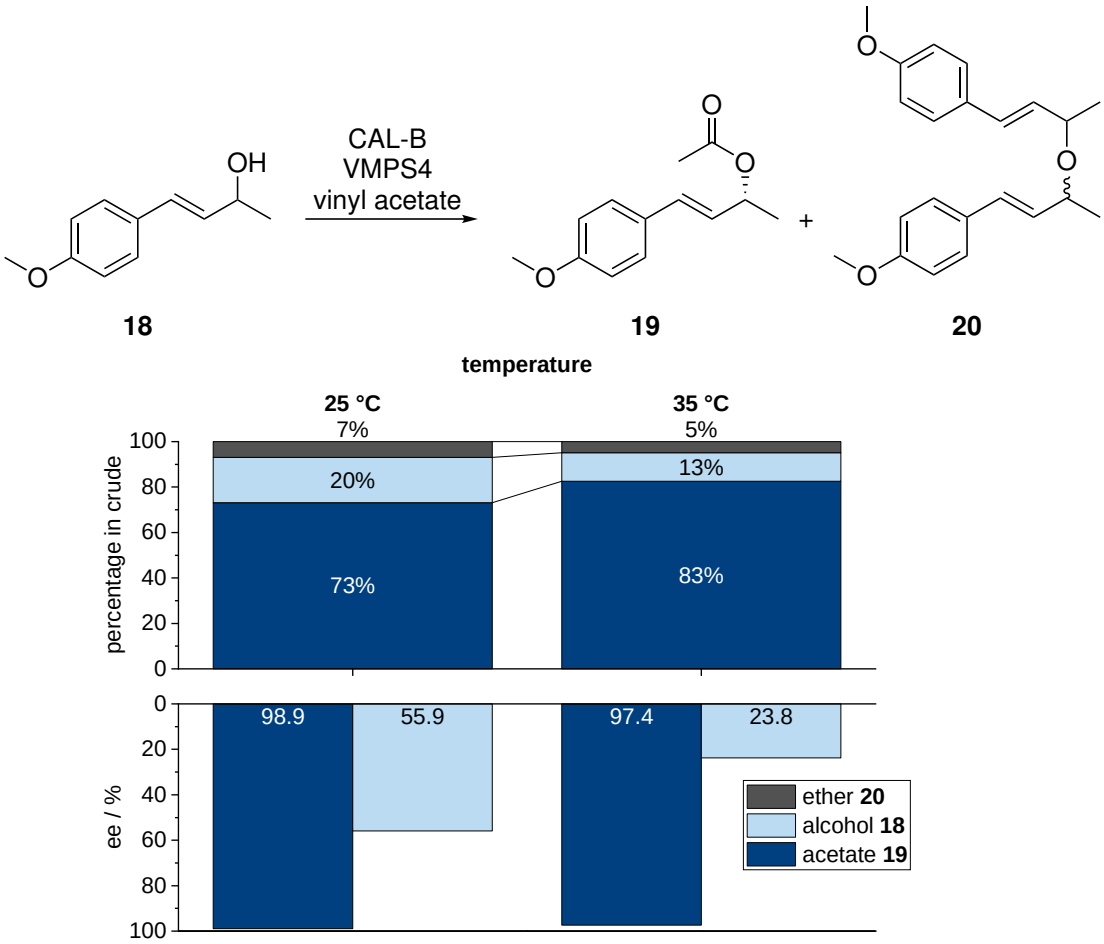

Figure 7.12: Percentage of compounds in the crude mixture and corresponding ee values of the dynamic kinetic resolution of alcohol (*rac*)-**18** under different reaction temperatures using a three-layer packed bed reactor with an average catalyst ratio of 1:5 for different collected fractions. A residence time of 10 min was used.

As expected, the conversion to the desired product (*R*)-**19** was higher (10%) when higher temperatures were used (Figure 7.12). In accordance with this finding, the ee values of the remaining alcohol **18** were much lower in the case of higher temperatures. However, the conversion to the undesired ether **20** was not significantly affected. The ee value of acetate **19** was slightly increased when lower temperatures were used.

7.3 Summary

In this study, the challenge of side product formation was successfully resolved by the development of an innovative gradient dual-catalyst packed bed reactor. Silica was shown to be an efficient filler material, especially in terms of reproducibility. Regarding the catalyst ratio, a multi-layer packed bed reactor was shown to be the best choice to avoid the formation of ether. A lower reaction temperature did not improve the reaction system regarding product and side product formation. Moreover, it was shown that the multi-layer packed bed reactor can be run stably for at least 18 h. The ee values of 94% for the desired product in the multi-layer packed bed reactor are relatively lower than those in batch experiments (99 %ee). Improvements may be achieved by further optimization of residence time and catalyst ratio.

7.4 Experimental

7.4.1 General Working Conditions

In general, the reactions were carried out in commercial anhydrous solvents. Argon was used as inert gas.

7.4.2 Chemicals & Equipment

The following equipment was used for the reactions in this Chapter 7. The equipment and chemicals were provided by the group of Shuji Akai (Osaka University, Japan). The commercial starting materials were used without further purification, unless noted otherwise.

Packed bed reactor: Omnifit® EZ SolventPlus™ column complete AF set (inner diameter 6.6 mm, bed length 100 mm) with an adjustable endpiece and a fixed endpiece, purchased from Diba Industries Inc., USA.

PTFE tubing: Outer diameter 1/16, inner diameter 1/32.

Syringe pump: Catamaran HII-10, purchased from Techno Applications Co., Ltd., Japan.

Candida antarctica lipase B (CAL-B) immobilized on an acrylic resin (commercial name: Novozym 435 or Chirazyme L-2 C4) was purchased from Roche Diagnostics K. K., Japan and was used as received without further purification.

VMPS4 (vanadium content: 0.2 mmol/mg) prepared according to literature was kindly provided by the group of Akai.[276]

Silica filler materials: DualPore™ silica beads (particle size: 0.020–0.063 mm, density: 0.16 g/mL) consisting of micro-sized through-pores (pore size 0.5–1 μm) and nano-sized pores (pore size 20 nm), available from DPS Inc., was used as received without further purification. Silica gel 60N pur-

chased from Kanto Chemical Co., Inc., Japan was used for column chromatography. All reagents were of reagent grade.

7.4.3 Analytics

^{1}H NMR spectra were recorded on a JEOL JNM-ECA500 spectrometer (500 MHz) in chloroform-d1, referenced internally to the residual solvent peaks in ppm (chloroform-d1: 7.26 ppm (s)), and analyzed using MestReNova. Chemical shifts σ are reported in ppm to the nearest 0.01 ppm. The multiplicity of ^{1}H signals are indicated as following: s = singlet, d = doublet, dd = doublet of doublet, t = triplet, q = quadruplet, m = multiplet, or combinations thereof. Coupling constants (J) are reported in Hz to the nearest 0.1 Hz.

HPLC analyses were carried out using a JASCO LC-2000Plus system (HPLC pump: PU-2080, UV detector: MD-2018) equipped with Daicel CHIRALPAK AD-3 with a size of 4.6 mm × 250 mm.

7.4.4 Synthesis of (*rac*)-(*E*)-4-(4-Methoxypehnyl)but-3-en-2-ol (18)

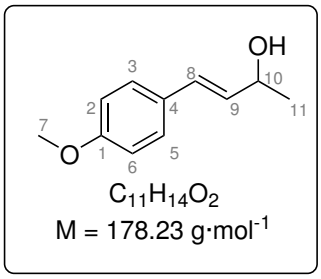

In a dried flask, *p*-methoxycinnamaldehyde (29.0 mmol, 4.70 g) was dissolved in dry diethyl ether (150 mL) and cooled in an acetone/dry ice bath (−78 °C). Methyl lithium solution (1.16 M in Et_2O, 29.0 mmol, 25 mL) was added over 20 min and the mixture was stirred at −78 °C for 30 min. Then, the cooling bath was removed, and the mixture was allowed to heat up to room temperature. The mixture was stirred for 2 h at room temperature and quenched with aqueous NH_4Cl solution (sat., 40 mL). Water (50 mL) was added, the phases were separated, and the aqueous phase was extracted with DCM (1 x 100 mL). The combined organic phases were dried over $MgSO_4$, the solvent was removed, and the crude product was purified with silica column chromatography (eluent: EtOAc) to give the product **18** in

1.9 g yield (10.7 mmol, 37%) as yellow solid. The product was analyzed with ^{1}H NMR.

^{1}H NMR (500 MHz, $CDCl_3$): δ [ppm] = 7.36–7.27 (m, 2H, Ar-*H*), 6.89–6.81 (m, 2H, Ar-*H*), 6.54–6.46 (m, 1H, C(8)*H*), 6.12 (dd, $^{3,3}J$ = 15.9, 6.6 Hz, 1H, C(9)*H*), 4.50–4.42 (m, 1H, C(10)*H*), 3.80 (s, 3H, C(7)*H*), 1.36 (d, ^3J = 6.4 Hz, 3H, C(11)*H*).

7.4.5 Synthesis of (*rac*)-(*E*)-4-(4-Methoxypehnyl)but-3-en-2-yl acetate (19)

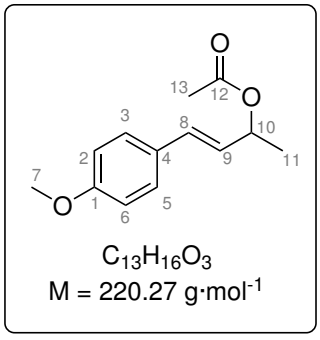

$C_{13}H_{16}O_3$
M = 220.27 g·mol^{-1}

(*E*)-4-(4-methoxypehnyl)but-3-en-2-ol (**18**; 1 eq, 1.8 mmol, 312 mg) and acetic anhydride (1.9 eq, 3.5 mmol, 331 μL) were filled into a dried flask, dissolved in DCM (5 mL) and cooled to 0 °C. Triethylamine (1.9 eq, 3.5 mmol, 486 μL) and DMAP (0.09 eq, 0.17 mmol, 21 mg) were dissolved in DCM (5 mL) and added to the reaction mixture. After stirring for 15 min at 0 °C, the mixture was allowed to warm up to room temperature and stirred for 3 h. The organic phase was washed with $NaHCO_3$ solution, phases were separated, and the aqueous phase was extracted with DCM (2 x 5 mL). Finally, the combined organic phases were dried over $MgSO_4$, the solvent was removed under reduced pressure and the crude mixture was purified by column chromatography to yield the desired racemic acetate **19**.

^{1}H NMR (500 MHz, $CDCl_3$): δ [ppm] = 7.37–7.28 (m, 2H, Ar-*H*), 6.87–6.81 (m, 2H, Ar-*H*), 6.59–6.51 (m, 1H, C(8)*H*), 6.04 (dd, $^{3,3}J$ = 15.9, 6.9 Hz, 1H, C(9)*H*), 5.50 (pd, $^{3,4}J$ = 6.5, 1.1 Hz, 1H, C(10)*H*), 3.80 (s, 3H, C(13)*H*), 2.06 (s, 3H, C(7)*H*), 1.39 (d, ^3J = 6.5 Hz, 3H, C(11)*H*).

7.4.6 Kinetic Resolution of Alcohol 18 in Flow

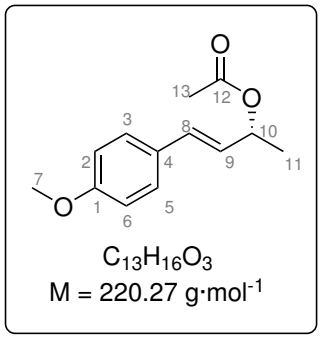

A glass reactor (Omifit® column) was charged with CAL-B (300 mg) and silica gel (for column chromatography, 100 mg), evacuated in a desiccator and flushed with argon. Then, the reactor bed was homogenized by shaking of the reactor tube with loosely attached end pieces. After the reactor was firmly packed by screwing in the end pieces, the reactor volume was determined visually by flushing with acetonitrile. The reactor was placed in a column oven and heated to 35 °C. The substrate solution was prepared by dissolving (*E*)-4-(4-methoxypehnyl)but-3-en-2-ol (**18**; 2.0 mmol, 356 mg) and vinyl acetate (4 eq, 8.0 mmol, 0.74 mL) in dry acetonitrile (20 mL) and then partially transferred into a syringe (gas-tight, 10 mL). The syringe was connected to the reactor using PTFE tubing and attached to the syringe pump. To start the reaction, the syringe pump was set to different flow rates corresponding to a residence time of 2–20 min and switched on. When the syringe was empty, it was refilled with the reaction mixture. Fractions of the reaction mixture collected after a certain equilibration time (3 x residence time) in glass vials were analyzed *via* ^{1}H NMR and HPLC.

Acetate **19**:
^{1}H NMR (500 MHz, $CDCl_3$): δ [ppm] = 7.37–7.28 (m, 2H, Ar-*H*), 6.87–6.81 (m, 2H, Ar-*H*), 6.59–6.51 (m, 1H, C(8)*H*), 6.04 (dd, $^{3,3}J$ = 15.9, 6.9 Hz, 1H, C(9)*H*), 5.50 (pd, $^{3,4}J$ = 6.5, 1.1 Hz, 1H, C(10)*H*), 3.80 (s, 3H, C(13)*H*), 2.06 (s, 3H, C(7)*H*), 1.39 (d, ^3J = 6.5 Hz, 3H, C(11)*H*).

Ether **20** (1:1 mixture of diastereomeres):
^{1}H NMR (500 MHz, $CDCl_3$): δ [ppm] = 7.38–7.24 (m, 4H, Ar-*H*), 6.91–6.78 (m, 4H, Ar-*H*), 6.45 (d, ^3J = 14.1 Hz, 1H, Ar-C*H*-), 6.42 (d, ^3J = 13.5 Hz, 1H, Ar-C*H*-), 5.96 (dd, $^{3,3}J$ = 15.9, 7.9 Hz, 2H, Ar-CH=C*H*-), 4.23–4.16 (m, 1H, -C*H*-CH_3), 4.16–4.10 (m, 1H, -C*H*-CH_3), 3.82 (s, 3H, CO-CH_3), 3.80 (s, 3H, CO-CH_3), 1.33 (d, ^3J = 6.3 Hz, 3H, -CH_3-CH-), 1.30 (d, ^3J = 6.4 Hz, 3H, -CH_3-CH-).

HPLC: Alcohol (*R*)-**18** 10.28 min, (*S*)-**18** 11.58 min, acetate (*R*)-**19** 9.77 min, (*S*)-**19** 11.65 min.

Table 7.3: Lipase-catalyzed kinetic resolution of alcohol **18** in a packed bed reactor using vinyl acetate **21** as acetyl donor. The experiments were carried out in random order.

Entry	*Residence time / min*	*Flow rate / mL min^{-1}*	*Percentage in crude mixture (ee-value)*[a]	
			*acetate (R)-**19***	*alcohol **18***
1	0.5	1.64	16% (99.9 %ee)	84%
2	1	0.82	26% (99.9 %ee)	72%
3	1.5	0.62	31% (99.9 %ee)	67%
4	2	0.41	38% (99.8 %ee)	60%
5	5	0.164	49% (99.7 %ee)	51%

[a] Determined by HPLC and ^{1}H NMR.

7.4.7 Racemization of Alcohol 18 in Flow

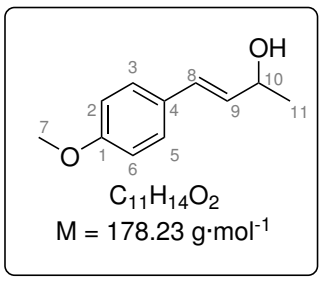

VMPS4 (100 g) and silica (DualPore silica, 100 mg) were filled in the reactor (Omifit® column) before it was evacuated and flushed with argon. Then, the reactor bed was homogenized by shaking of the reactor tube with loosely attached end pieces. After the reactor was firmly packed by screwing in the end pieces, the reactor volume was determined by flushing with acetonitrile. The reactor was placed in a column oven and heated to 35 °C. The substrate solution was prepared by dissolving (*E*)-4-(4-methoxypehnyl)but-3-en-2-ol (**18**; 1.5 mmol, 267.4 mg, 95 %ee) in dry acetonitrile (15 mL) and then partially transferred into a syringe (gas-tight, 10 mL). The syringe was connected to the reactor using PTFE tubing and attached to the syringe pump. To start the reaction, the syringe pump was set to different flow rates corresponding to a residence time of 2–20 min and switched on. Fractions of the reaction mixture collected after a certain equilibration time (3 x residence time) in glass vials were analyzed *via* ^{1}H NMR and HPLC.

Acetate **19**:
^{1}H NMR (500 MHz, $CDCl_3$): δ [ppm] = 7.37–7.28 (m, 2H, Ar-*H*), 6.87–6.81 (m, 2H, Ar-*H*), 6.59–6.51 (m, 1H, C(8)*H*), 6.04 (dd, $^{3,3}J$ = 15.9, 6.9 Hz, 1H, C(9)*H*), 5.50 (pd, $^{3,4}J$ = 6.5, 1.1 Hz, 1H, C(10)*H*), 3.80 (s, 3H, C(13)*H*), 2.06 (s, 3H, C(7)*H*), 1.39 (d, ^3J = 6.5 Hz, 3H, C(11)*H*).

Ether **20** (1:1 mixture of diastereomeres):
^{1}H NMR (500 MHz, $CDCl_3$): δ [ppm] = 7.38–7.24 (m, 4H, Ar-*H*), 6.91–6.78 (m, 4H, Ar-*H*), 6.45 (d, ^3J = 14.1 Hz, 1H, Ar-C*H*-), 6.42 (d, ^3J = 13.5 Hz, 1H, Ar-C*H*-), 5.96 (dd, $^{3,3}J$ = 15.9, 7.9 Hz, 2H, Ar-CH=C*H*-), 4.23–4.16 (m, 1H, -C*H*-CH_3), 4.16–4.10 (m, 1H, -C*H*-CH_3), 3.82 (s, 3H, CO-CH_3), 3.80 (s, 3H, CO-CH_3), 1.33 (d, ^3J = 6.3 Hz, 3H, -CH_3-CH-), 1.30 (d, ^3J = 6.4 Hz, 3H, -CH_3-CH-).

HPLC: Alcohol (*R*)-**18** 10.28 min, (*S*)-**18** 11.58 min, acetate (*R*)-**19** 9.77 min, (*S*)-**19** 11.65 min.

Table 7.4: Lipase-catalyzed kinetic resolution of alcohol **18** in a packed bed reactor using vinyl acetate **21** as acetyl donor. The experiments were carried out in random order.

Entry	*Residence time / min*	*Flow rate / mL min^{-1}*	*Percentage in crude mixture (ee-value)*[a]	
			*alcohol **18***	*ether **20***
1	20	0.045	20% (n. d.)	80%
2	10	0.09	36% (n. d.)	64%
3	5	0.18	55% (18 %ee)	45%
4	2	0.45	72% (42 %ee)	28%

[a] Determined by HPLC and ^{1}H NMR.

7.4.8 DKR of Alcohol 18 in Flow

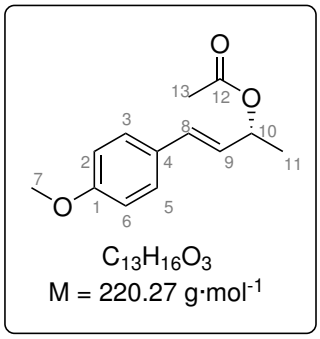

A glass reactor (Omifit® column) was charged with CAL-B (300 mg), silica gel (for column chromatography) and VMPS4 before it was evacuated and flushed with argon. Then, the reactor bed was homogenized by shaking of the reactor tube with loosely attached end pieces. After the reactor was firmly packed by screwing in the end pieces, the reactor volume was determined visually by flushing with acetonitrile. The reactor was placed in a column oven and heated to 35 °C. The substrate solution was prepared by dissolving the (*E*)-4-(4-methoxypehnyl)but-3-en-2-ol (**18**; 2.0 mmol, 356 mg) and vinyl acetate (4.0 eq·, 8.0 mmol, 0.74 mL) in dry acetonitrile (20 mL) and then partially transferred into a syringe (gas-tight, 10 mL). The syringe was connected to the reactor using PTFE tubing and attached to the syringe pump. To start the reaction, the syringe pump was set to different flow rates corresponding to a residence time of 5–50 min and switched on. For each flow rate, after a volume of 2.5 mL was pumped, a volume of 1 mL was collected in glass vials and analyzed *via* ^{1}H NMR and HPLC.

Acetate **19**:
^{1}H NMR (500 MHz, $CDCl_3$): δ [ppm] = 7.37–7.28 (m, 2H, Ar-*H*), 6.87–6.81 (m, 2H, Ar-*H*), 6.59–6.51 (m, 1H, C(8)*H*), 6.04 (dd, $^{3,3}J$ = 15.9, 6.9 Hz, 1H, C(9)*H*), 5.50 (pd, $^{3,4}J$ = 6.5, 1.1 Hz, 1H, C(10)*H*), 3.80 (s, 3H, C(13)*H*), 2.06 (s, 3H, C(7)*H*), 1.39 (d, ^3J = 6.5 Hz, 3H, C(11)*H*).

Ether **20** (1:1 mixture of diastereomeres):
^{1}H NMR (500 MHz, $CDCl_3$): δ [ppm] = 7.38–7.24 (m, 4H, Ar-*H*), 6.91–6.78 (m, 4H, Ar-*H*), 6.45 (d, ^3J = 14.1 Hz, 1H, Ar-C*H*-), 6.42 (d, ^3J = 13.5 Hz, 1H, Ar-C*H*-), 5.96 (dd, $^{3,3}J$ = 15.9, 7.9 Hz, 2H, Ar-CH=C*H*-), 4.23–4.16 (m, 1H, -C*H*-CH_3), 4.16–4.10 (m, 1H, -C*H*-CH_3), 3.82 (s, 3H, CO-CH_3), 3.80 (s, 3H, CO-CH_3), 1.33 (d, ^3J = 6.3 Hz, 3H, -CH_3-CH-), 1.30 (d, ^3J = 6.4 Hz, 3H, -CH_3-CH-).

HPLC: Alcohol (*R*)-**18** 10.28 min, (*S*)-**18** 11.58 min, acetate (*R*)-**19** 9.77 min, (*S*)-**19** 11.65 min.

Table 7.5: Results for the DKR of alcohol **18** to acetate (*R*)-**19**. Reactor volume was determined as 850 µL. VMPS4 (33 mg), silica (167 mg). The experiments were carried out in random order.

Entry	*Residence time / min*	*Flow rate / mL min^{-1}*	*Percentage in crude mixture (ee-value)*[a]		
			*acetate (R)-**19***	*alcohol **18***	*ether **20***
1	5	0.17	52% (99.2 %ee)	45% (75.5 %ee)	3%
2	10	0.085	67% (98.6 %ee)	28% (77.6 %ee)	5%
3	15	0.057	76% (98.1 %ee)	17% (73.6 %ee)	7%
4	20	0.043	86% (95.9 %ee)	10% (53.1 %ee)	5%
5	50	0.017	87% (97.6 %ee)	< 1% (60.7 %ee)	13%

[a] Determined by HPLC and ^{1}H NMR.

Table 7.6: Results for the DKR of alcohol **18** to acetate (*R*)-**19**. Reactor volume was determined as 870 µL. VMPS4 (50 mg), silica (150 mg). The experiments were carried out in random order.

Entry	*Residence time / min*	*Flow rate / mL min^{-1}*	*Percentage in crude mixture (ee-value)*[a]		
			*acetate (R)-**19***	*alcohol **18***	*ether **20***
1	5	0.17	59% (95.4 %ee)	35% (56.6 %ee)	7%
2	10	0.087	76% (98.2 %ee)	17% (37.3 %ee)	7%
3	15	0.058	86% (97.8 %ee)	6% (30.0 %ee)	7%
4	20	0.044	91% (97.2 %ee)	3% (17.6 %ee)	6%
5	50	0.017	90% (95.4 %ee)	< 1% (26.6 %ee)	10%

[a] Determined by HPLC and ^{1}H NMR.

Table 7.7: Results for the DKR of alcohol **18** to acetate (*R*)-**19**. Reactor volume was determined as 900 μL. VMPS4 (100 mg), silica (100 mg). The experiments were carried out in random order.

Entry	*Residence time / min*	*Flow rate / mL min^{-1}*	*Percentage in crude mixture (ee-value)*[a]		
			*acetate (R)-**19***	*alcohol **18***	*ether **20***
1	5	0.18	62% (98.8 %ee)	21% (6.9 %ee)	17%
2	10	0.09	79% (98.0 %ee)	5% (0.3 %ee)	16%
3	15	0.06	82% (97.4 %ee)	2% (2.4 %ee)	17%
4	20	0.045	86% (96.7 %ee)	1% (1.4 %ee)	13%

[a] Determined by HPLC and ^{1}H NMR.

Table 7.8: Results for the DKR of alcohol **18** to acetate (*R*)-**19**. Reactor volume was determined as 1320 μL. VMPS4 (100 mg), DualPore silica (100 mg) instead of silica for column chromatography. The experiments were carried out in random order.

Entry	*Residence time / min*	*Flow rate / mL min^{-1}*	*Percentage in crude mixture (ee-value)*[a]		
			*acetate (R)-**19***	*alcohol **18***	*ether **20***
1	5	0.264	52% (99.4 %ee)	32% (5.7 %ee)	16%
2	10	0.132	69% (98.1 %ee)	6% (0.5 %ee)	25%
3	20	0.066	82% (97.4 %ee)	3% (1.6 %ee)	16%
4	50	0.026	92% (94.4 %ee)	< 1% (5.8 %ee)	8%

[a] Determined by HPLC and ^{1}H NMR.

7.4.9 DKR of Alcohol 18 in Flow with a Gradient Packed Bed Reactor

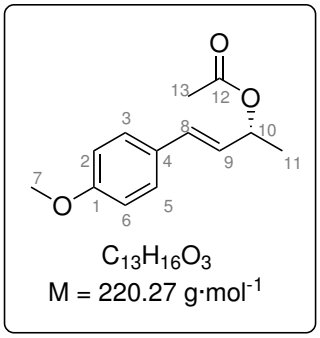

A glass reactor (Omifit® column) was charged with different layers of a mixture of VMPS4, silica and CAL-B. The mixture for each layer was mixed in a dried flask, portion-wise filled with a spatula in the reactor and the layer was then carefully mixed inside the reactor with a small spatula. After the reactor was firmly packed by screwing in the end pieces, the reactor volume was determined visually by flushing with acetonitrile. The reactor was placed in a column oven and heated to 35 °C. The substrate solution was prepared by dissolving the (*E*)-4-(4-methoxypehnyl)but-3-en-2-ol (**18**; 1 eq, 2.0 mmol, 356 mg) and vinyl acetate (4.0 eq, 8.0 mmol, 0.74 mL) in dry acetonitrile (20 mL) and then partially transferred into a syringe (gas-tight, 10 mL). The syringe was connected to the reactor using PTFE tubing and attached to the syringe pump. To start the reaction, the syringe pump was set to different flow rates corresponding to a residence time of 10–30 min and switched on. For each flow rate, after a volume of 2.5 mL was pumped, a volume of 1 mL was collected in glass vials and analyzed *via* ^{1}H NMR and HPLC.

Acetate **19**:
^{1}H NMR (500 MHz, $CDCl_3$): δ [ppm] = 7.37–7.28 (m, 2H, Ar-*H*), 6.87–6.81 (m, 2H, Ar-*H*), 6.59–6.51 (m, 1H, C(8)*H*), 6.04 (dd, $^{3,3}J$ = 15.9, 6.9 Hz, 1H, C(9)*H*), 5.50 (pd, $^{3,4}J$ = 6.5, 1.1 Hz, 1H, C(10)*H*), 3.80 (s, 3H, C(13)*H*), 2.06 (s, 3H, C(7)*H*), 1.39 (d, ^3J = 6.5 Hz, 3H, C(11)*H*).

Ether **20** (1:1 mixture of diastereomeres):
^{1}H NMR (500 MHz, $CDCl_3$): δ [ppm] = 7.38–7.24 (m, 4H, Ar-*H*), 6.91–6.78 (m, 4H, Ar-*H*), 6.45 (d, ^3J = 14.1 Hz, 1H, Ar-C*H*-), 6.42 (d, ^3J = 13.5 Hz, 1H, Ar-C*H*-), 5.96 (dd, $^{3,3}J$ = 15.9, 7.9 Hz, 2H, Ar-CH=C*H*-), 4.23–4.16 (m, 1H, -C*H*-CH_3), 4.16–4.10 (m, 1H, -C*H*-CH_3), 3.82 (s, 3H, CO-CH_3), 3.80 (s, 3H, CO-CH_3), 1.33 (d, ^3J = 6.3 Hz, 3H, -CH_3-CH-), 1.30 (d, ^3J = 6.4 Hz, 3H, -CH_3-CH-).

HPLC: Alcohol (*R*)-**18** 10.28 min, (*S*)-**18** 11.58 min, acetate (*R*)-**19** 9.77 min, (*S*)-**19** 11.65 min.

Table 7.9: Results for the DKR of alcohol **18** to acetate (*R*)-**19**. Reactor volume was determined as 890 µL. First layer: VMPS4 (11 mg), silica (89 mg), second layer: VMPS4 (17 mg), silica (83 mg), third layer: VMPS4 (33 mg), silica (77 mg). The experiments were carried out in random order expect Entry 3 was the first experiment and Entry 4 was the last.

Entry	*Residence time / min*	*Flow rate / mL min^{-1}*	*Percentage in crude mixture (ee-value)*[a]		
			acetate ***19***	*alcohol* ***18***	*ether* ***20***
1[b]	10	0.089	83% (97.4 %ee)	13% (23.8 %ee)	5%
2	10	0.089	73% (98.9 %ee)	20% (55.9 %ee)	7%
3	20	0.045	94% (96.4 %ee)	2% (14.9 %ee)	5%
4	20	0.045	94% (96.0 %ee)	3% (n. d.)	3%
5	30	0.030	97% (95.0 %ee)	< 1% (n. d.)	3%

[a] Determined by HPLC and ^{1}H NMR. [b] Temperature: 25 °C.

Table 7.10: Results for the DKR of alcohol **18** to acetate (*R*)-**19**. Reactor volume was determined as 710 µL. First layer: VMPS4 (2.5 mg), silica (47.5 mg), second layer: VMPS4 (8 mg), silica (42 mg), third layer: VMPS4 (13 mg), silica (37 mg), fourth layer: VMPS4 (20 mg), silica (30 mg).

Entry	*Run time*	*Percentage in crude mixture (ee-value)*[a]		
		acetate (R)- ***19***	*alcohol* ***18***	*ether* ***20***
1	1–2 h	97% (94.6 %ee)	1% (42.3 %ee)	3%
2	2–3 h	96% (94.4 %ee)	1% (43.3 %ee)	3%
3	3–4 h	96% (94.3 %ee)	1% (40.4 %ee)	3%
4	4–5 h	96% (94.3 %ee)	1% (39.0 %ee)	3%
5	5–16.5 h	96% (93.6 %ee)	2% (30.4 %ee)	3%

[a] Determined by HPLC and ^{1}H NMR.

References

1. Loarie, S. R. *et al.* The velocity of climate change. *Nature* **462,** 1052–1055 (2009).
2. Shafiee, S. & Topal, E. When will fossil fuel reserves be diminished? *Energy Policy* **37,** 181–189 (2009).
3. Tollefson, J. & Weiss, K. R. Nations approve historic global climate accord. *Nature* **528,** 315–316 (2015).
4. *United Nations Treaty Collection* `https://treaties.un.org/Pages/ViewDetails.aspx?src=TREATY&mtdsg_no=XXVII-7-d&chapter=27&clang=_en` (2021).
5. Lipinsky, E. S. Chemicals from biomass: Petrochemical substitution options. *Science* **212,** 1465–1471 (1981).
6. Wang, F. *et al.* Lignocellulosic biomass as sustainable feedstock and materials for power generation and energy storage. *J. Energy Chem.* **57,** 247–280 (2021).
7. Alonso, D. M. *et al.* Increasing the revenue from lignocellulosic biomass: Maximizing feedstock utilization. *Sci. Adv.* **3,** e1603301 (2017).
8. Ragauskas, A. J. *et al.* Lignin valorization: Improving lignin processing in the biorefinery. *Science* **344,** 1246843 (2014).
9. Abomohra, A. E. F. *et al.* Microalgal biomass production as a sustainable feedstock for biodiesel: Current status and perspectives. *Renew. Sustain. Energy Rev.* **64,** 596–606 (2016).
10. Wargacki, A. J. *et al.* An engineered microbial platform for direct biofuel production from brown macroalgae. *Science* **335,** 308–313 (2012).
11. Tuck, C. O., Pérez, E., Horváth, I. T., Sheldon, R. A. & Poliakoff, M. Valorization of biomass: Deriving more value from waste. *Science* **337,** 695–699 (2012).
12. Pulidindi, I. N., Kimchi, B. B. & Gedanken, A. Can cellulose be a sustainable feedstock for bioethanol production? *Renew. Energy* **71,** 77–80 (2014).

13. Appel, A. M. *et al.* Frontiers, opportunities, and challenges in biochemical and chemical catalysis of CO2 fixation. *Chem. Rev.* **113,** 6621–6658 (2013).

14. Cokoja, M., Bruckmeier, C., Rieger, B., Herrmann, W. A. & Kühn, F. E. Transformation of Carbon Dioxide with Homogeneous Transition-Metal Catalysts: A Molecular Solution to a Global Challenge? *Angew. Chem. Int. Ed.* **50,** 8510–8537 (2011).

15. Aresta, M., Dibenedetto, A. & Angelini, A. Catalysis for the valorization of exhaust carbon: From CO2 to chemicals, materials, and fuels. technological use of CO2. *Chem. Rev.* **114,** 1709–1742 (2014).

16. Langanke, J. *et al.* Carbon dioxide (CO2) as sustainable feedstock for polyurethane production. *Green Chem.* **16,** 1865–1870 (2014).

17. Kadam, K. L. & McMillan, J. D. Availability of corn stover as a sustainable feedstock for bioethanol production. *Bioresour. Technol.* **88,** 17–25 (2003).

18. Gui, M. M., Lee, K. T. & Bhatia, S. Feasibility of edible oil vs. non-edible oil vs. waste edible oil as biodiesel feedstock. *Energy* **33,** 1646–1653 (2008).

19. Kumar, A. & Sharma, S. Potential non-edible oil resources as biodiesel feedstock: An Indian perspective. *Renew. Sustain. Energy Rev.* **15,** 1791–1800 (2011).

20. Coma, M. *et al.* Organic waste as a sustainable feedstock for platform chemicals. *Faraday Discuss.* **202,** 175–195 (2017).

21. Sheldon, R. A. Green and sustainable manufacture of chemicals from biomass: State of the art. *Green Chem.* **16,** 950–963 (2014).

22. Takkellapati, S., Li, T. & Gonzalez, M. A. An overview of biorefinery-derived platform chemicals from a cellulose and hemicellulose biorefinery. *Clean Technol. Environ. Policy* **20,** 1615–1630 (2018).

23. Bungay, H. R. Biomass Refining. *Science* **218,** 643–646 (1982).

24. Palsson, B. O., Fathi-Afshar, S., Rudd, D. F. & Lightfoot, E. N. Biomass as a source of chemical feedstocks: An economic evaluation. *Science* **213,** 513–517 (1981).

25. Kucherov, F. A., Romashov, L. V., Galkin, K. I. & Ananikov, V. P. Chemical Transformations of Biomass-Derived C6-Furanic Platform Chemicals for Sustainable Energy Research, Materials Science, and Synthetic Building Blocks. *ACS Sustain. Chem. Eng.* **6,** 8064–8092 (2018).

26. Alonso, D. M., Wettstein, S. G. & Dumesic, J. A. Gamma-valerolactone, a sustainable platform molecule derived from lignocellulosic biomass. *Green Chem.* **15,** 584–595 (2013).

27. Rosatella, A. A., Simeonov, S. P., Frade, R. F. & Afonso, C. A. 5-Hydroxymethylfurfural (HMF) as a building block platform: Biological properties, synthesis and synthetic applications. *Green Chem.* **13,** 754–793 (2011).

28. Su, Y. *et al.* Single-step conversion of cellulose to 5-hydroxymethylfurfural (HMF), a versatile platform chemical. *Appl. Catal. A* **361,** 117–122 (2009).

29. Mariscal, R., Maireles-Torres, P., Ojeda, M., Sádaba, I. & López Granados, M. Furfural: A renewable and versatile platform molecule for the synthesis of chemicals and fuels. *Energy Environ. Sci.* **9,** 1144–1189 (2016).

30. Dutta, S., De, S., Saha, B. & Alam, M. I. Advances in conversion of hemicellulosic biomass to furfural and upgrading to biofuels. *Catal. Sci. Technol.* **2,** 2025–2036 (2012).

31. Chen, S., Wojcieszak, R., Dumeignil, F., Marceau, E. & Royer, S. How Catalysts and Experimental Conditions Determine the Selective Hydroconversion of Furfural and 5-Hydroxymethylfurfural. *Chem. Rev.* **118,** 11023–11117 (2018).

32. Lima, C. G., Monteiro, J. L., de Melo Lima, T., Weber Paixão, M. & Corrêa, A. G. Angelica Lactones: From Biomass-Derived Platform Chemicals to Value-Added Products. *ChemSusChem* **11,** 25–47 (2018).

33. Liu, S. *et al.* Renewable lubricants with tailored molecular architecture. *Sci. Adv.* **5** (2019).

34. Karan, H., Funk, C., Grabert, M., Oey, M. & Hankamer, B. Green Bioplastics as Part of a Circular Bioeconomy. *Trends Plant Sci.* **24,** 237–249 (2019).

35. Brodin, M., Vallejos, M., Opedal, M. T., Area, M. C. & Chinga-Carrasco, G. Lignocellulosics as sustainable resources for production of bioplastics – A review. *J. Clean. Prod.* **162,** 646–664 (2017).

36. Schneiderman, D. K. & Hillmyer, M. A. 50th Anniversary Perspective: There Is a Great Future in Sustainable Polymers. *Macromolecules* **50,** 3733–3749 (2017).

37. Dietrich, K., Dumont, M. J., Del Rio, L. F. & Orsat, V. Producing PHAs in the bioeconomy — Towards a sustainable bioplastic. *Sustain. Prod. Consum.* **9,** 58–70 (2017).

38. Álvarez-Chávez, C. R., Edwards, S., Moure-Eraso, R. & Geiser, K. Sustainability of bio-based plastics: General comparative analysis and recommendations for improvement. *J. Clean. Prod.* **23,** 47–56 (2012).

39. Umweltbundesamt. *Grüne Produkte in Deutschland 2017* tech. rep. (2017).

40. Sheldon, R. A. Engineering a more sustainable world through catalysis and green chemistry. *J. R. Soc. Interface* **13,** 20160087 (2016).

41. Hermann, B. G., Blok, K. & Patel, M. K. Producing bio-based bulk chemicals using industrial biotechnology saves energy and combats climate change. *Environ. Sci. Technol.* **41,** 7915–7921 (2007).

42. Clift, R. Sustainable development and its implications for chemical engineering. *Chem. Eng. Sci.* **61,** 4179–4187 (2006).

43. Anderson, K. & Peters, G. The trouble with negative emissions. *Science* **354,** 182–183 (2016).

44. Van Vuuren, D. P. *et al.* Alternative pathways to the 1.5 °C target reduce the need for negative emission technologies. *Nat. Clim. Change* **8,** 391–397 (2018).

45. Bomtempo, J. V., Chaves Alves, F. & De Almeida Oroski, F. Developing new platform chemicals: What is required for a new bio-based molecule to become a platform chemical in the bioeconomy? *Faraday Discuss.* **202,** 213–225 (2017).

46. Burnett, L. W., Johns, I. B., Holdren, R. F. & Hixon, R. M. Production of 2-Methylfuran by Vapor-Phase Hydrogenation of Furfural. *Ind. Eng. Chem. Res.* **40,** 502–505 (1948).

47. Vorotnikov, V., Mpourmpakis, G. & Vlachos, D. G. DFT study of furfural conversion to furan, furfuryl alcohol, and 2-methylfuran on Pd(111). *ACS Catal.* **2,** 2496–2504 (2012).

48. Sitthisa, S., An, W. & Resasco, D. E. Selective conversion of furfural to methylfuran over silica-supported NiFe bimetallic catalysts. *J. Catal.* **284,** 90–101 (2011).

49. Li, X. & Zhang, Y. The conversion of 5-hydroxymethyl furfural (HMF) to maleic anhydride with vanadium-based heterogeneous catalysts. *Green Chem.* **18,** 643–647 (2016).

50. Lan, J., Chen, Z., Lin, J. & Yin, G. Catalytic aerobic oxidation of renewable furfural to maleic anhydride and furanone derivatives with their mechanistic studies. *Green Chem.* **16,** 4351–4358 (2014).

51. Chatzidimitriou, A. & Bond, J. Q. Oxidation of levulinic acid for the production of maleic anhydride: breathing new life into biochemicals. *Green Chem.* **17,** 4367–4376 (2015).

52. Miller, R. & Bennett, G. Producing 2-Ethylhexanol by the Guerbet Reaction. *Ind. Eng. Chem. Res.* **53,** 33–36 (1961).

53. Poulikidou, S., Heyne, S., Grahn, M. & Harvey, S. Lifecycle energy and greenhouse gas emissions analysis of biomass-based 2-ethylhexanol as an alternative transportation fuel. *Energy Sci. Eng.* **7,** 851–867 (2019).

54. Bocqué, M., Voirin, C., Lapinte, V., Caillol, S. & Robin, J. J. Petro-based and bio-based plasticizers: Chemical structures to plasticizing properties. *J. Polym. Sci. A: Polym. Chem.* **54,** 11–33 (2016).

55. Diels, O. & Alder, K. Synthesen in der hydroaromatischen Reihe. *Liebigs Ann. Chem.* **460,** 98–122 (1928).

56. Kürti, L. & Czakó, B. *Strategic Applications of Named Reactions in Organic Synthesis* p. 810 (Elsevier B.V., 2005).

57. Nicolaou, K. C., Snyder, S. A., Montagnon, T. & Vassilikogiannakis, G. The Diels-Alder reaction in total synthesis. *Angew. Chem. Int. Ed.* **41,** 1668–1698 (2002).

58. Funel, J. A. & Abele, S. Industrial applications of the Diels-Alder reaction. *Angew. Chem. Int. Ed.* **52,** 3822–3863 (2013).

59. Domingo, L. R. & Sáez, J. A. Understanding the mechanism of polar Diels-Alder reactions. *Org. Biomol. Chem.* **7,** 3576–3583 (2009).

60. Kumar, A. Salt effects on Diels-Alder reaction kinetics. *Chem. Rev.* **101,** 1–19 (2001).

61. Goldstein, E., Beno, B. & Houk, K. N. Density functional theory prediction of the relative energies and isotope effects for the concerted and stepwise mechanisms of the Diels-Alder reaction of butadiene and ethylene. *J. Am. Chem. Soc.* **118,** 6036–6043 (1996).

62. Sauer, J. & Sustmann, R. Mechanistic Aspects of Diels-Alder Reactions: A Critical Survey. *Angew. Chem. Int. Ed.* **19,** 779–807 (1980).

63. Vermeeren, P., Hamlin, T. A., Fernández, I. & Bickelhaupt, F. M. How Lewis Acids Catalyze Diels–Alder Reactions. *Angew. Chem. Int. Ed.* **59,** 6201–6206 (2020).

64. Domingo, L. R., Ríos-Gutiérrez, M. & Pérez, P. Unveiling the lewis acid catalyzed diels-alder reactions through the molecular electron density theory. *Molecules* **25,** 2535 (2020).

65. Reymond, S. & Cossy, J. Copper-catalyzed diels - Alder reactions. *Chem. Rev.* **108,** 5359–5406 (2008).

66. Moyano, A. & Rios, R. Asymmetric Organocatalytic Cyclization and Cycloaddition Reactions. *Chem. Rev.* **111,** 4703–4832 (2011).

67. Vermeeren, P., Brinkhuis, F., Hamlin, T. A. & Bickelhaupt, F. M. How Alkali Cations Catalyze Aromatic Diels-Alder Reactions. *Chem. Asian J.* **15,** 1167–1174 (2020).

68. Beker, W., Gajewska, E. P., Badowski, T. & Grzybowski, B. A. Prediction of Major Regio-, Site-, and Diastereoisomers in Diels–Alder Reactions by Using Machine-Learning: The Importance of Physically Meaningful Descriptors. *Angew. Chem. Int. Ed.* **131,** 4563–4567 (2019).

69. Brückner, R. *Reaktionsmechanismen* (Springer, 2004).

70. Hoffmann, R. & Woodward, R. B. Orbital Symmetries and endo-exo Relationships in Concerted Cycloaddition Reactions. *J. Am. Chem. Soc.* **87,** 4388–4389 (1965).

71. Rehbein, J. & Carpenter, B. K. Do we fully understand what controls chemical selectivity? *Phys. Chem. Chem. Phys.* **13,** 20906–20922 (2011).

72. Wannere, C. S. *et al.* The existence of secondary orbital interactions. *J. Comput. Chem.* **28,** 344–361 (2007).

73. García, J. I., Mayoral, J. A. & Salvatella, L. Do secondary orbital interactions really exists? *Acc. Chem. Res.* **33,** 658–664 (2000).

74. Schneider, H. J. & Sangwan, N. K. Changes of Stereoselectivity in Diels-Alder Reactions by Hydrophobic Solvent Effects and by β-Cyclodextrin. *Angew. Chem. Int. Ed.* **26,** 896–897 (1987).

75. Berson, J. A., Hamlet, Z. & Mueller, W. A. The Correlation of Solvent Effects on the Stereoselectivities of Diels-Alder Reactions by Means of Linear Free Energy Relationships. A New Empirical Measure of Solvent Polarity. *J. Am. Chem. Soc.* **84,** 297–304 (1962).

76. Fringuelli, F., Piermatti, O., Pizzo, F. & Vaccaro, L. Recent Advances in Lewis Acid Catalyzed Diels-Alder Reactions in Aqueous Media. *Eur. J. Org. Chem.,* 439–455 (2001).

77. Houk, K. N. & Strozier, R. W. On Lewis Acid Catalysis of Diels-Alder Reactions. *J. Am. Chem. Soc.* **95,** 4094–4096 (1973).

78. Cadogan, D. F. & Howick, C. J. *Plasticizers* (Wiley-VCH, 2000).

79. Chandola, M. & Marathe, S. A QSPR for the plasticization efficiency of polyvinylchloride plasticizers. *J. Mol. Graph. Model.* **26,** 824–828 (2008).

80. Bundesinstitut für Arzneimittel und Medizinprodukte. *DEHP als Weichmacher in Medizinprodukten aus PVC Referenz-Nr.: 9211/0506* tech. rep. (2006).

81. European plasticisers. *Plasticisers* tech. rep. (2021).

82. EPA. *Draft Scope of the Risk Evaluation for Di-ethylhexyl Phthalate (1,2-Benzenedicarboxylic acid, 1,2-bis(2-ethylhexyl) ester)* tech. rep. (2020).

83. BASF SE. *Press release: Weichmacher für die PVC-Industrie nun auch auf Basisnachwachsenderund chemisch recycelter Rohstoffe erhältlich* `https://www.basf.com/global/de/media/news-releases/2021/04/p-21-187.html` (2021).

84. Kumar, S. Recent Developments of Biobased Plasticizers and Their Effect on Mechanical and Thermal Properties of Poly(vinyl chloride): A Review. *Ind. Eng. Chem. Res.* **58,** 11659–11672 (2019).

85. Chen, J. *et al.* Synthesis and application of environmental soybean oil-based epoxidized glycidyl ester plasticizer for poly(vinyl chloride). *Eur. J. Lipid Sci. Technol.* **119,** 1600216 (2017).

86. He, W. *et al.* Green plasticizers derived from epoxidized soybean oil for poly (vinyl chloride): Continuous synthesis and evaluation in PVC films. *Chem. Eng. J.* **380,** 122532 (2020).

87. Tan, J. *et al.* Design and synthesis of ethoxylated esters derived from waste frying oil as anti-ultraviolet and efficient primary plasticizers for poly(vinyl chloride). *J. Clean. Prod.* **229,** 1274–1282 (2019).

88. Feng, G. *et al.* An efficient bio-based plasticizer for poly (vinyl chloride) from waste cooking oil and citric acid: Synthesis and evaluation in PVC films. *J. Clean. Prod.* **189,** 334–343 (2018).

89. Chen, J. *et al.* Synthesis and properties of a novel environmental epoxidized glycidyl ester of ricinoleic acetic ester plasticizer for poly(vinyl chloride). *Polymers* **9,** 640 (2017).

90. Zawada, K. *et al.* Esters of Tartaric Acid, A New Class of Potential "double Green" Plasticizers. *ACS Sustain. Chem. Eng.* **5,** 5999–6007 (2017).

91. Greco, A., Ferrari, F., Velardi, R., Frigione, M. & Maffezzoli, A. Solubility and durability of cardanol derived plasticizers for soft PVC. *Int. Polym. Process.* **31,** 577–586 (2016).

92. Briou, B., Caillol, S., Robin, J. J. & Lapinte, V. Non-endocrine disruptor effect for cardanol based plasticizer. *Ind. Crops Prod.* **130,** 1–8 (2019).

93. Plass, C. *Dissertation* (Bielefeld University, 2021).

94. Altemeier, B. *Masterthesis* (Bielefeld University, 2020).

95. Hayashi, Y., Nakamura, M., Nakao, S., Inoue, T. & Shoji, M. The HfCl4-mediated Diels-Alder reaction of furan. *Angew. Chem. Int. Ed.* **41,** 4079–4082 (2002).

96. Shannon, R. D. Revised effective ionic radii and systematic studies of interatomic distances in halides and chalcogenides. *Acta Cryst. A* **32,** 751–767 (1976).

97. Diedrich, M. *Bachelorthesis* (Bielefeld University, 2020).

98. Riisager, A., Wasserscheid, P., Van Hal, R. & Fehrmann, R. Continuous fixed-bed gas-phase hydroformylation using supported ionic liquid-phase (SILP) Rh catalysts. *J. Catal.* **219,** 452–455 (2003).

99. Riisager, A. *et al.* Very stable and highly regioselective supported ionic-liquid-phase (SILP) catalysis: Continuous-flow fixed-bed hydroformylation of propene. *Angew. Chem. Int. Ed.* **44,** 815–819 (2005).

100. Hagiwara, H., Sugawara, Y., Isobe, K., Hoshi, T. & Suzuki, T. Immobilization of Pd(OAc)2 in ionic liquid on silica: Application to sustainable Mizoroki-Heck reaction. *Org. Lett.* **6,** 2325–2328 (2004).

101. Gooch, J. W. in *Encyclopedic Dictionary of Polymers* p. 94 (Springer, 2011).

102. Matsuda, S. & Kikkawa, S. Properties of. Cyclohexane-carboxylates for Use as Plasticizers. *J. Soc. Chem. Ind. Jpn.* **62,** 1838–1841 (1959).

103. Adebar, N. *Masterthesis* (Bielefeld University, 2018).

104. Ihlenfeldt, W. D. & Gasteiger, J. Computer-assisted planning of organic syntheses: The second generation of programs. *Angew. Chem. Int. Ed.* **34,** 2613–2633 (1996).

105. Shen, Y. *et al.* Automation and computer-assisted planning for chemical synthesis. *Nat. Rev. Methods Primers* **1,** 23 (2021).

106. Coley, C. W., Green, W. H. & Jensen, K. F. Machine Learning in Computer-Aided Synthesis Planning. *Acc. Chem. Res.* **51,** 1281–1289 (2018).

107. Segler, M. H., Preuss, M. & Waller, M. P. Planning chemical syntheses with deep neural networks and symbolic AI. *Nature* **555,** 604–610 (2018).

108. Todd, M. H. Computer-aided organic synthesis. *Chem. Soc. Rev.* **34,** 247–266 (2005).

109. Sanderson, K. Automation: Chemistry shoots for the Moon. *Nature* **568,** 577–579 (2019).

110. Olsen, K. The first 110 years of laboratory automation: Technologies, applications, and the creative scientist. *J. Lab. Autom.* **17,** 469–480 (2012).

111. Tinnemans, S. J. *et al.* Combining operando techniques in one spectroscopic-reaction cell: New opportunities for elucidating the active site and related reaction mechanism in catalysis. *Catal. Today* **113,** 3–15 (2006).

112. Eifert, T. & Liauw, M. A. Process analytical technology (PAT) applied to biomass valorisation: A kinetic study on the multiphase dehydration of xylose to furfural. *React. Chem. Eng.* **1,** 521–532 (2016).

113. Nelder, J. A. & Mead, R. A Simplex Method for Function Minimization. *J. Comput.* **7,** 308–313 (1965).

114. Zettel, V. & Hitzmann, B. Optimization of the production parameters for bread rolls with the Nelder–Mead simplex method. *Food Bioprod. Process.* **103,** 10–17 (2017).

115. Sacco, W. F., Filho, H. A., Henderson, N. & de Oliveira, C. R. A Metropolis algorithm combined with Nelder-Mead Simplex applied to nuclear reactor core design. *Ann. Nucl. Energy* **35,** 861–867 (2008).

116. Fath, V., Kockmann, N., Otto, J. & Röder, T. Self-optimising processes and real-time-optimisation of organic syntheses in a microreactor system using Nelder-Mead and design of experiments. *React. Chem. Eng.* **5,** 1281–1299 (2020).

117. Cortés-Borda, D. *et al.* Optimizing the Heck-Matsuda Reaction in Flow with a Constraint-Adapted Direct Search Algorithm. *Org. Process Res. Dev.* **20,** 1979–1987 (2016).

118. McMullen, J. P., Stone, M. T., Buchwald, S. L. & Jensen, K. F. An integrated microreactor system for self-optimization of a heck reaction: From micro-to mesoscale flow systems. *Angew. Chem. Int. Ed.* **49,** 7076–7080 (2010).

119. Fitzpatrick, D. E., Battilocchio, C. & Ley, S. V. A Novel Internet-Based Reaction Monitoring, Control and Autonomous Self-Optimization Platform for Chemical Synthesis. *Org. Process Res. Dev.* **20,** 386–394 (2016).

120. Fitzpatrick, D. E., Maujean, T., Evans, A. C. & Ley, S. V. Across-the-World Automated Optimization and Continuous-Flow Synthesis of Pharmaceutical Agents Operating Through a Cloud-Based Server. *Angew. Chem. Int. Ed.* **57,** 15128–15132 (2018).

121. Clayton, A. D. *et al.* Algorithms for the self-optimisation of chemical reactions. *React. Chem. Eng.* **4,** 1545–1554 (2019).

122. Leardi, R. Experimental design in chemistry: A tutorial. *Anal. Chim. Acta* **652,** 161–172 (2009).

123. Lee, R. Statistical Design of Experiments for Screening and Optimization. *Chem. Ing. Tech.* **91,** 191–200 (2019).

124. Lazic, Z. R. *Design of Experiments in Chemical Engineering: A Practical Guide* p. 623 (Wiley-VCH, 2006).

125. Reizman, B. J. & Jensen, K. F. Simultaneous solvent screening and reaction optimization in microliter slugs. *Chem. Commun.* **51,** 13290–13293 (2015).

126. McMullen, J. P. & Jensen, K. F. An Automated Microfluidic System for Online Optimization in Chemical Synthesis. *Org. Process Res. Dev.* **14,** 1169–1176 (2010).

127. Moore, J. S. & Jensen, K. F. Automated multitrajectory method for reaction optimization in a microfluidic system using online IR analysis. *Org. Process Res. Dev.* **16,** 1409–1415 (2012).

128. Krishnadasan, S., Brown, R. J., DeMello, A. J. & DeMello, J. C. Intelligent routes to the controlled synthesis of nanoparticles. *Lab Chip* **7,** 1434–1441 (2007).

129. Skilton, R. A., Parrott, A. J., George, M. W., Poliakoff, M. & Bourne, R. A. Real-Time Feedback Control Using Online Attenuated Total Reflection Fourier Transform Infrared (ATR FT-IR) Spectroscopy for Continuous Flow Optimization and Process Knowledge. *Appl. Spectrosc.* **67,** 1127–1131 (2013).

130. Cherkasov, N., Bai, Y., Expósito, A. J. & Rebrov, E. V. OpenFlowChem-a platform for quick, robust and flexible automation and self-optimisation of flow chemistry. *React. Chem. Eng.* **3,** 769–780 (2018).

131. Holmes, N. *et al.* Self-optimisation of the final stage in the synthesis of EGFR kinase inhibitor AZD9291 using an automated flow reactor. *React. Chem. Eng.* **1,** 366–371 (2016).

132. Holmes, N. *et al.* Online quantitative mass spectrometry for the rapid adaptive optimisation of automated flow reactors. *React. Chem. Eng.* **1,** 96–100 (2016).

133. Schweidtmann, A. M. *et al.* Machine learning meets continuous flow chemistry: Automated optimization towards the Pareto front of multiple objectives. *Chem. Eng. J.* **352,** 277–282 (2018).

134. Kondo, M. *et al.* Exploration of flow reaction conditions using machine-learning for enantioselective organocatalyzed Rauhut-Currier and [3+2] annulation sequence. *Chem. Commun.* **56,** 1259–1262 (2020).

135. Mateos, C., Nieves-Remacha, M. J. & Rincón, J. A. Automated platforms for reaction self-optimization in flow. *React. Chem. Eng.* **4,** 1536–1544 (2019).

136. Yano, M. *nelder_mead* `https://github.com/owruby/nelder_mead` (2021).

137. Plotly Technologies Inc. *Collaborative data science* `https://plot.ly` (2015).

138. Br3ttb. *Arduino-PID-Library* `https://github.com/br3ttb/Arduino-PID-Library` (2021).

139. Hunter, J. D. Matplotlib: A 2D graphics environment. *Comput. Sci. Eng.* **9,** 90–95 (2007).

140. Nastke, A. unpublished results (2021).

141. Davies, A. N. & Lampen, P. JCAMP-DX for NMR. *Appl. Spectrosc.* **47,** 1093–1099 (1993).

142. Helmus, J. J. & Jaroniec, C. P. Nmrglue: An open source Python package for the analysis of multidimensional NMR data. *J. Biomol. NMR* **55,** 355–367 (2013).

143. Helmus, J. J. *nmrglue* `https://github.com/jjhelmus/nmrglue` (2021).

144. *nmrglue; Reading Magritek Jcamp #117* `https://github.com/jjhelmus/nmrglue/issues/117` (2021).

145. Yeh, K. C. & Kwan, K. C. A comparison of numerical integrating algorithms by trapezoidal, Lagrange, and spline approximation. *J. Pharmacokinet. Pharmacodyn.* **6,** 79–98 (1978).

146. *Ullmann's Encyclopedia of Industrial Chemistry* (Wiley-VCH, 2010).

147. Arthur, P., England, D. C., Pratt, B. C. & Whitman, G. M. Addition of Hydrogen Cyanide to Unsaturated Compounds. *J. Am. Chem. Soc.* **76,** 5364–5367 (1954).

148. Nagata, W. & Yoshioka, M. in *Organic Reactions* pp. 255–476 (John Wiley & Sons, 1977).

149. Tolman, C. A. Steric and electronic effects in olefin hydrocyanation at du pont: A scientific and industrial success story. *J. Chem. Educ.* **63,** 199–201 (1986).

150. Schuppe, A. W., Borrajo-Calleja, G. M. & Buchwald, S. L. Enantioselective Olefin Hydrocyanation without Cyanide. *J. Am. Chem. Soc.* **141,** 18668–18672 (2019).

151. Callahan, J. L., Grasselli, R. K., Milberger, E. C. & Strecker, H. A. Oxidation and Ammoxidation of Propylene over Bismuth Molybdate Catalyst. *Ind. Eng. Chem. Res.* **9,** 134–142 (1970).

152. Grasselli, R. K. & Trifirò, F. Acrylonitrile from Biomass: Still Far from Being a Sustainable Process. *Top. Catal.* **59,** 1651–1658 (2016).

153. Jagadeesh, R. V., Junge, H. & Beller, M. Green synthesis of nitriles using non-noble metal oxides-based nanocatalysts. *Nat. Commun.* **5,** 4123 (2014).

154. Dennis, W. E. Nitrile Synthesis. The Dehydration of Amides by Silazanes, Chlorosilanes, Alkoxysilanes, and Aminosilanes. *J. Org. Chem.* **35,** 3253–3255 (1970).

155. Zhou, S., Junge, K., Addis, D., Das, S. & Beller, M. A general and convenient catalytic synthesis of nitriles from amides and silanes. *Org. Lett.* **11,** 2461–2464 (2009).

156. Yin, W., Wang, C. & Huang, Y. Highly practical synthesis of nitriles and heterocycles from alcohols under mild conditions by aerobic double dehydrogenative catalysis. *Org. Lett.* **15,** 1850–1853 (2013).

157. Betke, T., Rommelmann, P., Oike, K., Asano, Y. & Gröger, H. Cyanide-Free and Broadly Applicable Enantioselective Synthetic Platform for Chiral Nitriles through a Biocatalytic Approach. *Angew. Chem. Int. Ed.* **56,** 12361–12366 (2017).

158. Betke, T., Maier, M., Gruber-Wölfler, H. & Gröger, H. Biocatalytic production of adiponitrile and related aliphatic linear α,ω-dinitriles. *Nat. Commun.* **9,** 5112 (2018).

159. Hinzmann, A., Glinski, S., Worm, M. & Gröger, H. Enzymatic Synthesis of Aliphatic Nitriles at a Substrate Loading of up to 1.4 kg/L: A Biocatalytic Record Achieved with a Heme Protein. *J. Org. Chem.* **84,** 4867–4872 (2019).

160. Betke, T. *et al.* Biocatalytic Synthesis of Nitriles through Dehydration of Aldoximes: The Substrate Scope of Aldoxime Dehydratases. *ChemBioChem* **19,** 768–779 (2018).

161. Asano, Y. & Kato, Y. Z -phenylacetaldoxime degradation by a novel aldoxime dehydratase from Bacillus sp. strain OxB-1. *FEMS Microbiol. Lett.* **158,** 185–190 (1998).

162. Kato, Y., Ooi, R. & Asano, Y. A new enzymatic method of nitrile synthesis by Rhodococcus sp. strain YH3-3. *J. Mol. Catal. B Enzym.* **6,** 249–256 (1999).

163. Hinzmann, A., Stricker, M. & Gröger, H. Chemoenzymatic cascades toward aliphatic nitriles starting from biorenewable feedstocks. *ACS Sustain. Chem. Eng.* **8,** 17088–17096 (2020).

164. Plass, C. *et al.* Approaching Bulk Chemical Nitriles from Alkenes: A Hydrogen Cyanide-Free Approach through a Combination of Hydroformylation and Biocatalysis. *ACS Catal.* **9,** 5198–5203 (2019).

165. Hinzmann, A., Adebar, N., Betke, T., Leppin, M. & Gröger, H. Biotransformations in Pure Organic Medium: Organic Solvent-Labile Enzymes in the Batch and Flow Synthesis of Nitriles. *Eur. J. Org. Chem.,* 6911–6916 (2019).

166. Bago Rodriguez, A. M., Schober, L., Hinzmann, A., Gröger, H. & Binks, B. P. Effect of Particle Wettability and Particle Concentration on the Enzymatic Dehydration of n-Octanaloxime in Pickering Emulsions. *Angew. Chem. Int. Ed.* **60,** 1450–1457 (2021).

167. Choi, J. E., Shinoda, S., Asano, Y. & Gröger, H. Aldoxime dehydratase mutants as improved biocatalysts for a sustainable synthesis of biorenewables-based 2-furonitrile. *Catalysts* **10,** 362 (2020).

168. Yavuzer, H., Gröger, H. & Asano, Y. Rationalizing the unprecedented stereochemistry of an enzymatic nitrile synthesis through a combined computational and experimental approach. *Angew. Chem. Int. Ed.* **60,** 19162–19168 (2021).

169. Adebar, N., Nastke, A., Löwe, J. & Gröger, H. Segmented Flow Processes to Overcome Hurdles of Whole-Cell Biocatalysis in the Presence of Organic Solvents. *Angew. Chem. Int. Ed.* **60,** 15863–15869 (2021).

170. Sagandira, M. B., Sagandira, C. R. & Watts, P. Continuous flow synthesis of xylidines via biphasic nitration of xylenes and nitroreduction. *J. Flow Chem.* **11,** 193–208 (2021).

171. Sagandira, C. R. & Watts, P. A study on the scale-up of acyl azide synthesis in various continuous flow reactors in homogeneous and biphasic systems. *J. Flow Chem.* **8,** 69–79 (2018).

172. Von Keutz, T., Cantillo, D. & Kappe, C. O. Enhanced mixing of biphasic liquid-liquid systems for the synthesis of gem-dihalocyclopropanes using packed bed reactors. *J. Flow Chem.* **9,** 27–34 (2019).

173. Ahmed-Omer, B., Barrow, D. & Wirth, T. Effect of segmented fluid flow, sonication and phase transfer catalysis on biphasic reactions in capillary microreactors. *Chem. Eng. J.* **135,** S280–S283 (2008).

174. Chow, E. *et al.* Flow-controlled synthesis of gold nanoparticles in a biphasic system with inline liquid-liquid separation. *React. Chem. Eng.* **5,** 356–366 (2020).

175. De Zani, D. & Colombo, M. Phase-transfer catalysis under continuous flow conditions: An alternative approach to the biphasic liquid/liquid O-Alkylation of phenols. *J. Flow Chem.* **2,** 5–7 (2012).

176. Mellouli, S., Bousekkine, L., Theberge, A. B. & Huck, W. T. S. Investigation of "On Water" Conditions Using a Biphasic Fluidic Platform. *Angew. Chem. Int. Ed.* **51,** 7981–7984 (2012).

177. Wang, S., Patehebieke, Y., Zhou, Z., Zhang, Z. & Wang, X. Catalyst-free biphasic oxidation of Thiophenes in continuous-flow. *J. Flow Chem.* **10,** 597–603 (2020).

178. Liu, Y., Zhao, Q., Yue, J., Yao, C. & Chen, G. Effect of mixing on mass transfer characterization in continuous slugs and dispersed droplets in biphasic slug flow microreactors. *Chem. Eng. J.* **406,** 126885 (2021).

179. Zhang, M. *et al.* Compartmentalized Droplets for Continuous Flow Liquid-Liquid Interface Catalysis. *J. Am. Chem. Soc.* **138,** 10173–10183 (2016).

180. Matsumoto, H., Hoshino, Y., Iwai, T., Sawamura, M. & Miura, Y. Polystyrene-Cross-Linking Triphenylphosphine on a Porous Monolith: Enhanced Catalytic Activity for Aryl Chloride Cross-Coupling in Biphasic Flow. *Ind. Eng. Chem. Res.* **59,** 15179–15187 (2020).

181. Bogdan, A. & McQuade, D. T. A biphasic oxidation of alcohols to aldehydes and ketones using a simplified packed-bed microreactor. *Beilstein J. Org. Chem.* **5,** 17 (2009).

182. Abolhasani, M., Bruno, N. C. & Jensen, K. F. Oscillatory three-phase flow reactor for studies of bi-phasic catalytic reactions. *Chem. Commun.* **51,** 8916–8919 (2015).

183. Hwang, Y. J. *et al.* A segmented flow platform for on-demand medicinal chemistry and compound synthesis in oscillating droplets. *Chem. Commun.* **53,** 6649–6652 (2017).

184. Yoshida, A., Hao, X. & Nishikido, J. Development of the continuous-flow reaction system based on the Lewis acid-catalysed reactions in a fluorous biphasic system. *Green Chem.* **5,** 554–557 (2003).

185. Kendall, A. J. *et al.* Highly efficient biphasic ozonolysis of alkenes using a high-throughput film-shear flow reactor. *Tetrahedron Lett.* **57,** 1342–1345 (2016).

186. Hosoya, M., Manaka, A., Nishijima, S. & Tsuno, N. Development of a Liquid-Liquid Biphasic Reaction Using a Taylor Vortex Flow Reactor. *Asian J. Org. Chem.* **10,** 1414–1418 (2021).

187. Schachtner, J., Bayer, P. & Von Wangelin, A. J. A flow reactor setup for photochemistry of biphasic gas/liquid reactions. *Beilstein J. Org. Chem.* **12,** 1798–1811 (2016).

188. Weeranoppanant, N. Enabling tools for continuous-flow biphasic liquid-liquid reaction. *React. Chem. Eng.* **4,** 235–243 (2019).

189. Mo, Y., Lin, H. & Jensen, K. F. High-performance miniature CSTR for biphasic C–C bond-forming reactions. *Chem. Eng. J.* **335,** 936–944 (2018).

190. Adamo, A., Heider, P. L., Weeranoppanant, N. & Jensen, K. F. Membrane-Based, Liquid–Liquid Separator with Integrated Pressure Control. *Ind. Eng. Chem. Res.* **52,** 10802–10808 (2013).

191. O'Brien, M., Koos, P., Browne, D. L. & Ley, S. V. A prototype continuous-flow liquid-liquid extraction system using open-source technology. *Org. Biomol. Chem.* **10,** 7031–7036 (2012).

192. O'Brien, M. & Cooper, D. Continuous Flow Liquid–Liquid Separation Using a Computer-Vision Control System: The Bromination of Enaminones with N-Bromosuccinimide. *Synlett* **27,** 164–168 (2015).

193. Allison, G. *et al.* Regulatory and Quality Considerations for Continuous Manufacturing May 20–21, 2014 Continuous Manufacturing Symposium. *J. Pharm. Sci.* **104,** 803–812 (2015).

194. Lee, S. L. *et al.* Modernizing Pharmaceutical Manufacturing: from Batch to Continuous Production. *J. Pharm. Innov.* **10,** 191–199 (2015).

195. Sagmeister, P. *et al.* Advanced Real-Time Process Analytics for Multistep Synthesis in Continuous Flow**. *Angew. Chem. Int. Ed.* **60,** 8139–8148 (2021).

196. Hessel, V., Kralisch, D., Kockmann, N., Noël, T. & Wang, Q. Novel process windows for enabling, accelerating, and uplifting flow chemistry. *ChemSusChem* **6,** 746–789 (2013).

197. Huynh, F. *et al.* Accelerating Biphasic Biocatalysis through New Process Windows. *Angew. Chem. Int. Ed.* **59,** 16490–16495 (2020).

198. *Flow Chemistry Volume 1: Fundermentals* (eds Darvas, F., Hessel, V. & Dorman, G.) (De Gruyter, 2014).

199. Znidar, D. *et al.* Scalable Wolff-Kishner Reductions in Extreme Process Windows Using a Silicon Carbide Flow Reactor. *Org. Process Res. Dev.* **23,** 2445–2455 (2019).

200. Woitalka, A., Kuhn, S. & Jensen, K. F. Scalability of mass transfer in liquid-liquid flow. *Chem. Eng. Sci.* **116,** 1–8 (2014).

201. Movsisyan, M. *et al.* Taming hazardous chemistry by continuous flow technology. *Chem. Soc. Rev.* **45,** 4892–4928 (2016).

202. Müller, S., Smith, D., Hellier, P. & Wirth, T. Safe Generation and Direct Use of Diazoesters in Flow Chemistry. *Synlett* **25,** 871–875 (2014).

203. Müller, S. T. R. *et al.* Rapid Generation and Safe Use of Carbenes Enabled by a Novel Flow Protocol with In-line IR spectroscopy. *Chem. Eur. J.* **21,** 7016–7020 (2015).

204. Winterson, B., Rennigholtz, T. & Wirth, T. Flow electrochemistry: a safe tool for fluorine chemistry. *Chem. Sci.* **12,** 9053–9059 (2021).

205. Rebrov, E. V., De Croon, M. H. & Schouten, J. C. Design of a microstructured reactor with integrated heat-exchanger for optimum performance of a highly exothermic reaction. *Catal. Today* **69,** 183–192 (2001).

206. Brahma, A. *et al.* An orthogonal biocatalytic approach for the safe generation and use of HCN in a multistep continuous preparation of chiral O-acetylcyanohydrins. *Synlett* **27,** 262–266 (2016).

207. Adebar, N., Nastke, A. & Gröger, H. Concepts for flow chemistry with whole-cell biocatalysts. *React. Chem. Eng.* **6,** 977–988 (2021).

208. Adebar, N. *et al.* Overcoming Work-Up Limitations of Biphasic Biocatalytic Reaction Mixtures Through Liquid-Liquid Segmented Flow Processes. *ChemCatChem* **11,** 5788–5793 (2019).

209. Karande, R., Schmid, A. & Buehler, K. Miniaturizing biocatalysis: Enzyme-catalyzed reactions in an aqueous/organic segmented flow capillary microreactor. *Adv. Synth. Catal.* **353,** 2511–2521 (2011).

210. Tamborini, L., Fernandes, P., Paradisi, F. & Molinari, F. Flow Bioreactors as Complementary Tools for Biocatalytic Process Intensification. *Trends Biotechnol.* **36,** 73–88 (2018).

211. De Santis, P., Meyer, L.-E. & Kara, S. The rise of continuous flow biocatalysis – fundamentals, very recent developments and future perspectives. *React. Chem. Eng.* **5,** 2155–2184 (2020).

212. Žnidaršič-Plazl, P. Let the biocatalyst flow. *Acta Chim. Slov.* **68,** 1–16 (2021).

213. Santi, M. *et al.* Flow Biocatalysis: A Challenging Alternative for the Synthesis of APIs and Natural Compounds. *Int. J. Mol. Sci.* **22,** 990 (2021).

214. Benítez-Mateos, A. I., Contente, M. L., Roura Padrosa, D. & Paradisi, F. Flow biocatalysis 101: Design, development and applications. *React. Chem. Eng.* **6,** 599–611 (2021).

215. Britton, J., Majumdar, S. & Weiss, G. A. Continuous flow biocatalysis. *Chem. Soc. Rev.* **47,** 5891–5918 (2018).

216. Clayton, A. D., Labes, R. & Blacker, A. J. Combination of chemocatalysis and biocatalysis in flow. *Curr. Opin. Green Sustain. Chem.* **26,** 100378 (2020).

217. Fernandes, P. Miniaturization in biocatalysis. *Int. J. Mol. Sci.* **11,** 858–879 (2010).

218. Palma, B. G., Nascimento, M. A., Leão, R. A. C., Pandoli, O. G. & Souza, R. O. M. A. in *Biocatalysis for Practitioners* pp. 297–315 (John Wiley & Sons, 2021).

219. Bolivar, J. M. & López-Gallego, F. Characterization and evaluation of immobilized enzymes for applications in flow reactors. *Curr. Opin. Green Sustain. Chem.* **25,** 100349 (2020).

220. Jiao, J. *et al.* Multi-Step Continuous-Flow Organic Synthesis: Opportunities and Challenges. *Chem. Eur. J.* **27,** 4817–4838 (2021).

221. Bloemendal, V. R., Janssen, M. A., Van Hest, J. C. & Rutjes, F. P. Continuous one-flow multi-step synthesis of active pharmaceutical ingredients. *React. Chem. Eng.* **5,** 1186–1197 (2020).

222. Britton, J. & Raston, C. L. Multi-step continuous-flow synthesis. *Chem. Soc. Rev.* **46,** 1250–1271 (2017).

223. Baxendale, I. R. & Ley, S. V. in *Ernst Schering Foundation symposium proceedings* 3, pp. 151–185 (Springer, 2006).

224. Adamo, A. *et al.* On-demand continuous-flow production of pharmaceuticals in a compact, reconfigurable system. *Science* **352,** 61–67 (2016).

225. Mascia, S. *et al.* Continuous Drug Manufacturing Hot Paper End-to-End Continuous Manufacturing of Pharmaceuticals: Integrated Synthesis, Purification, and Final Dosage Formation**. *Angew. Chem. Int. Ed* **52,** 1–6 (2013).

226. Rudroff, F. *et al.* Opportunities and challenges for combining chemo- and biocatalysis. *Nat. Catal.* **1,** 12–22 (2018).

227. Gröger, H. & Hummel, W. Combining the 'two worlds' of chemocatalysis and biocatalysis towards multi-step one-pot processes in aqueous media. *Curr. Opin. Chem. Biol.* **19,** 171–179 (2014).

228. Bisogno, F. R., López-Vidal, M. G. & de Gonzalo, G. Organocatalysis and Biocatalysis Hand in Hand: Combining Catalysts in One-Pot Procedures. *Adv. Synth. Catal.* **359,** 2026–2049 (2017).

229. Burda, E., Hummel, W. & Gröger, H. Modular chemoenzymatic one-pot syntheses in aqueous media: Combination of a palladium-catalyzed cross-coupling with an asymmetric biotransformation. *Angew. Chem. Int. Ed.* **47,** 9551–9554 (2008).

230. Litman, Z. C., Wang, Y., Zhao, H. & Hartwig, J. F. Cooperative asymmetric reactions combining photocatalysis and enzymatic catalysis. *Nature* **560,** 355–359 (2018).

231. Grabner, B., Schweiger, A. K., Gavric, K., Kourist, R. & Gruber-Woelfler, H. A chemo-enzymatic tandem reaction in a mixture of deep eutectic solvent and water in continuous flow. *React. Chem. Eng.* **5,** 263–269 (2020).

232. Döbber, J., Pohl, M., Ley, S. V. & Musio, B. Rapid, selective and stable HaloTag-Lb ADH immobilization directly from crude cell extract for the continuous biocatalytic production of chiral alcohols and epoxides. *React. Chem. Eng.* **3,** 8–12 (2018).

233. Fernandes, P. & de Carvalho, C. C. Multi-enzyme systems in flow chemistry. *Processes* **9,** 1–23 (2021).

234. Nagy-Győr, L. *et al.* Co-immobilized Whole Cells with ω-Transaminase and Ketoreductase Activities for Continuous-Flow Cascade Reactions. *ChemBioChem* **19,** 1845–1848 (2018).

235. Döbber, J., Gerlach, T., Offermann, H., Rother, D. & Pohl, M. Closing the gap for efficient immobilization of biocatalysts in continuous processes: HaloTag™ fusion enzymes for a continuous enzymatic cascade towards a vicinal chiral diol. *Green Chem.* **20,** 544–552 (2018).

236. Gruber, P. *et al.* Enzymatic synthesis of chiral amino-alcohols by coupling transketolase and transaminase-catalyzed reactions in a cascading continuous-flow microreactor system. *Biotechnol. Bioeng.* **115,** 586–596 (2018).

237. Babich, L., Hartog, A. F., Van Hemert, L. J., Rutjes, F. P. & Wever, R. Synthesis of carbohydrates in a continuous flow reactor by immobilized phosphatase and aldolase. *ChemSusChem* **5,** 2348–2353 (2012).

238. Finnigan, W., Citoler, J., Cosgrove, S. C. & Turner, N. J. Rapid Model-Based Optimization of a Two-Enzyme System for Continuous Reductive Amination in Flow. *Org. Process Res. Dev.* **24,** 1969–1977 (2020).

239. Romero-Fernandez, M. & Paradisi, F. Biocatalytic access to betazole using a one-pot multienzymatic system in continuous flow. *Green Chem.* **23,** 4594–4603 (2021).

240. Jacquet, P. & Draye, J. P. Toxicity of chromium salts to cultured mouse embryos. *Toxicol. Lett.* **12,** 53–57 (1982).

241. Omura, K. & Swern, D. Oxidation of alcohols by "activated" dimethyl sulfoxide. a preparative, steric and mechanistic study. *Tetrahedron* **34,** 1651–1660 (1978).

242. Kawaguchi, T., Miyata, H., Ataka, K., Mae, K. & Yoshida, J.-i. Room-Temperature Swern Oxidations by Using a Microscale Flow System. *Angew. Chem. Int. Ed.* **117,** 2465–2468 (2005).

243. Wu, A., Yang, W. & Pan, X. Preparation of triacetoneamine, an improved method. *Synth. Commun.* **26,** 3565–3569 (1996).

244. Anelli, P. L., Biffi, C., Montanari, F. & Quici, S. Fast and Selective Oxidation of Primary Alcohols to Aldehydes or to Carboxylic Acids and of Secondary Alcohols to Ketones Mediated by Oxoammonium Salts under Two-Phase Conditions. *J. Org. Chem.* **52,** 2559–2562 (1987).

245. Anelli, P. L., Banfi, S., Montanari, F. & Quici, S. Oxidation of Diols with Alkali Hypochlorites Catalyzed by Oxammonium Salts under Two-Phase Conditions. *J. Org. Chem.* **54,** 2970–2972 (1989).

246. Hinzmann, A. *et al.* Selective TEMPO-Oxidation of Alcohols to Aldehydes in Alternative Organic Solvents. *Eur. J. Org. Chem.,* 2399–2408 (2020).

247. Hamlin, T. A. *et al.* Toward a Unified Mechanism for Oxoammonium Salt-Mediated Oxidation Reactions: A Theoretical and Experimental Study Using a Hydride Transfer Model. *J. Org. Chem.* **80,** 8150–8167 (2015).

248. Leduc, A. B. & Jamison, T. F. Continuous flow oxidation of alcohols and aldehydes utilizing bleach and catalytic tetrabutylammonium bromide. *Org. Process Res. Dev.* **16,** 1082–1089 (2012).

249. Vanoye, L. *et al.* Continuous flow oxidation of benzylic and aliphatic alcohols using bleach: Process improvement by precise pH adjustment in flow with CO2. *React. Chem. Eng.* **3,** 188–194 (2018).

250. Greene, J. F., Hoover, J. M., Mannel, D. S., Root, T. W. & Stahl, S. S. Continuous-Flow Aerobic Oxidation of Primary Alcohols with a Copper(I)/TEMPO Catalyst. *Org. Process Res. Dev.* **17,** 1247–1251 (2013).

251. Ambreen, N., Kumar, R. & Wirth, T. Hypervalent iodine/TEMPO-mediated oxidation in flow systems: A fast and efficient protocol for alcohol oxidation. *Beilstein J. Org. Chem.* **9,** 1437–1442 (2013).

252. Hill-Cousins, J. T. *et al.* TEMPO-Mediated Electrooxidation of Primary and Secondary Alcohols in a Microfluidic Electrolytic Cell. *ChemSusChem* **5,** 326–331 (2012).

253. Dayagi, S. & Degani, Y. in *Carbon-Nitrogen Double Bonds (1970)* pp. 61–147 (John Wiley & Sons, 1970).

254. Adebar, N. & Gröger, H. Heterogeneous Catalysts "on the Move": Flow Chemistry with Fluid Immobilised (Bio)Catalysts. *Eur. J. Org. Chem.,* 6062–6067 (2020).

255. Gal, J. Pasteur and the art of chirality. *Nat. Chem.* **9,** 604–605 (2017).

256. Pasteur, L. Sur les relations qui peuvent exister entre la forme cristalline, la composition chimique et le sens de la polarisation rotatoire. *Ann. Chim. Phys.* **24,** 442–459 (1848).

257. Friedman, L. & Miller, J. G. Odor incongruity and chirality. *Science* **172,** 1044–1046 (1971).

258. H. Brooks, W., C. Guida, W. & G. Daniel, K. The Significance of Chirality in Drug Design and Development. *Curr. Top. Med. Chem.* **11,** 760–770 (2011).

259. Kagan, H. B. & Gopalaiah, K. Early history of asymmetric synthesis: Who are the scientists who set up the basic principles and the first experiments? *New J. Chem.* **35,** 1933–1937 (2011).

260. Gawley, R. E. & Aubé, J. in *Principles of Asymmetric Synthesis* pp. 1–62 (Elsevier, 2012).

261. Ward, R. S. Dynamic kinetic resolution. *Tetrahedron Asymmetry* **6,** 1475–1490 (1995).

262. Pàmies, O. & Bäckvall, J. E. Combination of enzymes and metal catalysts. A powerful approach in asymmetric catalysis. *Chem. Rev.* **103,** 3247–3261 (2003).

263. Vedejs, E. & Jure, M. Efficiency in nonenzymatic kinetic resolution. *Angew. Chem. Int. Ed.* **44,** 3974–4001 (2005).

264. Pellissier, H. Recent developments in non-enzymatic catalytic oxidative kinetic resolution of secondary alcohols. *Tetrahedron* **74,** 3459–3468 (2018).

265. Kirchner, G., Scollar, M. P. & Klibanov, A. M. Resolution of Racemic Mixtures via Lipase Catalysis in Organic Solvents. *J. Am. Chem. Soc.* **107,** 7072–7076 (1985).

266. Ghanem, A. & Aboul-Enein, H. Y. Lipase-mediated chiral resolution of racemates in organic solvents. *Tetrahedron Asymmetry* **15,** 3331–3351 (2004).

267. Huerta, F. F., Minidis, A. B. & Bäckvall, J. E. Racemisation in asymmetric synthesis. Dynamic kinetic resolution and related processes in enzyme and metal catalysis. *Chem. Soc. Rev.* **30,** 321–331 (2001).

268. Persson, B. A., Larsson, A. L., Le Ray, M. & Bäckvall, J. E. Ruthenium- and enzyme-catalyzed dynamic kinetic resolution of secondary alcohols. *J. Am. Chem. Soc.* **121,** 1645–1650 (1999).

269. Moustafa, G. A., Oki, Y. & Akai, S. Lipase-Catalyzed Dynamic Kinetic Resolution of C1- and C2-Symmetric Racemic Axially Chiral 2,2'-Dihydroxy-1,1'-biaryls. *Angew. Chem. Int. Ed.* **57,** 10278–10282 (2018).

270. Richardson, M. F. & Warren, F. L. The Senecio alkaloids. Part I. Rosmarinine. *J. Chem. Soc.,* 452–454 (1943).

271. Nemoto, H. *et al.* Protecting-group-free catalytic asymmetric total synthesis of (–)-rosmarinecine. *Tetrahedron* **68,** 7295–7301 (2012).

272. Faulds, D., Hollingshead, L. M. & Goa, K. L. Formoterol: A Review of its Pharmacological Properties and Therapeutic Potential in Reversible Obstructive Airways Disease. *Drugs* **42,** 115–137 (1991).

273. Kawanishi, S., Sugiyama, K., Oki, Y., Ikawa, T. & Akai, S. Preparation of optically active cycloalkenes bearing all-carbon quaternary stereogenic centres: Via lipase-oxovanadium combo-catalysed dynamic kinetic resolution. *Green Chem.* **19,** 411–417 (2017).

274. Sugiyama, K. *et al.* Lipase-catalyzed asymmetric synthesis of naphtho[2,3-c]furan-1(3H)-one derivatives by a one-pot dynamic kinetic resolution/intramolecular Diels–Alder reaction: Total synthesis of (–)-himbacine. *Bioorg. Med. Chem.* **26,** 1378–1386 (2018).

275. Sugiyama, K. *et al.* Spatial effects of oxovanadium-immobilized mesoporous silica on racemization of alcohols and application in lipase-catalyzed dynamic kinetic resolution. *Catal. Sci. Technol.* **6,** 5023–5030 (2016).

276. Akai, S., Hanada, R., Fujiwara, N., Kita, Y. & Egi, M. One-pot synthesis of optically active allyl esters via lipase-vanadium combo catalysis. *Org. Lett.* **12,** 4900–4903 (2010).

277. Akai, S. *et al.* A dynamic kinetic resolution of allyl alcohols by the combined use of lipases and [VO(OSiPh3)3]. *Angew. Chem. Int. Ed.* **45,** 2592–2595 (2006).

278. Higashio, K. *et al.* Continuous-Flow Dynamic Kinetic Resolution of Racemic Alcohols by Lipase–Oxovanadium Cocatalysis. *Eur. J. Org. Chem.,* 1961–1967 (2020).

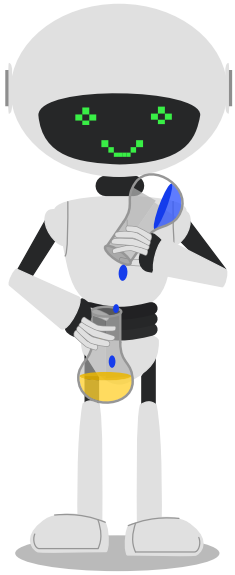

"The best way to predict your future is to create it."

– Abraham Lincoln

Appendix A: Gene sequences

Oxd from *Bacillus* sp. OxB-1 (OxdB)

(Accession number: GenBank: AP013294.1)
Vector: pET21
Nucleic acid sequence:
ATGAAAAATATGCCGGAAAATCACAATCCACAAGCGAATGCCTGGAC
TGCCGAATTTCCTCCTGAAATGAGCTATGTAGTATTTGCGCAGATTG
GGATTCAAAGCAAGTCTTTGGATCACGCAGCGGAACATTTGGGAAT
GATGAAAAAGAGTTTCGATTTGCGGACAGGCCCCAAACATGTGGAT
CGAGCCTTGCATCAAGGAGCCGATGGATACCAAGATTCCATCTTTTT
AGCCTACTGGGATGAGCCTGAAACATTTAAATCATGGGTTGCGGAT
CCTGAAGTACAAAAGTGGTGGTCGGGTAAAAAAATCGATGAAAATA
GTCCAATCGGGTATTGGAGTGAGGTAACGACCATTCCGATTGATCA
CTTTGAGACTCTTCATTCCGGAGAAAATTACGATAATGGGGTTTCAC
ACTTTGTACCGATCAAGCATACAGAAGTCCATGAATATTGGGGAGCA
ATGCGCGACCGCATGCCGGTGTCTGCCAGTAGTGATTTGGAAAGCC
CCCTTGGCCTTCAATTACCGGAACCCATTGTCCGGGAGTCTTTCGGA
AAACGGCTAAAAGTCACGGCGCCGGATAATATTTGCTTGATTCGAAC
CGCTCAAAATTGGTCTAAATGTGGTAGCGGGGAAAGGGAAACGTAT
ATAGGACTAGTGGAACCGACCCTCATAAAAGCGAATACGTTTCTTCG
TGAAAATGCTAGTGAAACAGGCTGTATTAGTTCAAAATTAGTCTATG
AACAGACCCATGACGGCGAAATAGTAGATAAATCATGTGTCATCGG
ATATTATCTCTCCATGGGGCATCTTGAACGCTGGACGCATGATCATC
CAACACATAAAGCGATCTACGGAACCTTTTATGAGATGTTGAAAAGG
CATGATTTTAAGACCGAACTTGCTTTATGGCACGAGGTTTCGGTGCT
TCAATCCAAAGATATCGAGCTTATCTATGTCAACTGCCATCCGAGTA
CTGGATTTCTTCCATTCTTTGAAGTGACAGAAATTCAAGAGCCTTTA
CTGAAAAGCCCTAGCGTCAGGATCCAGTGA

Amino acid sequence:
MKNMPENHNPQANAWTAEFPPEMSYVVFAQIGIQSKSLDHAAEHLGMM
KKSFDLRTGPKHVDRALHQGADGYQDSIFLAYWDEPETFKSWVADPEV
QKWWSGKKIDENSPIGYWSEVTTIPIDHFETLHSGENYDNGVSHFVPIKH
TEVHEYWGAMRDRMPVSASSDLESPLGLQLPEPIVRESFGKRLKVTAPD
NICLIRTAQNWSKCGSGERETYIGLVEPTLIKANTFLRENASETGCISSKL
VYEQTHDGEIVDKSCVIGYYLSMGHLERWTHDHPTHKAIYGTFYEMLK

RHDFKTELALWHEVSVLQSKDIELIYVNCHPSTGFLPFFEVTEIQEPLLKS
PSVRIQ

Appendix B: Code availability

Sofalab software and hardware requirements

Raspberry Pi 4B or 3B with Raspbian GNU/Linux 10 (buster)

Python Version 3.7.3

Python packages: Flask 1.0.2, Flask-SocketIO 4.3.2, Flask-HTTPAuth 4.4.0, Werkzeug 0.14.1, numpy 1.16.2, scipy 1.7.0, nmrglue 0.8, pyserial 3.4, matplotlib 3.4.2

CSS Libraries: Bootstrap 4.3.1

JS Libraries: Bootstrap 4.3.1, plotly 1.8.0, socket 1.7.3

Install the server for *sofalab*

Operating System

Please follow the following instructions to install an operating system (OS) on the Raspberry Pi.

1. Download Raspberry Pi Imager
2. Format SD card (FAT32). exFAT, which is commonly used for larger cards will not work
3. Start Raspberry Pi Imager
4. Select OS: For sofalab, Raspberry Pi OS with desktop is recommended; Kernel version: 5.10 was used for development of sofalab
5. Select the micro-SD card
6. Press write to write the OS on the SD card
7. When finished: Remove SD card and insert into Raspberry Pi

Booting the System

1. Connect to screen (must be done before switched on), keyboard/-mouse, and connect to network with ethernet cable
2. Power on the Raspberry Pi (plug in power supply)
3. Follow instructions to set up

Update & Setup

1. Set up new password if not done. Open terminal and type `passwd` (default password is "raspberry" for the user "pi")
2. Load and install updates

   Open terminal and enter `sudo apt update`

   Enter `sudo apt full-upgrade`
3. Set up SSH

   Open terminal and enter `sudo systemctl enable ssh`

   Enter `sudo systemctl start ssh`

   Start SSH server `sudo /etc/init.d/ssh start`

   To automatically start SSH server: `sudo update-rc.d ssh defaults`

Increase security

See also in the Raspberry documentation here:
(https://www.raspberrypi.org/documentation/configuration/security.md).

1. Change user name (for example nik)

   To add a user enter `sudo adduser nik`

   Add user to `sudo` (admin) group and allow all necessary permissions type:

   ```
   sudo usermod -a -G adm,dialout,cdrom,sudo,audio,video,
   plugdev,games,users,input,netdev,gpio,i2c,spi,tty nik
   ```

   Check if permissions are in place `sudo su - nik`

   When the new user is working as expected, delete the user pi by typing first `sudo pkill -u pi` to close its processes and `sudo deluser pi`

   Remove the pi user files: `sudo deluser -remove-home pi`

2. Install latest security fixes

   Enter `sudo apt install openssh-server`

3. Install firewall. One simple solution is ufw (uncomplicated firewall)

   Install by typing `sudo apt install ufw`

   Activate firewall `sudo ufw enable` (and disable firewall `sudo ufw disable` if needed)

   Single ports can be allowed by `sudo ufw allow 22`

   Allow ssh if needed: `sudo ufw allow ssh`

   Limit attempts `sudo ufw limit ssh/tcp` (denies connection after six attempts for 30 s)

   Reboot system `sudo reboot`

Set up git if required

1. Install git

   Install the git code `sudo apt install git`

   Add user for git `sudo useradd -m -c "Git-Repo-User" -s $(which bash) git`

   Assign password to new user `sudo passwd git`

   Test new user `su - git`

   Create folder for repositories `mkdir -p repos`

   `exit` and `reboot sudo reboot`

3. Clone repository

   Type `sudo git clone`

   `https://github.com/USERNAME/weboptimisation.git` into terminal

   folders should appear in git/repos/ ...

Set up UART

1. Configure UART via GPIOs for GC (Shimadzu GC2010) communication

   Add user to required groups if not happened during user creation:

   Check user groups `USERNAME groups`

   If user is not in `tty` and `dialout` add user:

   `sudo adduser USERNAME dialout and/or sudo adduser USERNAME tty`

   If groups are not available create groups

   `sudo groupadd dialout` and/or `sudo groupadd tty`

2. Disable serial shell interfacing

   Start raspi config: `sudo raspi-config` at: `Would you like a login shell to be accessible over serial?` Answer: "No", at: `Would you like the serial port hardware to be enabled?` Answer: "Yes"

   Exit raspi-config and reboot the Pi for changes to take effect

Install *sofalab*

SSH connection

SSH connection can be used to control Server remotely. Also remote programming using VS Code can be done. Alternatively, all steps can be done on the Raspberry Pi itself.

Using Putty Putty is a lightweight program to connect remotely to SSH servers.

1. Find IP of raspberry Pi

   open terminal on Raspberry and type `ifconfig` to read the current IP

   IP can be found under `eth0 > intnet` if connected via ethernet cable

   If user is not in `tty` and `dialout` add user:
2. Start Putty on client device
3. Type IP and username in `Host`

Install sofalab

If the source-code is in a git repository, please follow the following steps. If local files are used only, no installation of git is required, and the files can be copied into a folder on the Raspberry Pi. Then, follow from step 2).

1. Install git and load repository (see above)
2. Check and update python

   Check python version `python -version`

   Make python 3 default by `alias python='/usr/bin/python3'`

   Make pip3 (python package management) default by `alias pip='/usr/bin/pip3'`

   Update python if <3.7.3
3. Install required python packages (see list of packages)

   `pip install flask_socketio` and other required packages
4. Run `python server.py` (or `python3 server.py` depending on installed python versions)